

Lista 10 articole relevante recente pentru obtinerea Atestatului de abilitare
Articolele studiază
proprietățile fizice ale materialelor compozite cu cristale lichide

DOINA-LUMINITA MANAILA-MAXIMEAN

1. **D. Manaila-Maximean**, “Effective Permittivity of a Multi-Phase System: Nanoparticle-Doped Polymer-Dispersed Liquid Crystal Films”, 2021. *Molecules*, 26(5), nr.art.1441. doi:10.3390/molecules26051441, WOS: 000628425600001, Q1, IF: 3,267
2. Constantin Paul Ganea, **Doina Manaila Maximean***, Viorel Cîrcu, “Dielectric investigations on carbon nanotubes doped polymer dispersed liquid crystal films”, *European Physical Journal plus*, 135, Article number: 797, 2020, DOI:10.1140/epjp/s13360-020-00795-w, WOS:000581548500002, Q1, IF=3.228
3. C.P. Ganea, V. Cîrcu, **Doina Manaila Maximean***, “Effect of titanium oxide nanoparticles on the dielectric properties and ionic conductivity of a new smectic bis-imidazolium salt with dodecyl sulfate anion and cyanobiphenyl mesogenic groups”, *Journal of Molecular Liquids*, 314, p.113939, 2020, DOI:10.1016/j.molliq.2020.113939, WOS:000580655700057, Q1, IF: 5,065
4. **D. Manaila Maximean***, O. Danila, P.L. Almeida, C.P. Ganea, Electrical properties of a liquid crystal dispersed in an electrospun cellulose acetate network. *Beilstein Journal of Nanotechnology*, 9(1), pp.155-163, (2018), doi:10.3762/bjnano.9.18 WOS:000423189900002, Q1, IF: 3.13.
5. Loiko, V.A., Konkolovich, A.V., Miskevich, A.A., **D. Manaila-Maximean**, Danila, O., Cîrcu, V., Bărar, A., Optical model to describe coherent transmittance of polymer dispersed liquid crystal film doped with carbon nanotubes. *Journal of Quantitative Spectroscopy and Radiative Transfer*, 245, p.106892, 2020 DOI:10.1016/j.jqsrt.2020.106892, WOS:000534641000027, Q1, IF=3.047
6. L. Chiriac, P. Ganea, **D. Manaila-Maximean**, I. Pasuk, V. Carcu, Synthesis and thermal, emission and dielectric properties of liquid crystalline Eu(III), Sm(III) and Tb(III) complexes based on mesogenic 4-pyridone ligands functionalized with cyanobiphenyl groups, *Journal of Molecular Liquids*, Volume 290, 15 September 2019, 111184, (2019), DOI:10.1016/j.molliq.2019.111184; WOS:000423190900001, Q1, IF: 5,065
7. **D. Manaila-Maximean***, O. Danila, C.P. Ganea, P.L. Almeida, “Filling in the voids of electrospun hydroxypropyl cellulose network: Dielectric investigations”. *The European Physical Journal Plus*, 133(4), 159. 2018, DOI:10.1140/epjp/i2018-11997-8, WOS:000431461800003, Q1, IF: 1.753
8. **D. Manaila-Maximean***, V. Cîrcu, C.P. Ganea, “Dielectric properties of a bisimidazolium salt with dodecyl sulfate anion doped with carbon nanotubes”. *Beilstein Journal of Nanotechnology*, 9(1), 164-174, 2018, DOI:10.3762/bjnano.9.19; WOS:000423190900001, Q1, IF: 3.13.
9. **D. Manaila-Maximean**, “New grafted ferrite particles/liquid crystal composite under magnetic field”, *Journal of Magnetism and Magnetic Materials*, Volume 452, 15, 343-348, 2018, DOI:10.1016/j.jmmm.2017.12.096, WOS:000425547700051, Q2, IF: 2.63,
10. **D. Mănăilă-Maximean***, C. Cîrtoaje, O. Dănilă, D. Donescu, “Novel colloidal system: Magnetite-polymer particles/lyotropic liquid crystal under magnetic field”, *Journal of Magnetism and Magnetic Materials*, 438,132-137, 2017, DOI:10.1016/j.jmmm.2017.12.096, WOS:000402480500021, Q2, IF: 2.63,

* AUTOR CORRESPONDENT

Article

Effective Permittivity of a Multi-Phase System: Nanoparticle-Doped Polymer-Dispersed Liquid Crystal Films

Doina Manaila-Maximean

Department of Physics, University Politehnica of Bucharest, Splaiul Independentei 313, 060042 Bucharest, Romania; doina.manaila@physics.pub.ro

Abstract: This paper studies the effective dielectric properties of heterogeneous materials of the type particle inclusions in a host medium, using the Maxwell Garnet and the Bruggeman theory. The results of the theories are applied at polymer-dispersed liquid crystal (PDLC) films, nanoparticles (NP)-doped LCs, and developed for NP-doped PDLC films. The effective permittivity of the composite was simulated at sufficiently high frequency, where the permittivity is constant, obtaining results on its dependency on the constituents' permittivity and concentrations. The two models are compared and discussed. The method used for simulating the doped PDLC retains its general character and can be applied for other similar multiphase composites. The methods can be used to calculate the effective permittivity of a LC composite, or, in the case of a composite in which one of the phases has an unknown permittivity, to extract it from the measured composite permittivity. The obtained data are necessary in the design of the electrical circuits.

Keywords: effective permittivity; liquid crystal; polymer-dispersed liquid crystal; nanoparticle



Citation: Manaila-Maximean, D.

Effective Permittivity of a Multi-Phase System: Nanoparticle-Doped Polymer-Dispersed Liquid Crystal Films. *Molecules* **2021**, *26*, 1441. <https://doi.org/10.3390/molecules26051441>

Academic Editor: Richard G. Weiss

Received: 7 January 2021

Accepted: 2 March 2021

Published: 7 March 2021

Publisher's Note: MDPI stays neutral with regard to jurisdictional claims in published maps and institutional affiliations.



Copyright: © 2021 by the author. Licensee MDPI, Basel, Switzerland. This article is an open access article distributed under the terms and conditions of the Creative Commons Attribution (CC BY) license (<https://creativecommons.org/licenses/by/4.0/>).

1. Introduction

Composite electro-optic materials, such as polymer/liquid crystal (LC) blends cover a large area of two phase mixtures as, for example: polymer-Dispersed liquid crystal (PDLC) films [1], liquid crystal dispersed in an electrospun cellulose acetate network [2,3], cellulose film/LC composite [4], polymer balls/nematic LC films [5].

Polymer-dispersed liquid crystal (PDLC) films consist of micrometer or sub-micrometer-sized nematic droplets dispersed in a polymer matrix [6]. Their optical transmission response is based on the electrically controlled light scattering properties of the droplets. An applied electric field aligns the nematic droplets, and due to the refractive index match of the polymer and the aligned LC, a transparent non-scattering state is obtained. In the absence of the field, the molecules inside the droplets return to their original orientation and results in a scattering opaque state.

The reorientation of the LC molecules depends on the electric field across the droplet [6,7], and at a macroscopic scale, it depends on the dielectric permittivity. The LC droplets inside the polymer matrix form a bi-phase system, and to study the dielectric permittivity, the Maxwell Garnet [8] and the Bruggeman [9,10] effective medium models are considered in this paper. Generally, the permittivity has frequency dispersion, but conductivity effects become unimportant compared to dielectric effects at relatively high frequencies, where the ionic motion is frozen out, and at high resistivities, where the small number of mobile ions will not give rise to a significant depolarization field [1], and the present study considers this situation.

At present, many studies are dedicated to nanoparticles (NPs)-doped LCs [11] and PDLC films, in order to take advantage to each constituent beneficial contribution [12–14]. The contribution of the third phase formed by the dispersed NPs both in the LC droplets and in the polymer matrix is taken into account at the calculation of the effective dielectric permittivity of NPs-doped PDLC films.

It is generally accepted that the LC form droplets encapsulated in the polymer up till a concentration of about 50%. For greater concentrations, interconnecting channels will form between the LC droplets, the structure passing gradually in a sponge-like one.

Because LC doping with small fractions of NP is a very delicate process that might lead to tricky experimental results, it is important to use models to gain information about the effective dielectric constant of NPs containing multiphase systems.

2. Theoretical Models

The investigated medium is a heterogeneous composite at microscopic scale, where we can evaluate the effective dielectric function of the macroscopic uniform medium depending on the permittivity of the individual components and their respective volume fractions. Two of the most used effective medium approaches are the Maxwell Garnet [15,16] and the Bruggeman theories which are discussed further.

2.1. Maxwell Garnett (MG) Model

Let us consider a dense medium formed by molecular dipoles. Firstly, one should evaluate the local field at the site of a molecule, supposing that the molecule is surrounded by a spherical cavity of radius R , as seen in Figure 1. The space inside the sphere has free space permittivity, since it is the space between two molecules. When applying an external electric field \vec{E}_{ext} , the electrical charges will move according to their sign, producing the electric field \vec{E}_S due to the polarization charges, which, in the case of the considered sphere, is $E_S = \frac{P}{3\epsilon_0}$, where P is the macroscopic polarization. The local field acting in the central of the dipole is

$$\vec{E}_L = \vec{E}_{ext} + \vec{E}_S + \vec{E}_d + \vec{E}_{near} \quad (1)$$

where \vec{E}_d is the depolarization field lying at the external surface of the medium, $E_d = \frac{-P}{\epsilon_0}$; \vec{E}_{near} is the field induced by other dipoles lying within the sphere, which, in the case of a symmetric cubic lattice, vanishes. Since the sum $\vec{E}_{ext} + \vec{E}_d = \vec{E}$, where \vec{E} is the macroscopic electric field, the local field becomes:

$$\vec{E}_L = \vec{E} + \frac{\vec{P}}{3\epsilon_0} \quad (2)$$

$$P = N\alpha E_L = N\alpha \left(E + \frac{P}{3\epsilon_0} \right) \quad (3)$$

where α is the polarizability of one molecule and N is the volume density of dipoles.

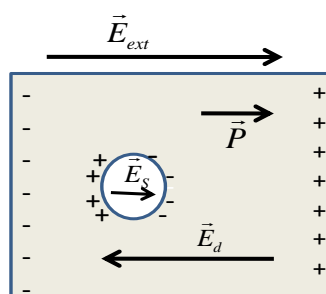


Figure 1. Auxiliary sphere around a molecule for determining the local electric field.

The electric induction being

$$\vec{D} = \epsilon_0 \vec{E} + \vec{P} = \epsilon_0 \epsilon_r \vec{E} \quad (4)$$

Using Equations' (3) and (4) results, the Clausius–Mossotti relation is

$$\frac{N\alpha}{3\epsilon_0} = \frac{\epsilon_r - 1}{\epsilon_r + 2} \quad (5)$$

Considering the Clausius–Mossotti relation for a composite formed of spherical particles of relative permittivity ϵ_1 embedded in a host medium of relative permittivity ϵ_h :

$$\frac{N\alpha}{3\epsilon_0\epsilon_h} = \frac{\epsilon_{eff,MG} - \epsilon_h}{\epsilon_{eff,MG} + 2\epsilon_h} \quad (6)$$

where $\epsilon_{eff,MG}$ is the effective permittivity obtained using the MG formula. Considering f the volume filling factor of the spheres, the polarizability in relation (5) becomes:

$$\alpha = \frac{3\epsilon_0\epsilon_h f}{N} \frac{\epsilon_1 - \epsilon_h}{\epsilon_1 + 2\epsilon_h} \quad (7)$$

By substituting Equation (7) in (6), the MG formula is obtained:

$$\frac{\epsilon_{eff,MG} - \epsilon_h}{\epsilon_{eff,MG} + 2\epsilon_h} = f \frac{\epsilon_1 - \epsilon_h}{\epsilon_1 + \epsilon_h} \quad (8)$$

$$\epsilon_{eff,MG} = \epsilon_h \frac{1 + 2f \frac{\epsilon_1 - \epsilon_h}{\epsilon_1 + 2\epsilon_h}}{1 - f \frac{\epsilon_1 - \epsilon_h}{\epsilon_1 + 2\epsilon_h}} \quad (9)$$

To model the capacity properties of the pure PDLC, we have chosen the MG formula adapted for the LC-polymer bi-phase system:

$$\epsilon_{eff,MG} = \epsilon_{ply} \frac{1 + 2f_{LC} \frac{\epsilon_{LC} - \epsilon_{ply}}{\epsilon_{LC} + 2\epsilon_{ply}}}{1 - f_{LC} \frac{\epsilon_{LC} - \epsilon_{ply}}{\epsilon_{LC} + 2\epsilon_{ply}}} \quad (10)$$

where $\epsilon_{eff,MG}$ is the effective dielectric constant of the composite PDLC film, ϵ_{ply} is the dielectric constant of the polymeric matrix, ϵ_{LC} is the dielectric constant of the dispersed liquid crystal, and f_{LC} is the volume fraction of the LC.

LCs are anisotropic materials and the dielectric anisotropy in the uniaxial nematic phase is characterized by two principal components, one component is parallel, ϵ_{II} , and the other component is perpendicular ϵ_{\perp} to the director of the LC. The dielectric anisotropy $\Delta\epsilon$ in the uniaxial phases is $\Delta\epsilon = \epsilon_{II} - \epsilon_{\perp}$ and its sign depends on the chemical structure of the constituent molecules [17]. The average permittivity of the LC is defined as $\epsilon_{LC} = \epsilon_{LC,random} = \frac{\epsilon_{II} + 2\epsilon_{\perp}}{3}$ and is used in our discussion. By measuring the capacitance of the film, one can determine an effective permittivity in zero-applied electric field (ϵ_{\perp}) and in the high-applied electric field (corresponding to the oriented LC, and to ϵ_{II}) states. Equation (9) can be applied to obtain the effective permittivity of the film (corresponding to ϵ_{\perp} , ϵ_{II} , and $\epsilon_{LC,random}$) and the results are presented in Section 4.

2.2. Bruggeman Effective Medium Model

The model considers spherical particles of two different materials, of permittivities ϵ_1 , ϵ_2 dispersed in a host matrix of dielectric constant ϵ_h [9,15]. For a two inclusion composite, induced in a symmetric manner, the following expression was obtained:

$$\frac{\epsilon_{eff,B} - \epsilon_h}{\epsilon_{eff,B} + 2\epsilon_h} = f_1 \frac{\epsilon_1 - \epsilon_h}{\epsilon_1 + 2\epsilon_h} + f_2 \frac{\epsilon_2 - \epsilon_h}{\epsilon_2 + 2\epsilon_h} \quad (11)$$

where $\epsilon_{eff,B}$ is the Bruggeman's effective permittivity of the medium.

For a two phase system, $f_1 + f_2 = 1$, if each material is considered as one inclusion and the host medium is the material itself. In this case $\varepsilon_{eff,B} = \varepsilon_h$ and the left hand side

of Equation (6) becomes zero. It follows:

$$f_1 \frac{\varepsilon_1 - \varepsilon_{eff,B}}{\varepsilon_1 + 2\varepsilon_{eff,B}} + f_2 \frac{\varepsilon_2 - \varepsilon_{eff,B}}{\varepsilon_2 + 2\varepsilon_{eff,B}} = 0 \quad (12)$$

The solution of Equation (12) is

$$\varepsilon_{eff,B} = \frac{1}{4} \left\{ (3f_1 - 1)\varepsilon_1 + (3f_2 - 1)\varepsilon_2 \pm \sqrt{[(3f_1 - 1)\varepsilon_1 + (3f_2 - 1)\varepsilon_2]^2 + 8\varepsilon_1\varepsilon_2} \right\} \quad (13)$$

The sign in Equation (13) is chosen such that the imaginary part of the effective permittivity is positive. For the pure PDLC, the effective permittivity considering the Bruggeman expression, $\varepsilon_{eff,B}$ becomes:

$$\varepsilon_{eff,B} = \frac{1}{4} \left\{ (3f_{LC} - 1)\varepsilon_{LC} + (3f_{ply} - 1)\varepsilon_{ply} \pm \sqrt{[(3f_{LC} - 1)\varepsilon_{LC} + (3f_{ply} - 1)\varepsilon_{ply}]^2 + 8\varepsilon_{LC}\varepsilon_{ply}} \right\} \quad (14)$$

2.3. NPs-Doped LC

The LC droplet is doped with NPs and the effective permittivity of the doped LC considering the MG formula is (15), resulted from (10), and considering the Bruggeman expression is presented in (16) (resulted from (14)), respectively.

$$\varepsilon_{LC_NP, MG} = \varepsilon_{LC} \frac{1 + 2f_{NP} \frac{\varepsilon_{NP} - \varepsilon_{LC}}{\varepsilon_{NP} + 2\varepsilon_{LC}}}{1 - f_{NP} \frac{\varepsilon_{NP} - \varepsilon_{LC}}{\varepsilon_{NP} + 2\varepsilon_{LC}}} \quad (15)$$

$$\varepsilon_{LC_NP, B} = \frac{1}{4} \left\{ (3f_{NP} - 1)\varepsilon_{NP} + (3(1 - f_{NP}) - 1)\varepsilon_{LC} \pm \sqrt{[(3(1 - f_{NP}) - 1)\varepsilon_{LC} + (3f_{NP} - 1)\varepsilon_{NP}]^2 + 8\varepsilon_{LC}\varepsilon_{NP}} \right\} \quad (16)$$

where we have taken into consideration that the sum between the NPs volume fraction (in LC) and the LC volume fraction (in NPs) is 1.

2.4. NPs-Doped PDLC Films

To obtain the effective permittivity for the doped PDLC, the following system is considered: the NPs-doped polymer matrix, LC droplets doped with NPs, as presented in Figure 2.

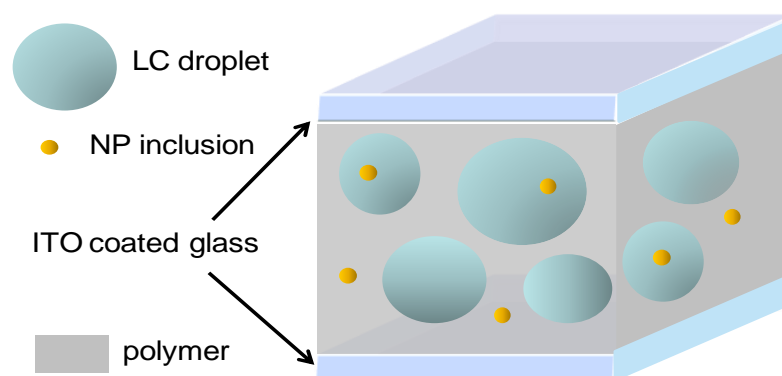


Figure 2. Schematic presentation of a nanoparticles (NPs) polymer-dispersed liquid crystal (PDLC)-doped film between two indium tin oxide (ITO) glass coated plates: LC droplets are spherical.

Since the fraction of NPs in LC is very small, we may consider the MG formula for the NPs doped polymer, and using Equation (10) it follows:

$$\epsilon_{ply,NP_MG} = \epsilon_{ply} \frac{1 + 2f_{NP} \frac{\epsilon_{NP} - \epsilon_{ply}}{\epsilon_{NP} + 2\epsilon_{ply}}}{1 - f_{NP} \frac{\epsilon_{NP} - \epsilon_{ply}}{\epsilon_{NP} + 2\epsilon_{ply}}} \quad (17)$$

For the doped LC, we consider Equation (14).

Finally, for the NPs-doped PDLC, we use the Bruggeman formula:

$$\epsilon_{PDLC,NP} = \frac{1}{4} \left\{ (3f_{LC} - 1)\epsilon_{LC_NP,MG} + (3(1 - f_{LC}) - 1)\epsilon_{ply_NP,MG} \pm \sqrt{\Delta} \right\} \quad (18)$$

$$\Delta = \left[(3(1 - f_{LC}) - 1)\epsilon_{ply_NP,MG} + (3f_{LC} - 1)\epsilon_{LC_NP,MG} \right]^2 + 8\epsilon_{LC_NP,MG}\epsilon_{ply_NP,MG} \quad (19)$$

3. Results and Discussions

3.1. PDLC Film

Figure 3 shows the numerical representation of PDLC effective permittivity, vertical colour bar, Ox axis represents LC permittivity ϵ_{LC} , Oy axis represents polymer permittivity ϵ_{ply} , obtained using the Maxwell Garnett model (Equation (10)), for LC volume fractions of 20%, 30%, and 40%, commonly used in the study of PDLC films and for whom LC forms individual droplets. The numerical values in the following discussions refer to the relative permittivity of the materials. The polymer permittivity variation domain is chosen between 3 and 10, and the LC permittivity between 4 and 20, considering their values at high frequency [17–20]. As easily seen in Figure 3a, at constant volume fraction and constant LC permittivity, the effective MG permittivity increases with the polymer permittivity, and at constant polymer permittivity, the effective MG permittivity increases with the LC permittivity.

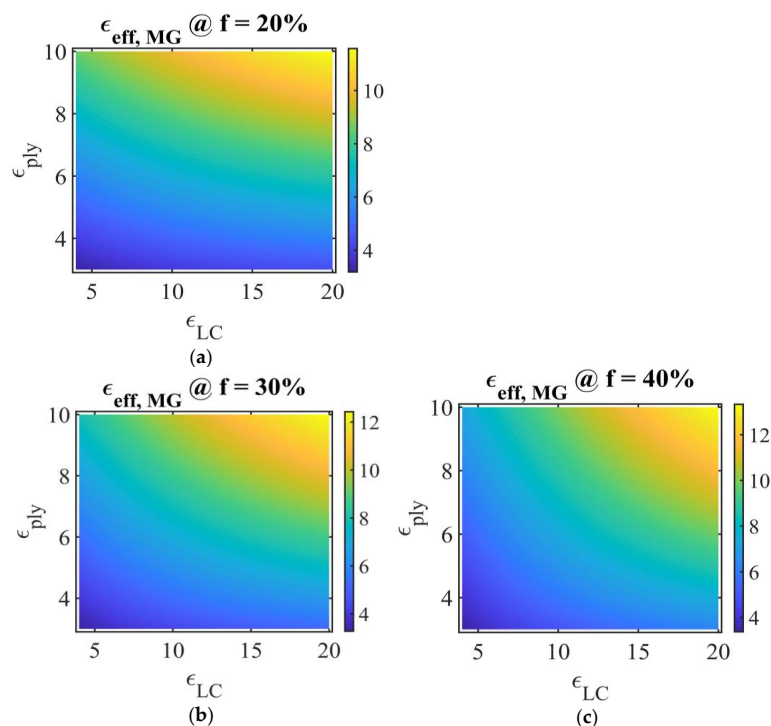


Figure 3. Representation of PDLC permittivity in the Maxwell Garnett model, for different LC fractions: (a) $f_{LC,a} = 0.2$; (b) $f_{LC,b} = 0.3$; (c) $f_{LC,c} = 0.4$. Ox: LC permittivity ϵ_{LC} , Oy: polymer permittivity ϵ_{ply} ; vertical color bar: PDLC film effective permittivity using the Maxwell Garnet model, symbol @ stands for “at”.

In Figure 4, the numerical simulations of PDLC effective permittivity (vertical colour bar) are presented, obtained using the Bruggeman model (Equation (14)), for LC volume fractions of 20%, 30%, and 40%, Ox axis: LC permittivity ϵ_{LC} , Oy axis: polymer permittivity ϵ_{ply} . At constant LC permittivity, the effective PDLC permittivity increases with the polymer permittivity. Considering, for example, the lower limit for the LC permittivity and the upper limit for the polymer permittivity, $\epsilon_{LC} = 4$ and $\epsilon_{ply} = 10$, the effective Bruggeman permittivity for the PDLC film decreases with the increase of the LC fraction.

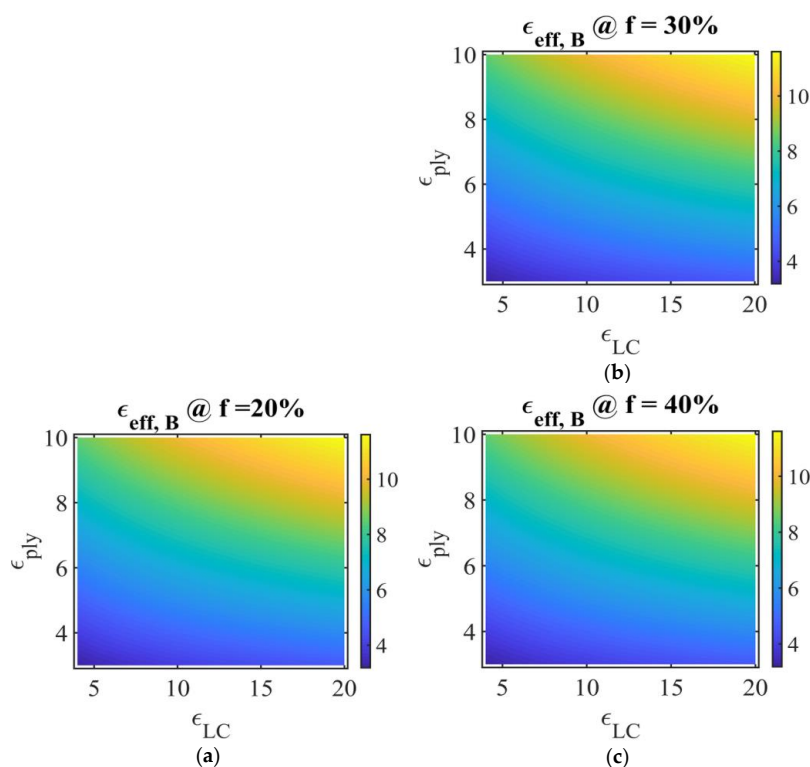


Figure 4. Representation of PDLC film effective permittivity in the Bruggeman model for different LC fractions: (a) $f_{LC,a} = 0.2$, (b) $f_{LC,b} = 0.3$, (c) $f_{LC,c} = 0.4$. Ox: LC permittivity ϵ_{LC} , Oy: polymer permittivity ϵ_{ply} ; vertical color bar: PDLC film effective permittivity using the Bruggeman model, symbol @ stands for “at”.

To compare the results predicted by the two models, Figure 5 presents the difference between the MG and Bruggeman effective permittivity, $\epsilon_{eff, MG} - \epsilon_{eff, B}$, for three LC fractions. Considering, for example, the LC fraction of 20%, $\epsilon_{ply} = 3$, $\epsilon_{LC} = 10$, it results in an effective Bruggeman permittivity greater than the effective MG one. At $\epsilon_{ply} = 10$ and $\epsilon_{LC} = 5$, the MG effective permittivity is greater than the Bruggeman one. The modulus $|\epsilon_{eff, MG} - \epsilon_{eff, B}|$ increases with the LC fraction, at constant constituents’ permittivity.

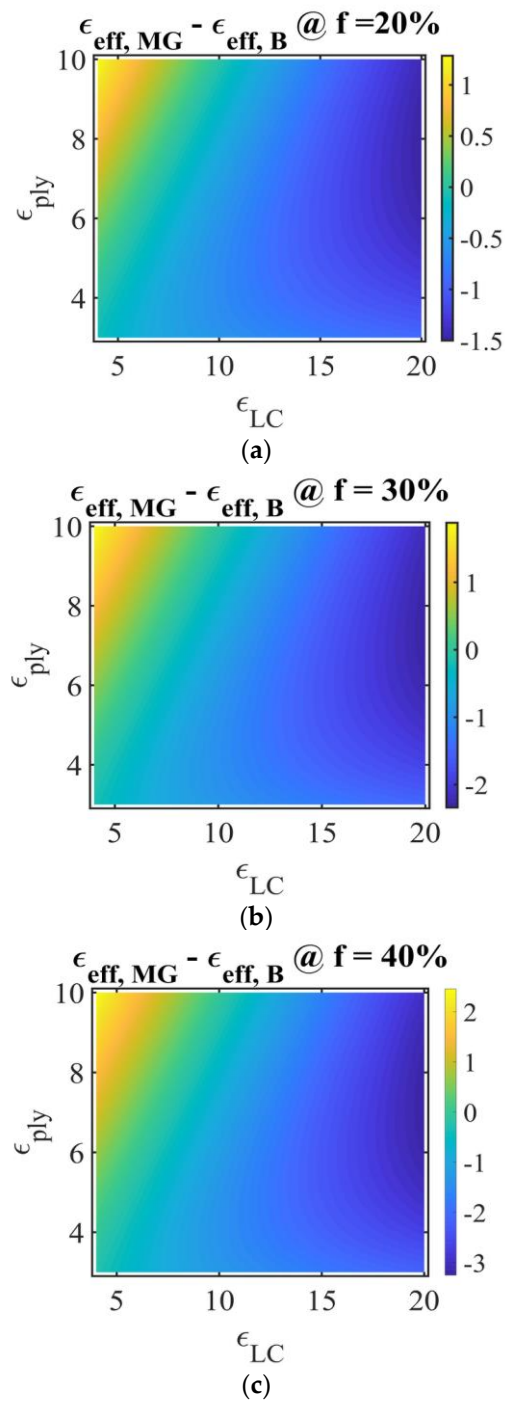
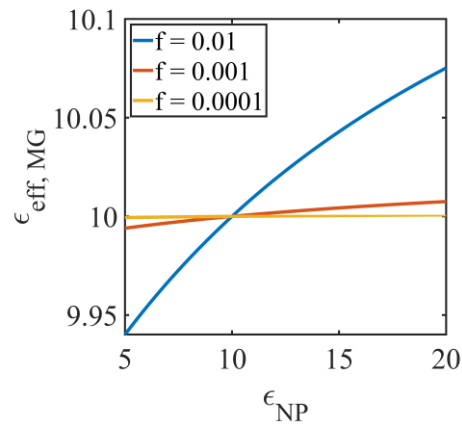


Figure 5. The difference between the Maxwell Garnett (MG) and Bruggeman effective permittivity, $\epsilon_{\text{eff, MG}} - \epsilon_{\text{eff, B}}$, (a) $f_{\text{LC}, a} = 0.2$; (b) $f_{\text{LC}, b} = 0.3$; (c) $f_{\text{LC}, c} = 0.4$. Ox: LC permittivity ϵ_{LC} , Oy: polymer permittivity ϵ_{ply} ; vertical color bar: the difference between the MG and Bruggeman effective permittivity of the PDLC film, $\epsilon_{\text{eff, MG}} - \epsilon_{\text{eff, B}}$ symbol @ stands for “at”.

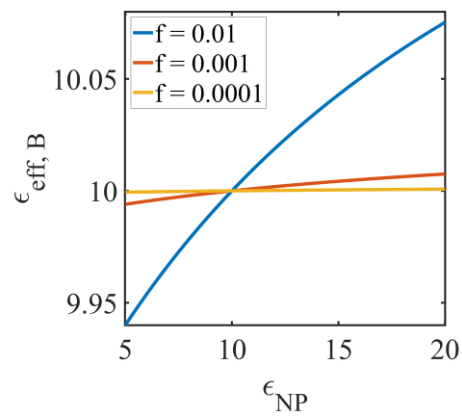
3.2. NPs-Doped LCs

Figure 6 presents the effective permittivity for NPs-doped LC versus NPs' permittivity, ϵ_{NP} , for three NP volume fractions: 0.01; 0.001; and 0.0001, using the MG model (Equation (15), Figure 6a) and the Bruggeman model (Equation (16) Figure 6b). The LC permittivity is considered 10. In both cases, the effective permittivity increases with ϵ_{NP} and with the NP volume fraction, excepting the case $\epsilon_{\text{NP}} = \epsilon_{\text{LC}}$ (in our case equal 10),

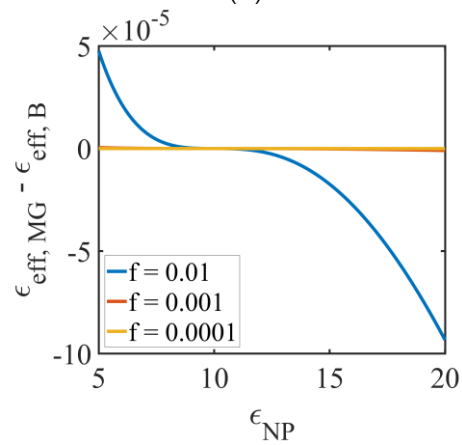
when the volume fraction of NP does not influence the result (intersection of the three curves corresponding to the difference of NP volume fractions).



(a)



(b)



(c)

Figure 6. Representation of effective permittivity for NPs-doped LC versus NP permittivity, ϵ_{NP} , for three NP volume fractions: 0.01; 0.001; and 0.0001, (a) MG model (Equation (14)); (b) Bruggeman model (Equation (15)), and (c) the difference of the effective permittivity obtained using these models.

Comparing the two models, Figure 6c shows the difference $\epsilon_{eff, MG} - \epsilon_{eff, B}$ for the NPs-doped LCs. It results that $\epsilon_{eff, MG} > \epsilon_{eff, B}$, when $\epsilon_{NP} < 10$ (which corresponds to $\epsilon_{NP} = \epsilon_{LC}$) and then it changes its sign, the difference being noticeable at NP volume fraction of 0.01, but still of the order of 10^{-4} .

Figure 7a represents the effective permittivity for the NPs-doped PDLC (Equation (17)), versus ϵ_{NP} , at a constant LC volume fraction $f_{LC} = 0.4$ and for three NP volume fractions f_{NP} : 0.01; 0.001; and 0.0001. For the LC permittivity, the value of a commercial LC mixture, E7, was chosen at high frequency [18] $\epsilon_{LC} = 10$, and for the polymer, the permittivity of polyvinyl alcohol (PVA), $\epsilon_{ply} = 8$ [21–25]. The effective permittivity shows a modest increase at very low NP concentrations, and a more significant variation at $f_{NP} = 0.01$. Figure 7b shows the effective Bruggeman permittivity versus LC concentration, for the undoped PDLC film.

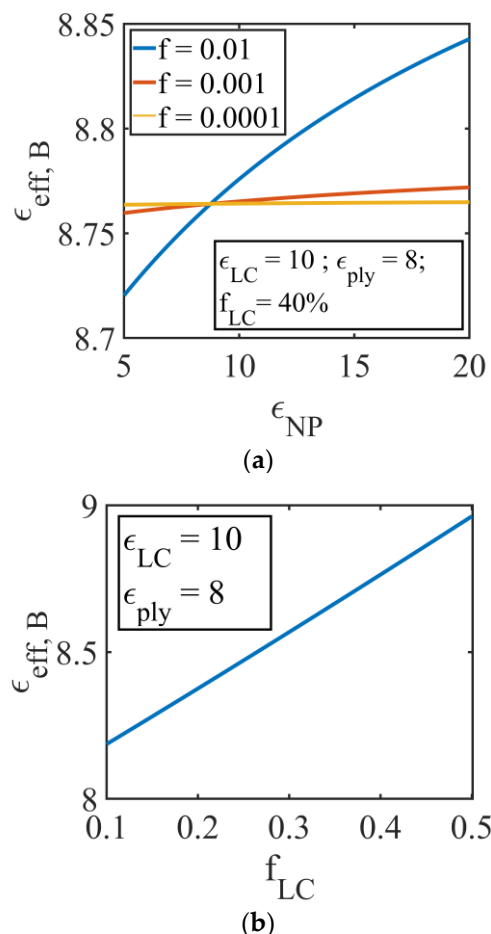


Figure 7. (a) Effective permittivity for the NPs-doped PDLC, versus NP permittivity, ϵ_{NP} , (Equation (18)) at a constant LC volume fraction $f_{LC} = 0.4$ and for different NP volume fractions f_{NP} : 0.01; 0.001; and 0.0001. LC permittivity $\epsilon_{LC} = 10$, polymer permittivity $\epsilon_{ply} = 8$; (b) representation of undoped PDLC effective permittivity in the Bruggeman model versus LC volume fractions, Equation (14), at constant LC permittivity $\epsilon_{LC} = 10$, polymer permittivity $\epsilon_{ply} = 8$.

When comparing the experimental values with the simulated ones, differences might appear due to the errors in the determination of the geometrical dimensions of the sample. To avoid this problem, in many dielectric spectroscopy studies, the aim is to obtain the characteristic time of the dielectric relaxation processes, independent on the sample's dimension [10,11].

4. Comparison of Model Predictions with Test Data for PDLC Films

In order to compare the methods presented with experimental data from the literature [21–25], we chose a PDLC film consisting of the polyvinyl alcohol (PVA) polymer and nematic LCs [25]. The volume fraction is $f_1 = f_2 = 0.5$. The dielectric constant of PVA is 8. Table 1 presents the permittivity of the LC (according to the producers' data sheet [25])

and the LC used for the calculation of the effective permittivity to test the Maxwell Garnett (Equation (10)) and Bruggeman (Equation (14)) models. The effective permittivity of the PDLC film is calculated considering the LC permittivity, each of the corresponding values for ϵ_{\perp} , ϵ_{\parallel} and $\epsilon_{LC,random}$. The dielectric constant of the PDLC film was measured in [25], in the “rest” states (corresponding to ϵ_{\perp}), zero electric field permittivity, and in the field-aligned states (corresponding to ϵ_{\parallel}) high electric field permittivity.

Table 1. Comparative presentation of calculated PDLC film permittivity using Maxwell Garnett (Equation (10)) and Bruggeman (Equation (14)) formulas, and experimental results [25]; the field permittivity measured at low electric field corresponds to ϵ_{\perp} of the LC and at high electric field to the ϵ_{\parallel} of the LC (LC aligned in the direction of the field).

Nematic Liquid Crystal	LC Permittivity		Calculated Film		Measured Film Permittivity [25]
			Permittivity Maxwell Garnett ¹ , Equation (9)	Permittivity Bruggeman ¹ , Equation (13)	
E7	ϵ_{\perp}	5.2	6.5	6.5	6.7
	ϵ_{\parallel}	19.0	12.5	12.7	14.5
	$\epsilon_{LC,random}$	9.8	8.9	8.8	-
ZLI 1840	ϵ_{\perp}	4.3	6.0	5.9	5.7
	ϵ_{\parallel}	16.2	11.5	11.6	12.6
	$\epsilon_{LC,random}$	8.3	8.2	8.2	-

¹ The calculated values are rounded in accordance with LC permittivity values.

The relative deviation of the calculated permittivity values is small. The calculated values in these particular cases show that the two models are correct, in agreement with the experiment, and with the ones calculated in [25] and suitable for the calculation of the composites' permittivity [24,25]. The methods can be used to calculate the effective permittivity of a LC composite. If a series of LC composites are studied, measurements can be done only on some particular ones and the other can be calculated. In the case of a composite in which one of the phases has an unknown permittivity, this can be obtained by measuring the permittivity of the composite and using one of the models presented. The effective permittivity is necessary in the design of the electrical circuits where these opto-electronic materials are applied.

5. Conclusions

LC composites have a great importance in applications and are the subject of numerous theoretical studies. Knowing their permittivity helps us to calculate the electric field at which the reorientation effects of LC molecules occur, which gives rise to the desired electro-optical effects.

Unlike other models of permittivity calculation (volumetric models—linear or logarithmic [18,26]), MG and Bruggeman models have a theoretical basis, by virtue of their derivation from electrical principles.

PDLC being composites containing LC droplets in polymer form and a biphasic system for which the MG and Bruggeman mixing models can be used. This paper applies, develops, and compares the two models by mixing the permittivity of the constituents to obtain the effective permittivity of the material. NP doping of LCs and PDLC films is a current research topic of great interest. The MG and Bruggeman models were also applied in case of NP doping of LCs.

To study NP-doped PDLCs, given the very low concentrations used in doping, we used the MG model to obtain two biphasic media, one consisting of NP in LC and the other of NP in polymer. The three-phase polymer-NP-LC medium was treated by the Bruggeman method, considering the effective permittivity obtained for the NP-LC medium and the permittivity of the NP-polymer medium.

Numerical simulations were performed in high frequency mode, in typical intervals of variation of the permittivity of the constituents.

For the PDLC system, the effective permittivity was obtained and the differences between the two models were discussed. The results are in agreement with the experiments [25]. The modulus of the difference between the Maxwell Garnet effective permittivity and the Bruggeman one increases with the LC fraction, at constant constituents' permittivity.

In the case of NPs-doped LCs, the difference between the two methods is modest at low NP concentrations (0.0001–0.001), increasing in importance at higher values. If the NP permittivity is equal to that of the LC host, the volume fraction does not influence the calculated effective permittivity.

Using MG and Bruggeman models, the effective permittivity of the NPs-doped PDLCs was simulated, obtaining information on its dependency on NPs permittivity and volume fractions.

The developed method can be applied for the calculation of the effective permittivity in the case of composites of LCs with quasi-spherical NPs such as titanium dioxide and zinc oxide. In the case of a composite in which one of the phases has an unknown permittivity, the models can be applied to extract it from the measured composite permittivity. The method also retains a general character and can be applied to other similar multiphase composites.

Funding: The APC for this paper was funded by University “Politehnica” of Bucharest. This research was partly funded by the Romanian Governmental Representative at JINR Dubna through scientific project RO-JINR Theme 04-4-1122-2015/2020, No. 58 in Order IUCN no. 269/20.05.2020 and Theme 04-4-1141-2020/2022.

Conflicts of Interest: The author declares no conflict of interest.

Sample Availability: Not available.

References

1. Drzaic, P.S.; Scheffer, T.J. *Liquid Crystal Dispersions*; Word Scientific: Singapore, 1995.
2. Manaila-Maximean, D.; Danila, O.; Almeida, P.L.; Ganea, C.P. Electrical properties of a liquid crystal dispersed in an electrospun cellulose acetate network. *Beilstein J. Nanotechnol.* **2018**, *9*, 155–163. [[CrossRef](#)] [[PubMed](#)]
3. Maximean, D.M.; Danila, O.; Ganea, C.P.; Almeida, P.L. Filling in the voids of electrospun hydroxypropyl cellulose network: Dielectric investigations. *Eur. Phys. J. Plus* **2018**, *133*, 159. [[CrossRef](#)]
4. Rosu, C.; Mănăilă-Maximean, D.; Godinho, M.H.; Almeida, P.L. Thermally stimulated depolarization currents and optical transmissionon liquid crystal/cellulose derivative composite devices. *Mol. Cryst. Liq. Cryst.* **2003**, *391*, 1–11. [[CrossRef](#)]
5. Chang, S.J.; Lin, C.M.; Fuh, A.Y.G. Studies of polymer ball type polymer dispersed liquid crystal films. *Liq. Cryst.* **1996**, *21*, 19–23. [[CrossRef](#)]
6. Mănăilă-Maximean, D.; Cîrcu, V.; Ganea, P.; Bărar, A.; Danila, O.; Staicu, T.; Loiko, V.A.; Konkolovich, A.V.; Miskevich, A.A. Polymer dispersed liquid crystals films doped with carbon nanotubes: Preparation methods. In *Advanced Topics in Optoelectronics, Microelectronics, and Nanotechnologies IX, Constanta, Romania, 23–26 August 2018*; International Society for Optics and Photonics: Bellingham, WA, USA, 2018; Volume 10977, p. 1097702. [[CrossRef](#)]
7. Wu, B.-G.; Erdmann, J.H.; Doane, J.W. Response times and voltages for PDLC light shutters. *Liq. Cryst.* **1989**, *5*, 1453–1465. [[CrossRef](#)]
8. Garnett, J.M., XII. Colours in metal glasses and in metallic films. *Philos. Trans. R. Soc.* **1904**, *203*, 385–420. [[CrossRef](#)]
9. Bruggeman, D.A.G. Calculation of different physical constants of heterogen substances I Dielectric constants and conductivity of mixtures from isotrop substances. *Ann. Phys.* **1935**, *24*, 665–679. [[CrossRef](#)]
10. Polder, D.; van Santeen, J. The effective permeability of mixtures of solids. *Physica* **1946**, *12*, 257–271. [[CrossRef](#)]
11. Ganea, C.P.; Cîrcu, V.; Manaila-Maximean, D. Effect of titanium oxide nanoparticles on the dielectric properties and ionic conductivity of a new smectic bis-imidazolium salt with dodecyl sulfate anion and cyanobiphenyl mesogenic groups. *J. Mol. Liq.* **2020**, *317*, 113939. [[CrossRef](#)]
12. Ganea, C.P.; Manaila-Maximean, D.; Cîrcu, V. Dielectric investigations on carbon nanotubes doped polymer dispersed liquid crystal films. *Eur. Phys. J. Plus* **2020**, *135*, 1–14. [[CrossRef](#)]
13. Dănilă, O. Spectroscopic assessment of a simple hybrid si-Au cell metasurface-based sensor in the mid-infrared domain. *J. Quant. Spectrosc. Radiat. Transf.* **2020**, *254*, 107209. [[CrossRef](#)]
14. Loiko, V.; Konkolovich, A.; Miskevich, A.; Manaila-Maximean, D.; Danila, O.; Cîrcu, V.; Bărar, A. Optical model to describe coherent transmittance of polymer dispersed liquid crystal film doped with carbon nanotubes. *J. Quant. Spectrosc. Radiat. Transf.* **2020**, *245*, 106892. [[CrossRef](#)]
15. Cai, W.; ShalaeV, V. *Optical Metamaterials*; Springer: New York, NY, USA, 2010; Volume 10, p. 40. [[CrossRef](#)]

16. Blinov, L.M. *Structure and Properties of Liquid Crystals*; Springer Science & Business Media: Berlin/Heidelberg, Germany, 2010; Volume 123.
17. De Gennes, P. *The Physics of Liquid Crystals*; Oxford University Press: Oxford, UK, 1974.
18. Vaz, N.A.; Montgomery, J.G.P. Electrical properties of polymer-dispersed liquid crystal films. In *Liquid Crystal Materials, Devices, and Applications, Proceedings of the SPIE/IS&T 1992 Symposium on Electronic Imaging: Science and Technology, San Jose, CA, USA, 9–14 February 1992*; International Society for Optics and Photonics: Bellingham, WA, USA, 1992; Volume 1665, pp. 64–79. [[CrossRef](#)]
19. Wypych, A.; Bobowska, I.; Tracz, M.; Opasinska, A.; Kadlubowski, S.; Krzywania-Kaliszewska, A.; Grobelny, J.; Wojciechowski, P. Dielectric properties and characterisation of titanium dioxide obtained by different chemistry methods. *J. Nanomater.* **2014**, *2014*, 1–9. [[CrossRef](#)]
20. Zhong, Z.Z.; Schuele, D.E.; Gordon, W.L.; Adamić, K.J.; Akins, R.B. Dielectric properties of a PMMA/E7 polymer-dispersed liquid crystal. *J. Polym. Sci. Part B Polym. Phys.* **1992**, *30*, 1443–1449. [[CrossRef](#)]
21. Viciosa, M.T.; Nunes, A.M.; Fernandes, A.; Almeida, P.L.; Godinho, M.H.; Dionísio, M.D. Dielectric studies of the nematic mixture E7 on a hydroxypropylcellulose substrate. *Liq. Cryst.* **2002**, *29*, 429–441. [[CrossRef](#)]
22. Rout, D.K.; Jain, S.C. Dielectric properties of polymer-liquid crystal composites. *Jpn. J. Appl. Phys.* **1992**, *31 Pt 1*, 1396–1398. [[CrossRef](#)]
23. Polymer Properties Database. Dielectric Constants. Available online: <http://polymerdatabase.com/polymer%20physics/Epsilon%20Table.html> (accessed on 4 March 2021).
24. Wang, Y.-M.; Snyder, D.D.; Nelson, G.J. AC Impedance Spectroscopy (ACIS) Analysis of a Polymer Dispersed Liquid Crystal (PDLC) film. *Mol. Cryst. Liq. Cryst.* **1987**, *149*, 163–176. [[CrossRef](#)]
25. Drzaic, P.S.; Muller, A. Droplet shape and reorientation fields in nematic droplet/polymer films. *Liq. Cryst.* **1989**, *5*, 1467–1475. [[CrossRef](#)]
26. Lichtenecker, K. Zur Widerstandsberechnung mischkristallfreier Legierungen. *Phys. Z.* **1909**, *10*, 1005–1008.



Dielectric investigations on carbon nanotubes doped polymer dispersed liquid crystal films

Constantin Paul Ganea¹, Doina Manaila-Maximean^{2,a}, Viorel Cîrcu^{3,b}

¹ National Institute of Materials Physics, POBox MG 07, 077125 Magurele, Romania

² Department of Physics, University Politehnica of Bucharest, 313 Spl. Independentei, 060042 Bucharest, Romania

³ Department of Inorganic Chemistry, University of Bucharest, 23 Dumbrava Rosie st, Sector 2, Bucharest 020464, Romania

Received: 29 May 2020 / Accepted: 22 September 2020

© Società Italiana di Fisica and Springer-Verlag GmbH Germany, part of Springer Nature 2020

Abstract We obtained carbon nanotubes (CNTs) doped polymer dispersed liquid crystal (PDLC) films using the nematic E7 and polymethyl methacrylate, a composite that combines the benefic characteristic of the liquid crystals (LC) and carbon nanoparticles. The clearing temperatures recorded by differential scanning calorimetry for the PDLC blends were found to be lower than the value recorded for pure E7 LC mixture with no significant impact of the CNTs' concentration. Broadband dielectric spectroscopy (DS) measurements were performed in the ($10^{-1} \div 10^7$) Hz frequency range, in the temperature domain (280–350) K. From the DS study, a two order magnitude variation of the conductivity over the entire temperature range was observed. The presence of CNTs results in an increase of electrical conductivity, with increasing concentration. Because the loss tangent spectra have complex shapes, they were fitted using the generalized Havriliak–Negami functions, and the characteristic relaxation times were extracted. The dependency of the characteristic relaxation time on temperature was modeled using the Vogel–Fulcher–Tammann function, and it showed a temperature variation according to the Arrhenius law. The increase of the CNT concentration increases the activation energy of the molecular electric dipoles of the LC. The interface LC-polymer interactions influence the nematic to isotropic phase transition of the LC.

1 Introduction

The composites known as Polymer Dispersed Liquid crystals (PDLCs) are soft films consisting of liquid crystal (LC) domains embedded in a continuous polymer matrix [1]. Usually, in these composites the dimensions of the confined LC droplets vary from hundreds of nanometers till a few microns. For LCs with positive dielectric anisotropy, $\Delta\varepsilon > 0$, when the device is in the field “OFF” state, the LC molecules are randomly oriented and the PDLC film scatters the light. When applying an alternative electric field, the LC dipoles orient in the direction of the electric field, thus changing the refractive index of the LC droplet, which becomes (ideally) equal to that of the polymer, and the film turns transparent [1]. Besides the

^a emails: doina.manaila@physics.pub.ro; doina.manaila@upb.ro (corresponding author)

^b e-mail: viorel.circu@chimie.unibuc.ro (corresponding author)

applications of these devices as light shutters [1], electrically controlled blinds, fast-acting optical attenuators [2], large-sized display boards [3], inventive original application have been reported as eye cataract simulator [4] and artificial iris [5].

In the age of nanotechnologies, research is being done in the field of LCs to improve their characteristics specific to the fields of application by their nanoparticles (NPs) doping.

NPs introduced as dopants interact with LC molecules and, consequently, they will be reoriented in the electric field together with the LC molecules and will change the electrical, the optical properties and the phase transition temperatures [6–13]. Numerous types of dopants, such as carbon-based NPs, gold NPs, aerosils, magnetic NPs, have been studied to improve the electro-optical, electro-magnetic, nonlinear optical response characteristics of LCs [14–21]. To vary the dielectric characteristics and thus ameliorate the electro-optical response of LCs, many studies used the addition of CNTs [22] It is considered that single wall carbon nanotubes (SWCNTs) are cylinders formed by rolling up a graphene layer [23]; only their diameter is in the nanometer range, their typical length values being of a few micrometers. Interestingly, a SWCNT can be metallic or semiconductor, depending on how the graphene sheet is folded, or on the arrangement of the carbon “honey-comb” lattice in the sheet of graphene. A mixture of the two electrical conduction possibilities exists depending on the preparation of SWCNTs. It is important to mention that CNTs show high anisotropy of their properties, with high electrical conductivity, of the order 10^6 – 10^7 S/m, and high thermal conductivity along the tube axis [16, 24]. From the anisotropic properties of CNTs result the importance of controlling their orientation. As compared to SWCNTs, LCs have a smaller aspect ratio, but a long-range orientational order, the molecules spontaneously aligning to a common direction, characterized by the director n . The close interaction between LC molecules and CNTs results in the alignment of the latter with their long axes parallel to n [25, 26].

The purpose of this paper is to investigate the influence of SWCNT’ doping on the dielectric properties of PDLC [27, 28], study important in applications since the conductivities of the constituents play an important role in their electro-optical applications.

2 Experimental

2.1 Sample preparation

PDLC samples were prepared by the solvent induced phase separation (SIPS) method, using the nematic E7 (Merck, ordinary refractive index $n_O = 1.51$ and positive dielectric anisotropy $\Delta\varepsilon > 0$) and the polymethyl methacrylate (PMMA, refractive index $n_P = 1.49$), in a ratio of 40/60 (E7/PMMA) w./w. Besides these control samples, CNT doped samples have been made. CNTs employed in this experiment have been Single Walled CNT (Aldrich code 519308) with diameter between 1.2 and 5 nm. E7 is an eutectic mixture of cyanobiphenyls and cyanoterphenyls, (51% 5CB, 25% 7CB, 16% 8OCB and 8% 5CT) with the crystal (K) to nematic (N) phase transition temperature: $T_{KN} = 263$ K and the nematic to isotropic (I) temperature $T_{NI} = 333.5$ K [29]; the glass transition of PMMA is at 383 K.

In order to prepare the PDLC samples with lower concentration of CNT (0.002% and 0.004%) a dispersion of 1% CNTs in E7 was firstly obtained; 4 mg of CNTs were thoroughly mixed together with 396 mg of E7. Then, by successive dilutions, final concentrations of 0.01% and 0.005% CNT in E7 were obtained. All these samples were checked by polarizing optical microscopy (POM) to assess the uniform dispersion of CNTs in E7 mixture. From each of this mixture, 40 mg were taken and mixed together with 60 mg of PMMA in 1 ml

of chloroform to achieve the concentrations of 0.004 and 0.002% CNTs in the PDLCs. All samples were thoroughly homogenized by a combination of magnetic stirring for several hours and sonication for achieving a fine dispersion of CNTs. Thin films were solvent casted on glass slides by evaporating slowly the solvent (CHCl_3) at room temperature.

2.2 Differential scanning calorimetry (DSC) and polarized optical microscopy (POM)

The thermal behaviour of the PDLC films was investigated by using DSC technique employing a Diamond DSC PerkinElmer instrument with Intracooler 1P cooling accessories. The PDLC samples were studied at 10 K min^{-1} scanning rate. An amount of $10 \pm 1 \text{ mg}$ of each sample was encapsulated in aluminium pans, and at least two heating/cooling cycles were performed.

The PDLC films were evaluated by polarizing optical light microscopy (POM), using a Nikon 50iPol microscope equipped with a Linkam THMS600 hot stage and TMS94 control processor.

2.3 Dielectric spectroscopy

The dielectric spectroscopy measurements were performed using a Broadband Dielectric Spectrometer, Novocontrol, consisting in the Alpha-A High Performance Frequency Analyzer in the LF domain equipped with WinDETA software. We have performed measurements in the $0.1 \div 10^7 \text{ Hz}$ range, and temperatures were controlled within 0.2 K. Alternative voltage is set to 0.5 V. The measurements were performed in constant temperature conditions in the $280 \div 350 \text{ K}$ range with a variation rate of 3 K.

The sample is placed between circular, metallic electrodes, gold plated, in a configuration of capacitor with plan-parallel armatures. The diameter of the electrodes is of 20 mm, the distance between the electrodes is equal to the thickness of the PDLC film.

The temperature is regulated and controlled with the Quatro-Cryosystem, Novocontrol, with the following technical possibilities, specified by the manufacturer: sample temperature reading error 0.01 K, adjustment and control error of 0.05 K.

3 Results and discussion

3.1 DSC and POM studies

The PDLC samples were analyzed by differential scanning calorimetry on a broad temperature range, from room temperature up to 413 K with a scanning rate of 10 K min^{-1} . Three heating-cooling cycles were performed for each sample. A clear and rather broad peak corresponding to the N-Iso transition of the liquid crystalline mixture confined in the PDLC matrix was seen only during the first heating run with T_{peak} in the 327–329 K range (Fig. 1).

In fact, for each analyzed PDLC blend, the transition started around 320 K, and this behaviour was confirmed by polarizing optical microscopy (POM). On the following DSC heating or cooling runs this N-Iso transition was not clearly evidenced because of the scanning rate employed which seems to prevent reaching the thermal equilibrium for the given conditions (Fig. 2). Still the recorded temperatures are lower than the temperature recorded for pure E7 ($\sim 5 \text{ K}$ for undoped sample, 6 K for 0.002% CNT and 7 K for 0.004% CNT, when these values are compared as T_{peak}). Previous studies have shown that an increase of the polymer content in the PDLC blend led to a depression of the N-Iso transition temperature

Fig. 1 First heating DSC traces of the E7/PMMA mixture (black) and the E7/PMMA doped with CNT (0.002%—red and 0.004%—blue)

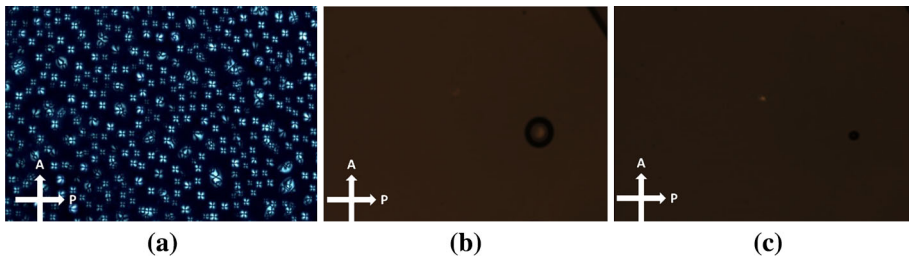
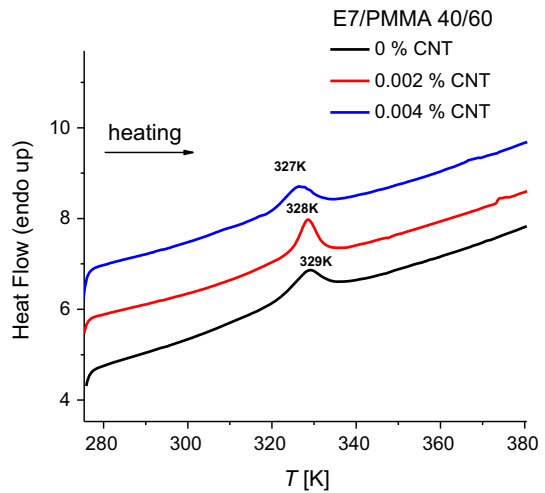


Fig. 2 Polarized optical micrographs of E7/PMMA (40/60 by weight) as separated by SIPS, at room temperature (a); PDLC film heated at 398 K (b) and cooled down to 308 K with 10 K min^{-1} cooling rate (c)

(T_{NI}) [30]. For instance, Zhong et al. found that for a 50% E7/PMMA sample the N-Iso phase transition is shifted with 16 K compared to pure E7 (334 K) [27].

Moreover, the presence and the concentration of CNTs in LCs can have a significant impact on the transition temperatures in general and, more specific, on the N-Iso transition temperature (T_{NI} or clearing temperature). The studies reported so far showed that the addition of CNTs leads to an increase of the clearing point of LCs due to the strong attraction between CNTs and LC. For example, Duran et al. [31] have found an enhanced T_{NI} on increasing the content of CNTs up to 0.2% in the CNT/E7 mixture which could be attributed to the anisotropic alignment of E7 induced by the CNT bundles. Further increase of the MWNT content above 0.3% resulted in the change of the T_{NI} back to 334 K close to the value found for pure E7 giving a chimney-type phase diagram. The same shift of transitions to higher temperatures was seen for other CNTs–LC mixtures when compared to the pure LC. (8CB [32] or 9OO4, 4-butyloxyphenyl 4'-nonyloxybenzoate [33]) In our case, the effect of the CNTs' content on the T_{NI} is rather undetectable and unclear; the low concentrations of CNTs together with the high content of the polymer resulted in almost unchanged T_{NI} recorded for the undoped and CNTs doped E7/PMMA samples because of the dominant influence of the E7/PMMA host (Fig. 1).

A schematic representation of the orientation of LC molecules and CNTs in electric field is presented in Fig. 3 [18, 25, 26].

Fig. 3 Schematic presentation of the CNT doped PDLC film under the action of electric field when the conductivity of the LC is much higher than that of the polymer

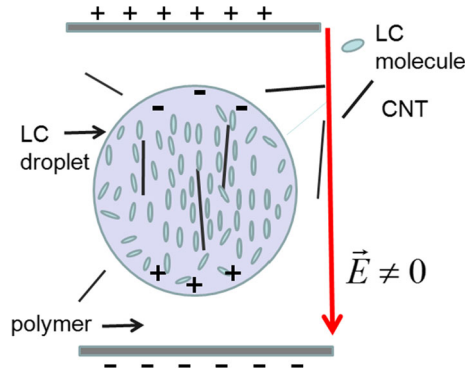
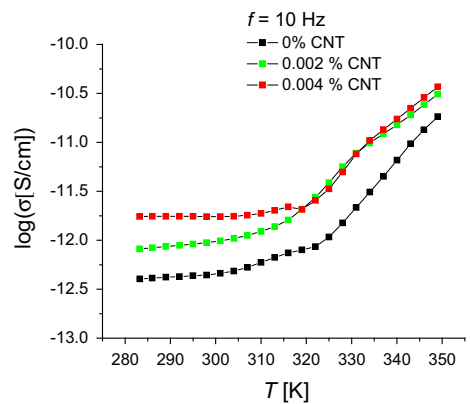


Fig. 4 Temperature dependency of the electric conductivity σ at 10 Hz: -■- pure PDLC; -■- 0.002% CNTs; -■- 0.004% CNTs



In the absence of the electric field, the CNTs are randomly distributed in the LC droplet and in the polymer. LC molecules tend to align tangent to the CNT (along the length). When the electric field is applied, the LC molecules reorient in the direction of the field, driving the reorientation of the CNTs in the same direction.

Due to the relatively very high conductivity of the LC as compared to the conductivity of the polymer ($\sigma_{LC} \approx 10^{-7}$ S/m and $\sigma_{PMMA} \approx 10^{-10}$ S/m in 40/60 E7/PMMA systems [34]), electric charges will built up at the interface polymer/LC, as shown in Fig. 3, and will reduce the field across the droplet.

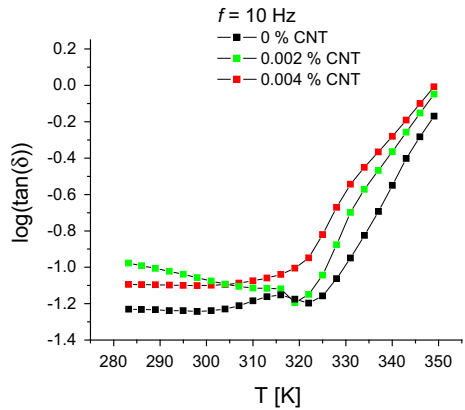
3.2 DS analysis

3.2.1 Temperature dependency

The liquid crystal E7 has the nematic to isotropic transition at 333.5 K, and it has been studied in literature [35]. Figure 4 shows the temperature dependency of the electric conductivity at a 10 Hz signal frequency, the purpose of the representation being the observation of the phase transition, in a more or less attenuated form, in the studied samples. Figure 5 shows the temperature variation of the loss tangent at fixed frequency, 10 Hz.

As shown in Fig. 4, the curves have a complicated shape: this complexity is easy to understand due to the presence of the two or three components of the samples (E7/PMMA, E7/PMMA-CNT) and their mutual interactions.

Fig. 5 Temperature dependency of $\log(\tan(\delta))$ at fixed frequency, 10 Hz: \blacksquare —pure PDLC, \blacksquare —0.002% CNTs, \blacksquare —0.004% CNTs



It should be noted the variation with two orders of magnitude of conductivity over the entire temperature range. The curves do not show any phase transition. We suppose that the nematic to isotropic transition of the E7 LC is hidden by the PMMA component, as it is seen both in the curves corresponding to the pure and doped samples. The PMMA component induces a higher, pre-existing state of order of LC molecules, an order that is maintained even above the transition temperature, very probable due to the anchoring of the LC molecules to the PMMA interface.

In the temperature range 310–330 K the curves in Figs. 4 and 5 show inflection points, a change in the rate of variation with temperature. The temperature domain can be divided in two subintervals, with very different variation rates: the range of relatively low temperatures, below $T = 320$ K, in which the variation rate values are very small, close to zero and the range of relatively high temperatures, above $T = 320$ K, where the values of the variation rate are significantly higher.

As seen in Fig. 4, the presence of CNT has the effect of increasing electrical conductivity, with increasing concentration, which obviously occurs in the region of low temperatures. At high temperatures, the values tend to approach the same limit and obviously the influence of the E7-PMMA host becomes dominant compared to the effect of CNTs.

According to Fig. 5, the loss tangent versus temperature, there is a “turning point” at temperature $T = 330$ K for the two samples doped with CNTs. The pure and the 0.002%—CNT doped samples show a complicated, non-monotonous variation with temperature. These behaviours are the result of the interaction between the two (E7-PMMA) or three (CNT-E7-PMMA) components of the samples. It is found that, at high temperatures, the values of $\tan(\delta)$, corresponding to the different samples, tend to have the same limit.

3.2.2 Frequency dependence at fixed temperatures

The experimental results obtained with DS, which describe the electrical properties, are usually represented by the complex function of the permittivity.

$$\varepsilon * (\omega) = \varepsilon'(\omega) - i\varepsilon''(\omega). \tag{1}$$

Equivalently, other representations can be used: components of electrical conductivity, $\sigma *(\omega)$, dielectric modulus, $M^*(\omega)$ or loss tangent, $\tan(\delta)$.

The following simple relationships between the mentioned electrical quantities can be established:

The electrical conductivity and the dielectric permittivity of a material are linked by a direct general relation. For a sinusoidal electric field, this is:

$$\sigma^*(\omega) = \sigma'(\omega) + i\sigma''(\omega) = \sigma_0 + i\varepsilon_0\varepsilon^*(\omega) \quad (2)$$

The real and the imaginary parts are:

$$\sigma'(\omega) = \sigma_0 + \omega\varepsilon_0\varepsilon''(\omega), \quad \sigma''(\omega) = \omega\varepsilon_0\varepsilon'(\omega) \quad (3)$$

The *dielectric modulus* is defined as the inverse of the complex dielectric function: $M^*(\omega) = 1/\varepsilon^*(\omega)$, and the loss tangent is equal to the ratio between the imaginary and the real component of the complex dielectric function:

$$\tan(\delta(\omega)) = \varepsilon''(\omega)/\varepsilon'(\omega), \quad (4)$$

where δ is complementary to the phase shift angle.

In the following section, we will call “spectrum” the graphical representation of both electrical quantities considered above depending on the frequency or angular velocity.

3.2.3 Loss tangent spectra

Figure 6 presents the loss tangent spectra at three fixed temperatures: $T = 283$ K (a), $T = 315$ K (b) and $T = 349$ K (c).

At low temperature, $T = 283$ K, below the E7 transition temperature, there are two maxima, two net relaxation processes, narrow, “sharp” and well demarcated, one at medium frequencies (100 Hz), called the α -process, and another at high frequencies (1 MHz), the β -process. The α -dielectric relaxation process is attributed to the movement of LC molecules around their short axis. The rotational motion is “slowed” by the additional interaction between the molecular electric dipoles and the polymer. The β process is attributed to the movement of molecules around their long axis. This type of movement is less influenced by the interaction mentioned above.

At a higher temperature, $T = 315$ K, still in the nematic phase of the LC, the maxima of the α -process, initially in the middle frequency region, shift to higher frequencies, as it was expected. The β processes can no longer be observed because the frequency corresponding to their maximum has exceeded the upper limit of the registered frequency band.

In the isotropic state of the LC, at high temperature, $T = 349$ K, the α -process flattens and shifts to even higher frequencies, so that they might exceed the maximum frequency (10 MHz) of the frequency band. The samples show a descending branch in the region of low frequencies (below 100 Hz). This behaviour is due to the mobile charge carriers’ contribution of electrical conductivity, but the curvature of these branches at very low frequencies, below 0.5 Hz, shows the approach of a maximum point. This tendency indicates the manifestation of polarization at the electrode, the accumulation of free carriers on the surface of the electrodes.

3.2.4 Electrical conductivity spectra

Figure 7 represents the conductivity spectra at fixed temperatures, nematic state: $T = 283$ K (a) and $T = 315$ K (b) and isotropic phase: $T = 349$ K (c).

The curves show the increase of the electrical conductivity influence due to the CNTs.

For these samples, at high frequencies, the influence of the dielectric relaxation process of the host, the pure sample, is still observed. The plateau region, where the conductivity is relatively constant, which is barely noticeable at the temperature $T = 315$ K, extends

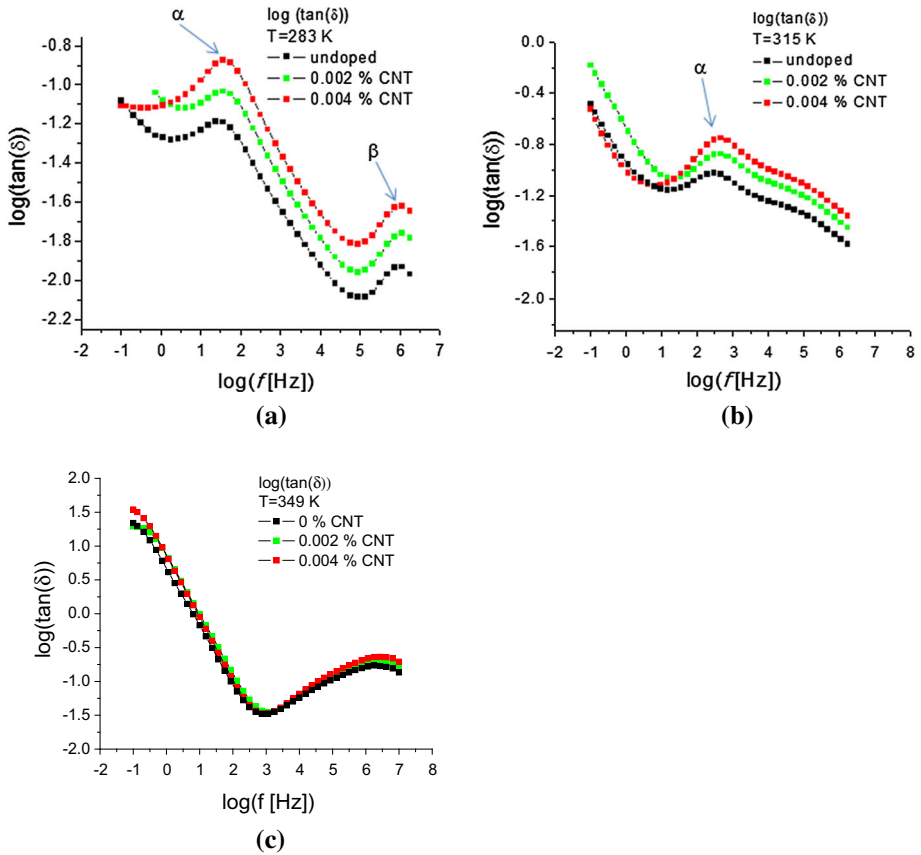


Fig. 6 Loss tangent spectra— $T = 283 \text{ K}$ (a); $T = 315 \text{ K}$ (b); $T = 349 \text{ K}$ (c). ■- pure PDLC, ■-0.002% CNTs, ■-0.004% CNTs

even further, to higher frequencies at the temperature of $T = 349 \text{ K}$. At the same time, the conductivity values, in this frequency range, are higher than the conductivity measured at lower temperatures.

3.2.5 Fitting examples

(a) Spectra fitting

To study the response of the molecular system to the applied alternative electric field we have used the Havriliak–Negami (HN) [36, 37] fitting function, which is a generalization of the dipolar relaxation functions Debye, and has the form:

$$\varepsilon_{HN,i}^*(\omega) = \varepsilon_i'(\omega) - i\varepsilon_i''(\omega) = \varepsilon_{(r,\infty),i} + \frac{\varepsilon_{(r,0),i} - \varepsilon_{(r,\infty),i}}{(1 + (i\omega \cdot \tau_{\max,i})^{a_i})^{b_i}} \quad (5)$$

$i = 1, 2$ corresponding to the respective order number of H-N function. In Eq. (5), $0 < a_i < 1$; $0 < b_i < 1$; $\varepsilon_{(r,0),i}$ is the relative permittivity at very low frequencies (the limit $\omega \rightarrow 0$), and $\varepsilon_{(r,\infty),i}$ is the relative permittivity at very high frequencies ($\omega \rightarrow \infty$), $\tau_{\max,i}$ is the

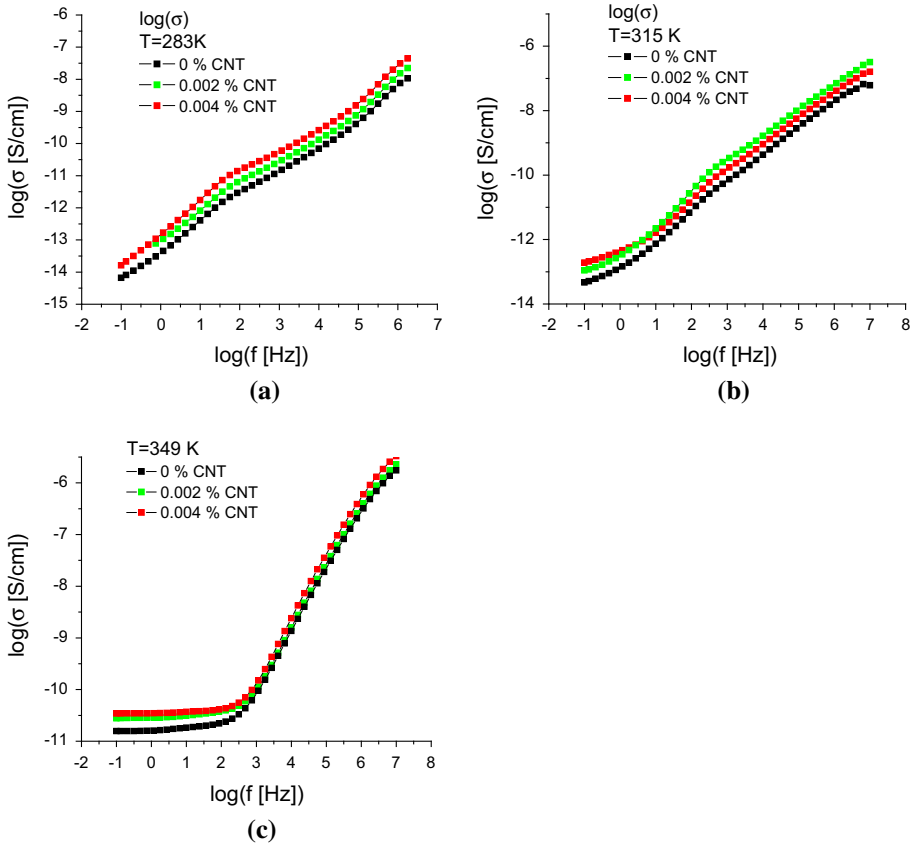


Fig. 7 Conductivity spectra at three fixed temperatures:— $T = 283$ K (a); $T = 315$ K (b); $T = 349$ K (c). ■—pure PDLC, ■—0.002% CNTs, ■—0.004% CNTs

characteristic relaxation time. The shape parameters, a_i and b_i , influence the broadening and the asymmetry of the relaxation curve, around the maximum of the losses. The characteristic time is the quantity that best characterizes the molecular dynamics.

The parameters of H-N functions are obtained by fitting on the loss tangent spectra, $\tan(\delta)$. The important result is how the characteristic time depends on the temperature at which the electrical quantities spectra have experimentally been obtained.

Upon careful analysis, we notice that the spectra have a rather complicated shape. For this reason, concretely, for the adjustment to the experimental curves, the generalized function of the complex permittivity is used, which includes two H-N functions and a conduction term, as follows:

$$\varepsilon * (\omega) = -i \left(\frac{\sigma_0}{\varepsilon_0 \omega} \right)^N + \varepsilon_{HN,1} * + \varepsilon_{HN,2} * \tag{6}$$

where σ_0 is the specific dc-conductivity, N is a positive, subunit exponent. Using the generalized H-N function fitting, the characteristic relaxation time was obtained, by choosing its value corresponding to the medium frequency range.

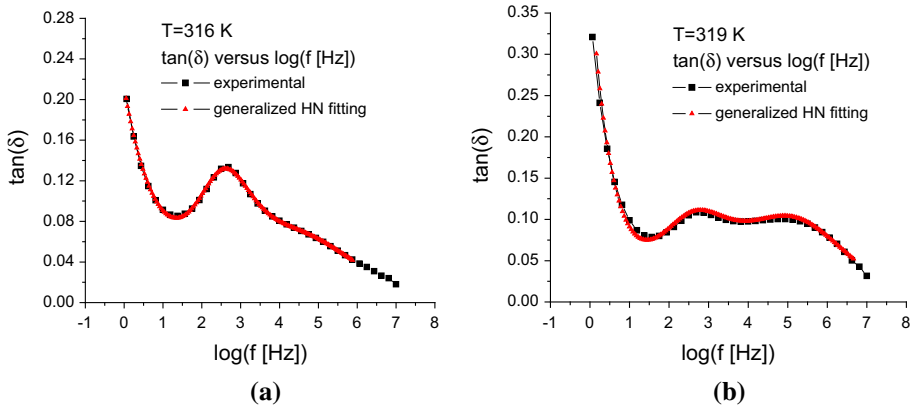
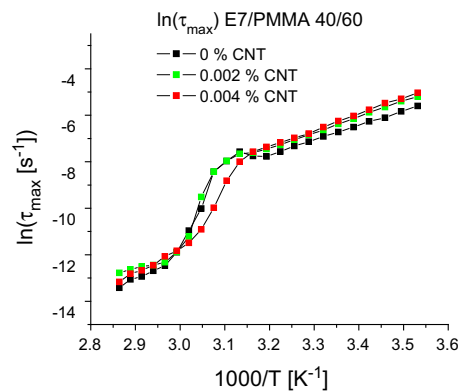


Fig. 8 The experimental spectrum (solid black square) and the generalized H-N fitting function (solid red triangle) at **a** 316 K and **b** 319 K

Fig. 9 Arrhenius diagram: $\ln(\tau_{\max})$ versus $1000/T$ for the studied samples



All CNT doped E7/PMMA samples show a sudden change in the shape of the spectra at the transition from temperature $T = 316$ K to temperature $T = 319$ K. For exemplification, we chose the spectra of the tangent of the losses of the pure E7-PMMA sample.

The experimental $\tan(\delta)$ spectra and their corresponding fitting functions, at the above mentioned temperatures, $T = 316$ K and $T = 319$ K are shown in Fig. 8a, b.

Up to the temperature of $T = 316.15$ K, there is a well pronounced and dominant maximum in the region of average frequencies ($f = 100$ – 1000 Hz). At the immediately higher temperature, $T = 319$ K, the existence of two maxima is observed, that are comparable in “intensity” and much flattened.

The flat shape of the spectrum, at frequencies higher than 500 kHz, is the effect of overlapping several relaxation processes. It results that the location of the maximum points through the fitting process (deconvolution) can no longer be done with great precision, as can be seen in the Arrhenius diagram presented in Fig. 9 and discussed in the following subsection.

(b) Activation energy for the CNT doped E7-PMMA samples

The curves $\ln(\tau_{\max})$ versus $1000/T$ presented in Fig. 9 show different variation rates, in the temperature domains: 280–316 K (corresponding to the nematic state of the LC), 316–333 K and 333–350 K (corresponding to the isotropic state of the LC). The middle,

Table 1 DS characteristic constants for E7/PMMA and E7/PMMA-CNT doped samples

	Sample composition	τ_0 (s) 10^{-13}	A (E_A) (eV)	T_V (K)	Least squares method error
1	Undoped E7/PMMA	3.9	0.507	0.100	8.800×10^{-03}
2	E7/PMMA-0.002% CNT	0.27	0.589	0.033	1.144×10^{-02}
3	E7/PMMA-0.004% CNT	0.12	0.603	0.100	1.227×10^{-02}

relatively large transitory temperature range is attributed to the interface interaction LC-polymer chains and to the LC nematic to isotrop phase transition.

As seen in Figs. 5 and 6, the absolute values of the conductivity, or $\tan(\delta)$, increase at the increase of the CNT concentration, but they are quite close. In some regions of the graphs, the curves overlap or intersect.

The influence of CNT concentration can be highlighted, in a more subtle way, by descending to the molecular level, and calculating the activation energy of the α -relaxation process for all three samples considered so far.

The dependency $\tau_{\max} = f\left(\frac{1}{T}\right)$ can be modeled using the Vogel–Fulcher–Tammann (VFT) law [23, 38]:

$$\tau_{\max} = \tau_{\infty} \exp \left[\frac{A}{k_B(T - T_V)} \right] \quad (7)$$

where A is a material constant, associated with the energy of activating the rotational motion of the electric dipoles, k_B is Boltzmann's constant, T is the current temperature and T_V is the Vogel temperature, τ_{∞} is a pre-exponential factor.

All fitting parameters, τ_{∞} , T_V and A , were left free so that they could be obtained by the program, using the least squares method. We have adopted this path, because we intentionally did not want to introduce any additional assumptions or hypotheses related to the dependency law of the characteristic time on temperature. The temperature range was chosen between 283 and 316 K, for all samples, a range in which the characteristic time dependence of temperature is predictable. The fitting results are summarized in Table 1.

Because the obtained Vogel temperature is very small, the VFT equation passes into the Arrhenius one, the material constant A being assimilated to the activation energy E_A .

The first two fitting parameters have a monotonous variation with the CNT concentration. The values obtained for parameter A , show a very good confidence, because it describes the characteristic time behaviour over the entire temperature range.

After analyzing the values in the Table 1, one comes to the conclusion that the activation energy increases with increasing CNT concentration.

The increase of the activation energy with the CNT concentration is due to the interaction between the electric dipoles of the LC and CNT molecules, which leads to the increase of the potential barrier that must be overcome to change the orientation under the action of the applied electric field. CNTs, through their concentration, have a double effect, increasing the electrical conductivity of direct current and increasing the activation energy of the movement of LC molecules.

4 Conclusions

We obtained PDLC samples, E7/PMMA, 40/60 (w.w.) and the corresponding CNTs doped films.

For the N-I phase transition temperature, DSC spectra show a slight shift towards smaller values for the doped samples as compared to the pure one.

The clearing temperatures (nematic to isotropic transition) recorded by DSC for the PDLC blends were found to shift to lower values than the value recorded for pure E7 LC mixture with no significant impact of the CNTs' concentration due to the dominant effect of the E7/PMMA host.

From the DS study, a two order magnitude variation of the conductivity over the entire temperature range was observed. The nematic to isotropic phase transition was not clearly evidenced on the conductivity plots due to the anchoring of the LCs at the polymer interface in the small existing droplets which hinders the partially ordered–disordered passage observation. However, the plot of the conductivity and loss tangent versus temperature, in the 310–330 K temperature range, display several inflection points and clear modifications of variation rates. These behaviours are the result of the interaction between the E7-PMMA and CNT-E7-PMMA components of the samples.

The presence of CNTs gives an increase of electrical conductivity, with increasing concentration.

At high temperatures, the conductivity and the loss tangent values get closer and tend to approach the same limit. The influence of the E7-PMMA host becomes dominant as compared to the CNTs.

Since a sudden change in the shape of the spectra was obtained in the (316–319) K interval, the loss tangent was studied at the lower and upper limit of the interval. Because a complex shape of the loss tangent spectra was observed, the generalized H-N functions have been used for fitting. A very good agreement with the experimental results was obtained, and the values of the characteristic times were extracted. The flat shape of the spectrum, at frequencies higher than 500 kHz, was assigned to overlapping effect of several relaxation processes.

The temperature variation of the characteristic time has three variation rate domains, which were attributed to: the nematic phase of the LC (at the lower temperature range), a transition, relatively large temperature range attributed to the interface interaction LC-polymer chains and to the LC nematic to isotrop phase transition and, at the highest temperature range, to the isotropic phase of the LC.

The dependency of the characteristic relaxation time on temperature was modeled using the Vogel–Fulcher–Tammann function and showed a temperature variation according to the Arrhenius law. The very low values of the Vogel temperature show that the characteristic time, for all samples, is subject to the Arrhenius law, and the fitting parameter, identified with the activation energy, increased with increasing CNT doping concentration.

The present study might be used in the optical transmission models in some frequency ranges and in the design of electrical circuits that incorporate PDLC films-based devices.

Acknowledgements Acknowledgement PCG acknowledges the funding through Core Program PN19-03 (Contract No. 21 N/08.02.2019), from Romanian Ministry of Research and Innovation.

References

1. P.S. Drzaic, *Liquid Crystal Dispersions* (Word Sci, Singapore, 1995)

2. H. Ramanitra, P. Chanclou, B. Vinouze, L. Dupont, *Mol. Cryst. Liq. Cryst.* **404**(1), 57–73 (2003). <https://doi.org/10.1080/15421400390249952>
3. H. Hakemi, *Liq. Cryst. Today* **26**(3), 70–73 (2017). <https://doi.org/10.1080/1358314X.2017.1359143>
4. M. Ozolinsh, G. Papelba, *Ferroelectrics* **304**(1), 207–212 (2004). <https://doi.org/10.1080/00150190490456790>
5. T.C. Hsu, C.H. Lu, Y.T. Huang, W.P. Shih, W.S. Chen, *Sens. Actuators, A* **169**(2), 341–346 (2011). <https://doi.org/10.1016/j.sna.2011.01.018>
6. J. Lagerwall, G. Scalia, *J. Mater. Chem.* **18**(25), 2890–2898 (2008). <https://doi.org/10.1039/b802707b>
7. M. Rahman, W.J. Lee, *Phys. D: Appl. Phys.*, 42(6), 42, (063001-1)-(063001-12), (2009), <https://doi.org/10.1088/0022-3727/42/6/063001>
8. L. Dolgov, O. Kovalchuk, N. Lebovka, S. Tomyloko, O. Yaroshchuk, Liquid crystal dispersions of carbon nanotubes: dielectric, electro-optical and structural peculiarities, in *Carbon Nanotubes*, ed. by J.M. Marulanda (InTechOpen, 2010). <https://doi.org/10.5772/39439>
9. I. Dierking, G. Scalia, P. Morales, D. LeClere, *Adv. Mat.* **16**(11), 865–869 (2004). <https://doi.org/10.1002/adma.200306196>
10. C.P. Ganea, D. Manaila-Maximean, *U.P.B. Sci. Bull. Ser. A* **73**(4), 209–216 (2011)
11. S. Frunza, A. Schönhals, L. Frunza, T. Beica, I. Zgura, P. Ganea, D. Stoenescu, *Chem. Phys.* **372**, 51–60 (2010). <https://doi.org/10.1016/j.chemphys.2010.04.031>
12. S. Frunza, A. Schonhals, L. Frunza, P. Ganea, H. Kosslick, J. Harloff, A. Schulz, *J. Phys. Chem. B* **114**, 12840–12846 (2010). <https://doi.org/10.1021/jp1071617>
13. S. Frunza, L. Frunza, C.P. Ganea, I. Zgura, A. Schoenhals, *UPB Sci. Bull. Ser. A* **81**, 223–236 (2019)
14. D. Manaila-Maximean, V. Cîrcu, P.C. Ganea, *Beilstein J. Nanotechnol.* **9**, 164–174 (2018). <https://doi.org/10.3762/bjnano.9.19>
15. D. Manaila-Maximean, V. Cîrcu, C.P. Ganea, A. Barar, O. Danila, T. Staicu, V.A. Loiko, A.V. Konkolovich, A.A. Miskevich, in *(SPIE) Conference Series* (Vol. 10977), p. 1097702, (2018). <https://doi.org/10.1117/12.2326186>
16. V.A. Loiko, A.V. Konkolovich, A.A. Miskevich, D. Manaila-Maximean, O. Danila, V. Cîrcu, A. Bărar, J. Quant. Spectrosc. Radiat. Transf. **245**, 106892 (2020). <https://doi.org/10.1016/j.jqsrt.2020.106892>
17. K.B. Zegadlo, H. El Ouazzani, I. Cieslik, R. Weglowski, J. Zmija, S. Klosowicz, A. Majchrowski, J. Mysliwiec, B. Sahraoui, M.A. Karpierz, *Opt. Mater.* **34**(10), 1704–1707 (2012). <https://doi.org/10.1016/j.optmat.2012.02.027>
18. D. Donescu, R.C. Fierascu, M. Ghiurea, D. Manaila-Maximean, C.A. Nicolae, R. Somoghi, C.I. Spataru, N. Stanica, V. Raditoiu, E. Vasile, *Appl. Surf. Sci.* **414**, 8–17 (2017). <https://doi.org/10.1016/j.apsusc.2017.04.061>
19. S. Tomyloko, O. Yaroshchuk, O. Kovalchuk, U. Maschke, R. Yamaguchi, *Mol. Cryst. Liq. Cryst.* **541**(1), 35–273 (2011). <https://doi.org/10.1080/15421406.2011.569658>
20. V.A. Loiko, Konkolovich, A.A. Miskevich et al., *Opt. Spectrosc.* **128**, 331–338 (2020). <https://doi.org/10.1134/s0030400x20030121>
21. T. Lahiri, S.K. Pushkar, P. Poddar, *Phys. B* **588**, 412177 (2020). <https://doi.org/10.1016/j.physb.2020.412177>
22. L. Lisetski, M. Soskin, N. Lebovka. Carbon nanotubes in liquid crystals: fundamental properties and applications, in *Physics of Liquid Matter: Modern Problems, Springer Proceedings in Physics*, ed. by L. Bulavin, N. Lebovka, (2015), p. 171. https://doi.org/10.1007/978-3-319-20875-6_10
23. S. Iijima, *Nature* **354**, 56–58 (1991). <https://doi.org/10.1038/354056a0>
24. M.S. Dresselhaus, G. Dresselhaus, R. Saito, *Carbon* **33**(7), 883–891 (1995). [https://doi.org/10.1016/0008-6223\(95\)00017-8](https://doi.org/10.1016/0008-6223(95)00017-8)
25. M.S.E. Peterson, G. Georgiev, T.J. Atherton, P. Cebe, *Liq. Cryst.* **45**, 450–458 (2018). <https://doi.org/10.1080/02678292.2017.1346212>
26. Y. Wu, H. Cao, M. Duan, E. Li, H. Wang, Z. Yang, D. Wang, W. He, *Liq. Cryst.* **7**, 1023–1031 (2018). <https://doi.org/10.1080/02678292.2017.1404153>
27. D. Manaila-Maximean, O. Danila, C.P. Ganea, P.L. Almeida, *Eur. Phys. J. Plus* **133**(4), 159 (2018). <https://doi.org/10.1140/epjp/i2018-11997-8>
28. O. Danila, *J. Quant. Spectrosc. Radiat. Transf.* **254**, 107209 (2020). <https://doi.org/10.1016/j.jqsrt.2020.107209>
29. Z.Z. Zhong, D.E. Schuele, W.L. Gordon, K.J. Adamic, R.B. Akins, *J. Pol. Sci. Part B Polym. Phys.* **30**(13), 1443–1449 (1992). <https://doi.org/10.1002/polb.1992.090301303>
30. T. Kyu, M. Mustafa, J.-C. Yang, J. Y. Kim, P. Palffy-Muhoray, in *Polymer Solutions, Blends, and Interfaces*, ed. by I. Noda, D.N. Rubingh, (Elsevier, 1992), p. 245
31. H. Duran, B. Gazdecki, A. Yamashita, T. Kyu, *Liq. Cryst.* **32**(7), 815–821 (2005). <https://doi.org/10.1080/02678290500191204>

32. K.P. Sigdel, G.S. Iannacchione, *Eur. Phys. J. E* **34**, 34 (2011)
33. P. Kalakonda, R. Basu, I.R. Nemitz, C. Rosenblatt, G.S. Iannacchione, *J. Chem. Phys.* **140**, 104908 (2014). <https://doi.org/10.1063/1.4867791>
34. J.R. Kelly, D. Seekola, in *Liquid Crystal Displays and Applications*, ed. by J.W. Doane, Z. Yaniv, SPIE, 1257,17, 17–28, (1990). <https://doi.org/10.1117/12.19923>
35. M.T. Viciosa, A.M. Nunes, A. Fernandes, P.L. Almeida, M.H. Godinho, M.D. Dionísio, *Liq. Cryst.* **29**, 429–441 (2002). <https://doi.org/10.1080/02678290110113478>
36. S. Urban, B. Gestblom, H. Kresse, A. Dabrowski, *Z. Naturforsch. A*, **51**(7), 834–842, (1996), <https://doi.org/10.1515/zna-1996-0707>
37. C.P. Ganea, *Rom. J. Phys.* **57**(3–4), 664–675 (2012)
38. A. Yildirim, P. Szymoniak, K. Sentker, M. Butschies, A. Buhlmeier, P. Huber, S. Laschat, A. Schonhals, *Phys. Chem. Chem. Phys.* **20**, 5626 (2018). <https://doi.org/10.1039/C7CP08186C>



Effect of titanium oxide nanoparticles on the dielectric properties and ionic conductivity of a new smectic bis-imidazolium salt with dodecyl sulfate anion and cyanobiphenyl mesogenic groups

Constantin Paul Ganea^a, Viorel Cîrcu^{b,*}, Doina Manaila-Maximean^{c,*}

^a National Institute of Materials Physics, POBox MG 07, 077125 Magurele, Romania

^b Department of Inorganic Chemistry, University of Bucharest, 23 Dumbrava Rosie st, sector 2, Bucharest 020464, Romania

^c University Politehnica of Bucharest, Department of Physics, 313 Spl. Independentei, 060042, Bucharest, Romania

ARTICLE INFO

Article history:

Received 14 May 2020

Received in revised form 8 July 2020

Accepted 27 July 2020

Available online 4 August 2020

Keywords:

Ionic liquid crystals

Nano-dopant

Dielectric spectroscopy

Relaxation characteristic time

Electrode polarization

ABSTRACT

A new bis-imidazolium salt with two cyanobiphenyl groups and dodecyl sulfate counterion (BIC) was prepared by the metathesis reaction of the bromide salt with sodium dodecyl sulfate. The ILC shows at room-temperature a stable smectic A phase, confirmed by differential scanning calorimetry, polarized optical microscopy, and powder X-ray diffraction investigations. The ILC was doped with TiO₂ nanoparticles, having a high specific area, in concentrations of 0.1%, 0.2%, 1% and 2%.

Broadband Dielectric Spectroscopy spectra have been registered in the (10⁻¹–10⁷) Hz frequency range, and (250–330) K temperature domain.

The study shows that at constant frequency, the conductivity increases with the temperature and dopant concentration. The characteristic times of the observed relaxation processes showed a temperature variation according to the Vogel-Fulcher-Tammann law. Higher values of characteristic times were calculated at the increase of the thickness of the sample. On the other hand, the increase of the concentration of TiO₂ nanoparticles leads to a decrease of the characteristic relaxation times.

In order to detect whether the obtained high permittivity increase is due to the Maxwell-Wagner or Electrode Polarization (EP) type phenomena, studies were made on samples of the same concentration, but different thicknesses, and EP was assigned as the main cause of this dielectric constant variation.

© 2020 Elsevier B.V. All rights reserved.

1. Introduction

Ionic liquid crystals (ILCs) are a class of materials integrating the special conductive properties of ionic liquids (ILs) and the self-organization characteristics of the liquid crystals (LCs) [1–4].

While being formed of cation/anion typical to the ILs, the attaching of long alkyl chains helps the setting up of mesophases characteristic to the LCs, such as the smectic ones. These types of materials are currently being studied extensively, and their field of utilization is constantly expanding due to their recent applications: solar cells [5], membranes, battery materials, electrochemical sensors, electroluminescent switches, etc.

On the other hand, in the last decade, attempts have been done to improve the LCs characteristics by doping with nanoparticles (NPs), in an attempt to combine some beneficial features of the LCs and NPs [6,7].

Due to the interaction with the host matrix, NPs can be aligned or reoriented by the LC, producing notable changes in their electrical and optical properties [8–11], accompanied by thermodynamic changes in phase transitions [12–14]. A wide range of NPs has been used as dopants: carbon nanotubes [15–18], graphenes [19], aerogels [10,11,20,21], gold, magnetic NPs [22–24], diamond [25] etc. The TiO₂ particles were used as dopant in LCs, obtaining increases in ionic conduction and decreases in switching voltage [26–28].

In this work we present the design and synthesis of a new ILC, a dimeric bis-imidazolium salt with cyanobiphenyl groups and dodecyl sulfate counterion. The ILC was characterized by ¹H and ¹³C NMR spectroscopy. Its crystalline properties have been analysed by polarizing optical microscopy (POM), differential scanning calorimetry (DSC) and powder X-ray diffraction (XRD) studies. The dielectric spectra of the ILC doped with different amounts of TiO₂ NPs have been registered in the frequency range from 10⁻¹ to 10⁷ Hz and in the temperature range from 250 to 330 K corresponding to the different phases of the ILC (mesophase and isotropic state). We discuss the influence of the dopant in the obtained permittivity, dielectric

* Corresponding authors.

E-mail addresses: viorel.circu@chimie.unibuc.ro (V. Cîrcu), doina.manaila@physics.pub.ro, doina.manaila@upb.ro (D. Manaila-Maximean).

loss and conductivity. The activation energy was calculated by employing the Vogel–Fulcher–Tammann law [29] and the characteristic time was obtained by fitting the spectra of the dielectric loss with the Havriliak–Negami functions [22,30]. Since electrode polarization [31] could shield the dielectric response of the studied material, we have also analyzed samples of difference thicknesses at constant dopant concentration.

2. Experimental

All the chemicals were from commercial sources and used as supplied (Sigma-Aldrich and Merck). TLC was performed on commercial coated aluminium plates with Silica Gel matrix with fluorescent indicator 254 nm (Sigma Aldrich), and the detection was done by an UV lamp. C, H, N analyses were carried out with an EuroVector EA 3300 instrument.

^1H and ^{13}C NMR spectra were recorded on a Bruker Fourier 300 spectrometer operating at 300 MHz, using CDCl_3 as solvent. ^1H and ^{13}C chemical shifts were referenced to the solvent peak position (7.26 ppm ^1H , 77.00 ppm ^{13}C). The proposed structure for the bis-imidazolium derivatives fully agrees with the recorded experimental data. The liquid crystalline properties of the new bis-imidazolium salt were analysed using a Nikon 50iPol polarized optical microscope connected with a Linkam THMS600 hot stage and TMS94 control processor. Untreated glass slides were used for these observations. The thermal behaviour and the enthalpies of the phase transitions for the bis-imidazolium salt as well as the samples doped with TiO_2 were recorded with a Diamond DSC Perkin Elmer instrument. The samples were encapsulated in aluminium pans and analysed at a scanning rate of 10 K/min. Two heating/cooling cycles were recorded for each sample. The powder X-ray diffraction measurements were performed on a D8 Advance diffractometer (Bruker AXS GmbH, Germany), in parallel beam setting, with monochromatized $\text{Cu-K}\alpha_1$ radiation ($\lambda = 1.5406 \text{ \AA}$), scintillation detector, and horizontal sample stage. The measurements were made in symmetric (θ - θ) geometry in the 2θ range from 1.5° to 35° in steps of 0.02° , with measuring times per step in the 5–40 s range. The sample was deposited on glass slides and measured at room temperature (298 K).

2.1. Dielectric spectroscopy (DS)

The Dielectric Spectroscopy measurements were performed using a Broadband Dielectric Spectrometer, NOVOCONTROL, consisting in the Alpha-A High Performance Frequency Analyzer in the LF domain $0.1\text{--}10^7$ Hz equipped with WinDETA software. The spectra have been registered in the (250–330) K temperature domain. Temperatures were controlled within 0.2 K. Alternative voltage is set to 0.5 V.

2.2. Synthesis of compound 1

This compound was prepared from 1,1'-(1,6-hexanediyl)bisimidazole and 4'-(6-bromohexyloxy)biphenyl-4-carbonitrile in a similar way with the procedure described in literature [32]. 1,1'-(1,6-hexanediyl)bisimidazole (1.36 g, 6.25 mmol) was dissolved in acetonitrile. To this solution, 4'-(6-bromohexyloxy)biphenyl-4-carbonitrile (5 g, 14 mmol) was added, and the reaction mixture was heated under reflux in nitrogen overnight. After this time, the solvent was removed via rotary evaporation. The residue was purified by column chromatography using silica gel with dichloromethane–methanol (9:1). Yield 95% ^1H NMR (300 MHz, ppm, CDCl_3) δ 10.52 (s, 2H), 7.72–7.62 (m, 10H), 7.53 (d, 4H, $J = 8.7$ Hz); 7.29 (s, 2H), 6.97 (d, 4H, $J = 8.7$ Hz), 4.40–4.28 (m, 8H), 3.98 (t, 4H, $J = 6.3$ Hz), 1.95 (m, 8H), 1.77 (m, 4H), 1.50–1.25 (m, 12H).

2.3. Synthesis of compound 2 (BIC)

A solution of sodium dodecyl sulfate (1.09 g, 3.75 mmol) in methanol (25 ml) was added dropwise over a solution of bis-imidazolium bromide salt 1 (1.40 g, 1.5 mmol) in dichloromethane (50 ml). The mixture was stirred at room temperature for 2 h. After this time 100 ml of deionized water was added and the organic layer was separated and washed several times with water until no further identification reaction of Br^- ion with AgNO_3 was noticed. The phase was dried over sodium sulfate followed by the removal of organic solvent by rotary evaporation. The solid was recrystallized two times from a mixture of dichloromethane and ethyl ether to give a waxy white solid. Yield 69%. Anal. Calcd. for $\text{C}_{74}\text{H}_{108}\text{N}_6\text{O}_{10}\text{S}_2$: C% 68.06, H% 8.34, N% 6.44. Found: C% 67.74, H% 8.55, N% 6.62. ^1H NMR (300 MHz, ppm, CDCl_3) δ 9.61 (s, 2H), 7.72 (s, 2H), 7.63 (m, 8H), 7.50 (d, $J = 8.6$ Hz, 4H), 7.28 (s, 2H), 6.95 (d, $J = 8.6$ Hz, 4H), 4.47–4.18 (m, 8H), 3.99 (m, 8H), 1.91–1.61 (m, 12H), 1.70–1.12 (m, 52H), 0.84 (t, $J = 6.5$ Hz, 6H). ^{13}C NMR (75 MHz, ppm, CDCl_3) δ 159.62, 145.19, 136.92, 132.56, 131.31, 128.33, 127.05, 123.18, 121.76, 119.11, 115.05, 110.00, 67.84, 49.85, 49.40, 31.90, 30.12, 29.75, 28.91, 28.91, 28.68, 25.96, 25.49, 24.39, 22.68, 14.13.

2.4. Preparation of the mixtures of ILC doped with TiO_2 nanoparticles

TiO_2 nanoparticles (Degussa, code name P25) with an average diameter of 20 nm, presenting the phase ratio Rutile/Anatase 85/15, were employed in this study. The samples with 2% and 1% TiO_2 were prepared by dissolving first the bis-imidazolium salt (200 mg) in a minimum volume of dichloromethane (1 mL) followed by the addition of TiO_2 (4 and 2 mg respectively). In each case the resulting mixture was sonicated for at least 60 min followed by the removal of solvent, drying in vacuum and cooling at 273 K. The samples having 0.1 and 0.2% TiO_2 were prepared by mixing 20 mg of previously prepared samples containing either 1 or 2% TiO_2 respectively with 180 mg of pure liquid crystal followed by the same procedure described for the first two samples. All samples were kept at 273 K before the physical measurements. Prior to dielectric measurements, the samples were heated to 323 K and sonicated for at least 15 min to ensure a homogeneous dispersion of TiO_2 in the liquid crystal sample.

In Table 1 are presented the TiO_2 /ILC concentrations and the distance between the electrodes used to perform the Dielectric Spectroscopy (DS) characterization. In order to study the electrode polarization (EP) phenomenon, three samples with the same concentration and different distances between the electrodes have been used.

3. Results and discussion

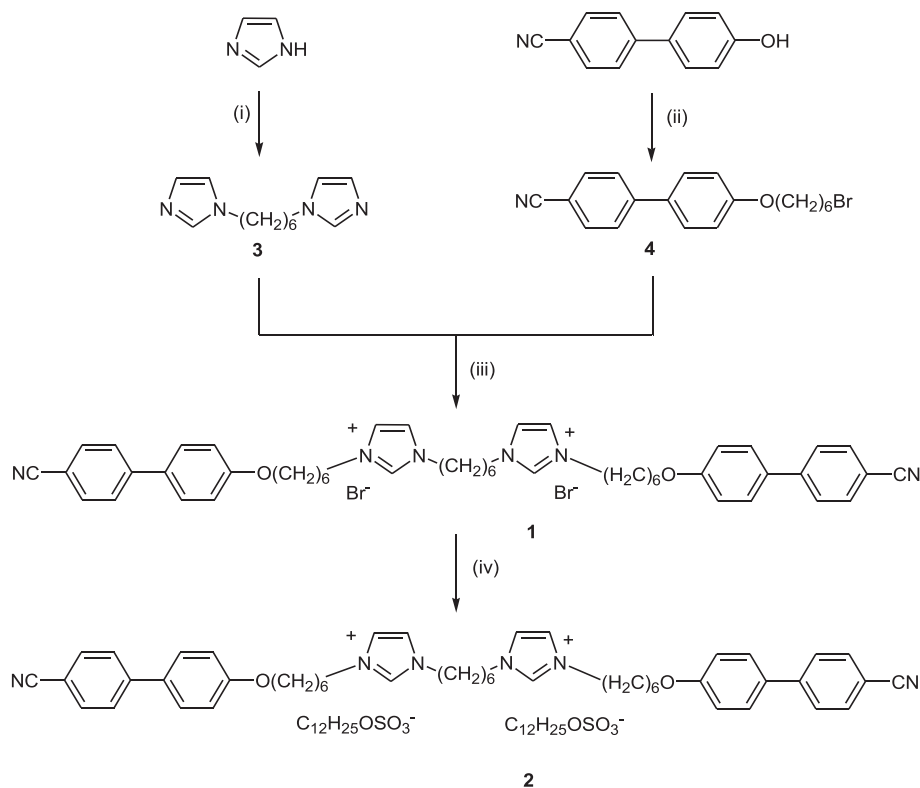
3.1. Synthesis

The synthesis of the new ionic liquid crystal (2-BIC) with two dodecyl sulfate groups as counterions is described in Scheme 1. The new bis-imidazolium salt was prepared starting from 1,1'-(1,6-hexanediyl)bisimidazole (3) [33] and 4'-(6-bromohexyloxy)biphenyl-4-carbonitrile

Table 1

Composition of investigated sample and distances between electrodes in dielectric spectroscopy measurements.

No.	Sample-code name	Composition TiO_2 /ILC concentration [%]	Electrods distance d [μm]
1	BIC	Pure ILC	50
2	BIC-01	0.1%	50
3	BIC-02	0.2%	50
4	BIC-1	1%	50
5	BIC-2	2%	50
6	BIC-2-B	2%	95
7	BIC-2-C	2%	19.5



Scheme 1. Synthesis of dimeric bis-imidazolium salt with cyanobiphenyl groups and dodecyl sulfate counterion: (i) $\text{Br}(\text{CH}_2)_6\text{Br}$, NaH ; (ii) $\text{Br}(\text{CH}_2)_6\text{Br}$, K_2CO_3 , butanone; (iii) acetonitrile, reflux; (iv) $\text{C}_{12}\text{H}_{25}\text{OSO}_3\text{Na}$, methanol/dichloromethane.

(4) in acetonitrile under reflux. The resulting bromide salt (**1**) was purified on silica using dichloromethane - methanol mixture as eluant and recrystallized from a mixture of dichloromethane and ethyl ether. In the next step, the metathesis reaction of the bromide anion with dodecyl sulfate gave the final product as a waxy solid in very good yield [15,34]. The exchange of bromide with dodecyl sulfate ion is clearly supported by ^1H and ^{13}C NMR spectroscopy. The NMR chemical shifts of the three protons of imidazolium rings are strongly dependent on the nature of counterion due to specific anion-cation interactions related to hydrogen bonding. But the most significant change, an upfield shift of the signal assigned to the proton located between the two nitrogen atoms of the imidazolium

ring, was observed in the ^1H NMR of sulfate salt **BIC**, from 10.52 ppm in the ^1H NMR of bromide salt **1** to 9.61 ppm for **BIC** (Fig. S1, SI).

3.2. Thermal behaviour

The thermal behaviour of the pure and the TiO_2 -doped LC samples were investigated by a combination of polarized optical microscopy (POM), differential scanning calorimetry (DSC) and powder X-ray diffraction at room temperature.

The DSC traces for different mixtures of BIC and TiO_2 nanoparticles are shown in Fig. 1. On the first heating run, the bis-imidazolium salt

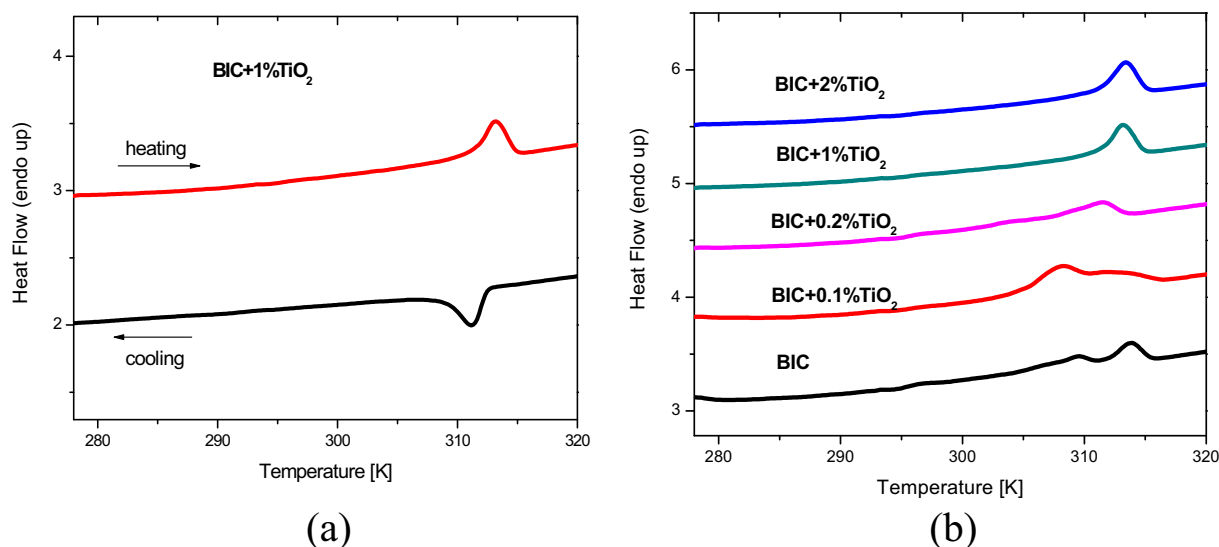


Fig. 1. DSC traces (second heating-cooling cycle) for **BIC** + **1%TiO₂** (a) and the second heating run for pure and doped with TiO_2 ionic liquid crystal (b).

shows a strong endothermic transition with $T_{\text{onset}} = 313.5$ K assigned to a combination of melting from the crystalline phase and clearing transition to the isotropic liquid. The following cooling and heating runs show one broad transition between the isotropic phase and a liquid crystalline phase with $T_{\text{onset}} = 308.6$ K. Cooling the sample below 273 K resulted in a second broad transition to a crystalline phase. Both transitions are reproducible on further heating-cooling cycles with no change of the transition temperature. An increase of the clearing point was seen on increasing the concentration of TiO_2 , from 308.6 K for pure ILC to 312.2 K for ILC doped with 2% TiO_2 concomitant with the sharpening of the SmA-Iso transition (Fig. 1b).

In Table 2 are presented the thermal parameters for bis-imidazolium salt with dodecyl sulfate counterions **2 (BIC)**.

The nature of the liquid crystalline phase was investigated by POM and X-ray diffraction measurements at room temperature. The POM observations evidenced the development of a fan shaped texture on cooling from the isotropic liquid together with large homeotropic areas leading to the assignment of a layered SmA phase, the typical phase seen for ionic liquid crystals (Fig. 2). Additionally, the same features and no significant changes of the textures were observed for the samples doped with TiO_2 which confirm that the nanoparticles are homogeneously dispersed in the liquid crystalline phase (Figs. 3 and 4). When increasing the nanoparticle concentration (2%), small TiO_2 aggregates might be formed. The formation of the SmA phase was confirmed by X-ray diffraction pattern recorded at 298 K after the sample was first heated to 323 K, in the isotropic phase, and then allowed to cool down to room temperature, well below the Iso-SmA transition. The X-ray diffractogram show two strong reflections in the small angle region in the 1: 2 ratio giving a calculated layer spacing of 29.62 Å, and a broad signal with the maximum located around 4.3 Å corresponding to the short-range order lateral intermolecular interactions confirming the liquid-like state of the sample (Fig. 5).

3.3. Dielectric permittivity: study of relaxation process

In Fig. 6 is presented the temperature dependencies of the permittivity for the pure ILC, code name BIC, at three frequencies: 10 Hz, 100 Hz and 1000 Hz. The curves do not present discontinuities.

Three regimes of permittivity variation can be observed: at low temperatures the permittivity is practically constant and the variation rate is very small, at medium temperatures the variation is moderate and at high temperatures the variation rate is important. Between the latter two regimes, there is a “transition” interval between (294–306) K.

The DS results allow the study of the TiO_2 influence on the permittivity variation of different ILC composites.

For comparison, the extreme concentrations (the lowest and the highest concentrations) BIC-01 and BIC-2 samples have been considered. In Fig. 7a and b is presented the real $\epsilon' = \epsilon'(T)$ part of the permittivity of these samples, at two TiO_2 concentrations (samples BIC-01 and BIC-2) at the same frequencies. The analysis of these figures shows that the three temperature regimes are almost unchanged. The “transition” temperature interval shifts slightly towards lower temperatures for the BIC-2 sample as compared to the BIC-01 one.

Table 2
Thermal parameters for bis-imidazolium salt with dodecyl sulfate counterions **BIC**.

Compound	Transition, T/K, $\Delta H/kJ\text{mol}^{-1}$
2(BIC)	1st heating-cooling: Cr ₁ 312 SmA 313.5(74.4) ^a Iso 312.4(−0.7) SmA 263 ^b Cr ₂
	2nd heating-cooling: Cr ₂ 278 SmA 308.4(0.6) Iso ^c 311.5(−0.6) SmA 263 ^b Cr ₂

^a Combined enthalpy for two Cr₁-SmA and SmA-Iso transitions. The first Cr₁-SmA transition was observed by POM.

^b Enthalpy of the SmA-Cr₂ transition was not calculated.

^c Broad transition.

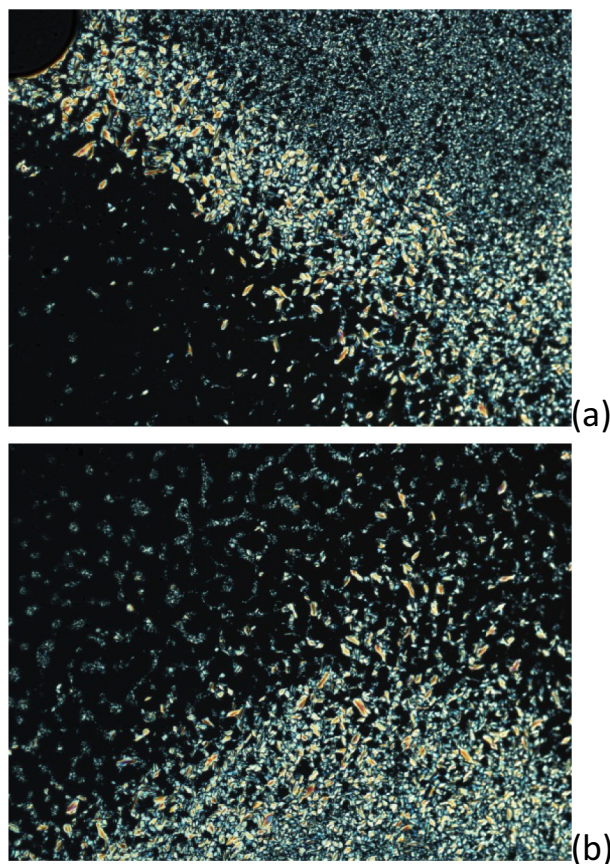


Fig. 2. POM pictures (200×) of **BIC + 0.1%TiO₂** at 308 K (a) and **BIC + 0.2%TiO₂** at 307 K (b).

The analysis of the molecular dynamics is permitted by the spectral study of the following quantities:

$$\epsilon^*(\omega) = \epsilon'(\omega) - i\epsilon''(\omega), \quad \sigma^*(\omega) = \sigma'(\omega) - i\sigma''(\omega), \quad \tan(\delta(\omega)) = \epsilon''(\omega)/\epsilon'(\omega) \quad (1)$$

where $\epsilon^*(\omega)$ is the complex permittivity function, $\epsilon'(\omega)$ is the permittivity and $\epsilon''(\omega)$ is the dielectric loss, $\sigma^*(\omega)$ is the complex conductivity, $\sigma'(\omega)$ is the conductivity and $\sigma''(\omega)$ is the imaginary part of the conductivity, $\tan(\delta(\omega))$ is the loss tangent ($\delta(\omega)$ is the loss angle, the complement of the phase lag angle).

Fig. 8 presents the spectra of the permittivity of sample BIC, at three temperature values, chosen in the range of interest, $T = 294$ K, 306 K and 324 K.

The analysis of the spectra shown in Fig. 8 is clearer by subdividing the frequency range in two sub-domains. The low-medium frequencies, $f = 10^{-1} - 10^3$ in which the two permittivity components, ϵ' and ϵ'' , have very high values, between $10^2 - 10^6$ for ϵ' , and $10^1 - 10^5$ for ϵ'' , respectively. The dielectric constant has a two slope variation. The 3–4 magnitude order permittivity increase in this range might be explained by one of the two dielectric relaxation processes specific to low frequencies: Maxwell-Wagner (M-W) type interfacial relaxation and electrode polarization (EP). These processes are caused by mobile ions accumulating at TiO_2 nanoparticle surfaces (M-W) or at the electrode-sample interface (EP).

The second range is that of the medium-high frequencies, where a dipolar relaxation process is present, attributed to the LC molecules dynamics.

The presence of TiO_2 particles does not modify essentially the shape of the ILC dielectric spectra, but their absolute values.

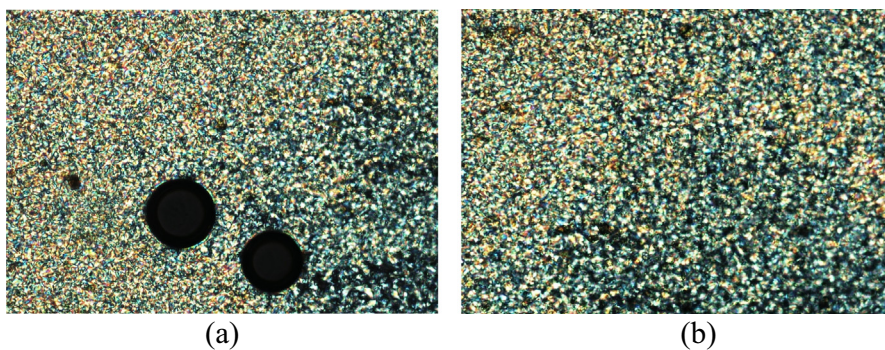


Fig. 3. POM pictures (200×) of BIC + 1%TiO₂ on cooling from the isotropic phase at different temperatures: 311 K (a), 310 K (b).

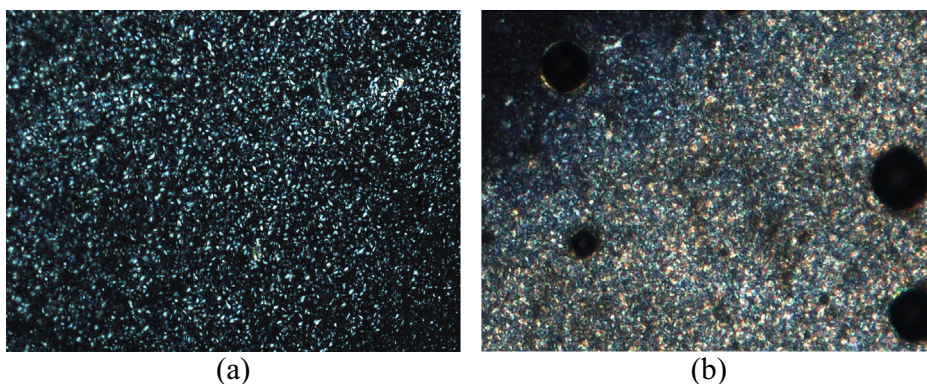


Fig. 4. POM pictures (200×) of BIC + 2%TiO₂ on cooling from the isotropic phase at different temperatures: 311 K (a), 309 K (b).

In Fig. 9a and b are shown the permittivity spectra for the samples BIC-01 and BIC-2, having the lowest and the highest particles concentrations.

For the study of relaxation processes, the most flexible fitting function is the Havriliak-Negami (HN) [22,29,30] one, which is a generalization of the dipolar relaxation functions Debye or Cole-Cole type:

$$\epsilon_{HN}^*(\omega) = \epsilon'(\omega) - i\epsilon''(\omega) = \epsilon_{r,\infty} + \frac{\epsilon_{r,0} - \epsilon_{r,\infty}}{(1 + (i\omega \cdot \tau_{max})^a)^b} \quad (2)$$

with $0 < a < 1$; $0 < b < 1$; where $\epsilon_{r,0}$ is the relative permittivity at very low frequencies (the limit $\omega \rightarrow 0$), and $\epsilon_{r,\infty}$ is the relative permittivity at very high frequencies ($\omega \rightarrow \infty$), τ_{max} is the characteristic relaxation time. The shape parameters, a and b , influence the broadening and the asymmetry of the relaxation curve, around the maximum of the losses. The characteristic relaxation times are obtained by fitting the spectra with the HN functions.

As resulted from the experimental data, the relaxation time depends on temperature and due to this dependency, a functional relation

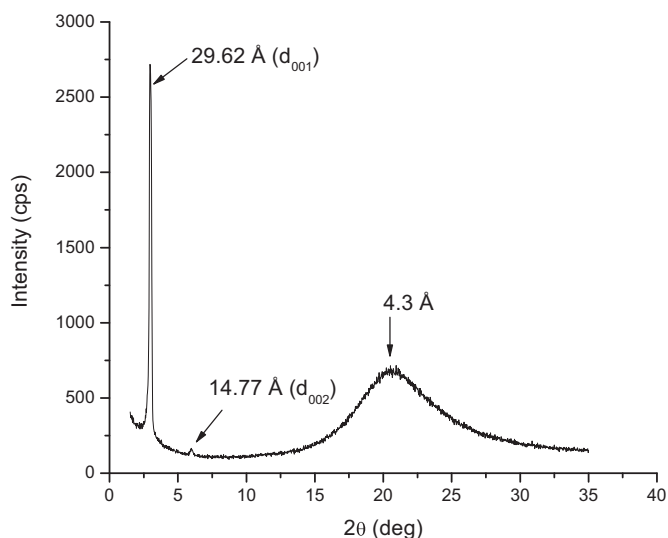


Fig. 5. Powder X-ray pattern for bis-imidazolium salt BIC recorded at 298 K.

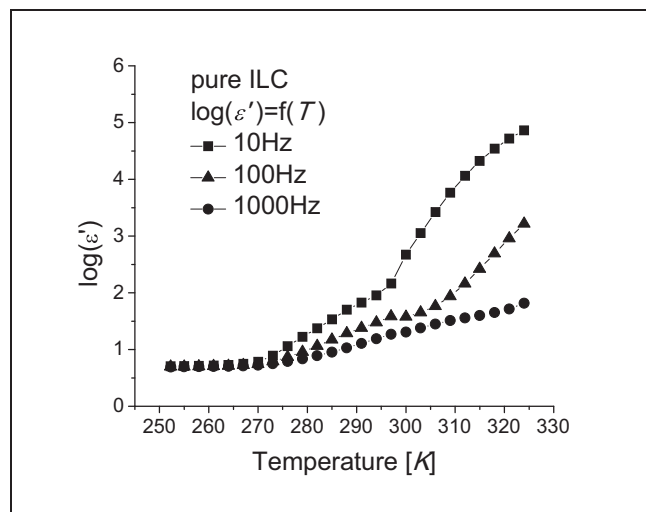


Fig. 6. Permittivity temperature dependency at three representative frequencies: ■: 10 Hz, ▲: 100 Hz, ●: 1000 Hz.

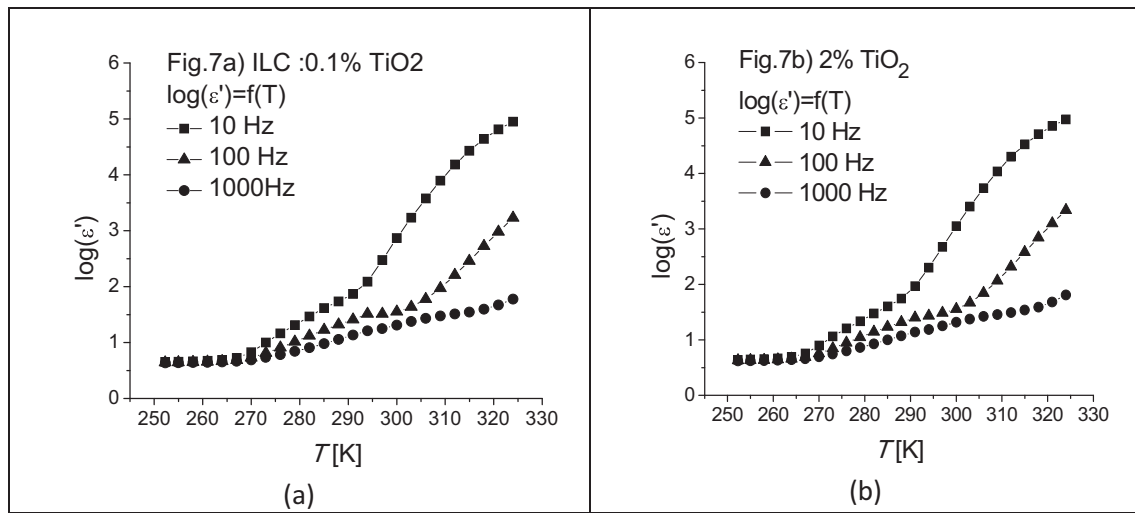


Fig. 7. Temperature dependency of the permittivity at the following frequencies: ■- 10 Hz; ▲- 100 Hz; ●- 1000 Hz. (a) Sample BIC-01; (b) sample BIC-2.

should be provided between the two quantities. The most convenient is the empirical Vogel-Fulcher-Tammann (VFT) [23,35] law:

$$\tau_{\max} = \tau_{\infty} \exp \left[\frac{A}{k_B(T - T_V)} \right] \quad (3)$$

where the fitting parameters have the following significations: A is a material constant quantitatively linked to the energy of the activation, T_V is the Vogel temperature, τ_{∞} is a pre-exponential factor equal to the value of the relaxation time at very high temperatures. Through logarithm of the VFT law, a more convenient form for obtaining the fitting parameters is obtained:

$$\ln(\tau_{\max}(x)) = \ln(\tau_{\infty}) + \frac{A}{k_B} \frac{x}{1 - T_V x}; \quad x = 1/T \quad (4)$$

From the graphical representation $\ln(\tau_{\max}) = f(1/T)$, the fitting parameters are obtained.

For exemplifying the HN fitting procedure on the dielectric spectra and consequently the fitting for the characteristic time in the VFT representation, the data for the sample BIC-02 have been used. In Fig. 10a is

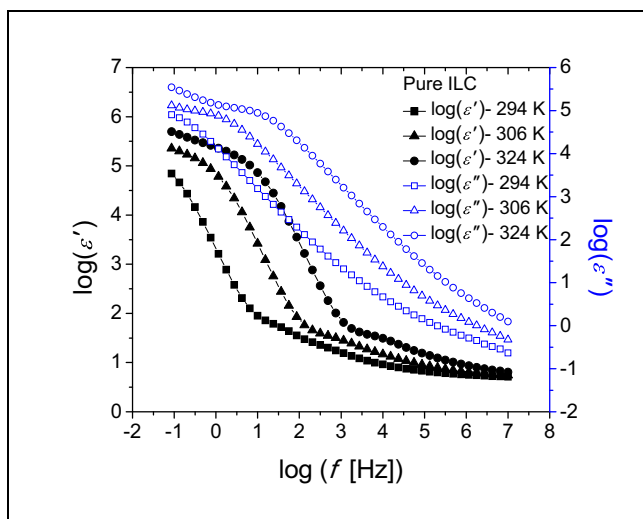


Fig. 8. Permittivity spectra of pure ILC at various temperatures: $T = 294$ K, $T = 306$ K and $T = 324$ K.

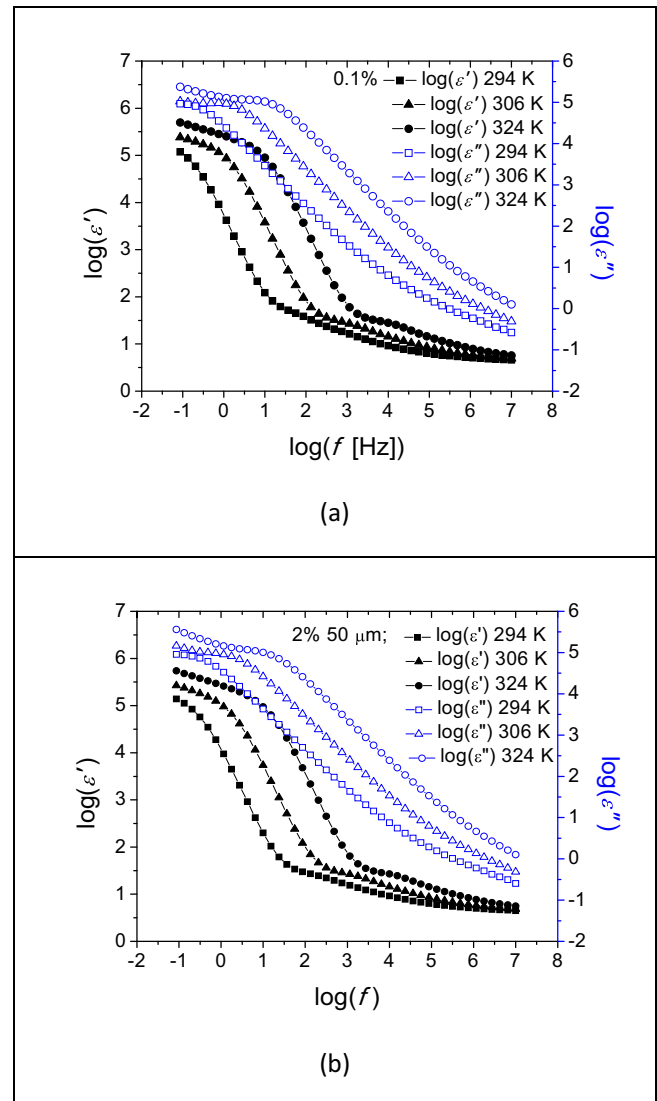


Fig. 9. Permittivity spectra at temperatures $T = 294$ K, $T = 306$ K, $T = 324$ K: (a) Sample BIC-01; (b) Sample BIC-2.

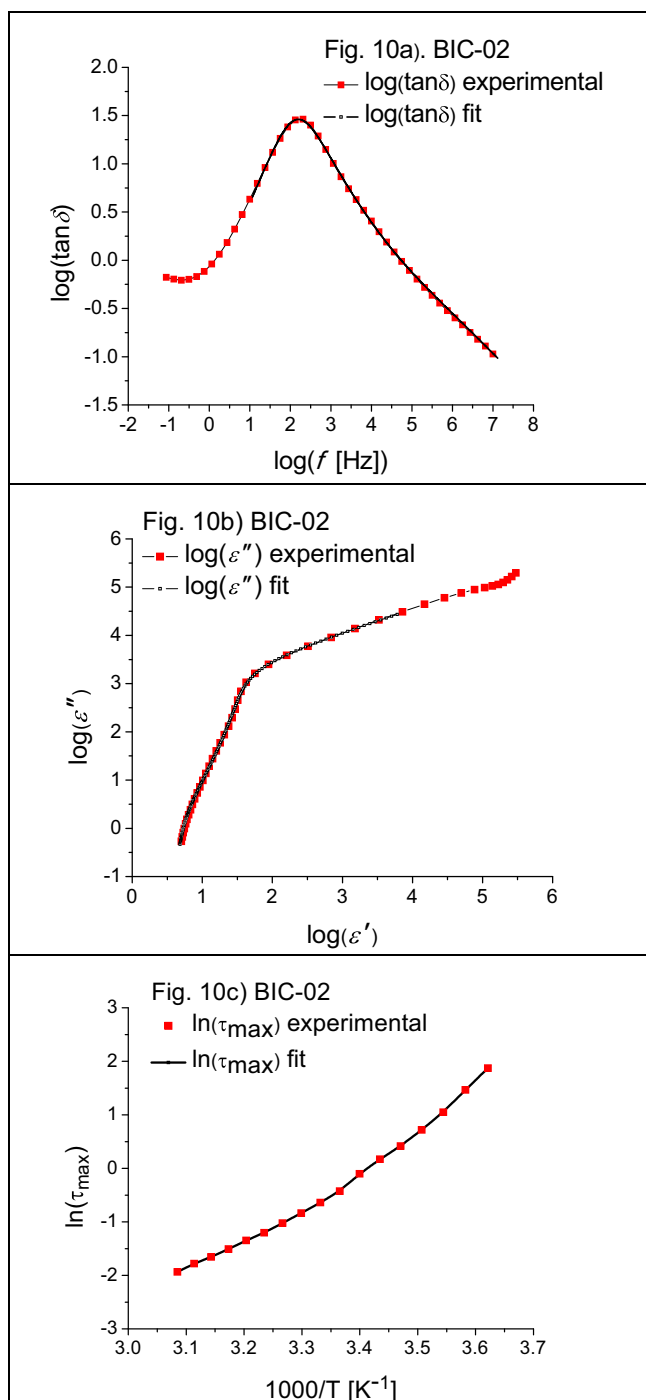


Fig. 10. Sample BIC-02: a) $\lg(\delta) = f(\omega)$ (solid red squares) and the two components HN fitting function (black line); b) Cole-Cole $\log(\varepsilon'') = \log(\varepsilon')$ diagram (solid red squares) and the two components HN fitting function (black line); c) VFT diagram, dependency of characteristic time on inverse of temperature, $\ln(\tau_{\max}) = f(1/T)$ (red squares) and the VFT fitting curve (black), Eq. (3).

presented the spectrum of the tangent of the losses and in Fig. 10b is the Cole-Cole diagram, representing the dependency of the dielectric losses, ε'' , on the dielectric constant, ε' , at the temperature $T = 309.15$ K. The shape of the curve (marked with red points) suggests the use of a two components fitting curve. The two representations (Fig. 10a and b) are equivalent: from the physical point of view, they contain the same information. The fact that the fitting curve is very well adapted to both representations proves that the hypothesis of using the HN functions is correct for the study of ILC [28]. If this would not have been the case, a

good superposition of the fitting function in one representation and a worse one in the other representation would have been obtained.

The next step is the assembly of the fitted values obtained for the characteristic times, associated to the same relaxation processes, at different temperatures in a VFT diagram (or Arrhenius diagram), as in Fig. 10c, from which, by fitting using the VFT law the corresponding parameters are obtained.

The obtained fitting parameters have the following values: $\tau_{\infty} = 2.000 \cdot 10^{-8}$ s, $A = 1.390 \cdot 10^{-01}$ eV, $T_V = 2.019 \cdot 10^{+02}$ K. The high values of the Vogel temperature, T_V , show that the sample has a behaviour specific to materials with glass transition, present in the isotropic phase in the case of some LCs.

3.4. Ionic conductivity

The electric conductivity and the dielectric permittivity of a material are linked by a direct general relation. For a sinusoidal electric field, this is:

$$\sigma^*(\omega) = \sigma'(\omega) + i\sigma''(\omega) = \sigma_0 + i\varepsilon_0\varepsilon^*(\omega) \quad (5)$$

The real and the imaginary parts are:

$$\sigma'(\omega) = \sigma_0 + \omega\varepsilon_0\varepsilon''(\omega), \quad \sigma''(\omega) = \omega\varepsilon_0\varepsilon'(\omega) \quad (6)$$

In the case of the pure electronic conduction there is no frequency contribution at the real part, ε' , of the dielectric function; its imaginary part, ε'' , has a linear increase with the decrease of the frequency, and the proportionality coefficient is given by the conductivity value in constant current regime. Reciprocally, in the conductivity function for an electronic conduction process, the real part, σ' , is constant in frequency, and the imaginary part, σ'' , increases linearly with the frequency. For the ions containing samples, it is experimentally proven that in the central frequency range, between 10^2 and 10^4 Hz, the electric conductivity has a slight increase with the frequency, which might be explained by the ions movements.

The temperature dependency of the electrical conductivity for the sample BIC is presented in Fig. 11, at three frequency values: $f = 10$ Hz, 100 Hz, 1000 Hz.

In the representation $\log(\sigma') = f(T)$, two regimes are noted, having different variation rates. At low temperatures, the conductivity has low values and it has a small variation ($10^{-13} - 10^{-11}$ S/cm). At temperature increase, the conductivity changes with approximately 4–5 magnitude orders, specific to the semiconductors ($10^{-08} - 10^{-06}$ S/cm), and the variation is rather exponential. This indicates a change in the conduction mechanism.

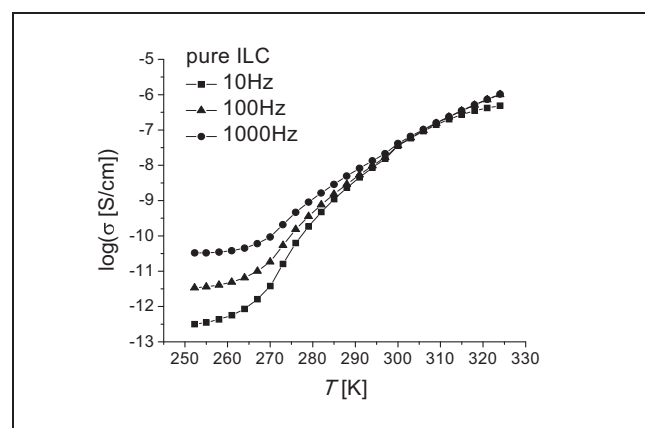


Fig. 11. Sample BIC; Temperature dependency of the electric conductivity σ' .

The electric conductivity of the majority of LCs containing mobile ions obeys the Arrhenius [36] law:

$$\sigma_{DC} = \sigma_0(T) \exp(-W_A/k_B T) \quad (7)$$

where σ_{DC} is the direct current (DC) conductivity at $\omega \rightarrow 0$, σ_0 is a material constant, W_A is the activation energy of the conduction, and the temperature dependency $\sigma_0 = \sigma_0(T)$ is not explicit. Approximately, if the temperature interval is not too large, one might consider that the temperature variation is predominantly exponential. Thus, a simpler and less precise relation might be used,

$$\sigma_{DC} = \sigma_{0,0} \exp(-W_A/k_B T) \quad (8)$$

where the fitting parameters are the pre-exponential factor $\sigma_{0,0}$, which is equal to the ionic conduction value for very high temperatures, and the activation energy W_A .

As can be seen from Fig. 11, the temperature dependency of the conductivity is much more complicated than the one foreseen by relation (7).

To investigate the influence of the TiO_2 nanoparticle concentration on the electric conductivity in Fig. 12 are presented the temperature dependencies of the conductivities for the samples BIC-01 and BIC-2, together with the pure ILC, sample BIC.

Interestingly, for all samples, three temperature intervals are to be remarked, where the conductivity variation is weaker or stronger (270–300) K.

In order to put into evidence the ionic conductivity, the conductivity spectra $\sigma' = \sigma'(f)$ are used.

In Fig. 13 are shown the conductivity spectra of the pure ILC BIC at three temperature values. In the medium frequency region, due to a slight increase of the conductivity with the frequency, the presence of the ionic conductivity is observed. The strong decrease of the conductivity at low frequencies is due to the electrode polarization (EP).

The influence of the concentration is best observed by the shifting of the maxima of the tangent loss spectra, $\tan(\delta) = f(\omega)$, for the samples with various electric conductivity. In the present discussion, the maxima are due to the influence of the electrode polarization. It is known that the characteristic time for the EP is inversely proportional to the square root of the charge carrier concentration, and the characteristic frequency, ω_{max} , which is equal to the inverse of the characteristic time, will increase at the increase of the electrical conductivity.

For comparison, in Fig. 14 are presented the spectra of the tangent loss, $\tan(\delta)$, associated to the samples BIC-01 and BIC-2, at the same

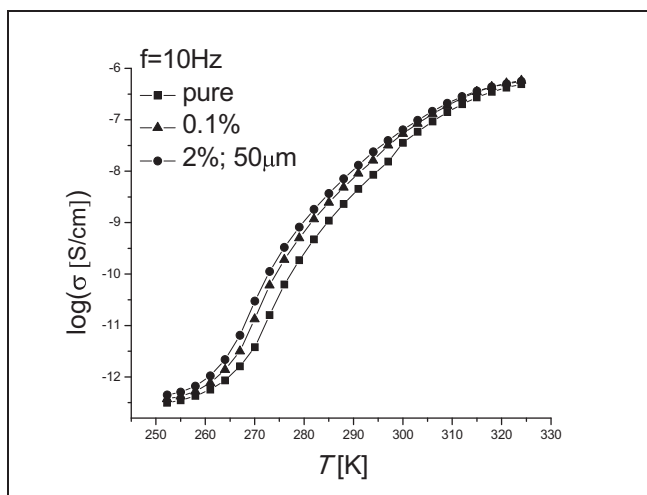


Fig. 12. Electric conductivity versus temperature at fixed frequency, $f = 10$ Hz, for the samples: BIC, BIC-01 and BIC-2.

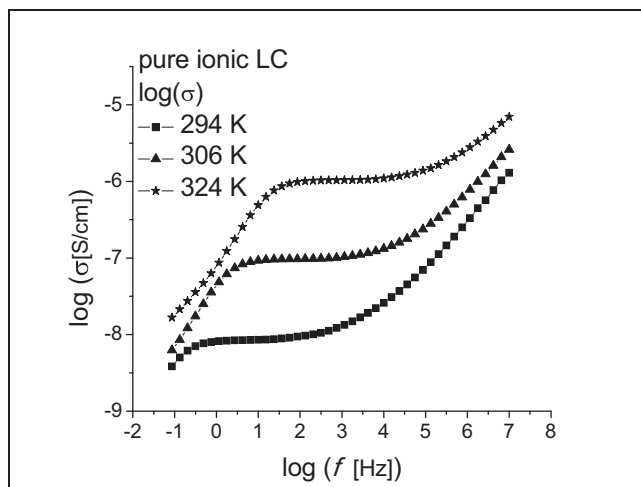


Fig. 13. Sample BIC; conductivity spectra at $T = 296$ K, $T = 306$ K, $T = 324$ K.

temperatures. The general tendency, experimentally observed, is that the maximum point shift towards higher frequencies for the samples with greater concentration.

Analyzing the diagram presented in Fig. 14, the shift of the maximum of $\log(\tan(\delta))$ is observed, towards the higher frequency region, at the increase of the concentration. Since the characteristic time is inversely proportional to the frequency correspondent to this maximum, it follows that at the increase of the concentration, the characteristic time decreases.

3.5. The electrode polarization

The electrode polarization is an unwanted effect during the dielectric measurements, because it might shield the intrinsic dielectric response of the sample. The polarization appears mainly for samples with medium and high conductivity and influences the dielectric properties at low frequencies. Both the magnitude and the position of the EP frequency depend on the conductivity of the sample and can lead to large values of the real and imaginary part of the complex function of permittivity.

In the ultra- low frequency range (100 Hz–1 KHz), at frequency decrease, the real part of the permittivity increases strongly to very high values; this can not be explained by molecular relaxation processes. For this reason, such behaviour must be attributed to EP.

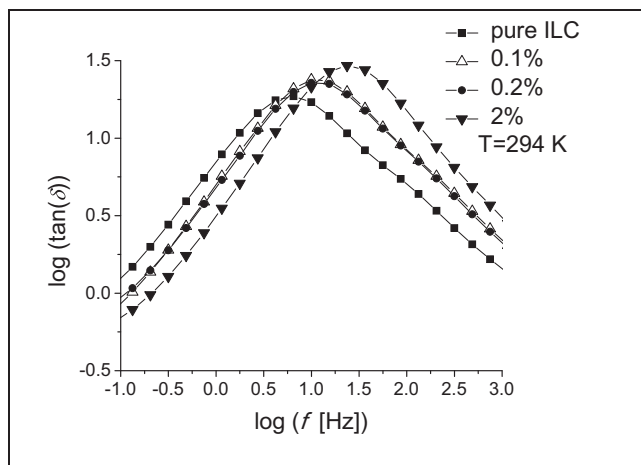


Fig. 14. Spectra of the tangent loss, associated to the samples: -■-BIC, -△-BIC-01, -●-BIC-02 and -▼-BIC-2, at 294 K.

In a sample containing mobile charge carriers, when subjected to electric field, an accumulation of carriers moving towards the electrodes may occur. Agglomeration of ions near electrodes gives rise to a spatial charge region. In the presence of the spatial charge, the electric field becomes inhomogeneous, so that near the electrodes the intensity is higher, and in the central area between the electrodes the intensity is smaller. The inhomogeneity is all the more accentuated as the frequency of the electric field is lower.

Based on a simple model, the blocking of the charge at the interface electrode/sample can be described by a double electric layer with an effective width characterized by the Debye length, L_D . This double layer produces a large electrical capacity in series with the studied sample.

The time dependency of the EP is due to the charge and the discharge of the double layer capacity. The considered model [37] can be used to estimate the effect of the EP. The dielectric complex function, ε_{EP}^* , is: $\varepsilon_{EP}^* = \varepsilon_r + \Delta\varepsilon_{EP}/(1 + i\omega\tau_{EP})$; where $\Delta\varepsilon_{EP} = [(L/2L_D) - 1]\varepsilon_r$, and $\tau_{EP} = (\varepsilon_0\varepsilon_r/\sigma_{DC})(L/2L_D)$ is the characteristic relaxation time, specific to EP, σ_{DC} was defined previously and L is the inter-electrode distance. The influence of the EP on the dielectric complex function increases with increasing conductivity, as the effect shifts to higher frequencies.

On the other hand, when increasing the sample thickness, L , the EP process shifts to lower frequencies. For this reason EP can be distinguished from sample volume behaviour by studying changes made to the spectra of the dielectric function when changing the electrode material and/or the thickness of the sample.

In reality, the physical processes describing EPs are much more complicated.

In this respect, several models based on hypotheses more or less simplifying have been elaborated [38,39]. More complete models are found in references [40–46].

Firstly, before using any of these models, one should have the confirmation that the dielectric relaxation process that occurs at low frequencies and high temperatures is EP.

For this purpose, we performed a series of DS measurements on the same concentration (0.2%) samples, BIC-2, BIC-2B and BIC-2C, with different inter-electrodes distances. The greater concentration sample has been chosen, where the EP effect should be most pronounced. From the specimen spectra the ones that are at the highest temperature have been chosen, where the EP appears obviously. The electrical quantity chosen is the loss tangent, $\tan(\delta)$, which shows a pronounced maximum point at relatively low frequencies, easy to locate. By fitting with a single HN function, the characteristic time, $\tau_{max} = \tau_{EP}$ is obtained and the angular velocity of the respective point is: $\omega_{max} = 1/\tau_{EP}$.

Fig. 15 presents the variation of the loss tangent versus frequency, double logarithmic scale, for the greatest (0.2%) concentration samples

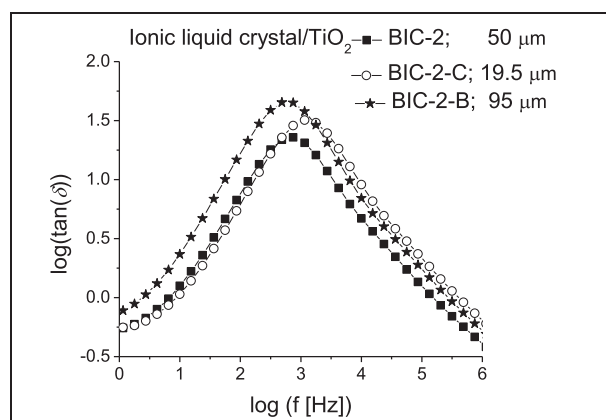


Fig. 15. The loss tangent versus frequency, double logarithmic scale, for the greatest (2%) concentration samples of different thickness.

Table 3

The dependence of the characteristic relaxation time on the thickness for samples with 0.2% TiO_2 and the ratio τ_m/d .

Sample	Thickness	τ_m [10^{-3} s]	Ratio τ_m/d
BIC-2-C	19.5	9.907	0.50805
BIC-2	50.0	12.87	0.2574
BIC-2-B	95.0	28.64	0.30147

of different thickness. According to Fig. 15, the position of the maximum depends on the sample thickness (electrodes inter-distances). It is known that the loss tangent is independent on sample dimensions but EP depends on the distance between the electrodes. Thus, the shift of the maximum point is given by the EP effect.

In Table 3 is presented the characteristic relaxation time for three thicknesses, d , and the calculated ratio between the relaxation time and the thickness, τ_m/d .

The mean value of the ratio $\tau_m/d = 0.3556$, indicating an acceptable error of the experimental results.

4. Conclusions

A new dimeric ILC based on bis-imidazolium salt with two cyanobiphenyl groups and dodecyl sulfate counterion (BIC) was prepared by the metathesis reaction of the corresponding bromide salt with sodium dodecyl sulfate and its structure was confirmed by ^1H and ^{13}C NMR spectroscopy and elemental analysis. The bis-imidazolium salt shows a room-temperature smectic A phase stable in the 278–309 K temperature range as confirmed by a combination of the DSC, POM and powder X-ray diffraction investigations.

The ILC was doped with TiO_2 nanoparticles in concentrations of 0.1%, 0.2%, 1% and 2%. The DSC measurements performed in the 263–323 K revealed a sharpening of the transition as well as a shift of the T_{onset} towards higher values, from 308.6 to 312.2 K, on going from pure to ILC doped with 2% TiO_2 nanoparticles. The EP study was performed on samples of the same concentration and different thickness. The dielectric spectra have been registered in a 10^{-1} to 10^7 Hz frequency range and 250–330 K temperature domain.

The molecular dynamics and the ionic conductivity of the ILC and the ILC – TiO_2 composites have been studied in detail by DS and it has been concluded that the ionic component of the LC has a dominant influence in the composites.

The study of ionic conductivity involves rates of variation of permittivity with different temperatures over clearly observed temperature intervals and which can be connected with phase transitions.

At constant frequency, the conductivity increased with the temperature and dopant concentration. In the analysed frequency range, at least two dielectric relaxation processes are present. The characteristic times of the observed relaxation processes show a temperature dependency obeying the Vogel-Fulcher-Tammann law. It was found that the characteristic relaxation time increases with the thickness of the sample and it decreases at the increase of the TiO_2 concentration.

At high temperatures and low frequency range the electrode polarization phenomena are more visible. The large extend increase of the dielectric permittivity was assigned to the EP type phenomena.

Author statement

All authors have equally contributed to the elaboration of this paper and have equal relevant credit roles.

Declaration of competing interest

The authors declare that they have no known competing financial interests or personal relationships that could have appeared to influence the work reported in this paper.

References

- [1] K. Goossens, K. Lava, C.W. Bielawski, K. Binnemans, Ionic liquid crystals: versatile materials, *Chem. Rev.* 116 (8) (2016) 4643–4807, <https://doi.org/10.1021/cr400334b>.
- [2] K.V. Axenov, S. Laschat, Thermotropic ionic liquid crystals, *Materials* 4 (2011) 206–259, <https://doi.org/10.3390/ma4010206>.
- [3] V. Cîrcu, in: S. Handy (Ed.), *Ionic Liquid Crystals Based on Pyridinium Salts in Progress and Developments in Ionic Liquids*, InTechOpen 2017, pp. 285–311, <https://doi.org/10.5772/62621>.
- [4] S.K. Singh, A.W. Savoy, Ionic liquids synthesis and applications: an overview, *J. Mol. Liq.* 297 (2020) 112038, <https://doi.org/10.1016/j.molliq.2019.112038>.
- [5] R. Atasiei, M. Raicopol, C. Andronescu, A. Hanganu, A.L. Alexe-Ionescu, G. Barbero, Investigation of the conduction properties of ionic liquid crystal electrolyte used in dye sensitized solar cells, *J. Mol. Liq.* 267 (2018) 81–88, <https://doi.org/10.1016/j.molliq.2018.01.010>.
- [6] J. Lagerwall, G. Scalia, Carbon nanotubes in liquid crystals, *J. Mater. Chem.* 18 (25) (2008) 2890–2898, <https://doi.org/10.1039/b802707b>.
- [7] M. Rahman, W.J. Lee, Scientific duo of carbon nanotubes and nematic liquid crystals, *Phys. D: Appl. Phys.* 42 (6) (2009) 063001–1–(063001–12), <https://doi.org/10.1088/0022-3727/42/6/063001>.
- [8] L. Dolgov, O. Kovalchuk, N. Lebovka, S. Tomylo, O. Yaroshchuk, Liquid crystal dispersions of carbon nanotubes: dielectric, electro-optical and structural peculiarities, in: J.M. Marulanda (Ed.), *Carbon nanotubes*, InTechOpen, 2010, <https://doi.org/10.5772/39439>.
- [9] I. Dierking, G. Scalia, P. Morales, D. LeClere, Aligning and reorienting carbon nanotubes with nematic liquid crystals, *Adv. Mat.* 16 (11) (2004) 865–869, <https://doi.org/10.1002/adma.200306196>.
- [10] C. Rosu, D. Manaila-Maximean, D. Donescu, S. Frunza, A.R. Sterian, Influence of polarizing electric fields on the electrical and optical properties of polymer–clay composite system, *Mod. Phys. Lett. B* 24 (01) (2010) 65–73, <https://doi.org/10.1142/S0217984910022238>.
- [11] I. Palarie, C. Dascalu, G.E. Iacobescu, M.C. Varut, Surface morphology of doped nematic liquid crystals: role of dye concentration, *Liq. Cryst.* 39 (7) (2012) 833–837, <https://doi.org/10.1080/02678292.2012.684072>.
- [12] C.P. Ganea, D. Manaila-Maximean, Liquid crystal/copolymer–clay nanostructured systems: contribution to the conductivity of the electrode polarization, *U.P.B. Sci. Bull., Series A* 73 (4) (2011) 209–216.
- [13] S. Frunza, A. Schönhal, L. Frunza, T. Beica, I. Zgura, P. Ganea, D. Stoescu, Dynamics of cyanophenyl alkylbenzoate molecules in the bulk and in a surface layer adsorbed onto aerosil. Variation of the lengths of the alkyl chain, *Chem. Phys.* 372 (2010) 51–60, <https://doi.org/10.1016/j.chemphys.2010.04.031>.
- [14] S. Frunza, A. Schönhal, L. Frunza, P. Ganea, H. Kosslick, J. Harloff, A. Schulz, Molecular relaxation processes in a MOF-5 structure revealed by broadband dielectric spectroscopy: signature of phenylene ring fluctuations, *J. Phys. Chem. B* 114 (2010) 12840–12846, <https://doi.org/10.1021/jp1071617>.
- [15] D. Manaila-Maximean, V. Cîrcu, P.C. Ganea, Dielectric properties of a bisimidazolium salt with dodecyl sulfate anion doped with carbon nanotubes, *Beilstein J. Nanotechnol.* 9 (2018) 164–174, <https://doi.org/10.3762/bjnano.9.19>.
- [16] D. Manaila-Maximean, V. Cîrcu, C.P. Ganea, A. Barar, O. Danila, T. Staicu, V.A. Loiko, A.V. Konkolovich, A.A. Miskevich, Polymer dispersed liquid crystals films doped with carbon nanotubes: preparation methods, *Society of Photo-Optical Instrumentation Engineers (SPIE) Conference Series*, vol. 10977, 2018, p. 1097702, <https://doi.org/10.1117/12.2326186>.
- [17] V.A. Loiko, A.V. Konkolovich, A.A. Miskevich, D. Manaila-Maximean, O. Danila, V. Cîrcu, A. Bărar, Optical model to describe coherent transmittance of polymer dispersed liquid crystal film doped with carbon nanotubes, *J. Quant. Spectrosc. Radiat. Transf.* 245 (2020), 106892, <https://doi.org/10.1016/j.jqsrt.2020.106892>.
- [18] A. Bărar, O. Dănilă, D. Mănăilă-Maximean, V.A. Loiko, Active spectral absorption control in a tunable liquid crystal/metamaterial structure by polarization plane rotation, *International Conference on Nanotechnologies and Biomedical Engineering*, Springer, Cham 2019, pp. 299–303, https://doi.org/10.1007/978-3-030-31866-6_58.
- [19] C. Cîrtoaje, E. Petrescu, C. Stan, A. Rogachev, Electric Freedericksz transition in nematic liquid crystals with graphene quantum dot mixture, *Appl. Surf. Sci.* 487 (2019) 1301–1306, <https://doi.org/10.1016/j.apsusc.2019.05.073>.
- [20] S. Frunza, L. Frunza, C.P. Ganea, I. Zgura, A. Schönhal, Density of adsorbed surface species for cyanophenyl alkyl benzoates confined to Aerosil A380: development of the evaluating algorithm for attachment by two types of bonds, *UPB Sci Bull Series A* 81 (2019) 223–236.
- [21] A.V. Kovalchuk, S.S. Zakrevska, O.V. Yaroshchuk, U. Maschke, Electrooptical properties of three-component compositions “liquid crystal-aerosil-photopolymer”, *Molecular Crystals and Liquid Crystals Science and Technology. Section A. Molecular Crystals and Liquid Crystals* 368 (1) (2001) 129–136.
- [22] C. Cîrtoaje, E. Petrescu, C. Stan, D. Creangă, Ferromagnetic nanoparticles suspensions in twisted nematic, *Physica E Low Dimens. Syst. Nanostruct.* 79 (2016) 38–43, <https://doi.org/10.1016/j.physe.2015.12.006>.
- [23] D. Donescu, R.C. Fierascu, M. Ghiurea, D. Manaila-Maximean, C.A. Nicolae, R. Somoghi, C.I. Spataru, N. Stanica, V. Raditoiu, E. Vasile, Synthesis and magnetic properties of inverted core-shell polyaniline-ferrite composite, *Appl. Surf. Sci.* 414 (2017) 8–17, <https://doi.org/10.1016/j.apsusc.2017.04.061>.
- [24] G.E. Iacobescu, Freedericksz transitions of twisted ferronematics in magnetic field, *J. Magn. Magn. Mater.* 468 (2018) 65–68, <https://doi.org/10.1016/j.jmmm.2018.07.081>.
- [25] S. Tomylo, O. Yaroshchuk, O. Kovalchuk, U. Maschke, R. Yamaguchi, Dielectric and electro-optical properties of liquid crystals doped with diamond nanoparticles, *Mol. Cryst. Liq. Cryst.* 541 (1) (2011) 35–273, <https://doi.org/10.1080/15421406.2011.569658>.
- [26] W.K. Lee, J.H. Choi Na, J.H. Lim, J.M. Han, J.Y. Hwang, D.S. Seo, Low-power operation of vertically aligned liquid-crystal system via anatase-TiO₂ nanoparticle dispersion, *Opt. Lett.* 34 (2009) 3653–3655, <https://doi.org/10.1364/OL.34.003653>.
- [27] W.T. Chen, P.S. Chen, C.Y. Chao, Effect of insulating nanoparticles doping on electro-optical characteristics in nematic liquid crystal cells, *Mol. Cryst. Liq. Cryst.* 507 (2009) 253–263, <https://doi.org/10.1080/15421400903053602>.
- [28] A. Nafees, G. Kalita, A. Sinha, Effect of titanium dioxide nanoparticles on the dielectric and electro-optical properties of bent-core liquid crystals, *J. Mol. Liq.* 274 (2019) 592–597, <https://doi.org/10.1016/j.molliq.2018.11.013>.
- [29] F. Kremer, A. Schönhal (Eds.), *Broadband Dielectric Spectroscopy*, Springer-Verlag, Berlin-Heidelberg, 2003, <https://doi.org/10.1007/978-3-642-56120-7>.
- [30] S. Urban, B. Gestblom, H. Kresse, A. Dabrowski, Dielectric relaxation studies of 4-n-alkoxy-4'-cyanobiphenyls (nOCB, n = 5 ÷ 8), *Z. Naturforsch. A* 51 (7) (1996) 834–842, <https://doi.org/10.1515/zna-1996-0707>.
- [31] C.P. Ganea, New approach of the AC electrode polarization during the measurement of impedance spectra, *Rom. J. Phys.* 57/3–4 (2012) 664–675.
- [32] A. Pana, M. Iliis, M. Micutz, F. Dumitrascu, I. Pasuk, V. Cîrcu, Liquid crystals based on silver carbene complexes derived from dimeric bis(imidazolium) bromide salts, *RSC Adv.* 4 (2014) 59491–59497, <https://doi.org/10.1039/C4RA11023D>.
- [33] J.E. Bara, E.S. Hatakeyama, B.R. Wiesenauer, X. Zeng, R.D. Noble, D.L. Gin, Thermotropic liquid crystal behaviour of gemini imidazolium-based ionic amphiphiles, *Liq. Cryst.* 37 (2010) 1587–1599, <https://doi.org/10.1080/02678292.2010.521859>.
- [34] T.A. Ilincă, I. Pasuk, V. Cîrcu, Bis-imidazolium salts with alkyl sulfates as counterions: synthesis and liquid crystalline properties, *New J. Chem.* 41 (2017) 1113–11124, <https://doi.org/10.1039/C7NJ02561K>.
- [35] A. Yildirim, P. Szymoniak, K. Sentker, M. Butschies, A. Buhlmeyer, P. Huber, S. Laschat, A. Schönhal, Dynamics and ionic conductivity of ionic liquid crystals forming a hexagonal columnar mesophase, *Phys. Chem. Chem. Phys.* 20 (2018) 5626, <https://doi.org/10.1039/C7CP08186C>.
- [36] D. Manaila-Maximean, O. Danila, C.P. Ganea, P.L. Almeida, Filling in the voids of electrospun hydroxypropyl cellulose network: dielectric investigations, *Eur. Phys. J. Plus* 133 (4) (2018) 159, <https://doi.org/10.1140/epjp/i2018-11997-8>.
- [37] D. Manaila-Maximean, O. Danila, P.L. Almeida, C.P. Ganea, Electrical properties of a liquid crystal dispersed in an electrospun cellulose acetate network, *Beilstein J. Nanotechnol.* 9 (1) (2018) 55–163, <https://doi.org/10.3762/bjnano.9.18>.
- [38] L.F. Chiriac, C.P. Ganea, D. Manaila-Maximean, I. Pasuk, V. Cîrcu, Synthesis and thermal, emission and dielectric properties of liquid crystalline Eu (III), Sm (III) and Tb (III) complexes based on mesogenic 4-pyridone ligands functionalized with cyanobiphenyl groups, *J. Mol. Liq.* 290 (2019), 111184, <https://doi.org/10.1016/j.molliq.2019.111184>.
- [39] R. Coelho, Sur la relaxation d'une charge d'espace, *Rev. Phys. Appl.* 18 (1983) 137–146, <https://doi.org/10.1051/rphysap:01983001803013700>.
- [40] G. Barbero, Influence of adsorption phenomenon on the impedance spectroscopy of a cell of liquid, *Phys. Rev. E* 71 (2005) 062201–1–(062201–4), <https://doi.org/10.1103/PhysRevE.71.062201>.
- [41] J.R. Macdonald, Theory of ac space-charge polarization effects in photoconductors, semiconductors, and electrolytes, *Phys. Rev.* 92 (1953) 4–17, <https://doi.org/10.1103/PhysRev.92.4>.
- [42] C.P. Ganea, Modeling the charge transfer at the electrode-ionic liquid interface in dielectric spectroscopy measurements, *J. Mol. Liq.* 221 (2016) 422–433, <https://doi.org/10.1016/j.molliq.2016.06.026>.
- [43] A.R. Brás, S. Frunza, L. Guerreiro, I.M. Fonseca, A. Corma, L. Frunza, M. Dionísio, A. Schönhal, Molecular mobility of nematic E7 confined to molecular sieves with a low filling degree, *J. Chem. Phys.* 132 (22) (2010), 224508.
- [44] J. Jadzyn, C. Legrand, G. Czechowski, D. Bauman, Dielectric relaxation processes in the nematogen 4-cyanophenyl 4-n-heptylbenzoate, *Liq. Cryst.* 24 (5) (1998) 689–694.
- [45] J. Jadzyn, G. Czechowski, R. Douali, C. Legrand, On the molecular interpretation of the dielectric relaxation of nematic liquid crystals, *Liq. Cryst.* 26 (11) (1999) 1591–1597.
- [46] L. Frunza, S. Frunza, I. Zgura, T. Beica, N. Gheorghie, P. Ganea, D. Stoescu, A. Dinescu, A. Schönhal, Involvement of cyan and ester groups in surface interactions of aerosil–cyanophenyl alkyl benzoate systems with high silica density: infrared investigations, *Spectrochim. Acta A* 75 (4) (2010) 1228–1235.



Electrical properties of a liquid crystal dispersed in an electrospun cellulose acetate network

Doina Manaila Maximean^{*1}, Octavian Danila¹, Pedro L. Almeida^{*2,3} and Constantin Paul Ganea⁴

Full Research Paper

Open Access

Address:

¹University Politehnica of Bucharest, Department of Physics, 313 Spl. Independentei, 060042, Bucharest, Romania, ²IN - CENIMAT, Departamento de Ciência dos Materiais, Faculdade de Ciências e Tecnologia, FCT/UNL, 2829-516 Caparica, Portugal, ³Área Departamental de Física, ISEL, Instituto Superior de Engenharia de Lisboa, I.P.L., R. Conselheiro Emídio Navarro, 1959-007 Lisboa, Portugal and ⁴National Institute of Materials Physics, POBox MG 07, 077125 Magurele, Romania

Email:

Doina Manaila Maximean^{*} - doina.manaila@physics.pub.ro;
Pedro L. Almeida^{*} - palmeida@adf.isel.pt

* Corresponding author

Keywords:

cellulose nanocomposite; dielectric spectroscopy; impedance spectroscopy; liquid crystal; optical transmission

Beilstein J. Nanotechnol. **2018**, *9*, 155–163.

doi:10.3762/bjnano.9.18

Received: 27 July 2017

Accepted: 18 December 2017

Published: 15 January 2018

This article is part of the Thematic Series "Nanostructured liquid crystal systems and applications".

Guest Editor: A. Emelyanenko

© 2018 Maximean et al.; licensee Beilstein-Institut.
License and terms: see end of document.

Abstract

Electro-optical devices that work in a similar fashion as PDLCs (polymer-dispersed liquid crystals), produced from cellulose acetate (CA) electrospun fibers deposited onto indium tin oxide coated glass and a nematic liquid crystal (E7), were studied. CA and the CA/liquid crystal composite were characterized by multiple investigation techniques, such as polarized optical microscopy, dielectric spectroscopy and impedance measurements. Dielectric constant and electric energy loss were studied as a function of frequency and temperature. The activation energy was evaluated and the relaxation time was obtained by fitting the spectra of the dielectric loss with the Havriliak–Negami functions. To determine the electrical characteristics of the studied samples, impedance measurements results were treated using the Cole–Cole diagram and the three-element equivalent model.

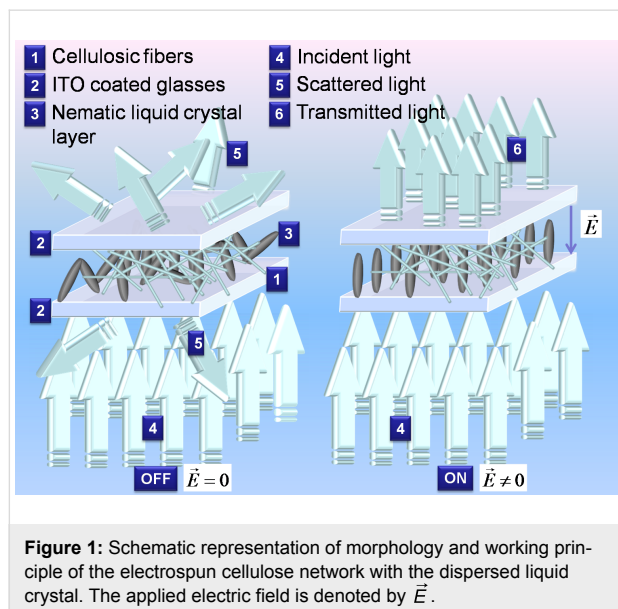
Introduction

The widely known polymer dispersed-liquid crystals (PDLCs) are a class of liquid crystal (LC)-based electro-optical devices, formed by LC droplets dispersed in a solid polymeric matrix [1-5]. The optical transmission of such devices is sensitive to external AC electric fields. Without external influence (the so called OFF state), PDLCs scatter the incident light due to the

fact that the LC molecules are anchored to the inner surface of the droplets in the polymeric matrix, having a non-uniform orientation between different droplets. Since there is no uniform direction of alignment of the LC director between different droplets, the optical path of the incident light travelling through a PDLC is different from point to point, due to the mismatch

between the effective refractive index of the LC and the refractive index of the polymer. The state where the device becomes transparent (the so called ON state) can be achieved by applying an electric field with adequate magnitude. Under the action of the field, the LC molecules inside each droplet align along the direction of the field, and the ordinary refractive index of the LC becomes equal to the refractive index of the polymeric matrix, creating a constant optical path for the incident light along the surface of the PDLC sample, reducing the light scattering to a minimum and increasing the transmission of light to a maximum. PDLC films have many interesting applications in optoelectronics (light valves, polarizers), architectural windows, reduction of solar heat load [2,6], nonlinear optics [7-9] and nanotechnological applications [10-20].

The macroscopic electro-optical effect in electrospun cellulose acetate/LC composites is similar to the one observed in traditional PDLC. The major difference is that instead of having small droplets of LC confined in a polymeric matrix, the LC fills the voids between fibers in mats of non-woven electro-spun cellulose acetate fibers [21-27]. The electrospun cellulose fibers were deposited on indium tin oxide (ITO)-coated glass, and two such fiber-coated glass plates form a sandwich type cell, where the nematic liquid crystal (NLC) is filled in by capillarity [21,22,28]. A schematic representation of the electrospun cellulose network with the dispersed liquid crystal as well as the working principle is given in Figure 1.



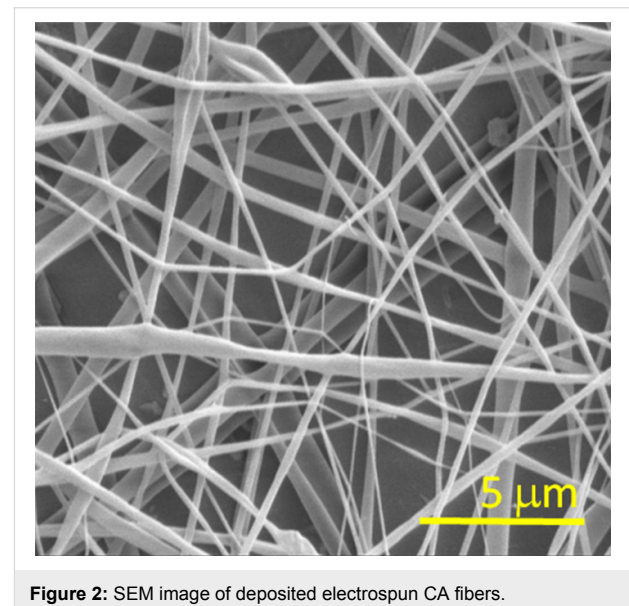
The cellulose acetate used in the preparation of the CA/LC samples [29-33] was obtained from green and renewable sources. The used nematic LC is E7, a mixture of alkylcyanobiphenyls with a cyano head group [34-36]. This paper presents the inves-

tigations of the electrical properties of an electrospun CA network with dispersed liquid crystals. Dielectric spectroscopy (DS) was performed over wide ranges of frequency and temperature to determine physical properties such as activation energy and characteristic time. The experimental results of DS were fitted to the Havriliak–Negami [37] model and further modelled by the Vogel–Fulcher–Tammann law. In addition to this, impedance spectroscopy measurements were performed, and the results were processed using a simple equivalent circuit model, that permits the extraction of electric circuit parameters.

Results and Discussion

Scanning electron microscopy

Figure 2 shows the SEM image of the deposited fibers [21,22,28]. In the SEM image, the fibers exhibit a wide dimension range, starting with dozens of nanometres.



Polarized optical microscopy

Figure 3 presents the polarizing optical microscopy images of the electrospun CA cell, (a) without LC and (b) filled with E7, taken between crossed polarizers.

As it can be perceived by the colors seen in the POM image, the LC fills the voids between the CA fibers (Figure 3b). The multiplicity of colors arises from the existence of liquid crystal polydomains imposed by the distortion of the nematic director field through the fibers.

Dielectric spectroscopy

The characterized samples were electrospun CA without LC, and the same CA sample after filling in the LC (denoted as CA/E7 composite). The DS measurements were carried out

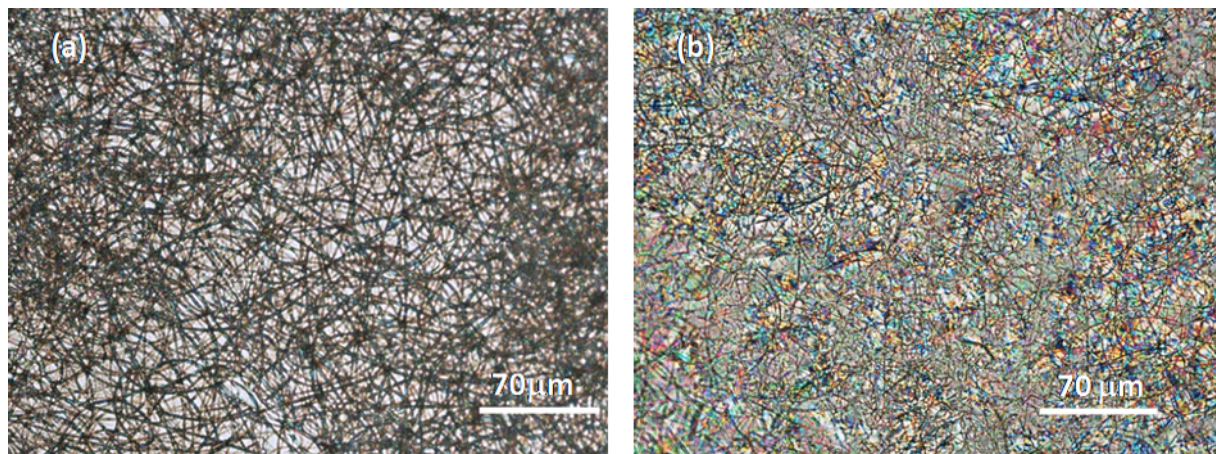


Figure 3: Polarizing optical microscopy images of the electrospun CA a) without LC and (b) filled with E7.

under isothermal conditions, in the frequency range from 10^{-1} to 10^7 Hz, in a temperature domain from 293 to 350 K.

The DS results were obtained by plotting the real and imaginary components of the complex permittivity function $\epsilon^*(\omega) = \epsilon'(\omega) - i\epsilon''(\omega)$. Here, $\epsilon^*(\omega)$ is the dielectric permittivity, the real part, $\epsilon'(\omega)$, is the dielectric constant, and the imaginary part, $i\epsilon''(\omega)$, is the dielectric loss [37].

Figure 4 shows dielectric constant and dielectric loss as functions of the temperature at two constant representative frequencies, 1 Hz and 10 Hz, for (a) the cell with CA fibers before filling in the LC, and (b) for the same cell after the LC was introduced. The changes of slope may indicate phase transitions. Thus, we can suppose that CA without LC might have a phase transition at $T = 315$ K. Similarly, the sample CA/E7

might have a phase transition at about 333 K. The verification of this supposition is based on the fitting parameters of the Vogel–Fulcher–Tammann law (see below in Figure 6 and Table 1).

Figure 5 presents dielectric constant and dielectric loss as functions of the frequency for the CA cell (a) before and (b) after filling in the LC, at three constant temperatures. For the CA sample without LC measured in the high frequency (HF) domain, one notices a relaxation process outside the measurement domain, while in the low frequency (LF) range, two CA-attributable almost overlapping relaxation processes can be observed at 1 Hz and 1000 Hz. The CA/E7 sample exhibits a relaxation process due to the LC in the HF measurement range, and two almost overlapping relaxation processes in the LF range.

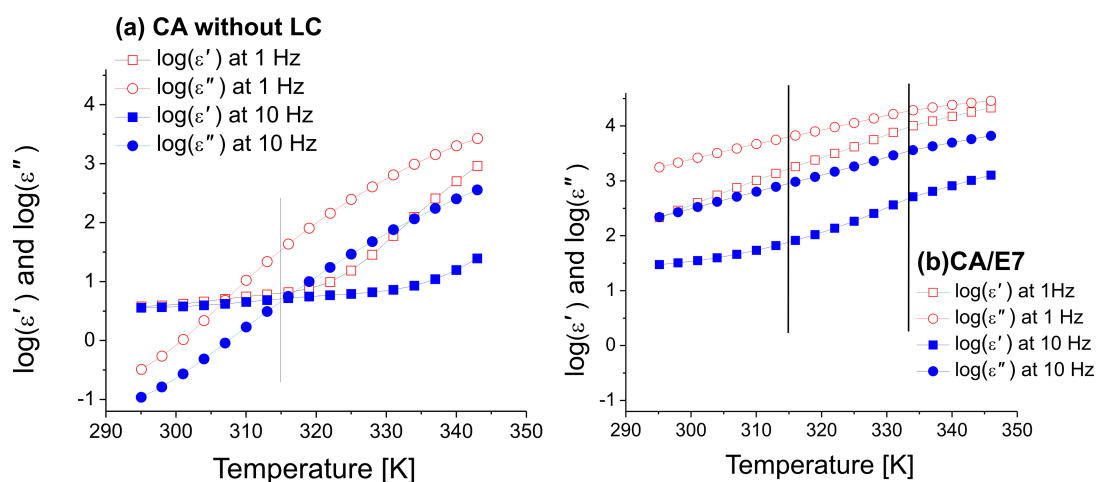


Figure 4: Dielectric constant and dielectric loss (logarithmic scale) as functions of the temperature for (a) the CA cell before filling in the LC and for (b) the CA/E7 cell, at 1 Hz and 10 Hz.

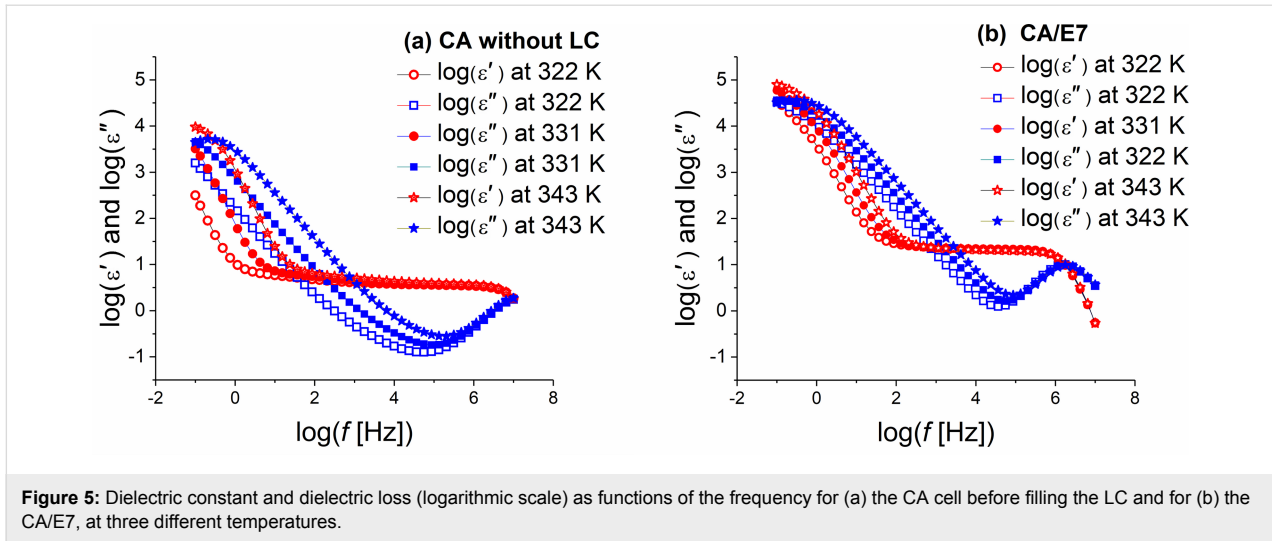


Figure 5: Dielectric constant and dielectric loss (logarithmic scale) as functions of the frequency for (a) the CA cell before filling the LC and for (b) the CA/E7, at three different temperatures.

The characteristic relaxation times were obtained by fitting the spectra of the dielectric constant and dielectric loss with the Havriliak–Negami function [37-40]:

$$\epsilon_{\text{HN}}^*(\omega) = \epsilon'(\omega) - i\epsilon''(\omega) = \epsilon_{\infty} + \frac{\epsilon_{\text{LF}} - \epsilon_{\infty}}{\left(1 + (i\omega \cdot \tau_{\text{max}})^{\alpha}\right)^{\beta}} \quad (1)$$

with $0 < \alpha < 1$ and $0 < \beta < 1$,

where $\epsilon'(\omega)$ is the dielectric constant and $\epsilon''(\omega)$ is the dielectric loss, ϵ_{LF} is the low frequency permittivity, ϵ_{∞} is the permittivity in the HF limit, and τ_{max} is the characteristic relaxation time of the medium. Figure 6 presents the characteristic relaxation time as a function of the inverse of temperature for the cellulose acetate sample with LC.

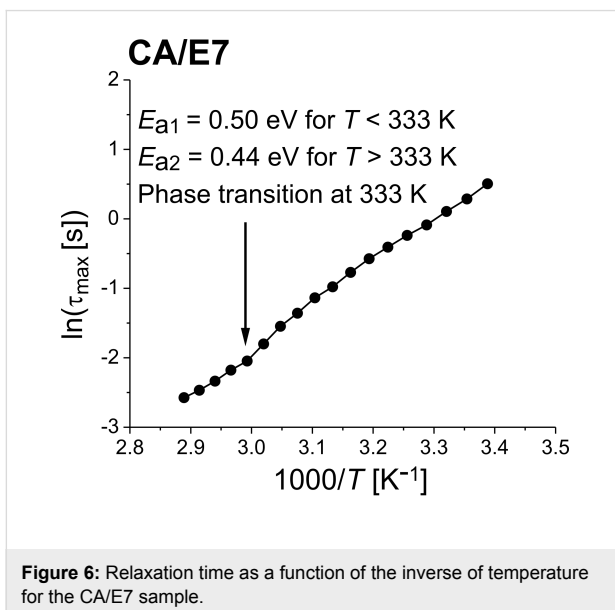


Figure 6: Relaxation time as a function of the inverse of temperature for the CA/E7 sample.

In the temperature range between 293 K and 350 K, where the DS measurements were performed, the pure liquid crystal E7 exhibits an anomalous behavior of the nematic phase around 305 K [26]. This behavior cannot be seen from the results presented here, since the CA component of the composite system has an important influence on the values of dielectric permittivity (Figure 5). Moreover, because of the interaction with the surface of the CA fibers, the dynamics of the E7 molecules is more or less attenuated, as compared to the pure LC. Thus, as in other composite systems, the phase transitions can be modified or even suppressed [38-40].

The dependency $\tau_{\text{max}} = f(1/T)$ can be modeled using the Vogel–Fulcher–Tammann (VFT) law:

$$\tau_{\text{max}} = \tau_{\infty} \exp\left[\frac{A}{k_{\text{B}}(T - T_{\text{V}})}\right], \quad (2)$$

where A is a material constant, k_{B} is Boltzmann's constant, T is the measured temperature, T_{V} is the Vogel temperature, and τ_{∞} is a pre-exponential factor. The results are summarized in Table 1.

The VFT data processed parameters are presented parallel to the previously published results obtained using the I - V curves and the Arrhenius formula [28]. A good agreement of the obtained activation energies is observed, with lower values in the high-temperature domain, after the nematic-to-isotropic phase transition.

Impedance spectroscopy

The impedance, Z , and the quality factor (dielectric loss tangent), θ , were measured using impedance spectroscopy [41-

Table 1: Extracted values of the DS characteristic constants for the CA/E7.

no.	sample type	investigation method	temperature range [K]	activation energy, E_a^a [eV]	Vogel temperature T_V [K]	relaxation time, τ_{max} [s]
1	CA/E7	DS, Vogel–Fulcher–Tammann	295–328	0.50	0.61	$3.79 \cdot 10^{-9}$
			333–346	0.44	0.22	$2.38 \cdot 10^{-8}$
2	CA/E7 [23]	I – V curves, Arrhenius	308–330	0.66	—	—
			333–353	0.54	—	—

^aBecause the obtained Vogel temperature is very small, the VFT equation approximates an Arrhenius-like expression, the material constant A being incorporated into the activation energy E_a .

43]. Based on the obtained data, the real (active) impedance component, Z' , and the imaginary (reactive) impedance component, Z'' impedance components were calculated using the equations

$$Z' = \frac{Z}{\sqrt{1 + \tan^2 \theta}} \quad (3)$$

and

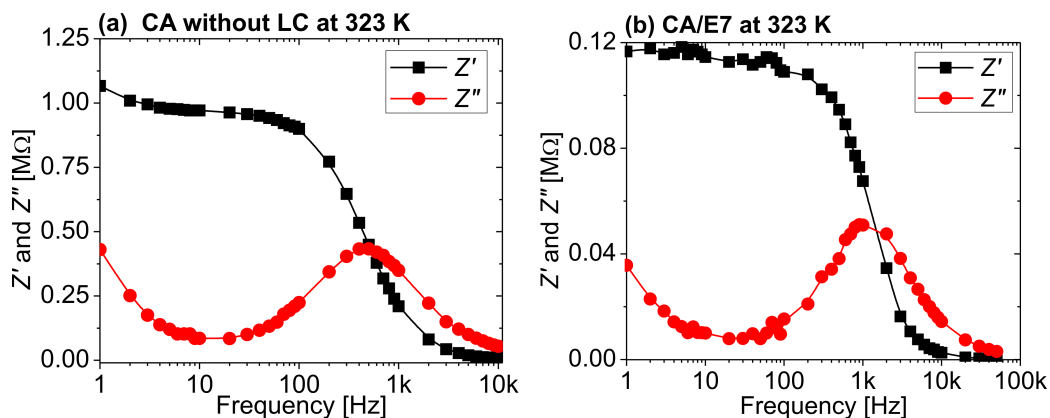
$$Z'' = \frac{Z \tan \theta}{\sqrt{1 + \tan^2 \theta}}. \quad (4)$$

Figure 7 presents selected plots of the active and reactive part of the impedance as functions of the frequency, for (a) the CA cell and for (b) the CA/E7 samples, at 323 K. The curves were obtained by standard interpolation. The reactive part of the impedance plays an important role in determining the components of the equivalent electrical model, and it is presented in Figure 8 for different temperatures. The curves were obtained by interpolation of the raw data.

The spectra of the two impedance components, Z' and Z'' , are different for the samples CA and CA/E7. Similar to the DS results, at low frequencies an E7 molecule-dynamic dipolar relaxation process is overlapping on the intrinsic CA processes (Figure 7b and Figure 5b). Another process is observed at high frequencies (1 MHz), attributed to LC molecules in the bulk, “far” from the CA fibers, as seen in Figure 5b. The slow process noticed at low frequencies (100 Hz), which is observed in Figure 7b and less evident in Figure 5b, is due to the additional interaction of dipoles with the surface. As the temperature increases, the peak values of the reactive impedance shift to higher frequencies (Figure 8).

The Cole–Cole [32] diagrams, $Z'' = f(Z')$, are presented in Figure 9. The semicircular shapes of the diagrams allow for modelling the raw data with a theoretical three-element electric circuit model, consisting of a series resistance, a parallel resistance and a parallel capacitor. The model is presented in Figure 10.

The values of the serial and parallel resistances can be calculated directly from the Cole–Cole diagrams using the equation:

**Figure 7:** Active and reactive part of the impedance as functions of the frequency, for (a) the CA cell and for (b) the CA/E7 sample, at 323 K.

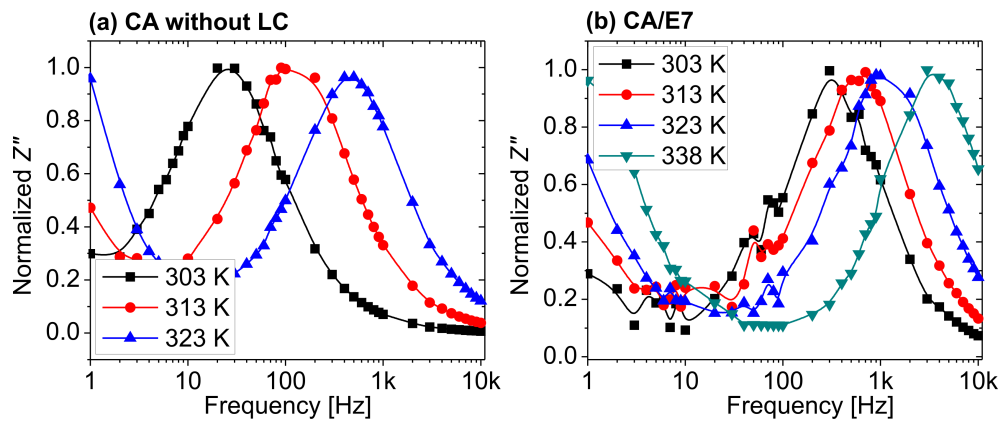


Figure 8: Normalized reactive part of the impedance as a function of the frequency for (a) the CA cell and for (b) the CA/E7 sample, at different temperatures.

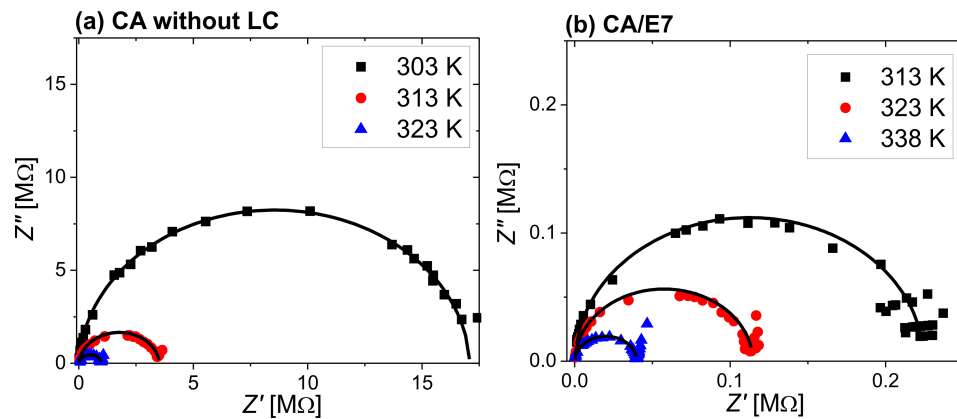


Figure 9: Cole–Cole diagrams for (a) the CA cell at 303 K (black solid squares), 313 K (red solid circles), and 323 K (blue solid upward triangles), and for (b) the composite CA/E7 at 313 K (black solid squares), 323 K (red solid circles), and 338 K (blue solid upward triangles).

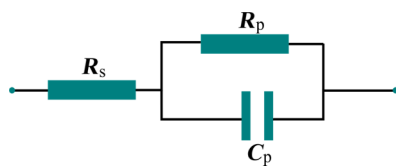


Figure 10: Equivalent three-element model circuit, formed by a serial resistance, R_s , a parallel resistance, R_p , and a parallel capacitance, C_p .

$$\left(x - \left(R_s + \frac{R_p}{2} \right)^2 \right)^2 + y^2 = \left(\frac{R_p}{2} \right)^2. \quad (5)$$

To determine the parallel capacitance for the two samples, we extracted relevant information from the frequency plot of Z'' (Figure 8) and the Cole–Cole diagram (Figure 9). In the

Cole–Cole diagram, for this particular model, the coordinate having a maximum Z'' is also the position at which $\omega\tau = 1$, where ω is the angular frequency. This angular frequency can be deduced by estimating the frequency at which the maximum value of Z'' is obtained (Figure 8). Also, the electrical response time is $\tau = 1/(R_p C_p)$, and knowing the angular frequency, the capacitance can be determined. Based on the fitting technique, we modeled the sample behavior by a simple three-element electric circuit (Figure 10), which describes a single relaxation process. The values of the determined electric parameters have an appropriate temperature variation (Table 2).

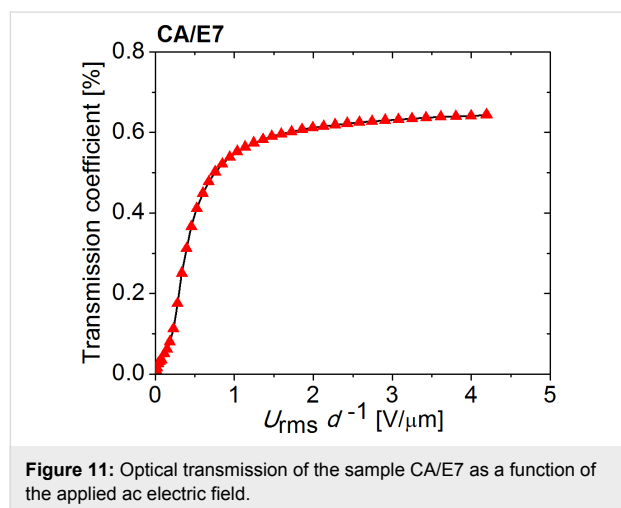
Electro-optical measurements

The optical transmission was measured using the setup described in the Experimental section of this paper and in [21,22,28]. The transmission coefficient is defined as the ratio between the light intensity passing through the sample and the incident light intensity. Figure 11 presents the transmission

Table 2: Characteristic elements of the equivalent three-element circuit, extracted from the Cole–Cole diagrams.

no.	T [K]	sample	R_S [k Ω]	R_p [M Ω]	τ [s]	C_p [nF]
1	313	CA	1810	714	0.5495	0.769
2	313	CA/E7	15.17	7.37	0.3616	49
3	323	CA	2350	1350	0.2936	0.218
4	323	CA/E7	17.58	12.8	0.3331	26
5	338	CA/E7	29.37	18.2	0.1667	9.1

coefficient versus the ac electric field. An improved characteristic is observed, as compared to the previous similar devices [21,22,28], with a stable “ON” state and a lower required electric field to switch between “OFF” and “ON”, at values of 1–1.5 V/ μm . No significant optical hysteresis was observed between the transmission curves obtained when increasing and decreasing the applied voltage. The electro-optical response remained stable when repeating the switching cycles.



Conclusion

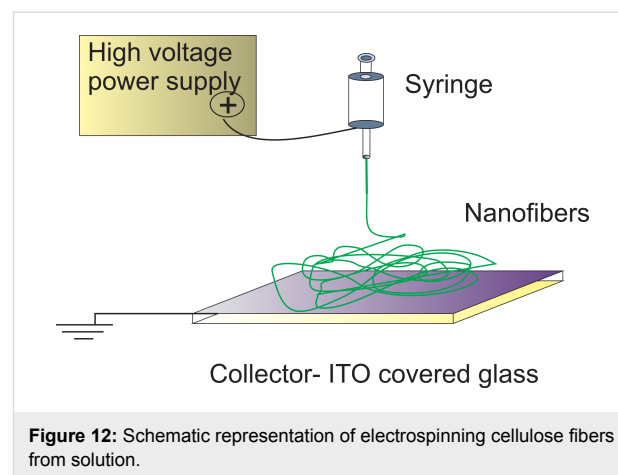
CA electrospun nanofibers were deposited onto ITO-coated glass and an electro-optic cell was formed by two such glass plates with fibers in between. By filling in the nematic liquid crystal E7 a light scattering device with a polymer-dispersed liquid crystal was obtained. Dielectric spectroscopy (DS) and impedance measurements were performed on the electro-optic cells before and after filling in the LC. Also, the dependency of the dielectric constant and electric energy loss on frequency and temperature was studied. The nematic–isotropic phase transition temperature of E7 and the activation energy were determined, and found to be in good agreement with previously obtained data. The relaxation time was obtained by fitting the spectra of the dielectric loss with the Havriliak–Negami function. Impedance measurements were evaluated using Cole–Cole diagrams and the three-element equivalent model, which

permits the estimation of the equivalent resistances and capacity, necessary in practical applications. To test the efficiency of the electro-optic device, optical transmission measurements in external ac fields were performed.

Experimental

Sample preparation

The non-woven nano- and micro-fiber cellulose mats used to prepare the electro-optical cells were produced by electrospinning [21,22,28] from an isotropic solution (15%) of cellulose acetate (CA, Aldrich, $M_W = 60.000 \text{ g}\cdot\text{mol}^{-1}$, 40% acetyl groups) in a mixture of dimethylacetamide/acetone (1:2). The solution was prepared at room temperature. After the first week, it was stirred every day and kept away from light for at least four weeks until used. To produce the fibers, the solution was poured into a 1 mL syringe (diameter 4.5 mm) fitted with a 27-gauge needle (diameter 0.2 mm), which was then placed on the infusion syringe, pump (KDS100) to better control the incoming flow of the polymer solution. A conducting ring is held coaxially with the needle tip. The needle and the ring were directly connected to the positive output of a high-power voltage supply (Glassman EL 30 kV), as schematically presented in Figure 12. After applying the electric potential between the metallic syringe tip and the plate, the fibers were deposited directly onto the ITO-coated glass, over the ITO surface. The fibers were then carefully dried in vacuum, at room temperature, for 72 h before further characterization and use.



To prepare a sample cell, two ITO-coated glasses with fibers were glued together with the fiber mat acting as a spacer. After assembly, the cells thickness between the two ITO-coated glasses was of around 20 μm . This sample was named CA. Before filling the cells with the liquid crystal, the CA cells were kept at 110 $^{\circ}\text{C}$ for 30 min and then allowed to cool slowly to 100 $^{\circ}\text{C}$. The nematic liquid crystal E7 (commercially available from Merck) was then filled in through capillarity. The liquid

crystal E7 is a mixture of alkylcyanobiphenyls with a cyano head group, exhibiting a nematic to isotropic transition at 333.5 K. The refractive index of the CA is 1.45 and the ordinary refractive index of E7 liquid crystal is 1.51. This sample type was named CA/E7.

Characterization techniques

Scanning electron microscopy

The fiber dimensions and distribution were characterized by SEM, using a SEM DSM 962 model from Zeiss Company after thermal evaporation under vacuum of gold onto the surface of the fibers.

Dielectric spectroscopy

The dielectric spectroscopy measurements were performed using a broadband dielectric spectrometer, NOVOCONTROL, consisting of two devices: an Alpha-A high-performance frequency analyzer in the LF domain (0.01 to 10^7 Hz) and an Agilent E4991A RF impedance/material analyzer for the HF range, (1 MHz to 3 GHz), equipped with WinDETA software. The temperature was controlled within 0.2 K, at a constant ac voltage of 0.5 V.

Impedance measurements

Impedance spectroscopy was performed using a high-resolution LCR meter, Hioki – 3200-50 in the frequency range from 1 Hz to 10 kHz and a temperature-controlled hot-stage Mettler-Toledo 3200 series.

Electro-optical transmission

The optical transmission was measured using the setup previously described [21,22,28] and presented in Figure 13. A He–Ne laser beam (wavelength 633.8 nm) passes through the sample, which is modulated by an ac voltage provided by a function generator–amplifier system. The laser beam is detected by a high-speed photodiode with adjustable gain (Thorlabs). The electrical signal generated by the photodiode was recorded with a high-resolution voltmeter Keithley 6517A.

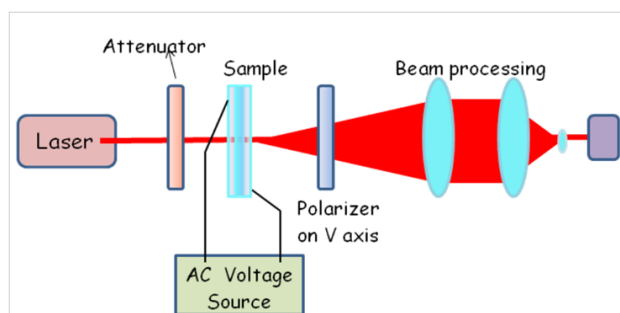


Figure 13: Experimental set-up for the optical transmission measurement.

Acknowledgements

This work was partially funded by FEDER funds through the COMPETE 2020 Program and National Funds through FCT - Portuguese Foundation of Science and Technology under the projects nos. POCI-01-0145-FEDER-007688 (Reference UID/CTM/50025) and PTDC/FIS-NAN/0117/2014. Constantin Paul Ganea thanks the Romanian Ministry of Education and Research for financial support under PN16-480101 of CORE Program. Doina Manaila Maximean thanks Ligia Frunza and Stefan Frunza for useful discussions.

ORCID® IDs

Pedro L. Almeida - <https://orcid.org/0000-0001-7356-8455>

References

- Mucha, M. *Prog. Polym. Sci.* **2003**, *28*, 837–873. doi:10.1016/S0079-6700(02)00117-X
- Drzaic, P. S. *Liquid crystal dispersions*; Series on Liquid Crystals, Vol. 1; World Scientific Publishing Co Pte Ltd: Singapore, 1995. doi:10.1142/2337
- Loiko, V. A. Polymer Films with Nanosized Liquid-Crystal Droplets: Extinction, Polarization, Phase, and Light Focusing. In *Nanodroplets*; Wang, Z., Ed.; Lecture Notes in Nanoscale Science and Technology, Vol. 18; Springer: New York, NY, U.S.A., 2013; pp 195–235. doi:10.1007/978-1-4614-9472-0_9
- Bedjaoui-Alachaher, L.; Semdani, F.; Meziane, R.; Maschke, U. *Mol. Cryst. Liq. Cryst.* **2011**, *546*, 87–157. doi:10.1080/15421406.2011.571925
- Manaila-Maximean, D.; Rosu, C.; Klosowicz, S.; Czuprynski, K. L.; Gilli, J. M.; Aleksander, M. *Mol. Cryst. Liq. Cryst.* **2004**, *417*, 199–205. doi:10.1080/15421400490478830
- Schmidt, J.; Dierking, I. *Prog. Photovoltaics* **2001**, *9*, 263–272. doi:10.1002/pp.378
- Zegadlo, K. B.; El Ouazzani, H.; Cieslik, I.; Weglowski, R.; Zmija, J.; Klosowicz, S.; Majchrowski, A.; Mysliwiec, J.; Sahraoui, B.; Karpierz, M. A. *Opt. Mater.* **2012**, *34*, 1704–1707. doi:10.1016/j.optmat.2012.02.027
- Miedzinski, R.; Ebothe, J.; Fuks-Janczarek, I.; Kityk, I. V.; Majchrowski, A.; Weglowski, R.; Klosowicz, S. J. *J. Mater. Sci.: Mater. Electron.* **2010**, *21*, 659–665. doi:10.1007/s10854-009-9973-5
- Manaila-Maximean, D.; Albu, A. M.; Umanski, B. A.; Rosu, C.; Bena, R. *Proc. SPIE* **2001**, *4430*, 554–559. doi:10.1117/12.432891
- Cîrcu, V.; Gibbs, T. J. K.; Omnès, L.; Horton, P. N.; Hursthouse, M. B.; Bruce, D. W. *J. Mater. Chem.* **2006**, *16*, 4316–4325. doi:10.1039/B608823F
- Micutz, M.; Iliş, M.; Staicu, T.; Dumitraşcu, F.; Pasuk, I.; Molard, Y.; Roisnel, T.; Cîrcu, V. *Dalton Trans.* **2014**, *43*, 1151–1161. doi:10.1039/C3DT52137K
- Roşu, C.; Manaila-Maximean, D.; Cîrcu, V.; Molard, Y.; Roisnel, T. *Liq. Cryst.* **2011**, *38*, 757–765. doi:10.1080/02678292.2011.573585
- Tsai, T.-Y.; Lee, C.-Y.; Lee, C.-J.; Chang, W.-C.; Lee, W.; Chen, P.-C. *J. Phys. Chem. Solids* **2010**, *71*, 595–599. doi:10.1016/j.jpcs.2009.12.045
- Shibaev, P. V.; Kopp, V. I.; Genack, A. Z. *J. Phys. Chem. B* **2003**, *107*, 6961–6964. doi:10.1021/jp0222189

15. Palffy-Muhoray, P.; Cao, W.; Moreira, M.; Taheri, B.; Munoz, A. *Philos. Trans. R. Soc. London, Ser. A* **2006**, *364*, 2747–2761. doi:10.1098/rsta.2006.1851
16. Hinojosa, A.; Sharma, S. C. *Appl. Phys. Lett.* **2010**, *97*, 081114. doi:10.1063/1.3482942
17. Rosu, C.; Manaila-Maximean, D.; Donescu, D.; Frunza, S.; Sterian, A. R. *Mod. Phys. Lett. B* **2010**, *24*, 65–73. doi:10.1142/S0217984910022238
18. Cirtoaje, C.; Petrescu, E.; Moțoc, C. *Physica E* **2013**, *54*, 242–246. doi:10.1016/j.physe.2013.07.005
19. Palarie, I.; Dascalu, C.; Iacobescu, G. E.; Varut, M. C. *Liq. Cryst.* **2012**, *39*, 833–837. doi:10.1080/02678292.2012.684072
20. Circu, V.; Mocanu, A. S.; Roșu, C.; Manaila-Maximean, D.; Dumitrașcu, F. J. *Therm. Anal. Calorim.* **2012**, *107*, 877–886. doi:10.1007/s10973-011-1609-3
21. Almeida, P. L.; Kundu, S.; Borges, J. P.; Godinho, M. H.; Figueirinhas, J. L. *Appl. Phys. Lett.* **2009**, *95*, 043501. doi:10.1063/1.3186640
22. Almeida, P. L.; Godinho, M. H.; Figueirinhas, J. L. *Phys. Rev. E* **2014**, *89*, 012507. doi:10.1103/PhysRevE.89.012507
23. Bouchakour, M.; Derouiche, Y.; Beyens, C.; Mechernène, L.; Riahi, F.; Maschke, U. *Liq. Cryst.* **2015**, *42*, 1527. doi:10.1080/02678292.2015.1044579
24. Boudraa, K.; Dali Youcef, B.; Bedjaoui, L.; Bouchaour, T.; Maschke, U. *Macromol. Symp.* **2014**, *336*, 61–67. doi:10.1002/masy.201300016
25. Loiko, V. A.; Krakhlev, M. N.; Konkolovich, A. V.; Prischepa, O. O.; Miskevich, A. A.; Zyryanov, V. Ya. *J. Quant. Spectrosc. Radiat. Transfer* **2016**, *178*, 263–268. doi:10.1016/j.jqsrt.2015.10.024
26. De Sousa, F. A.; Michels, R. N.; Cardoso, P. M. M.; De Jesus, M. M. A. *Mol. Cryst. Liq. Cryst.* **2013**, *576*, 106–117. doi:10.1080/15421406.2013.789711
27. De Jesus, M. M. A. Caracterização eletro-óptica de uma mistura líquido cristalina eutéctica em diferentes configurações de confinamento. Ph.D. Thesis, Universidade Estadual de Maringá, Maringá, Brazil, 2009.
28. Rosu, C.; Manaila-Maximean, D.; Kundu, S.; Almeida, P. L.; Danila, O. *J. Electrostat.* **2011**, *69*, 623–630. doi:10.1016/j.elstat.2011.08.009
29. Sena, C.; Godinho, M. H.; de Oliveira, C. L. P.; Figueiredo Neto, A. M. *Cellulose* **2011**, *18*, 1151–1163. doi:10.1007/s10570-011-9575-2
30. Geng, Y.; Brogueira, P.; Figueirinhas, J. L.; Godinho, M. H.; Almeida, P. L. *Liq. Cryst.* **2013**, *40*, 769–773. doi:10.1080/02678292.2013.783137
31. Godinho, M. H.; Almeida, P. L.; Figueirinhas, J. L. *Materials* **2014**, *7*, 4601–4627. doi:10.3390/ma7064601
32. Aflori, M.; Serbezeanu, D.; Carja, I.-D.; Fortunato, G. *Chem. Lett.* **2015**, *44*, 1440–1442. doi:10.1246/cl.150546
33. Tański, T.; Matysiak, W.; Hajduk, B. *Beilstein J. Nanotechnol.* **2016**, *7*, 1141–1155. doi:10.3762/bjnano.7.106
34. Viciosa, M. T.; Nunes, A. M.; Fernandes, A.; Almeida, P. L.; Godinho, M. H.; Dionísio, M. D. *Liq. Cryst.* **2002**, *29*, 429–441. doi:10.1080/02678290110113478
35. Rosu, C.; Manaila-Maximean, D.; Godinho, M. H.; Almeida, P. L. *Mol. Cryst. Liq. Cryst.* **2003**, *391*, 1–11. doi:10.1080/10587250216170
36. Manaila-Maximean, D.; Bena, R.; Albu, A.-M. *Mod. Phys. Lett. B* **1997**, *10*, 431–440. doi:10.1142/S0217984997000530
37. Kremer, F.; Schönhal, A., Eds. *Broadband Dielectric Spectroscopy*; Springer-Verlag: Berlin-Heidelberg, Germany, 2003. doi:10.1007/978-3-642-56120-7
38. Frunza, L.; Kosslick, H.; Frunza, S.; Schönhal, A. *Microporous Mesoporous Mater.* **2006**, *90*, 259–270. doi:10.1016/j.micromeso.2005.10.025
39. Frunza, S.; Schönhal, A.; Frunza, L.; Beica, T.; Zgura, I.; Ganea, P.; Stoenescu, D. *Chem. Phys.* **2010**, *372*, 51–60. doi:10.1016/j.chemphys.2010.04.031
40. Brás, A. R.; Frunza, S.; Guerreiro, L.; Fonseca, I. M.; Corma, A.; Frunza, L.; Dionísio, M.; Schönhal, A. *J. Chem. Phys.* **2010**, *132*, 224508. doi:10.1063/1.3432775
41. Cole, K. S.; Cole, R. H. *J. Chem. Phys.* **1941**, *9*, 341–352. doi:10.1063/1.1750906
42. Wang, Y.-M.; Snyder, D. D.; Nelson, G. J. *Mol. Cryst. Liq. Cryst.* **1987**, *149*, 163–176. doi:10.1080/00268948708082977
43. Rout, D. K.; Jain, S. C. *Mol. Cryst. Liq. Cryst.* **1992**, *210*, 75–81. doi:10.1080/10587259208030758

License and Terms

This is an Open Access article under the terms of the Creative Commons Attribution License (<http://creativecommons.org/licenses/by/4.0>), which permits unrestricted use, distribution, and reproduction in any medium, provided the original work is properly cited.

The license is subject to the *Beilstein Journal of Nanotechnology* terms and conditions: (<http://www.beilstein-journals.org/bjnano>)

The definitive version of this article is the electronic one which can be found at: [doi:10.3762/bjnano.9.18](https://doi.org/10.3762/bjnano.9.18)



Optical model to describe coherent transmittance of polymer dispersed liquid crystal film doped with carbon nanotubes

V.A. Loiko^{a,1,*}, A.V. Konkolovich^a, A.A. Miskevich^a, D. Manaila-Maximean^b, O. Danila^b, V. Cîrcu^c, A. Bărar^b

^aStepanov Institute of Physics, National Academy of Sciences of Belarus, Niezalezhnastsi avenue 68-2 Minsk, 220072, Belarus

^bUniversity Politehnica of Bucharest, Department of Physics, Spl. Independentei 313, Bucharest, R-060042, Romania

^cUniversity of Bucharest, Department of Inorganic Chemistry, 23 Dumbrava Rosie St., Bucharest, Sector 2, 020484, Romania

ARTICLE INFO

Article history:

Received 13 November 2019

Revised 22 January 2020

Accepted 6 February 2020

Available online 7 February 2020

Keywords:

Light transmittance

Polymer-dispersed liquid crystals

Liquid crystal droplets

Carbon nanotubes

ABSTRACT

An optical model has been developed for analyzing the coherent transmittance of a polymer dispersed liquid crystal films doped with carbon nanotubes (CNTs) at uniform normal droplet-polymer interface anchoring. It is based on the Foldy-Twersky and anomalous diffraction approximations, Maxwell-Garnett equations, and the order parameters concept. The model allows one to analyze the electro-optical response of films depending on their thickness, the refractive indices of the liquid crystal (LC) and polymer matrix, size and concentration of the LC droplets, concentration of nanotubes, conductivities of the LC and the polymer. Experimental verification of the model is performed.

© 2020 Elsevier Ltd. All rights reserved.

1. Introduction

The polymer-dispersed liquid crystal (PDLC) films [1,2] consist of a polymer matrix containing liquid crystal (LC) droplets, in which the orientation of the LC molecules can be changed under the electric or magnetic fields. This allows one to control the optical response of the films. They are used in displays, optoelectronic, microelectronic, and telecommunication systems, laser devices, etc. Electrically or magnetically controlled optical response of PDLC films is based on light scattering. It does not require the use of additional polaroids in comparison with the ordinary (homogeneous) LC layers.

In recent years, there is an increasing interest in studying the dielectric and optical properties of composite materials based on bulk LC and PDLC doped with carbon nanotubes (CNTs) [3–6]. Currently, studies of the electro-optical response of composite PDLC–CNTs films are mainly experimental [4,6]. As far as we know, there are no theoretical optical models that allow one to describe and predict electro-optical response of the PDLC–CNTs films as function of the component parameters (LC, polymer, NTs).

In this paper, we suggest an electro-optical model for analyzing the coefficient of coherent (directional, regular) transmission (coherent transmittance) of a PDLC–CNTs film with a homogeneous

normal interface anchoring. To determine the coherent transmittance of the film, the Foldy-Twersky approximation is used [7–9]. The optical characteristics of a single droplet of nematic LC are determined in the framework of the anomalous diffraction approximation [1,2,9,10] and effective medium theory [11–13] using the effective refractive indices of the droplets [8,14,15]. Based on the Maxwell-Garnett equations [16–18] a method has been developed to determine the refractive index of the polymer matrix, the effective refractive index of the LC droplets, and the threshold field of the reorientation of the director structure of LC droplets upon doping the PDLC film with NTs. A technique has been developed for determining the volume filling factor of the film with LC droplets, volume filling factors of the LC droplets and polymer matrix doped with NTs, depending on the mass fractions of the components in the PDLC–CNTs composite. The technique is applicable to single-wall (SWCNTs) and multiwall (MWCNTs) carbon nanotubes. Experimental verification of the developed model was carried out.

2. Coherent transmittance of PDLC film with uniform normal interface anchoring

A PDLC film with a homogeneous normal interfacial surface anchoring is characterized by a polarization-independent coherent transmittance at normal illumination, when the control electric field is directed normally to the surface. For such films, polarization independence is due to the symmetry properties of the director configuration of nematic LC droplets. In the absence of

* Corresponding author.

E-mail address: loiko@ifanbel.bas-net.by (V.A. Loiko).

¹ <http://loiko.org/>

a control field a radial configuration takes place [1,2] with central symmetry and a zero droplet order parameter. In the control field, the configuration of the director of the LC in the droplets is axisymmetric with respect to the normal to the film: the film order parameter equals $-1/2$ [15]. As a result, there is no difference between ordinary and extraordinary waves when light passes through the film and the state of polarization of the incident light is preserved.

Let us consider a PDLC film containing a polydisperse ensemble of spheroidal LC droplets with rotation symmetry relatively to small axis directed along the normal to the film and the radial configuration of their internal structure [1,2]. The anisotropy parameter ε_a , defined as the ratio of the major axis of the droplet in the film plane to the minor axis along the normal to the film, is the same for all droplets. In the framework of the Foldy–Twersky, anomalous diffraction, and an effective medium approximations, and based on the results of [8,9,15], it is possible to write the following expressions for the coherent transmittance T_c of a film in the absence of NTs:

$$T_c = \exp(-\gamma l), \quad (1)$$

$$\gamma = (3c_d Q)/(4a_{ef}), \quad (2)$$

$$a_{ef} = \langle a^3 \rangle / \langle a^2 \rangle, \quad (3)$$

$$Q = 4\text{Re}K_h, \quad (4)$$

$$\text{Re}K_h = 1/2 - \sin \nu / \nu + (1 - \cos \nu) / \nu^2, \quad (5)$$

$$\nu = 2ka_{ef}(n_d/n_p - 1), \quad (6)$$

$$n_d = n_{iso} - (\Delta n S S_d(E))/3, \quad (7)$$

$$n_{iso} = (2n_{\perp} + n_{\parallel})/3, \quad (8)$$

$$\Delta n = n_{\parallel} - n_{\perp}. \quad (9)$$

Here, γ is the attenuation coefficient of the film; l is the film thickness; c_d is the volume filling factor of the film with LC droplets (part of film volume occupied by droplets); Q is the extinction efficiency factor for single droplet; a_{ef} and $\langle a \rangle$ are the effective [9] and average lengths of the droplet's minor semiaxis a along the normal to the film; the angle brackets $\langle \dots \rangle$ mean the average over the a semiaxes of droplets; K_h is the Hulst function; $k = 2\pi n_p / \lambda$, λ is the wavelength of the incident light; n_p is the refractive index of the polymer matrix; Δn , n_{\perp} and n_{\parallel} are the birefringence, ordinary and extraordinary refractive indices of a LC; S is the molecular order parameter of LC [1,2]; $S_d(E)$ is the order parameter of LC droplets [2], depending on the control electric field E .

For droplets with normal interface anchoring, when a control field is applied along the normal to the film, using the results of [19–24], it is possible to write the following expression for the droplet order parameter:

$$S_d(E) = 1 - \exp(-e). \quad (10)$$

Here e is the dimensionless normalized value of the control field,

$$e = \frac{E2\langle a \rangle}{A} \left(\frac{\varepsilon_0 \Delta \varepsilon_{LC}}{K} \right)^{1/2} \left(\frac{3}{2 + \beta} \right) \left(1 - c_d \frac{\beta - 1}{\beta + 2} \right)^{-1}, \quad (11)$$

where

$$A = 10 \{ (\varepsilon_a^2 - 1) / \varepsilon_a^2 + 1 \}^{1/2}, \quad (12)$$

$$\beta = \sigma_d / \sigma_p, \quad (13)$$

$$\sigma_d = \sigma_{iso} + (2/3)(\sigma_{\parallel} - \sigma_{\perp}) S S_d(E), \quad (14)$$

$$\sigma_{iso} = (\sigma_{\parallel} + 2\sigma_{\perp})/3. \quad (15)$$

In Eqs. (11)–(15) parameter A takes into account anisotropy of the droplet shape [21], K is the average value of the elastic modulus of the LC; ε_0 is the electric constant; $\Delta \varepsilon_{LC}$ is the dielectric anisotropy of the LC; σ_p and σ_d are the electrical conductivities of the polymer matrix and LC droplets, respectively; σ_{\parallel} and σ_{\perp} are the conductivities of the LC in parallel and orthogonal directions to its optical axis (director).

Note that relations (10)–(15) are obtained for the low frequency control field [2,22,23] with the order parameter of the PDLC film equal to $-1/2$.

Eqs. (1)–(15) allow one to analyze the electro-optical response of the PDLC film depending on the control field and the parameters of the film with the initial radial droplet structure in the absence of NTs.

3. Modification of the PDLC film parameters upon doping with carbon nanotubes

Consider a PDLC film doped with CNTs. A schematic representation of the cross section of the film is shown in Fig. 1. In the absence of a control field, the orientation of the NTs is random over the entire volume of the composite. When a field is applied, the long axes of the LC molecules and NTs in the droplets are oriented along the field.

To describe the electro-optical response of a composite PDLC–CNT film, it is necessary to take into account the change in the electrical conductivities of the polymer, σ_p , and droplets, σ_d , in the dielectric anisotropy of the LC, $\Delta \varepsilon_{LC}$, which determines the normalized control field (see Eqs. (11)–(15)), and in refractive indices of polymer matrix, n_p , and LC droplets, n_d (see Eqs. (6)–(9)).

We use the Maxwell – Garnett equations [16–18] to find (i) the refractive indices of LC droplets and polymer matrix doped with CNTs, n_{d+CNT} and n_{p+CNT} ; (ii) the electrical conductivities of LC droplets and polymer matrix doped with CNTs, σ_{d+CNT} and σ_{p+CNT} ; (iii) the dielectric anisotropy of LC with CNTs $\Delta \varepsilon_{LC+CNT}$. Given that the electrical conductivity of CNTs ($\sim 10^6$ – 10^7 S/m) is much higher than the conductivity of LCs ($\sim 10^{-8}$ – 10^{-6} S/m) and

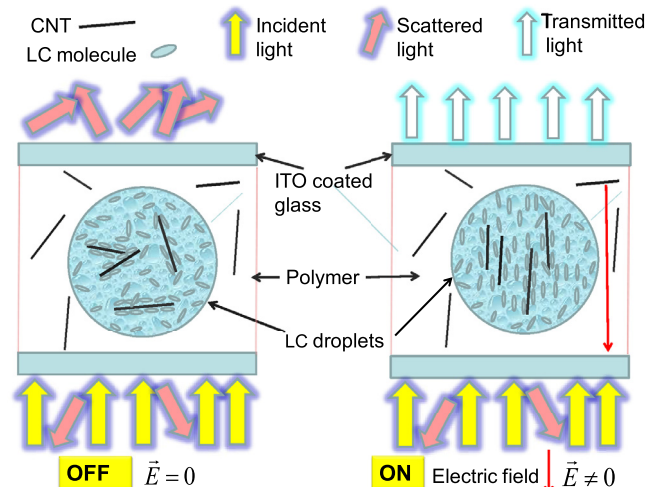


Fig. 1. Schematic representation of a PDLC film doped with CNTs.

polymers ($\sim 10^{-9}$ – 10^{-12} S/m), we have obtained:

$$n_{d+CNT} = n_d \left\{ (1 + 2c_d^{CNT}) / (1 - c_d^{CNT}) \right\}^{1/2}, \quad (16)$$

$$n_{p+CNT} = n_p \left\{ (1 + 2c_p^{CNT}) / (1 - c_p^{CNT}) \right\}^{1/2}, \quad (17)$$

$$\sigma_{d+CNT} = \sigma_d (1 + 2c_d^{CNT}) / (1 - c_d^{CNT}), \quad (18)$$

$$\sigma_{p+CNT} = \sigma_p (1 + 2c_p^{CNT}) / (1 - c_p^{CNT}), \quad (19)$$

$$\Delta \varepsilon_{LC+CNT} = \Delta \varepsilon_{LC} (1 + 2c_d^{CNT}) / (1 - c_d^{CNT}), \quad (20)$$

where c_d^{CNT} and c_p^{CNT} are the volume filling factors of the LC droplets and the polymer matrix with CNTs (characterizing the part of droplets and polymer matrix occupied by NTs).

The normalized field e for the composite PDLC–CNT film, as it follows from Eqs. (13), (14), (18)–(20), is:

$$e = E \frac{2\langle a \rangle}{A} \left(\frac{1 + 2c_d^{CNT}}{1 - c_d^{CNT}} \right)^{1/2} \left(\frac{\varepsilon_0 \Delta \varepsilon_{LC}}{K} \right)^{1/2} \times \left(\frac{3}{2 + x\beta} \right) \left(1 - c_d \frac{x\beta - 1}{x\beta + 2} \right)^{-1}, \quad (21)$$

where

$$x = \frac{1 - c_p^{CNT}}{1 + 2c_p^{CNT}} \frac{1 + 2c_d^{CNT}}{1 - c_d^{CNT}}. \quad (22)$$

Note that in the absence of nanotubes ($c_d^{CNT} = c_p^{CNT} = 0$), the parameter $x = 1$ and the expression (21) for the normalized field e coincides with the analogous expression (11).

As a result, the coherent transmittance T_c of the composite PDLC–CNT film is determined using Eqs. (1)–(15), where the effective refractive index of LC droplets, the refractive index of the polymer matrix, and the normalized control field are calculated by Eqs. (16), (17), (21), respectively.

In the experiment, the volume filling factors c_d , c_d^{CNT} and c_p^{CNT} , which determine the optical response of the PDLC–CNT film (see Eqs. (2), (16)–(22)), are usually unknown. In the preparation of samples, as a rule, the mass fractions of the used components are known. It can be shown that if the mass fraction f_{CNT} of CNTs is small (tenths of a percent) in comparison with the mass fractions of the LC, f_{LC} , and polymer, f_p , then:

$$c_d = f_{LC} (f_{LC} \rho_{LC} + f_p \rho_p) / \rho_{LC}. \quad (23)$$

$$c_d^{CNT} = c_{CNT} f_{LC} \rho_{LC} / (f_{LC} \rho_{LC} + f_p \rho_p), \quad (24)$$

$$c_p^{CNT} = c_{CNT} f_p \rho_p / (f_{LC} \rho_{LC} + f_p \rho_p), \quad (25)$$

where ρ_{LC} and ρ_p are the density of the LC and polymer; c_{CNT} is the volume filling factor of the PDLC–CNT film with NTs.

Let us find the equations linking the volume filling factor c_{CNT} and the mass fractions of the components f_p , f_{LC} and f_{CNT} in the composite PDLC–CNT film.

For closed MWCNTs; whose length exceeds significantly their outer diameter, at low f_{CNT} values and taking into account the polydispersity of NTs, we obtain:

$$c_{CNT} = f_{CNT} G (f_p \rho_p + f_{LC} \rho_{LC}) / \rho_{gr}. \quad (26)$$

where ρ_{gr} is the density of graphite; parameter G characterizes the filling of NTs with graphene layers (these is the ratio of the average

volume of NTs to the average volume of folded graphene layers in NTs),

$$G = N_{gr}^{-1} \left\{ \frac{2l_{gr} \langle r_2 \rangle - l_{gr}^2}{\langle r_2^2 \rangle} - \frac{(N_{gr} - 1)(l_{gr} + l_{\Delta})l_{gr}}{\langle r_2^2 \rangle} \right\}^{-1}, \quad (27)$$

$$\langle r_2^2 \rangle = \langle r_2 \rangle^2 (1 + 2/\mu_{CNT}) / (1 + 1/\mu_{CNT}), \quad (28)$$

$$\mu_{CNT} = 1/v_{CNT}^2 - 1, \quad (29)$$

$$N_{gr}^{\max} = [\langle r_2 \rangle / (l_{gr} + l_{\Delta})]. \quad (30)$$

In Eqs. (27)–(30) N_{gr} is the number of graphene layers (walls) in NTs (nesting of NTs); l_{gr} is the thickness of the graphene layer; l_{Δ} is the distance between graphene layers in NTs; $\langle r_2 \rangle$ is the average value of the outer radius of the MWCNTs (here, angle brackets mean averaging over the outer radius of NTs); μ_{CNT} and v_{CNT} are the parameter and the variation coefficient of the gamma distribution [9] used for averaging over the radius of NTs (for monodisperse nanotubes $v_{CNT} = 0$); N_{gr}^{\max} is the maximum possible value of nesting of NTs; square brackets in Eq. (30) mean that the integer part of the number is taken.

In the case of closed single wall carbon nanotubes ($N_{gr} = 1$), we have:

$$c_{CNT} = f_{CNT} \frac{f_p \rho_p + f_{LC} \rho_{LC}}{\rho_{gr}} \frac{\langle r_2^2 \rangle}{2l_{gr} \langle r_2 \rangle - l_{gr}^2}. \quad (31)$$

The results of calculation of the volume filling factor c_{CNT} for the PDLC–CNT film as a function of the average outer radius $\langle r_2 \rangle$ of nanotubes at different values of the variation coefficient v_{CNT} are presented in Fig. 2. The calculations are performed for singlewall and multiwall CNTs with the following parameters: $l_{gr} = 0.134$ nm, $l_{\Delta} = 0.334$ nm, $\rho_{gr} = 2.267$ g/cm³, $\rho_{LC} = 1.03$ g/cm³, $\rho_p = 1.18$ g/cm³. Mass fractions of components in the composite film are as follows: $f_{LC} = 0.4$, $f_p = 0.6$, $f_{CNT} = 0.004$.

4. Experimental verification of the model

To compare the results obtained in the framework of the developed model with the measurement data, we used the experimental dependences of the normalized transmittance $T_c^{\text{norm}} = T_c/T_c^{\text{max}}$ (T_c^{max} is maximum transmittance) on the control field E [25]. The measurements were carried out for PDLC films based on E7 LC and polymethyl methacrylate (PMMA) polymer without NTs and upon doping with NTs. The samples were illuminated along the normal to the surface by a He-Ne laser at the wavelength $\lambda = 0.6328$ μm . In the absence of NTs, ordinary n_{\perp} and extraordinary n_{\parallel} refractive indices of the LC are equal to: $n_{\perp} = 1.52$, and $n_{\parallel} = 1.745$, the refractive index of the polymer $n_p = 1.503$. Mass fractions of components without NTs, $f_{LC} = 0.4$, $f_p = 0.6$. The filling factor of the PDLC film $c_d = 0.435$. Mass fraction of NTs in the PDLC–CNT film $f_{CNT} = 0.004$. Films thickness $l = 50$ μm . Based on polarizing microscopy measurements, it was found that the internal structure of droplets without NTs is radial. The average radius of droplets in the plane of the samples is $\langle a \rangle = 1.07$ μm ; effective size of droplet $a_{ef} = 2.34$ μm . The experimental and theoretical dependences of $T_c^{\text{norm}}(E)$ are presented in Fig. 3. The following parameters were used in the calculation: $c_{CNT} = 0.03$ ($c_d^{CNT} = 0.011$, $c_p^{CNT} = 0.019$), $A = 0.456$ ($\varepsilon_d \approx 1$), $\rho_{LC} = 1.03$ g/cm³, $\rho_p = 1.18$ g/cm³, $\sigma_p = 10^{-9}$ S/m, $\sigma_{\parallel} = 5.7 \times 10^{-8}$ S/m, $\sigma_{\perp} = 2.6 \times 10^{-8}$ S/m, $K = 1.17 \times 10^{-11}$ N, $\Delta \varepsilon_{LC} = 14$. One can see a good agreement of the theoretical and experimental results for PDLC film doped with nanotubes. For a film without nanotubes, there is a discrepancy in the data. This may be due to different

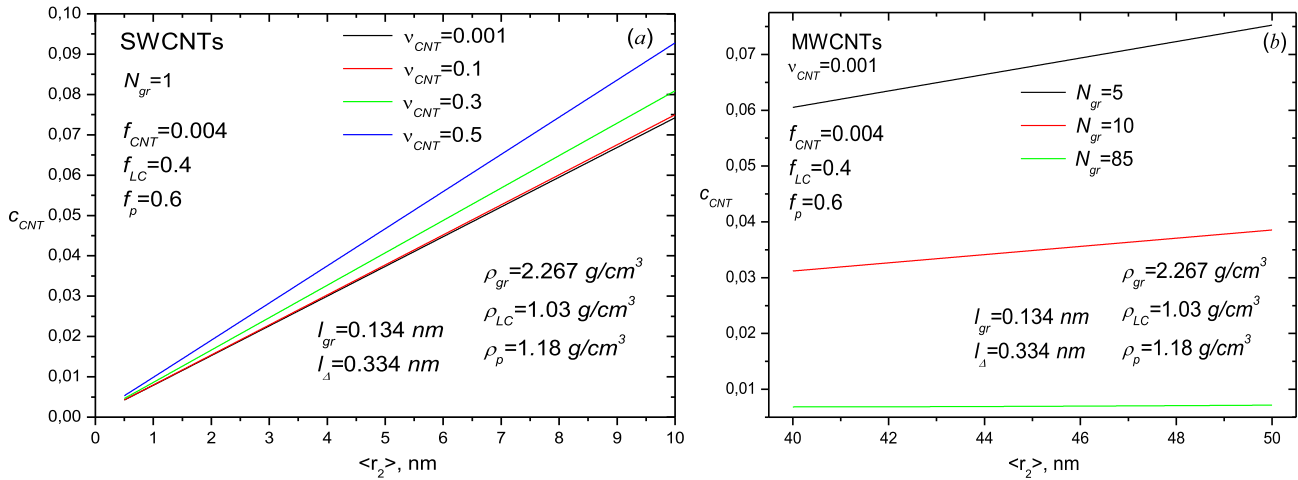


Fig. 2. The volume filling factor c_{CNT} of the PDLC–CNTs film as function of the average outer radius ($\langle r_2 \rangle$). (a) polydisperse SWCNTs at different values of the variation coefficient v_{CNT} . (b) monodisperse MWCNTs at different values of the number N_{gr} of graphene layers.

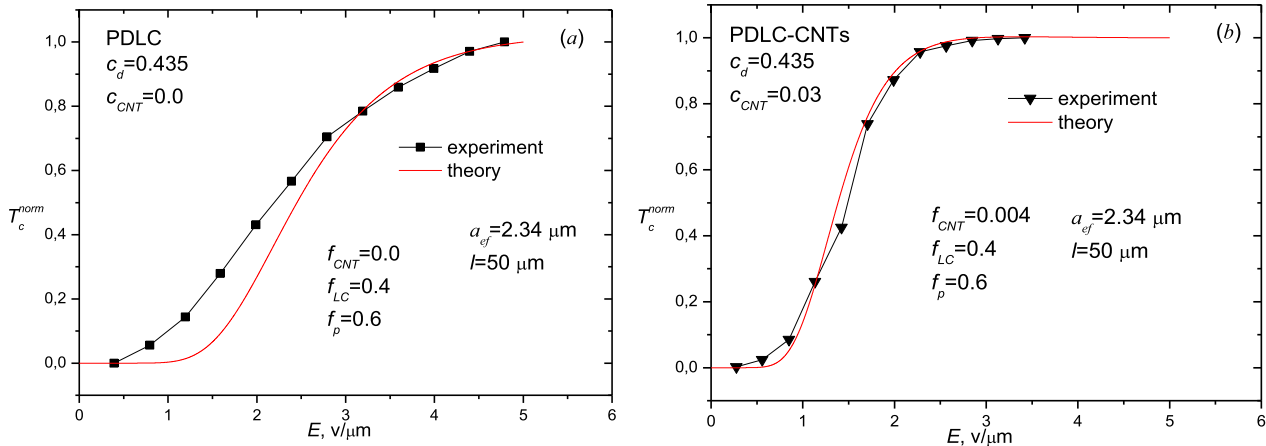


Fig. 3. Theoretical and experimental dependences of the normalized transmittance $T_c^{norm}(E)$ for the PDLC film (a) and for the PDLC–CNTs film (b). Mass fractions of components: $f_{LC} = 0.4$, $f_p = 0.6$, $f_{CNT} = 0.004$. Filling factors: $c_d = 0.435$, $c_{CNT} = 0.03$, $c_d^{CNT} = 0.011$, $c_p^{CNT} = 0.019$.

polydispersity of doped and undoped samples and needs more thorough investigation.

5. Conclusion

In the present work, for the first time, a model for describing the electro-optical response of PDLC–CNT films is developed. It is validated by comparison with experiment.

Pay attention that the theory is developed for the films with uniform normal interface anchoring. Such films are characterized by a polarization-independent coherent transmittance at normal illumination, when the control electric field is directed normally to the film. They are promising for applications in optoelectronic devices where modulation of light is required without changing its polarization state and to modulate the unpolarized light.

The model can be extended to PDLC–CNT films with uniform tangential interface anchoring and PDLC films doped with other nanoparticles (NPs): gold, ferroelectric, silica NPs, etc.

Declaration of Competing Interest

We have no conflict of interest.

CRediT authorship contribution statement

V.A. Loiko: Conceptualization, Methodology. **A.V. Konkolovich:** Writing - original draft, Validation. **A.A. Miskevich:** Software, Data curation. **D. Manaila-Maximean:** Supervision, Writing - review & editing. **O. Danila:** Resources. **V. Cîrcu:** Methodology. **A. Bărar:** Data curation.

Acknowledgments

We thank the [Belarusian Foundation for Fundamental Research \(F18RA-003\)](#) and the [Romanian Academy](#) (Joint Research Project – NAS of Belarus, 2018).

References

- [1] Drzaic PS. Liquid crystal dispersions. World Scientific; 1995.
- [2] Simoni F. Nonlinear properties of liquid crystals and polymer dispersed liquid crystals. World Scientific; 1997.
- [3] Rahman M, Lee W. Scientific duo of carbon nanotubes and nematic liquid crystals. Top Rev. J Phys D 2009;42 063001(1-12).
- [4] Yadav SP, Singh S. Carbon nanotube dispersion in nematic liquid crystals: an overview. Prog Mater Sci 2016;80:38–76.
- [5] Shriyan SK, Fontecchio AK. Improved electro-optic response of polymer dispersed liquid crystals doped with oxidized multiwalled carbon nanotubes. Mol Cryst Liq Cryst 2010;525:158–66.

- [6] Wu Y, Cao H, Duan M, Li E, Wang H, Yang Z, et al. Effects of a chemically modified multiwall carbon nanotubes on electro-optical properties of PDLC films. *Liq Cryst* 2017;45(7):1023–31.
- [7] Ishimaru A. Wave propagation and scattering in random media. New York, San Francisco, London: Academic; 1978.
- [8] Loiko VA. Polymer films with nanosized liquid-crystal droplets: extinction, polarization, phase, and light focusing. In: Wang ZM, editor. *Nanodroplets*. New York, Heidelberg, Dordrecht, London: Springer; 2013. p. 195–235.
- [9] Loiko VA, Konkolovich AV, Zyryanov VY, Miskevich AA. Polarization of light by a polymer film containing elongated droplets of liquid crystal with inhomogeneous interfacial anchoring. *Opt Spectr* 2017;122(6):984–94.
- [10] Zumer S. Light scattering from nematic droplets: anomalous-diffraction approach. *Phys Rev A* 1988;37:4006–15.
- [11] Reshetnyak VY, Sluckin TJ, Cox SJ. Effective medium theory of polymer dispersed liquid crystal droplet systems: II. Partially oriented bipolar droplets. *J. Phys D* 1997;30:3253–66.
- [12] Cox SJ, Reshetnyak VY, Sluckin TJ. Effective medium theory of light scattering in polymer dispersed liquid crystal films. *J. Phys D* 1998;31:1611–25.
- [13] Kiselev AD, Yaroshchuk OV, Dolgov L. Ordering of droplets and light scattering in polymer dispersed liquid crystal films. *J. Phys* 2004;16:7183–97.
- [14] Loiko VA, Miskevich AA, Konkolovich AV. Order parameter of elongated liquid crystal droplets: the method of retrieval by the coherent transmittance data. *Phys Rev E* 2006;74 031704-1-031704-7.
- [15] Loiko VA, Konkolovich AV, Miskevich AA. Retrieval of order parameters of a monolayer of liquid-crystal droplets with weak anchoring. *JETP* 2007;105(4):846–55.
- [16] Mishchenko MI, Hovenier JW, Travis LD. *Light scattering by nonspherical particles*. Academic Press; 2000.
- [17] Markel VA. Introduction to the Maxwell Garnett approximation: tutorial. *JOSA A* 2016;33(7):1244–56.
- [18] Markel VA. Maxwell Garnett approximation (advanced topics): tutorial. *JOSA A* 2016;33(11):2237–55.
- [19] Bloisi F, Ruocchio C, Terrecuso P, Vicari L. Angular dependence of light transmittance in polymer dispersed liquid crystals. *Phys Rev E* 1996;54(5):5242–8.
- [20] Kelly JR, Palfy-Muhoray P. The optical response of polymer dispersed liquid crystals. *Mol Cryst Liq Cryst* 1994;243:11–29.
- [21] Shabanov A, Presnyakov V, Zyryanov V, Vetrov S. Bipolar nematic droplets with rigidly fixed poles in the electric field. *Mol Cryst Liq Cryst* 1998;321:245–258.
- [22] Kelly J, Seekel D. Dielectric losses in a polymer-dispersed liquid crystal film. 1257. *SPIE*; 1990. p. 17–28.
- [23] Wu B-G, Erdmann JH, Doane JW. Response times and voltages for PDLC light shutters. *Liq Cryst* 1989;5(5):1453–65.
- [24] Sameet KS, Fontecchjo AK. Improved electro-optic response of polymer dispersed liquid crystals doped with oxidized multiwalled carbon nanotubes. *Mol Cryst Liq Cryst* 2010;525:158–66.
- [25] Mănăilă-Maximean D, Circu V, Ganea P, Bărar A, Danila O, Stăicu T, et al. Polymer dispersed liquid crystal films doped with carbon nanotubes – preparation methods. *Proc SPIE* 2018;10977 1097702(1-10).



Synthesis and thermal, emission and dielectric properties of liquid crystalline Eu(III), Sm(III) and Tb(III) complexes based on mesogenic 4-pyridone ligands functionalized with cyanobiphenyl groups

Laura F. Chiriac^a, Paul C. Ganea^b, Doina Manaila Maximean^c, Iuliana Pasuk^b, Viorel Cîrcu^{a,*}

^a Department of Inorganic Chemistry, University of Bucharest, 23 Dumbrava Rosie St., Bucharest, Sector 2, 020484, Romania

^b National Institute of Materials Physics, P.O. Box MG-7, Magurele 077125, Romania

^c Physics Department, University "Politehnica" of Bucharest, Romania

ARTICLE INFO

Article history:

Received 26 April 2019

Received in revised form 9 June 2019

Accepted 12 June 2019

Available online 18 June 2019

ABSTRACT

New thermotropic lanthanidomesogens based on Eu(III), Sm(III) and Tb(III) with *N*-alkylated 4-pyridones mesogenic ligands, having two cyanobiphenyl groups attached via long alkoxy spacers, with 6, 9 and 10 carbons atoms in 3,5 - positions of a benzyl unit, have been designed and investigated. The liquid crystal behavior was assessed by differential scanning calorimetry, the mesophases being assigned by polarized light microscopy based on their characteristic textures and confirmed by variable temperature X-ray powder diffraction analysis. The three *N*-alkylated 4-pyridones nematic ligands reacted with lanthanide nitrates to yield new lanthanidomesogens with a stable and reproducible smectic A phase up to 125 °C. The emission spectra of the complexes have shown the characteristic emission of the lanthanide trivalent ions, over the entire temperature range of SmA phase up to isotropic state. The dielectric spectroscopy measurements performed in the temperature range of existence of the liquid crystal phase, both in the low frequency (LF) domain 0.01–10 MHz and in the high frequency (HF) range, 1 MHz–3 GHz, revealed three dipolar relaxation processes. The characteristic times have been obtained by fitting the spectra of the dielectric loss with a two component Havriliak-Negami function. The activation constant/energy was determined from the Vogel-Fülcher-Tammann law.

© 2019 Elsevier B.V. All rights reserved.

1. Introduction

Liquid crystalline materials (LC) based on d- or f-block metals have appealing electronic, magnetic and optical properties and the interest to design and investigate such materials has constantly increased in the recent years [1,2]. The first reports on the special class of metallomesogens based on lanthanide ions (lanthanidomesogens) are relatively recent, dating back to 1990s [3]. The studies began with the idea to design new mesogenic complexes with high coordination numbers (typical coordination numbers of lanthanides are eight or nine). On the other hand, lanthanidomesogens are regarded as a promising class of light-emitting liquid crystals due to their interesting photophysical properties which could be useful for the construction of emissive LC based devices. Thus, these materials can display narrow emission lines with high purity colors besides the possibility to tune the emission color, [4–10] as well as polarized emission [11–13] in the liquid crystal state. Since then, several classes of lanthanidomesogens have been designed and investigated. Most of these complexes are based on Schiff

bases, but other ligands have been intensively studied such as: β -diketonate, alkanoates, 5,5'-substituted 2,2'-bipyridines, bis (benzimidazolyl) pyridines, macrocyclic ligands (phthalocyanine, porphyrine, etc.) or acylpyrazolones. All these classes of lanthanidomesogens have been reviewed in the recent years. [14] Besides these well-known lanthanidomesogens types, a new class of thermotropic lanthanidomesogens bearing monodentate mesogenic ligands derived from 4-pyridone has been proposed by us recently [15,16]. Liquid crystals having a 4-pyridone core have been known since long time ago [17,18]. Moreover, these derivatives show excellent coordination properties to metals, in particular to lanthanides, [19–29] but so far, these O-donor ligands have not been employed in the design of metal complexes with liquid crystalline properties. We have shown previously that the liquid crystalline properties of the lanthanidomesogens with such ligands can be tuned, both lamellar (SmA) and long range hexagonal columnar phases (Col_h) can be obtained by grafting various mesogenic groups to the 4-pyridone coordinating fragment. [15,16] Importantly, the emission properties of the lanthanide ions were preserved over the whole thermal range of the liquid crystal phase. For instance, depending on the alkyl length spacer, the Eu(III) complexes show lamellar phases (SmA) in the case of mesogenic monodentate ligands possessing cyanobiphenyl groups attached to the 4-pyridone

* Corresponding author.

E-mail address: viorel.circu@chimie.unibuc.ro (V. Cîrcu).

unit via a flexible long alkyl spacer. For such compounds, it was found that the number of mesogenic group employed and spacer length have a great impact on the transition temperatures of the Eu(III) complexes. Moreover, when *N*-alkylated 4-pyridones derivatives with mesogenic 3,4,5-tris(alkyloxy)benzyl moieties (alkyl chains with variable number of carbon atoms, 6 to 16) were employed, their new thermotropic lanthanidomesogens containing the Eu(III), Sm(III) and Tb(III) ions exhibit either a lamellar (in the case of shorter chains analogues, six and eight carbon atoms) or hexagonal columnar enantiotropic mesophases (for complexes with higher number of carbon atoms - twelve, fourteen and sixteen), over a large temperature range, in some cases >200 °C. Therefore, there is a need to further investigate the structural aspects related to mesogenic properties and thermal stability of such materials based on lanthanide ions and 4-pyridone ligands.

In this paper we extend these studies to new thermotropic lanthanidomesogens based on Eu(III), Tb(III) and Sm(III) by using a very efficient concept in promoting LC phases for different bulky entities, e.g. to decouple the mesogenic groups and the coordination units via a long flexible alkyl chain [30,31].

Previous dielectric measurements on several lanthanidomesogens based on terbium, ytterbium and gadolinium metals, with 2,2'-bipyridyl derivatives and β -diketonates as ligands, have been reported by Dobrun et al. [32–34]. In these studies, the magnitude and sign of the dielectric anisotropies of these lanthanidomesogens have been determined. The dielectric spectroscopy is an important tool for investigating the relaxation processes resulted from the rotational fluctuations of the molecular dipoles. For the selected samples, the relaxation dipolar processes have been identified and correlated with the phase transitions detected by DSC.

2. Experimental

All the chemicals were from commercial sources and used as supplied (Sigma-Aldrich and Merck). TLC was performed on commercial coated aluminium plates with Silica Gel matrix with fluorescent indicator 254 nm (Sigma Aldrich), and the detection was done by an UV lamp. C, H, N analyses were carried out with an EuroEA 3300 instrument. The IR spectra were measured on a Bruker Tensor V-37 spectrophotometer either by using an ATR device or as KBr pellets in the range of 4000–400 cm^{-1} . ^1H and ^{13}C NMR spectra were recorded on a Bruker Fourier 300 or Bruker Avance III spectrometer operating at 300 and 500 MHz, respectively, using CDCl_3 as solvent. ^1H and ^{13}C chemical shifts were referenced to the solvent peak position (7.26 ppm ^1H , 77.00 ppm ^{13}C). The proposed structure for the 4-pyridone derivatives fully agrees with the experimental data.

2.1. Physical measurements

2.1.1. Dielectric spectroscopy measurements

The Dielectric Spectroscopy (DS) measurements were performed using a Broadband Dielectric Spectrometer, NOVOCONTROL, Technologies GmbH & KG, consisting of two equipment: Alpha-A High Performance Frequency Analyzer, with ZGS interface, in the low frequency (LF) domain 0.01–10 MHz and Agilent E4991A RF Impedance/Material Analyzer for the high frequency (HF) range, 1 MHz–3GHz, equipped with WinDETA software [35]. Alternative voltage is set to 0.5 V. The sample under test was sandwiched between gold-plated electrodes (10 mm) with a quartz spacer of 0.050 mm. The measurements have been performed in isothermal conditions, the temperature being controlled by the Quatro Cryosystem (Novocontrol) control system with stability better than 0.2 K. The temperature was decreased in steps, with a 3 K step, in a wide enough interval to cover the domain in which the liquid crystal passes from its crystalline state to the isotropic state. The temperature domains for the measurements performed using the LF equipment are: 314.15 K–389.15 K for compound **5a** and

333.15 K–414.15 K for compound **5b**. For the HF measurements, the temperature intervals are: 323.15 K–425.15 K for **5a** and 333.15 K–435.15 K for **5b**. The DS results are presented separately for the two samples **5a** and **5b** by following the same steps: a) the influence of temperature on permittivity as resulted from the measurements at LF and at HF; b) dielectric permittivity spectra, with a qualitative discussion of the HF spectra and a quantitative analysis of the LF ones, by fitting the data with a function two Havriliak-Negami (HN) components, from which results the phase transition and the dependence on characteristic times on temperature; c) applying the Vogel-Fülcher-Tammann (VFT) law to find the activation energies or constants.

2.1.2. Polarizing optical microscopy analysis (POM)

The samples were investigated using a Nikon 50iPol polarized optical microscope equipped with a Linkam THMS600 hot stage and TMS94 control processor. These observations were performed on untreated glass slides.

2.1.3. Differential scanning calorimetry (DSC)

The temperatures and the associated enthalpies of phase transitions were recorded by DSC by employing a Diamond DSC Perkin Elmer instrument. The materials were encapsulated in aluminium pans and investigated at a scanning rate of 10 °C/min. For each sample, two or more heating/cooling cycles were performed.

2.1.4. Thermogravimetric analysis (TG)

Thermogravimetric analysis of the lanthanide complexes was performed on a TA Q50 TGA instrument using alumina crucibles and nitrogen as purging gas. The heating rate was 10 °C/min and the temperature range used for measurements was from 25 °C to 550 °C.

2.1.5. Powder X-ray diffraction (XRD)

The powder X-ray diffraction measurements were performed on a D8 Advance diffractometer (Bruker AXS GmbH, Germany), in parallel beam setting, with monochromatized $\text{Cu-K}\alpha_1$ radiation ($\lambda = 1.5406 \text{ \AA}$), scintillation detector, and horizontal sample stage. The measurements were made in symmetric (θ - θ) geometry in the 2θ range from 1.5° to 10° or 30° in steps of 0.02°, with measuring times per step in the 5–40 s range. The temperature control of the samples during measurements was achieved by adapting a home-made heating stage to the sample stage of the diffractometer. The samples were heated with a rate of 10.0 °C/min to the corresponding temperature.

2.1.6. Emission spectroscopy measurements

Photoluminescence (PL) spectra have been recorded at room temperature in solid state or dichloromethane solutions. The samples were deposited on a glass slide for solid state measurements and the spectra were recorded with an OceanOptics QE65PRO spectrometer attached to the polarizing optical microscope and using a Nikon Intensilight excitation source or a LED light source (LLS-LED, OceanOptics, $\lambda = 365$ and 270 nm). The excitation and PL spectra in solid state for the three 4-pyridone derivatives were performed with the use of a Jasco FP-6300 spectrofluorometer (operating parameters: band width – 3 nm; data pitch - 1 nm; scanning speed –200 nm/min; spectrum accumulation – 3).

2.2. Synthesis of 4-pyridone ligands and their lanthanide complexes

2.2.1. Synthesis of **1a-c**

The **1a-c** precursors were obtained by the alkylation reaction between 3,5-dihydroxybenzyl alcohol (3.3 g, 9.217 mmol) and 4'-[(6-Bromohexyl)oxy]-4-biphenylcarbonitrile (for **1a**), 4'-[(9-Bromononyl)oxy]-4-biphenylcarbonitrile (for **1b**) or 4'-[(10-Bromodecyl)oxy]-4-biphenylcarbonitrile (for **1c**) in the presence of K_2CO_3 (1.52 g, 11.01 mmol) and molecular sieves (1 g) in 150 mL butanone. The reaction mixture was heated under reflux for 72 h under a nitrogen

methanol (9.5/5) as eluents. White products were obtained with yields in the 70–77% range.

3a: Anal. Calcd. For $C_{50}H_{49}N_3O_5$: C% 77.80, H% 6.40, N% 5.44. Found: C% 77.27, H% 6.33, N% 5.65. 1H NMR ($CDCl_3$, 500 MHz): 7.69–7.60 (m, 10H), 7.52 (d, 4H, $J = 8.8$ Hz), 6.98 (d, 2H, $J = 8.7$ Hz), 6.70 (d, 2H, $J = 6.8$ Hz) 6.43(s, 1H), 6.31(d br, 2H, $J = 1.9$ Hz), 5.01 (s, 2H), 4.02 (t, 4H, $J = 6.4$ Hz), 3.92 (t, 4H, $J = 6.4$ Hz), 1.85–1.79 (m, 8H), 1.54 (m, 8H). ^{13}C -RMN ($CDCl_3$, 125 MHz): 161.11, 159.72, 145.22, 141.19, 136.18, 132.59, 131.38, 128.36, 127.09, 119.11, 118.30, 115.08, 110.10, 106.15, 101.41, 68.09, 67.97, 60.92, 29.15, 25.87. IR (ATR, cm^{-1}): 2942, 2867, 2223, 1639, 1601, 1575, 1470, 1315, 1179, 822, 731.

3b: [15] Anal. Calcd. For $C_{56}H_{61}N_3O_5$: C% 78.57, H% 7.18, N% 4.91. Found: C% 78.28, H% 6.93, N% 4.41. 1H NMR ($CDCl_3$, 500 MHz): 7.69–7.62 (m, 8H), 7.56–7.50 (m, 6H), 6.98 (d, 4H, $J = 8.8$ Hz), 6.65 (d, 2H, $J = 6.6$ Hz), 6.42 (t br, 1H), 6.29 (d, 2H, $J = 2$ Hz), 4.97 (s, 2H), 4.00 (t, 4H, $J = 6.5$ Hz), 3.89 (t, 4H, $J = 6.5$ Hz), 1.83–1.73 (m, 8H), 1.49–1.36 (m, 20H). ^{13}C -RMN ($CDCl_3$, 125 MHz): 161.14, 159.78, 145.27, 140.95, 136.24, 132.58, 131.29, 128.34, 127.08, 119.13, 118.20, 115.09, 110.06, 106.05, 101.30, 68.19, 60.79, 29.30, 26.03. IR (ATR, cm^{-1}): 2933, 2858, 2223, 1639, 1601, 1558, 1472, 1315, 1179, 823, 729.

3c: Anal. Calcd. For $C_{58}H_{65}N_3O_5$: C% 78.79, H% 7.41, N% 4.75. Found: C% 78.47, H% 7.17, N% 5.06. 1H NMR ($CDCl_3$, 300 MHz): 7.69–7.61 (m, 8H), 7.51 (d, 4H, $J = 8.8$ Hz), 7.37 (d, 2H, $J = 7.6$ Hz), 6.97 (d, 4H, $J = 8.8$ Hz), 6.46–6.40 (m, 3H), 6.26 (d br, 2H), 4.85 (s, 2H), 4.00 (t, 4H, $J = 6.5$ Hz), 3.89 (t, 4H, $J = 6.5$ Hz), 1.84–1.70 (m, 8H), 1.45–1.33 (m, 22H). ^{13}C -RMN ($CDCl_3$, 75 MHz): 161.04, 159.75, 145.22, 140.21, 136.6, 132.52, 131.21, 128.28, 127.02, 119.08, 115.04, 109.97, 105.80, 101.07, 68.14, 60.27, 29.26, 25.98. IR (ATR, cm^{-1}): 2925, 2852, 2224, 1639, 1601, 1578, 1469, 1316, 1180, 821, 726.

2.2.4. Synthesis of lanthanide complexes, 4–6 a–c

A solution of the appropriate lanthanide nitrate (0.019 mmol) in ethanol (5 mL) was added dropwise over a solution of the corresponding 4-pyridone derivative (0.060 mmol) in hot ethanol (5 mL) and the resulting mixture was stirred at room temperature for 2 h. The complexes were precipitated out of the solution and isolated as white solids and purified by recrystallization from dichloromethane and diethyl ether. Finally, the complexes were filtered, washed with diethyl ether and dried in vacuo. The products were obtained in relatively good yields (60–66%).

4a: Anal. Calcd. for $EuC_{150}H_{147}N_{12}O_{24}$: C% 67.89, H% 5.58, N% 6.33. Found: C% 67.25, H% 5.30, N% 6.17. IR (ATR, cm^{-1}): 2939, 2865, 2224, 1636, 1602, 1538, 1466, 1396, 1294, 1178, 1031, 822, 737, 468.

4b: [15] Calcd. For $C_{174}H_{195}EuN_{12}O_{24}$: %C 69.88; %H 6.57; %N 5.62; Found: %C 69.72; %H 6.73; %N 5.43. IR (KBr disc, cm^{-1}): 2925, 2853, 2224, 1637, 1602, 1536, 1494, 1467, 1394, 1349, 1293, 1250, 1178, 1055, 1030, 854, 822, 660, 562, 533.

4c: Anal. Calcd. for $EuC_{174}H_{195}N_{12}O_{24}$: C% 69.88, H% 6.57, N% 5.62. Found: C% 69.41, H% 6.29, N% 5.48. IR (ATR, cm^{-1}): 2941, 2867, 2219, 1638, 1602, 1538, 1462, 1371, 1294, 1174, 1032, 821, 728, 467.

5a: Anal. Calcd. for $SmC_{150}H_{147}N_{12}O_{24}$: C% 7.93, H% 5.59, N% 6.34. Found: C% 67.41, H% 5.33, N% 6.20. IR (ATR, cm^{-1}): 2938, 2862, 2223, 1636, 1602, 1537, 1462, 1395, 1348, 1294, 1030, 1177, 821, 735, 468.

5b: Anal. Calcd. for $SmC_{168}H_{183}N_{12}O_{24}$: C% 69.47, H% 6.35, N% 5.79. Found: C% 69.25, H% 6.23, N% 5.54. IR (ATR, cm^{-1}): 2930, 2854, 2224, 1636, 1601, 1537, 1465, 1395, 1349, 1294, 1031, 1177, 821, 736, 468.

5c: Anal. Calcd. for $SmC_{174}H_{195}N_{12}O_{24}$: C% 69.92, H% 6.58, N% 5.62. Found: C% 69.25, H% 6.42, N% 5.51. IR (ATR, cm^{-1}): 2935, 2864, 2221, 1638, 1602, 1537, 1466, 1392, 1293, 1038, 1181, 824, 738, 462.

6a: Anal. Calcd. for $TbC_{150}H_{147}N_{12}O_{24}$: C% 67.71, H% 5.57, N% 6.32. Found: C% 67.27, H% 5.48, N% 6.17. IR (ATR, cm^{-1}): 2939, 2864, 2224, 1636, 1601, 1539, 1468, 1396, 1347, 1293, 1031, 1178, 822, 739, 468.

6b: Anal. Calcd. for $TbC_{168}H_{183}N_{12}O_{24}$: C% 69.26, H% 6.33, N% 5.77. Found: C% 68.94, H% 6.52, N% 5.86. IR (ATR, cm^{-1}): 2931, 2853, 2224, 1636, 1602, 1539, 1466, 1395, 1350, 1294, 1030, 1176, 820, 737, 467.

6c: Anal. Calcd. for $TbC_{174}H_{195}N_{12}O_{24}$: C% 69.72, H% 6.56, N% 5.61. Found: C% 69.65, H% 6.42, N% 5.22. IR (ATR, cm^{-1}): 2939, 2863, 2220, 1634, 1602, 1539, 1469, 1395, 1294, 1030, 1188, 821, 735, 461.

3. Results and discussion

3.1. Synthesis and characterization of ligands and complexes

The organic ligands **3a–c** having two cyanobiphenyl mesogenic groups connected via a spacer with variable number of carbon atoms were prepared through a similar procedure as previously described for such *N*-alkylated 4-pyridone derivatives [15,16]. First, the benzyl bromide derivatives **2a–c** were synthesized by alkylation of the 3,5-dihydroxy benzyl alcohol with 4'-(ω -bromoalkoxy)-4-cyanobiphenyl followed by the treatment with PBr_3 in dry dichloromethane. [36] In the following step, the reaction of 4-hydroxypyridine with the corresponding 3,5-di(substituted)benzyl bromide derivatives **2a–c** in a mixture of THF and water, in the presence of NaOH and tetrabutylammonium bromide (TBABr) as phase transfer catalyst, produced the corresponding 4-pyridone derivatives **3a–c** in good yields (Scheme 1). These organic products were fully characterized by several techniques: elemental analyses as well as by 1H -, ^{13}C NMR and IR spectroscopies and the proposed structures agreed with the experimental data. The methylene signal of the benzyl fragment was found around 4.5 ppm in the NMR spectra of the bromide derivatives **2a–c** and this signal is downfield shifted in the NMR spectra of the 4-pyridone compounds **3a–c**. In addition, in the NMR spectra of the 4-pyridone compounds two new broad doublets were found, one of the two overlapped with the proton signals of the cyanobiphenyl unit, at 6.70 ppm (for **3a**), 6.65 ppm (for **3b**) and 6.43 ppm (for **3c**) and which were assigned to the protons belonging to the pyridone ring.

The nitrate lanthanide (III) complexes were prepared easily by the reaction between the corresponding *N*-alkylated 4-pyridone compounds **3a–c** with the appropriate $M(NO_3)_3 \cdot xH_2O$ salt ($M = Eu(III)$, $Sm(III)$, $Tb(III)$, where $x = 5$ or 6) in hot ethanol (Scheme 1). The new complexes were isolated as white solids which precipitated out of the reaction mixture and were further purified by recrystallization from a mixture of dichloromethane/ethyl ether 1/1 v/v at -25 °C. The complexes **4–6 a–c** do not have crystallization or coordination water nor solvent molecules, as revealed by TG (Fig. 4) and elemental analyses, as similarly found for the related lanthanide complexes with 4-pyridone ligands. [15,16] These new complexes were obtained as nine-coordinate complexes with the lanthanide ion bound by the three monodentate 4-pyridone ligands and three κ^2 -nitrates [15]. The IR spectroscopy is a useful tool to assign the coordination of the 4-pyridone ligands to the lanthanide ions. The pyridine ring stretching vibrations can be seen at ~ 1639 and 1601 cm^{-1} in the IR spectra of uncoordinated 4-pyridone ligands, while the $\nu(C=O)$ was found in the 1578 – 1558 cm^{-1} region. The latter stretching vibration is shifted to lower wavenumbers in the IR spectra of the lanthanide complexes: at 1538 cm^{-1} (1536 cm^{-1} for **4b**) in the IR spectra of $Eu(III)$ complexes, at 1537 cm^{-1} in the IR spectra of $Sm(III)$ complexes and at 1539 cm^{-1} in the IR spectra of $Tb(III)$ complexes, thus confirming the involvement of the O atom in the coordination to the lanthanide ions. [37] Additionally, a clear new absorption band was seen around 1294 cm^{-1} in the IR spectra of the lanthanide complexes and this band was assigned to the coordinated NO_3^- ion in a bidentate fashion.

3.2. Liquid crystalline properties

The mesomorphic behavior of the 4-pyridone based ligands as well as their corresponding lanthanide complexes **4–6 a–c** were studied by a combination of DSC measurements and POM observations. The thermal parameters are summarised in Table 1.

Table 1

Thermal parameters (transition temperatures^b in °C and the related enthalpies^c in kJ mol⁻¹, given in parenthesis) of ligands and their lanthanide (III) complexes.

Compd.	Heating/cooling scans ^a
3a	1st: Cr ₁ 47 (19.8) Cr ₂ 85 (16.1) Cr ₃ 96 (10) Cr ₄ 109 (10.2) Cr ₅ 139 (39.4) Iso 88 (1.5) N 42 g 2nd: g 45 N 88 (2.0) Iso 87 (2.1) N 42 g
3b	1st: Cr ₁ 65 (2.6) Cr ₂ 102 (21.4) Cr ₃ 118 (49.6) Iso 79 (2.9) N 38 g 2nd: g 41 N 78 (3.9) Cr ₁ 81 (-26.7) Cr ₂ 115 (37.2) Iso 79 (3.2) N 39 g
3c	1st: Cr ₁ 53 (1.8) Cr ₂ 117 (66.7) Iso 80 (3.0) N 29 g 2nd: g 31 N 80 (4.2) Cr ₁ 82 (-18.7) Cr ₂ 111 (21.7) Iso 80 (3.6) N 29 g
4a	1st: Cr 57 (7.9) SmA 97 (6.87) Iso 96 (6.1) SmA 58 g 2nd: g 58 SmA 97 (7.1) Iso 96 (6.7) SmA 56 g
4b	1st: Cr 58 (39.8) SmA 127 (21) Iso 125 (19.6) SmA 50 g 2nd: g 50 SmA 127 (20.5) Iso 125 (19.9) SmA 48 g
4c	1st: Cr 75 (72.2) SmA 100 (15.2) Iso 98 (15.0) SmA 41 g 2nd: g 41 SmA 100 (15.0) Iso 98 (14.8) SmA 40 g ^d
5a	1st: Cr 59 (24.7) SmA 96 (5.0) Iso 94 (5.6) SmA 56 g 2nd: g 57 SmA 95 (6.2) Iso 93 (5.9) SmA 57 g
5b	1st: Cr 61 (39.5) SmA 128 (20.9) Iso 126 (20.0) SmA 47 g 2nd: g 49 SmA 128 (21.1) Iso 126 (20.4) SmA 43 g
5c	1st: Cr 54 (11.1) SmA 98 (6.1) Iso 97 (14.3) SmA 42 g 2nd: g 43 SmA 98 (17.0) Iso 97 (14.0) SmA 42 g
6a	1st: Cr 56 (19.4) SmA 95 (5.6) Iso 91 (5.1) SmA 57 g 2nd: g 59 SmA 95 (6.1) Iso 91 (5.8) SmA 55 g
6b	1st: Cr 57 (47.2) SmA 125 (20.7) Iso 123 (20.1) SmA 45 g 2nd: g 47 SmA 125 (20.7) Iso 123 (20.5) SmA 43 g
6c	1st: Cr 50 (41.7) SmA 96 (15.1) Iso 95 (5.5) SmA 43 g 2nd: g 44 SmA 97 (15.9) Iso 96 (15.8) SmA 42 g

^a g, N, SmA, Iso, Cr denote glass transition, nematic, smectic A, isotropic and crystalline phases, respectively.

^b The estimated error of the transition temperatures was $\pm 0.5^\circ$.

^c The estimated error of the enthalpy ΔH values was ± 0.5 kJ mol⁻¹.

^d Values taken from Ref. [15].

The type of the LC phases was established based on their optical texture and confirmed by X-ray powder diffraction. In the case of the ligands **3a–c**, the POM observations showed the typical schlieren texture characteristic of a fluid nematic phase (Fig. 1).

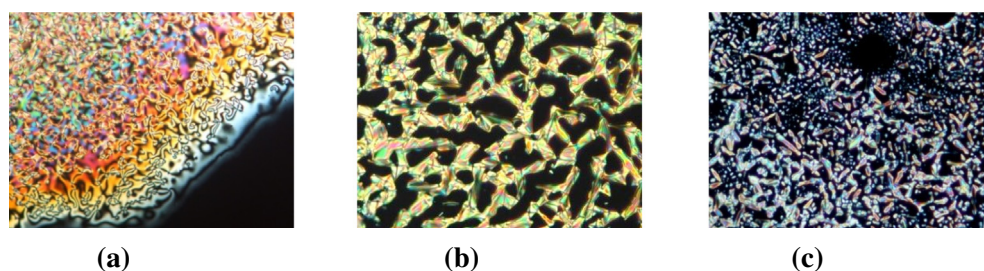


Fig. 1. POM picture for **3c** recorded at 75 °C (a) and for **4c** at 104 °C (b), and **5b** at 120 °C (c).

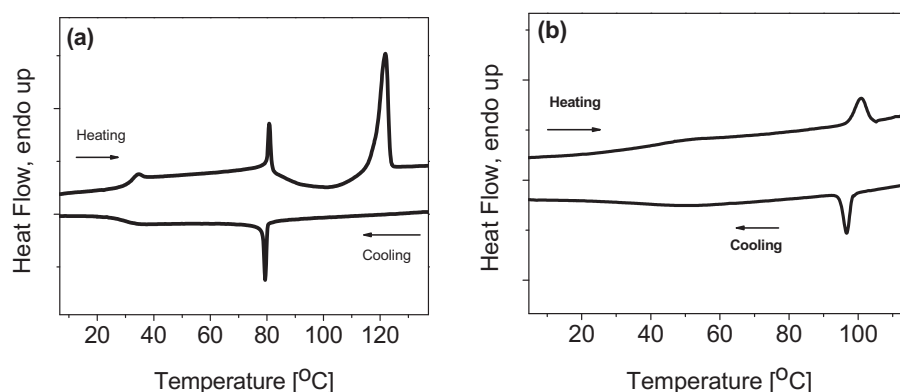


Fig. 2. Second DSC heating-cooling cycle for ligand **3c** (a) and its Sm(III) complex **5c** (b).

The nematic phase proved to be monotropic for all three ligands, as revealed by the DSC measurements, although for **3a** and **3b**, the texture was observed only after inducing birefringence by applying the pressure on the glass coverslips. The first heating run in the DSC recorded for **3a** shows a succession of several crystalline phases corresponding to both endothermic and exothermic processes, followed by the final transition assigned to crystalline state to isotropic liquid. Next, on cooling the material, two separate transitions were detected: isotropic to nematic (Iso–N) and the glass transition (N–g). The second heating-cooling cycles show the same two transitions either on heating or during the cooling run (Fig. S6, ESI). On the contrary, for the analogues with higher number of carbon atoms in the spacer, **3b** and **3c**, the glassy state is preserved on cooling the nematic phase, but a new transition assigned to a cold crystallization process occur at temperatures higher than the temperature of the N–Iso transition, during the heating runs (Fig. 2a).

The new lanthanidomesogens display similar mesogenic properties, no matter the lanthanide ion used. On heating these materials, the DSC trace recorded for the first run shows two thermal events assigned to the Cr–SmA and SmA–Iso transitions. For these samples, the LC phase was identified by POM observations as a smectic A (SmA) phase based on the typical focal conic fan shape texture developed on cooling the isotropic phase. Selected examples are shown in Fig. 1b and c.

The only exception is compound **5c** that exhibits multiple crystal-to-crystal transformations during the first heating run (Fig. S8, ESI). Further, the DSC of all complexes show during the cooling runs only two transitions and these were assigned to the glass transition at lower temperatures and the isotropization transition at higher temperatures, respectively. The glass transitions have been also confirmed by POM observations as no change of the textures has been evidenced at low temperatures. [5,7,14] These two transitions seen on the DSC curves are reproducible on the heating-cooling cycles, proving that these materials are stable in the thermal range used for their investigation. The glass transition and clearing temperatures of the three series of lanthanide complexes (Table 1, measured during the second heating run) do not show major modifications with the size of the lanthanide ion (Fig. 3) and these values are rather dependent on the number of carbon

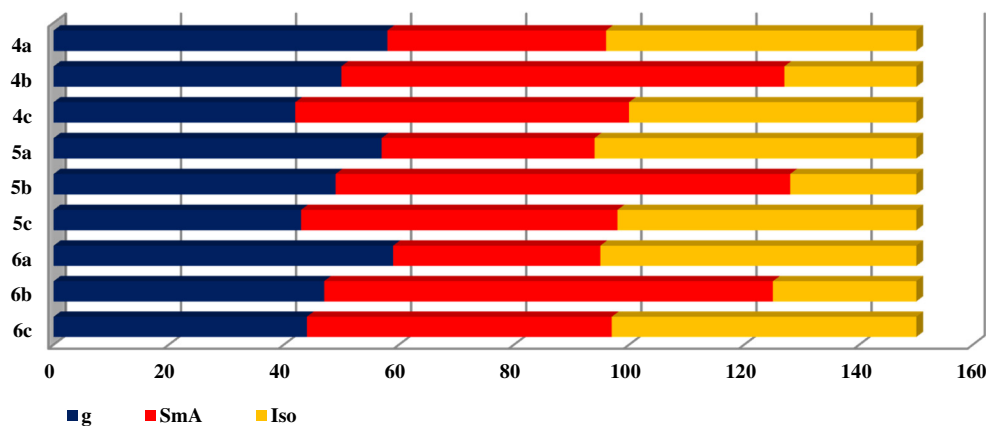


Fig. 3. Distribution of phase transitions for lanthanide complexes during the second heating run.

atoms contained by the aliphatic spacer. The lowest clearing temperature was seen for complexes **4-6a** having the 4-pyridone ligand with the shortest aliphatic spacer (six carbon atoms). Clearly, the highest isotropization temperatures and consequently the highest thermal stability of the LC phases were seen for complexes **4-6b** bearing aliphatic spacers with nine carbon atoms. It could be brought into discussion the parity of the number of carbon atoms contained by the aliphatic spacer to explain the higher transition temperatures for analogues with nine carbon atoms (**4-6b**) by comparison with the analogues having ten carbon atoms (**4-6c**). But the lack of additional data and the evidence of such an odd-even trend for an extended series of analogues, e.g. thermal behaviour of complexes with lower and higher number of carbon atoms – 8, 11 or 12, makes this assumption not fully reliable.

In the following step we have tested the thermal stability in the 25 °C–550 °C temperature range. The lanthanide complexes were heated with a rate of 10 °C/min under nitrogen atmosphere. There is no weight loss in the 25–250 °C temperature range, meaning that there are neither coordinated water molecules to the lanthanide ions nor any other solvent molecules in the lattice. The decomposition starts around 290 °C for Eu(III) complexes and around 300 °C for Sm(III) and Tb(III) complexes (Fig. 4) confirming that, in fact, these products are very stable on heating at temperatures up to about 300 °C and, importantly, in the temperature range of existence of the liquid crystalline phase.

Powder X-ray diffraction experiments at different temperatures corresponding to the thermal range of the mesophases were performed in order to confirm the assignment of nematic and smectic A phases by POM observations (Table 2). The XRD diffraction patterns of the ligands **3a–c**, recorded at temperatures in the temperature ranges of existence of the LC phase, show a very weak peak around $2\theta \approx 5^\circ$, and an

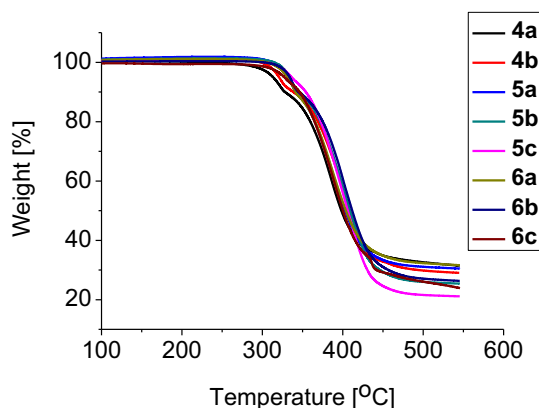


Fig. 4. The TG curves for Eu (III) and Tb (III) complexes.

additional broad peak around 20–22°, which is a typical feature for the nematic phases.

On the other hand, the X-ray diffraction pattern recorded for selected lanthanide complexes (**4a,b**, **5a,b** and **6a,b**) both on heating and on cooling the compounds near the transition temperatures, $T_{\text{SmA-Iso}}$ and $T_{\text{Iso-SmA}}$ respectively, show two small-angle reflections in the 1:2 ratios, characteristic of a lamellar organization. These two peaks were assigned to d_{001} and d_{002} , which are indexed as the reflections of a smectic A phase (Fig. 5). The additional broad peak found around 4.1–4.4 Å confirmed the fluid like nature of the LC phase, being assigned to the molten aliphatic chains. Moreover, the interplanar distances calculated by using the position of d_{001} were found to be very weakly temperature-dependent and thus, confirming the assignment of a SmA phase. Interestingly, the intensity of the d_{002} peak is higher or equal to that of the d_{001} peak in the XRD patterns for the two complexes having the spacer with nine carbon atoms **4b** and **5b** (Fig. 5c) which is an indication that the main repeat distance in the smectic phase is the half molecular length instead of the molecular length [38,39].

3.3. Emission properties

All complexes show appreciable luminescence both at room temperature in solid state and at higher temperature in the LC state. The emission spectra of the lanthanide complexes are presented in Fig. 6.

Table 2
X-ray powder diffraction data for lanthanide complexes.

Compound	Mesophase	T(°C)	Indexation	d-Spacing obs. (Å)	d-Spacing calc (Å)	
4a	SmA	95	001	37.40	37.40	
			002	19.03	18.70	
			85	001	37.72	37.72
				002	18.79	18.86
4b	SmA	115	001	41.64	41.64	
			002	20.63	20.82	
			105	001	42.03	42.03
				002	20.82	21.01
5a	SmA	90	001	36.48	36.48	
			001	36.18	36.18	
5b	SmA	120	001	40.49	40.49	
			002	20.72	20.25	
			105	001	40.87	40.87
				002	20.63	20.44
			100	001	41.64	41.64
				002	20.72	20.82
6a	SmA	90	001	35.03	35.03	
			002	17.76	17.52	
6b	SmA	95	001	41.25	41.25	
			002	20.53	20.62	

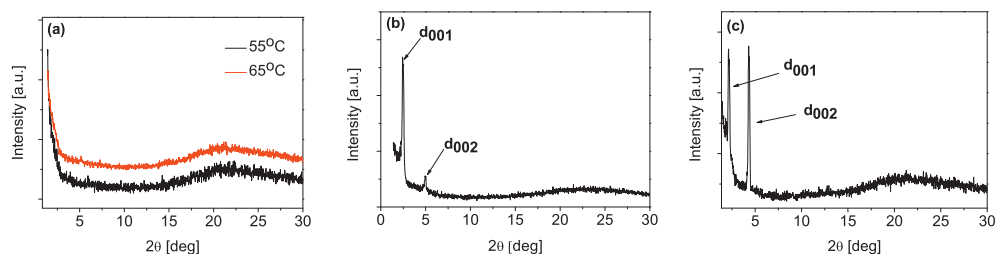


Fig. 5. XRD patterns recorded on cooling from the isotropic state for **3a** (a), complex **5a** at 90 °C (b) and for **5b** at 95 °C (c).

The measured luminescence spectra for all complexes show a strong emission band in the 375–410 nm range assigned to the 4-pyridone ligands. Additionally, the emission spectra of Eu(III) complexes display characteristic sharp peaks in the 530–720 nm region associated with the $^5D_0 \rightarrow ^7F_J$ ($J = 0 \div 4$) transitions of the Eu(III) ion (Fig. 6a) [40]. The emission spectra of Tb(III) complexes show a series of a well-defined peaks in the 550–720 nm range, assigned to the $^5D_4 \rightarrow ^7F_J$ ($J = 6 \div 3$) transitions of the lanthanide ion (Fig. 6b). The highest intensity of the emission was seen for Eu(III) complexes **4a–c**, and the emission is preserved throughout the entire temperature range of existence of the LC phase, up to the isotropic phase (Figs. 7 and 8). On the contrary, the emission spectra of the Sm(III) and Tb(III) complexes with all three 4-pyridone ligands are dominated by the emission band of the pyridine ligands (Fig. 9 and Fig. S19, ESI) and thus, the output color is rather light blue (Fig. 7d and f) than the normal emission color characteristic of these two lanthanide ions (red orange for Sm(III) [41,42] and green for Tb(III) [43]). The thermal stability of photoluminescence of the Eu(III) complexes in the LC phase was studied by measuring the temperature dependence of the emission intensity between room temperature and the clearing temperature. One example of variable-temperature luminescence spectra is shown in Fig. 8. For compound **4c**, the emission was recorded during heating the sample from 25 to 135 °C and cooling back from the isotropic state to the glassy state at room temperature. There is a significant decrease of the emission intensity with the

increasing of the molecular disorder produced by higher temperature. On cooling from the isotropic state, the reverse process takes place (Fig. 8b), and thus the emission intensity is higher with the molecular reordering in the mesophase and in the glassy state when the temperature reached the room temperature.

3.4. Dielectric spectroscopy measurements

Since the molecular dipoles are linked to some characteristic parts of the molecules or to the molecule as a whole, information about the dynamics of the assembly of molecules can be obtained from the analysis of the dielectric function $\epsilon^* = \epsilon'(\omega) - i\epsilon''(\omega)$. The characteristics of the relaxation processes can be determined from the frequency and temperature dependence of the real part of the dielectric permittivity complex function (named dielectric constant), or from its imaginary part (named dielectric loss).

For molecules with low molecular mass the dipole moment can be represented by a vector. The situation is different for the high molecular mass molecules. The total dipole moment of molecules with complex and extended structure, as it is the case for these liquid crystals, includes dipole moments of the structural units constituting the molecule and producing polarization by reorienting the molecule as a whole or by reorienting some of its parts.

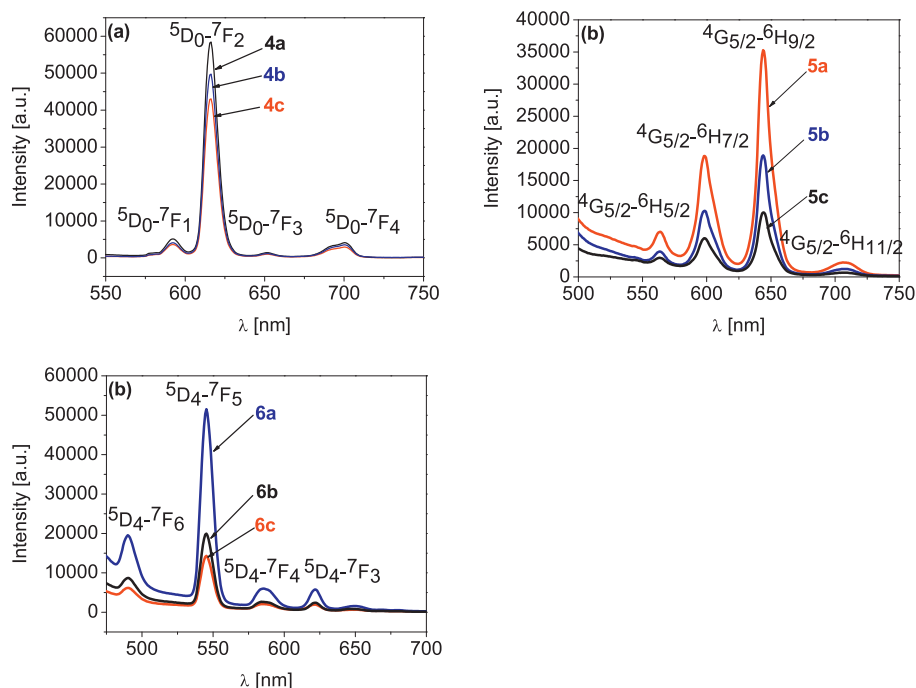


Fig. 6. The emission spectra for Eu(III) (a) Sm(III) (b) and Tb(III) complexes (c) recorded on solid state at room temperature.

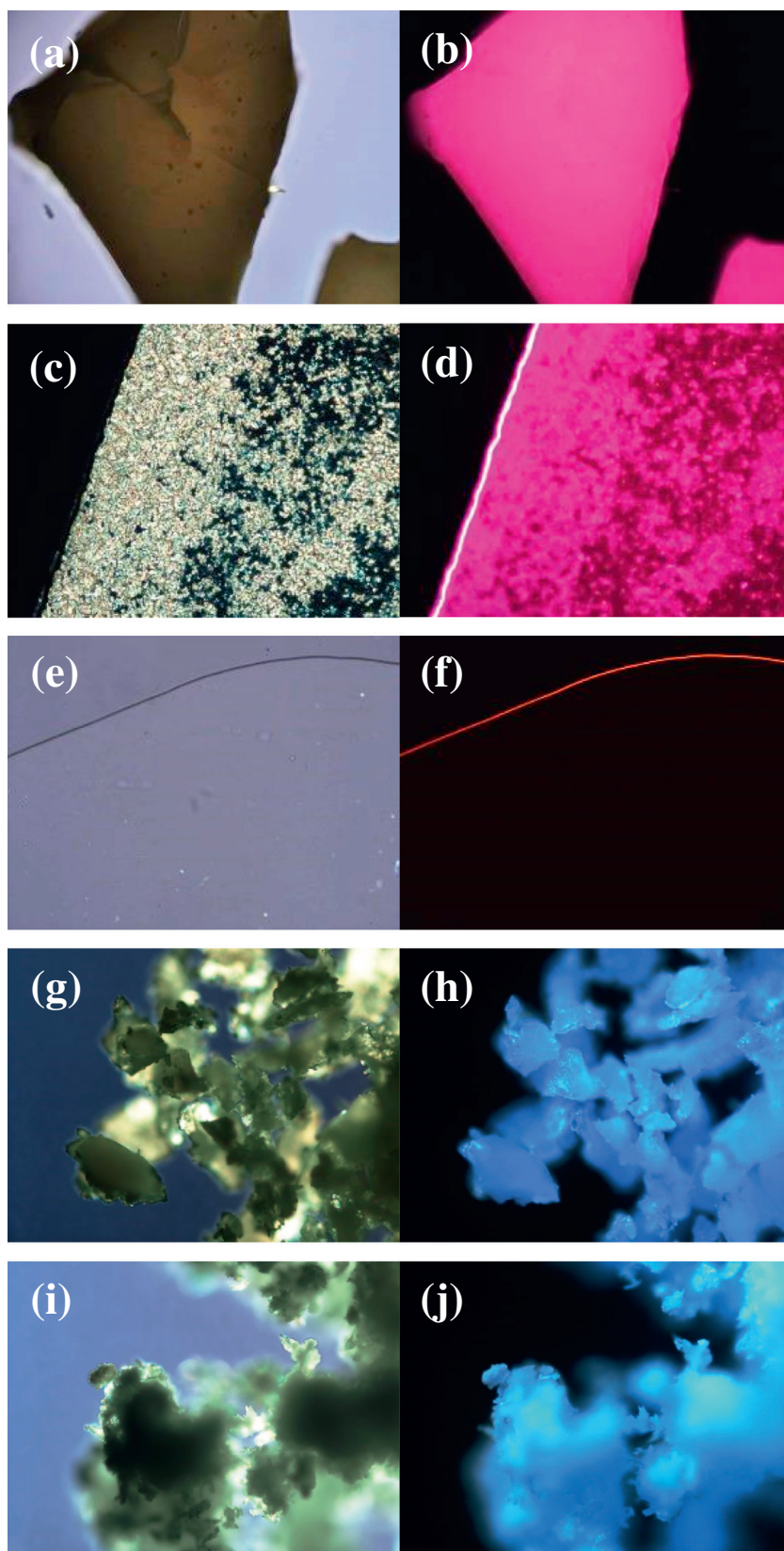


Fig. 7. Pictures of compound **4a**: solid state at room temperature in normal (a) and UV light (b); SmA phase at 85 °C in normal (c) and UV light (d); isotropic liquid at 135 °C in normal (e) and UV light (f). Pictures of compound **5a**: solid state at room temperature in normal (g) and UV light (h) and of compound **6a** in normal (i) and UV light (j).

The dipole moment per unit volume is obtained by summing over all types of dipole moments of the structural units in a molecule and over all the molecules in the unit volume.

The fluctuations of the net dipole moment are determined by the different molecular movement processes. The fluctuations due to some short parts of the molecule, to the local movement of some chain

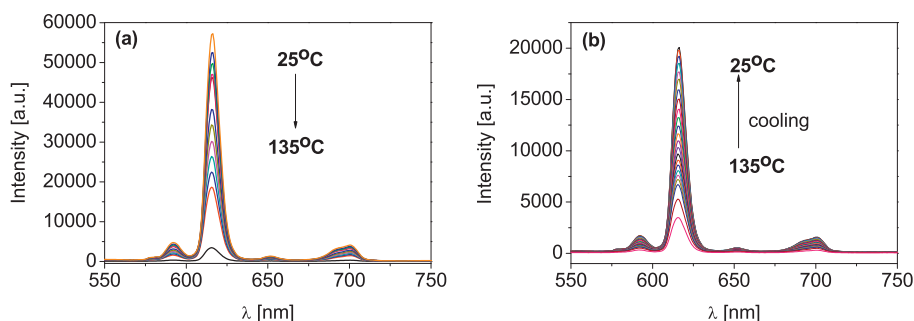


Fig. 8. Variable temperature emission spectra for **4c** recorded on heating in the 25 °C–135 °C range (a) and on cooling from the isotropic state (b).

segments or to side-groups (γ relaxation) are significant at relatively high frequencies. At relatively low frequencies the fluctuations of the dipole moment of the molecule as a whole are dominant, and these are associated to the Brownian motion of the molecules. This process is directly linked to the viscoelastic properties of the material. The relaxation behavior at the lowest frequencies is caused by the rotational fluctuations of the molecules around the short axis (α relaxation). Other relaxation modes, caused by the tumbling of the molecules around the long axis (tumbling mode, β relaxation), have approximately the same relaxation speed and form large relaxation processes, observed at relatively higher frequencies as compared to the α type relaxation.

The majority of dielectric spectroscopy studies present the molecular relaxation as several maxima of dielectric losses (ϵ''), in a $\log(\epsilon'')$ versus $\log(\omega)$ representation or in a ϵ'' versus $\log(\omega)$ one. Thus, the peaks observed in the representation of ϵ'' for non-conducting materials are typically assigned to the reorientation of dipoles. The dipolar relaxation time, which is numerically equal to the inverse of the angular speed for which ϵ'' has a relative maximum $\tau_{max} = 1/\omega_{max}$, $\epsilon''(\omega_{max}) = max$, is a relevant feature of these dielectric studies.

Alternatively other representations may be used: a) the tangent of the loss angle (also named dissipation factor), which is equal to the ratio between the imaginary and real part of the permittivity, $\tan(\delta) = \epsilon''(\omega)/\epsilon'(\omega)$, versus frequency; this representation shows the advantage that the value of the tangent does not depend on the geometric dimensions of the sample and in some situations the maximum of the same dipolar relaxation process appears at higher frequencies than the one obtained from the $\epsilon''(\omega)$; b) the Cole–Cole representation, presenting the imaginary part of the permittivity versus its real part $\epsilon'' = \epsilon''(\epsilon')$; in this representation the relaxation processes are semicircles, more or less flat; the semicircles might be incomplete and more or less overlapped; the number of circles indicate the number of dipolar relaxation processes.

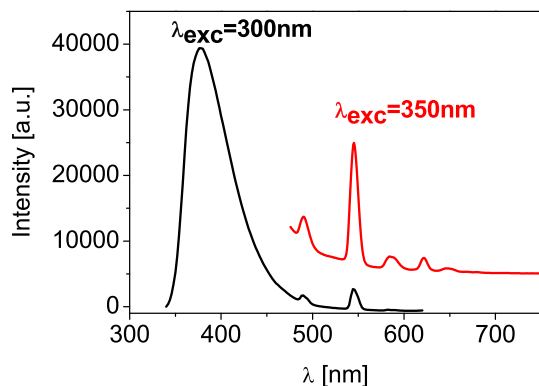


Fig. 9. The solid state emission spectrum of **6a** recorded with two different excitation wavelengths: 300 nm (black) and 350 nm (red).

Usually, the dielectric relaxation processes are analyzed using some model functions. The Debye function for the frequency dependence of the dielectric permittivity is: [44].

$$\epsilon^*(\omega) = \epsilon'(\omega) - i\epsilon''(\omega) = \epsilon_\infty + \frac{\Delta\epsilon}{1 + i\omega\tau_D} \quad (1)$$

where $\Delta\epsilon = \epsilon_S - \epsilon_\infty$ is the dielectric strength,

$$\begin{aligned} \epsilon_S &= \lim_{\omega \rightarrow 0} \epsilon'(\omega) \\ \epsilon_\infty &= \lim_{\omega \rightarrow \infty} \epsilon'(\omega) \end{aligned} \quad (2)$$

and τ_D , is the characteristic time, or the Debye relaxation time, obtained from the frequency corresponding to the maximum dielectric loss:

$$\epsilon''(\omega_p) = \epsilon''_{max}, \omega_p = 2\pi f_p = 1/\tau_D \quad (3)$$

Starting from the theoretical Debye function other relations have been proposed, both in frequency and time domains, in order to represent the experimental spectra.

The dielectric functions measured in the frequency domain are much more extensive than the Debye function. Furthermore, in some cases the dipolar function is asymmetric. For these reasons empiric model functions representing a generalization of the Debye function for the dipolar relaxation are used. The most flexible is the Havriliak–Negami (HN) [45,46] function which is currently employed for the study of the real processes of dielectric relaxation:

$$\epsilon_{HN}^*(\omega) = \epsilon_{r,\infty} + (\epsilon_{r,0} - \epsilon_{r,\infty}) / [1 + (i\omega \cdot \tau_{max})^a]^b \quad (4)$$

$0 < a < 1; 0 < b < 1$

where, $\epsilon_{r,0}$ is the low frequency permittivity (when $\omega \rightarrow 0$) and $\epsilon_{r,\infty}$ is the permittivity in the high frequency limit, $\omega \rightarrow \infty$, τ_{max} is the characteristic relaxation time of the medium.

The shape parameters, a and b , influence the widening and the asymmetry of the relaxation curve, around the loss maximum point. The relaxation characteristic times are obtained by fitting the experimental spectra to the HN functions.

As resulting from the experimental data, the relaxation time changes with temperature. A functional relationship should be considered due to the temperature dependence of the relaxation time. The encountered variations may fall into one of the following situations:

1) The Arrhenius law [44], describes an individual mechanism of escalating a potential barrier:

$$\tau_{max}(T) = \tau_\infty \exp(E_A/k_B T) \quad (5)$$

where E_A is the activation energy, τ_∞ pre-exponential factor, is the time-scale at which the dipole attempts to orient itself, k_B Boltzmann's

constant, T – current temperature. By applying the logarithm it is obtained:

$$\ln(\tau_{\max}(x)) = \ln(\tau_{\infty}) + E_{AX}/k_B, x = 1/T \quad (6)$$

2) The empiric Vogel-Fulcher-Tammann (VFT) law [47–50]:

$$\tau_{\max} = \tau_{\infty} \exp[A/k_B(T-T_V)] \quad (7)$$

where A , τ_{∞} and T_V are fitting parameters having the following meanings: A , a material constant, is a quantity related with the activation barrier and T_V is the Vogel temperature, the pre-exponential factor, τ_{∞} , is equal to the relaxation time for high temperatures. By applying the logarithm, a more convenient form for the fitting parameters is obtained:

$$\ln(\tau_{\max}(x)) = \ln(\tau_{\infty}) + A \cdot x/k_B(1-T_Vx) \quad (8)$$

$$x = 1/T$$

It is considered that the temperature dependence obtained according to the VFT approach is due to some collective effects, firstly discussed by Adam and Gibbs [51]. Importantly, at the phase transition the dielectric behaviour will change and consequently the transition temperatures can be obtained from the DS measurements and correlated with the temperatures deduced by other techniques (DSC and POM).

Two samples **5a** and **5b** have been selected as representative examples to be the subject of the dielectric investigations. As it will be shown in the following analysis, if the spectra are separately analyzed on the two frequency domains, low frequency (LF) domain, 0.01–10 MHz,

and high frequency (HF) range, 1 MHz–3GHz, apparently four dipolar relaxations (DR) are present: two in the LF range and two in the HF domain. However, when joining together the two frequency domains, one observes that actually only three distinct DR processes exist, that will be designated as follows: $DR-\alpha$, $DR-\beta$ si $DR-\gamma$.

Measurements of the complex permittivity, represented as the experimental dependencies $\log(\epsilon') = J_1(T)$ and $\log(\epsilon'') = J_2(T)$ at LF-range and at HF-range respectively, are shown in Fig. 10. It is interesting to observe the behavior of the two curves in the 340 K to 380 K temperature interval for compound **5a**. A clear change of the variation rate can be seen on going from low temperatures to high temperatures corresponding to LF range (Fig. 10a). This continuous change takes place around 365 K (92 °C), a temperature which is closely related to the one found by DSC for the isotropization transition (91 °C). These findings are confirmed as well by the HF results, presented in Fig. 10b.

A discontinuity and different variation rates of the values of the permittivity components (ϵ' and ϵ'') under and above the temperature $T \approx 400$ K have been observed in both plots (at HF and LF) corresponding to **5b** (Fig. 10c and d). In fact, the temperature $T \approx 400$ K (127 °C) is very close to the SmA-Iso phase transition temperature recorded by DSC (123 °C) (Table 1). The dielectric loss spectra and the fitting function with two HN components in the HF range, at two different temperatures, below and above the phase transition temperature $T = 400$ K for complex **5b** are shown in Fig. 11. Thus, in the HF range, two dipolar relaxation (DR) processes have been identified, namely $DR-\beta$ and $DR-\gamma$, based on the shape of the curves. The same behavior was seen for the complex **5a**; two processes of dielectric relaxation were observed by

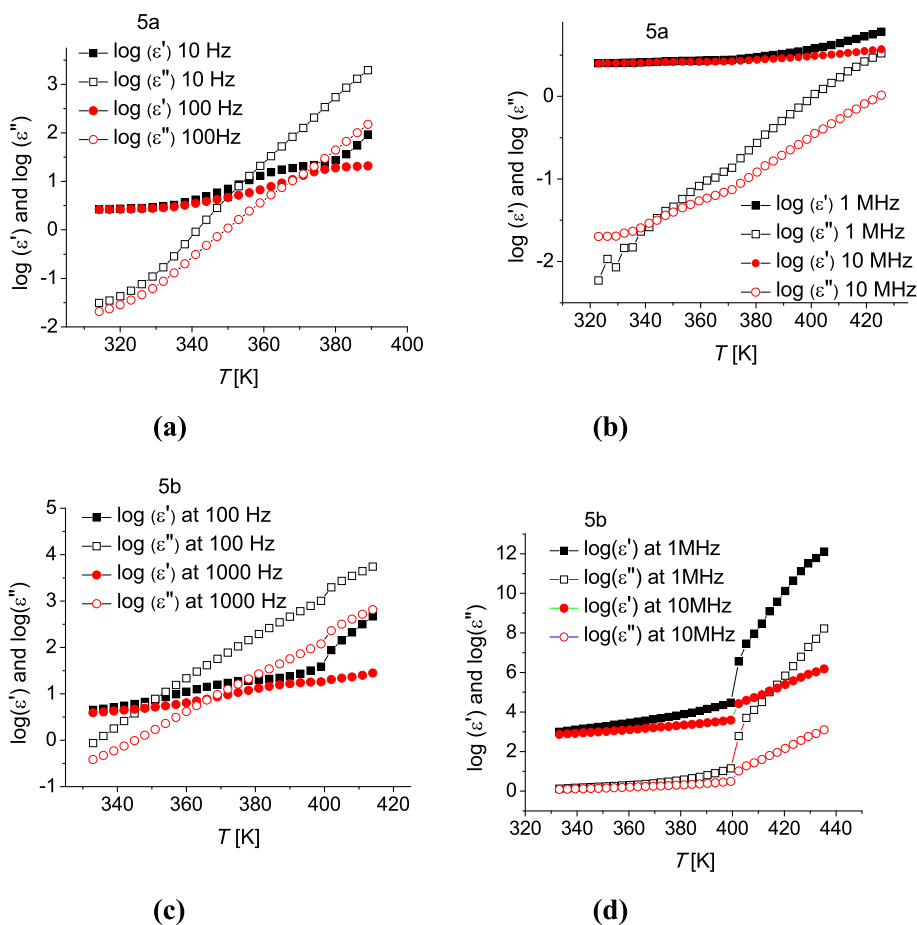


Fig. 10. Temperature dependence of the complex dielectric constant: real part and imaginary part of sample **5a** in the LF range (a) and HF range (b) and of sample **5b** in the LF range (c) and HF range (d).

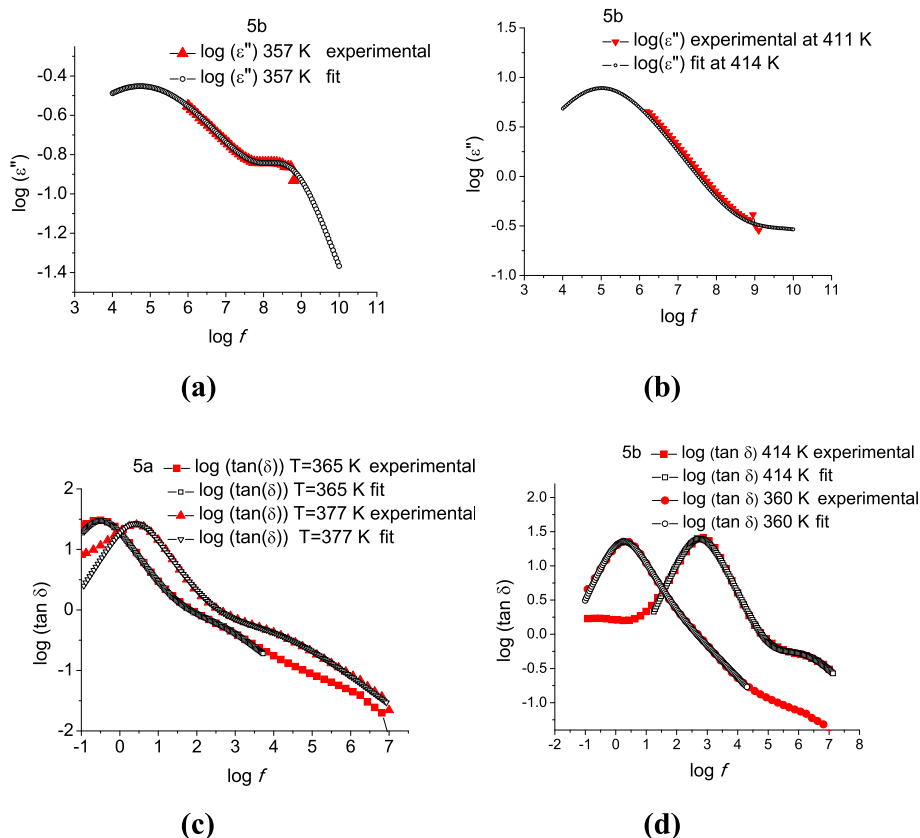


Fig. 11. Dielectric loss versus frequency, double logarithmic scales, experimental results and fitting for **5b** at two distinct temperatures at HF: 357 K (a) and 414 K (b); loss tangent, $\tan\delta$, versus logarithm of frequency at two distinct temperatures: 365 K and 377 K (at LF) for **5a** (c) and at 360 K and 414 K (at LF) for **5b** (d).

plotting the complex dielectric constant versus logarithm of frequency at two distinct temperatures: 362 K and 383 K, (Fig. S20 and S21, ESI) and these were assigned to $DR-\beta$ and $DR-\gamma$ relaxation processes. Only the descending branch of the $DR-\beta$ and the ascending branch of the $DR-\gamma$ are visible in the frequency domain, as shown in Fig. 11 for **5b**. For this reason the location of the maximum and the calculation of the characteristic times using the fitting function is affected by important errors. The results of the HF spectra analysis are not discussed here because the fitting parameters do not have “trust” values.

On the other hand, the experimental results obtained at LF –range are analyzed using a suitable representation for highlighting the relaxation processes: the dielectric loss tangent $\tan\delta$, versus frequency, at two temperatures in the vicinity of the phase transition temperature is shown in Fig. 11c and d, while the Cole-Cole representation, $\epsilon'' = \epsilon''(\epsilon')$

(ϵ'), at the same temperatures, $T = 365$ K for **5a** and $T = 360$ K for **5b** are presented in Fig. 12. The Cole-Cole plots, $\epsilon'' = \epsilon''(\epsilon')$, at different temperatures, $T = 377$ K for **5a** and $T = 414$ K for **5b** are given in Fig. S22, ESI. The intensity of the processes differs significantly and for this reason the double logarithmic scale representation was chosen in Figs. 11 and 12. For both samples, in the LF range, two dominant DR processes were observed: $DR-\alpha$ and $DR-\beta$, one at lower frequency ($DR-\alpha$) and another at medium frequencies ($DR-\beta$). These two relaxation processes are more or less superimposed and their relative position is temperature dependent.

Interestingly, by comparing the two samples, a better separation of the two relaxation processes was seen for **5b** (Fig. 12). Characteristic relaxation times at LF versus inverse of temperature for the two samples are shown in Fig. 13, while the values of the activation energies and/or

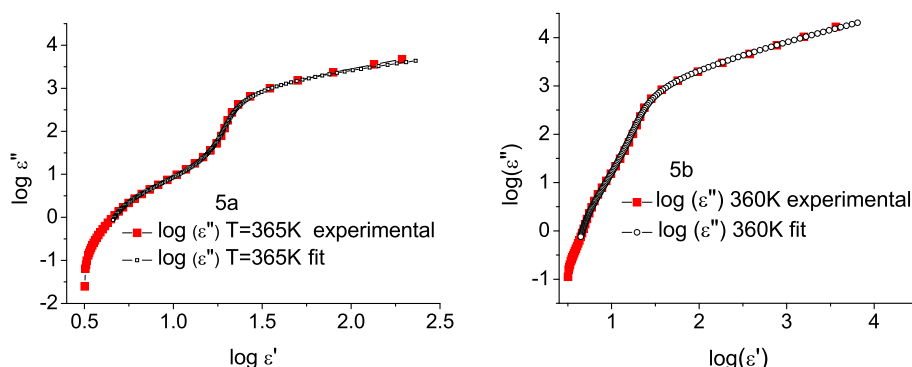


Fig. 12. Cole-Cole plot $\epsilon'' = \epsilon''(\epsilon')$, at $T = 365$ K for **5a** (a) and at $T = 360$ K for **5b** (b).

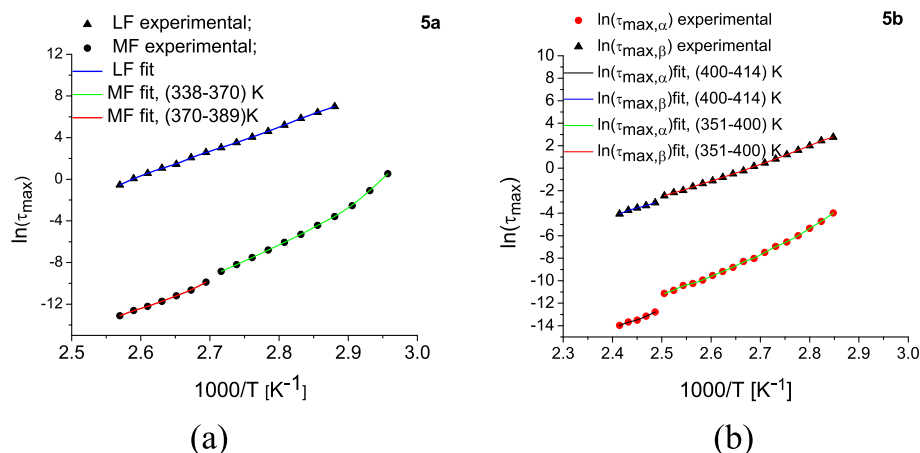


Fig. 13. Plot of the temperature dependence of the relaxation times for samples 5a (a) and 5b (b), experimental and fitted with Eq. (8) - the continuous curves. The values of the activation energies are given in Table 3.

activation constants are presented in Table 3. Their intensities are different by 2–3 orders of magnitude. The presence of the phase transition is hardly perceivable for 5a (Fig. 13a).

The small deviations, given at different temperatures, are due to the fitting process. The same behavior was observed for the temperature dependence of the complex dielectric constant in the LF and HF domains for 5a (Fig. 10a and b). It turns that the DR- α process obeys the Arrhenius law while the DR- β follows the VFT law. On the contrary, in the case of compound 5b, the two curves shown in Fig. 13b have a discontinuity around the same temperature, $T = 400$ K, which corresponds to the SmA-Iso transition. The branches corresponding to high temperatures (the left part of the curves) are in good agreement with the Arrhenius law, and the branches from low temperatures (the right side of the curves) have a variation according to the VFT law.

4. Conclusions

In this study we obtained a new series of lanthanidomesogens using 4-pyridone derivatives as ligands having two cyanobiphenyl units as the mesogenic group attached to the coordinating unit by flexible methylene spacer, with different number of carbon atoms: 6, 9 or 10. For the synthesis of lanthanide complexes, three lanthanide ions were used: Eu(III), Sm(III) and Tb(III). The mesomorphic behavior was investigated by a combination of differential scanning calorimetry and polarized light microscopy. While the ligands display a nematic phase, the corresponding lanthanide complexes show a stable smectic A phase. The repetitive heating-cooling cycles have highlighted the reproducibility of the mesophases both on heating and cooling for all compounds, ligands and complexes. The X-ray powder diffraction experiments confirmed the assignments of the SmA mesophase based on their characteristic texture by POM. All complexes show luminescence properties in solid state at room temperature and the luminescent

spectra displays well-defined peaks characteristic to the Eu(III), Sm(III) and Tb(III) ions and an additional emission band of the coordinated ligand. The dielectric relaxation spectroscopy analysis of each sample investigated shows three dipolar relaxation processes. The characteristic times have been obtained by fitting the spectra of the dielectric loss with a two component Havriliak-Negami function. The activation constant/energy was determined from the Vogel-Fülcher-Tammann (VFT) representation. The DS data show an evident phase transition for 5a and 5b when the phase transition temperatures obtained from the DSC are correlated to the ones found in the DS measurements.

Acknowledgements

PCG and IP thank the Romanian Ministry of Education and Research for financial support under Core Program, Project 21N/2019.

Appendix A. Supplementary data

Supplementary data to this article can be found online at <https://doi.org/10.1016/j.molliq.2019.111184>.

References

- [1] B. Donnio, D. Guillon, R. Deschenaux, D.W. Bruce, in: J.A. McCleverty, T.J. Meyer (Eds.), *Comprehensive Coordination Chemistry II*, vol. 7, Elsevier, Oxford 2003, p. 357, (Chap. 7.9).
- [2] J. Torroba and D.W. Bruce in *Comprehensive Inorganic Chemistry II* (Second Edition): From Elements to Applications. 2nd ed. Elsevier Ltd, 2013, Vol. 8, p. 837–917.
- [3] K. Binnemans, C. GÖrller-Walrand, *Chem. Rev.* 102 (2002) 2303.
- [4] J.-C.G. Bünzli, *Acc. Chem. Res.* 39 (2006) 53.
- [5] J.-C.G. Bünzli, C. Piguet, B. Donnio, D. Guillon, *Chem. Commun.* (2006) 3755.
- [6] Y. Yang, K. Driesen, P. Nockemann, K. Van Hecke, L. Van Meervelt, K. Binnemans, *Chem. Mater.* 18 (2006) 3698.
- [7] S. Guerra, T. Dutronc, E. Terazzi, K.-L. Buchwalder, L. Guénee, R. Deschenaux, S.V. Eliseeva, S. Petoud, C. Piguet, *Coord. Chem. Rev.* 340 (2017) 79.
- [8] H.A.R. Pramanik, G. Das, C.R. Bhattacharjee, P.C. Paul, P. Mondal, S.K. Prasad, D.S. Rao, *Chem. Eur. J.* 19 (2013) 13151.
- [9] I. Sánchez, C. Cuerva, G. Marcelo, E. Oliveira, H.M. Santos, J.A. Campo, C. Lodeiro, M. Cano, *Dyes Pigments* 159 (2018) 395.
- [10] E. Guillet, D. Imbert, R. Scopelliti, J.-C.G. Bünzli, *Chem. Mater.* 16 (2004) 4063.
- [11] A.A. Knyazev, A.S. Krupin, B. Heinrich, B. Donnio, Y.G. Galyametdinov, *Dyes Pigments* 148 (2018) 492.
- [12] Y.G. Galyametdinov, A.A. Knyazev, V.I. Dzhabarov, T. Cardinaels, Kr. Driesen, C. GÖrller-Walrand, K. Binnemans, *Adv. Mater.* 20 (2008) 252.
- [13] A.A. Knyazev, E.Yu. Molostova, A.S. Krupin, B. Heinrich, B. Donnio, W. Haase, Y.G. Galyametdinov, *Liq. Cryst.* 40 (2013) 857.
- [14] K. Binnemans, *Lanthanidomesogens*, in: J.-C.G. Bünzli, V.K. Pecharsky (Eds.), *Handbook on the Physics and Chemistry of Rare Earths*, vol. 43, Elsevier 2013, pp. 1–154.
- [15] A. Pană, F.L. Chiriac, M. Secu, I. Pasuk, M. Ferbinteanu, M. Micutz, V. Cîrcu, *Dalton Trans.* 44 (2015), 14196.
- [16] L.F. Chiriac, I. Pasuk, M. Secu, M. Micutz, V. Cîrcu, *Chem. Eur. J.* 24 (2018), 13512.
- [17] F. You, R.J. Twieg, D. Dyer, V. Lee, *Mol. Cryst. Liq. Cryst.* 332 (2006) 399.
- [18] D.J. Dyer, V.Y. Lee, R.J. Twieg, *Liq. Cryst.* 23 (2010) 551.

Table 3
Activation constants and characteristic times for lanthanidomesogens 5a and 5b.

Compd.	Temp. range [K]	Relaxation process	E_A [eV]	T_V [K]	τ_{\max} [s] $\cdot 10^{-18}$
5a	338–389	DR- α	1.18	88.6	$1 \cdot 10^{-2}$
	338–370	DR- β	0.471	211	1.097
	370–389	DR- β	0.581	183.7	0.109 ^a
5b	351–400	DR- α	1.249	12.19	4.640
	400–414	DR- α	0.735	89.38	–
	351–400	DR- β	0.733	133.2	0.150
	400–414	DR- β	0.851	55.95	1.036 ^b

^a Two processes of dielectric relaxation, DR- α and DR- β ; the process DR- β is better outlined.

^b Two processes of dielectric relaxation, DR- α and DR- β .

- [19] B. Kozlevčar, M. Radišek, Z. Jagličič, F. Merzel, L. Glažar, A. Golobič, P. Šegedin, *Polyhedron* 26 (2007) 5414.
- [20] M. Ueda, T. Mochida, H. Mori, *Polyhedron* 52 (2013) 755.
- [21] F.F. Awwadi, L.N. Dawe, C.P. Landee, M.M. Turnbull, *J. Coord. Chem.* 65 (2012) 3064.
- [22] D.M.L. Goodgame, S.P.W. Hill, D.J. Williams, *J. Chem.Soc., Chem. Commun.* 1019 (1993).
- [23] Y.-B. Shu, X.-L. Tang, W.-S. Liu, *Inorg. Chem. Front.* 1 (2014) 226.
- [24] D.M.L. Goodgame, M. Laliakantouri, D.J. Williams, *J. Cryst. Spectrosc. Res.* 5 (1993) 373.
- [25] D. John, W. Urland, *Eur. J. Inorg. Chem.* (2006) 3503.
- [26] Q.-Y. Yang, M. Pan, S.-C. Wei, C.-W. Hsu, J.-M. Lehn, L.-Y. Su, *CrystEngComm* 16 (2014) 6469.
- [27] J. Wang, S. Chorazy, K. Nakabayashi, B. Sieklucka, S.I. Ohkoshi, *J. Mater. Chem. C* 6 (2018) 473.
- [28] A.A. Essawy, *Sensors Actuators B Chem.* 196 (2014) 640.
- [29] L.F. Wang, J.Z. Qiu, Y.C. Chen, J.L. Liu, Q.W. Li, J.H. Jia, M.L. Tong ML, *Inorg. Chem. Frontiers* 4 (2017) 1311.
- [30] T. Cardinaels, K. Driesen, T.N. Parac-Vogt, B. Heinrich, C. Bourgogne, D. Guillon, B. Donnio, K. Binnemans, *Chem. Mater.* 17 (2005) 6589.
- [31] V. Circu, Y. Molard, M. Amela-Cortes, A. Bentaleb, P. Barois, V. Dorcet, S. Cordier, *Angew. Chem. Int. Ed.* 54 (2015), 10921.
- [32] L.A. Dobrun, A.P. Kovshik, E.I. Ryumtsev, A.A. Knyazev, Yu.G. Galyametdinov, *Phys. Solid State* 58 (2016) 1272.
- [33] L.A. Dobrun, A.P. Kovshik, E.I. Ryumtsev, Yu.G. Galyametdinov, A.A. Knyazev, *Crystallography Reports* 62 (2017) 753.
- [34] L.A. Dobrun, A.S. Sakhatskii, A.P. Kovshik, E.I. Ryumtsev, A.A. Knyazev, Yu.G. Galyametdinov, *JETP Lett.* 99 (2014) 133.
- [35] S. Frunza, A. Schonhals, L. Frunza, P. Ganea, H. Kosslick, J. Harloff, A. Schulz, *J. Phys. Chem. B* 114 (2010), 12840.
- [36] A. Demortiere, S. Buathong, B.P. Pichon, P. Panissod, D. Guillon, S. Begin-Colin, B. Donnio, *Small* 6 (2010) 1341.
- [37] A.R. Katritzky, A. Jones, *J. Chem. Soc.* (1960) 2947.
- [38] K. Kishikawa, T. Inoue, N. Hasegawa, M. Takahashi, M. Kohri, T. Taniguchi, S. Kohmoto, *J. Mater. Chem. C* 3 (2015) 3574.
- [39] K. Kishikawa, S. Aikyo, S. Akiyama, T. Inoue, M. Takahashi, S. Yagai, H. Aonuma, Shigeo Kohmoto, *Soft Matter* 7 (2011) 5176.
- [40] K. Binnemans, *Coord. Chem. Rev.* 295 (2015) 1.
- [41] H.F. Brito, O.L. Malta, M.C.F.C. Felinto, E.E.S. Teotonio, J.F.S. Menezes, C.F.B. Silva, C.S. Tomiyama, C.A.A. Carvalho, *J. Alloys and Compounds* 344 (2002) 293.
- [42] K. Lunstroot, P. Nockemann, K. Van Hecke, L. Van Meervelt, C. Görlner-Walrand, K. Binnemans, *Inorg. Chem.* 48 (2009) 3018.
- [43] J.-C.G. Bünzli, *Coord. Chem. Rev.* 293-294 (2015) 19.
- [44] N. Hill, *Dielectric Properties and Molecular Behaviour*, Van. Nostrand, London, 1969.
- [45] S. Havriliak, S. Negami, *J. Polymer Sci. C* 14 (1966) 99.
- [46] F. Kremer, A. Schönhalz (Eds.), *Broadband Dielectric Spectroscopy*, Springer-Verlag, Berlin-Heidelberg, 2003.
- [47] H. Vogel, *Phys. Z.* 22 (1921) 645.
- [48] G.S. Fulcher, *J. Am. Ceramic Soc.* 8 (1925) 339.
- [49] G. Tammann, W. Hesse, *Z. Anorg. Allgemeine Chem.* 156 (1926) 245.
- [50] S. Urban, B. Gestblom, H. Kresse, A. Dabrowski, *Z. Naturforsch.* 51a (1996) 834.
- [51] G. Adam, J.H. Gibbs, *J. Chem. Phys.* 43 (1965) 139.

Eur. Phys. J. Plus (2018) **133**: 159

DOI 10.1140/epjp/i2018-11997-8

Filling in the voids of electrospun hydroxypropyl cellulose network: Dielectric investigations

Doina Manaila Maximean, Octavian Danila, Constantin Paul Ganea and Pedro L. Almeida



Filling in the voids of electrospun hydroxypropyl cellulose network: Dielectric investigations

Doina Manaila Maximean¹, Octavian Danila¹, Constantin Paul Ganea², and Pedro L. Almeida^{3,4,a}

¹ University Politehnica of Bucharest, Department of Physics, 313 Spl. Independentei, 060042, Bucharest, Romania

² National Institute of Materials Physics, POBox MG 07, 077125 Magurele, Romania

³ I3N - CENIMAT, Departamento de Ciência dos Materiais, Faculdade de Ciências e Tecnologia, FCT/UNL, 2829-516 Caparica, Portugal

⁴ Área Departamental de Física, ISEL, Instituto Superior de Engenharia de Lisboa, I.P.L., R. Conselheiro Emídio Navarro, 1959-007 Lisboa, Portugal

Received: 11 December 2017 / Revised: 5 March 2018

Published online: 23 April 2018 – © Società Italiana di Fisica / Springer-Verlag 2018

Abstract. Here we describe an organic electro-optic device, obtained using electrospun hydroxypropyl cellulose (HPC) polymer fibres and nematic liquid crystals (LC). Its working mechanism is similar to that of a classic polymer-dispersed liquid crystal (PDLC) device. The scanning electron microscopy of the HPC deposited fibres shows a mat of fibres with diameters in the nano and micron size range. Dielectric spectroscopy measurements allow the determination of the dependence of the dielectric constant and electric energy loss on frequency and temperature as well as the determination of the activation energy. The electro-optic study shows a very good optical transmission curve, with an “on”-“off” switching voltage of less than $1\text{ V}/\mu\text{m}$.

1 Introduction

This paper presents an organic electro-optic device obtained using a network of electrospun hydroxypropyl cellulose (HPC) polymer fibres and thermotropic nematic liquid crystals (LC). The working principle is that of a classic polymer-dispersed liquid crystal (PDLC); thus, under the action of an external electric field, LC molecules change their orientation, changing the optical characteristics of the LC and the PDLC film as a whole [1–5]. The polymer refractive index matches the LC ordinary refractive index and the film goes from the light-scattering (“off”) state to the light-transmitting (“on”) state. In fig. 1, the schematic presentation of the HPC-LC composite and the working principle for the electro-optic device (a) and the SEM image of obtained electrospun HPC fibres (b) are shown.

The well-known methods for obtaining “classic” PDLC devices, such as solvent induced phase separation, polymerization induced phase separation and thermally induced phase separation, are based on the preparation of a LC-polymer (or pre-polymer) mixture and the induction of the phase separation of the LC from the polymer matrix by one of the above-mentioned methods. In the dielectric studies, the contribution of the two elements (LC and polymer) cannot be experimentally separated. Since, in the presented sample preparation method, the HPC fibres are firstly deposited and then the electro-optic cell is filled in with LC, the dielectric measurements could be performed before and after filling it in with LC, thus the contribution of each element becomes measurable.

New LC have been synthesized and many LC/polymer systems have been developed for their applications in optoelectronics (light valves, polarizers, solar panels, spatial optical light modulator) [6–9], photonics (phase modulators) and nonlinear optics [10–12].

The HPC used in the sample preparation is an eco-friendly, recyclable, natural cellulose derivative that is obtained from renewable sources [13–19]. The nematic LC used was E7 (Merck), a mixture of alkylcyanobiphenyls with a cyano head group.

^a e-mail: palmeida@adf.isel.pt (corresponding author)

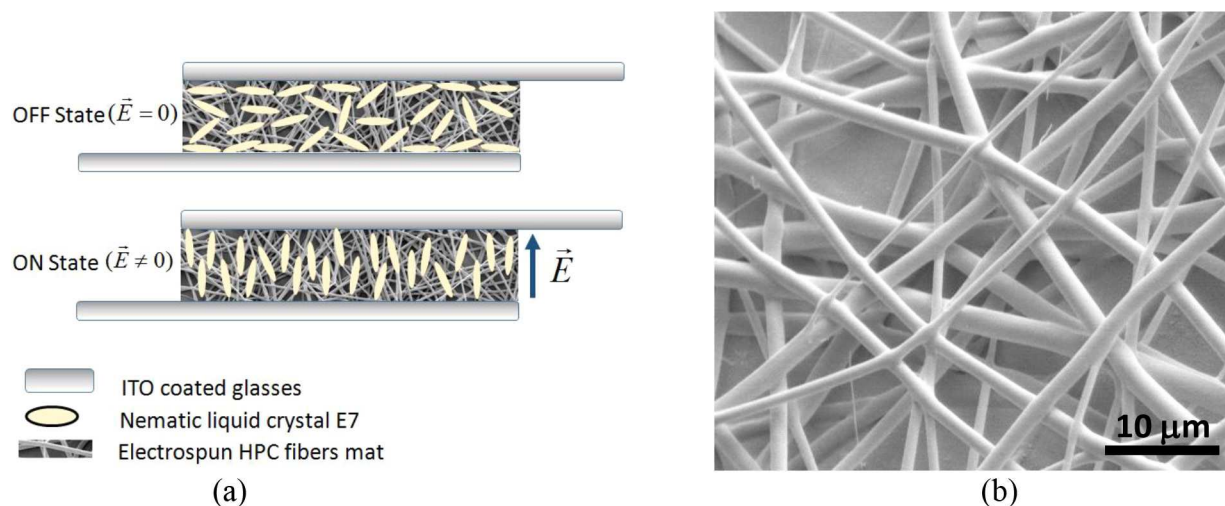


Fig. 1. (a) Schematic presentation of electrospun HPC-LC composite. The applied electric field is denoted by \vec{E} . When the applied electric field is zero, the sample scatters the incident light (off state). When the applied electric field is higher than a certain characteristic value, the LC molecules align with the direction of the field and the sample goes into the on state. (b) SEM image of the obtained electrospun HPC fibres.

2 Experimental method

2.1 Sample preparation

Hydroxypropylcellulose (HPC) is a non-ionic ether of native cellulose. The water solubility of this polymer is dependent on the temperature and is also soluble in other organic solvents, such as acetone and ethanol. HPC is frequently used in industries, such as alimentary and pharmaceutical ones, due to its renewable source, non-toxicity, biocompatibility, biodegradability and optical properties.

The non-woven fibre mats, used to distort the nematic liquid crystal director field in the “off” state, were produced by electrospinning [20–24], a technique that takes advantage of the electrical forces to produce polymeric fibres with diameters in the sub-micrometer to a few micrometer scale (see fig. 1(b)).

The mats were produced using solutions (15 wt%) of HPC ($M_W = 100.000 \text{ g mol}^{-1}$) in ethanol (without further purification). The solutions were constantly stirred for 2 days to ensure homogenization. A 5 ml syringe fitted to a 23 gauge needle was filled with the solution and placed in the infusion syringe pumping machine (KDS100) in order to control the solution feed rate through the tip of the needle. To avoid backflow of the electrospun jet, a conducting ring, with 0.15 m diameter, was assembled coaxially with the syringe’s needle and was electrically connected to it, so that it is at the same potential. The metallic set (needle + ring) was connected to the positive output of a high-voltage power supply (Glassman EL 30 kV). The collector, holding the indium tin oxide (ITO) coated glasses, was assembled in front of the needle with 0.15 m between nozzle and collector. The collector was grounded to create an intense electric field (15 kV) between the needle and the target. After application of the electric field between the syringe’s needle and the target, the polymeric solution was forced through the needle at a constant flow rate of 0.04 ml/h, being afterward accelerated and electrospun towards the target by the influence of the imposed electric field (standard electrospinning setup).

The electrospun fibres were deposited directly onto the ITO-coated glasses. The thickness of the thin non-woven mats was quantified using a profilometer and was in the range of few microns depending on the duration of the deposition and electrospinning parameters, such as distance from target, atmosphere humidity, flow rate and magnitude of the electric field.

On the preparation of each cell, two ITO-coated glasses were used, one with the HPC non-woven mat deposited on and the other as received. The two ITO-coated glasses were glued to each other, separated by the distance of the mat thickness; a small area on each glass was reserved for electrical contact. Two openings were left accessible to allow the filling of each cell with a nematic liquid crystal.

The liquid crystal used was a Merck’s E7 nematic mixture of four nematic compounds (51 wt% of 5CB + 25 wt% of 7CB, 16 wt% of 8OCB and 8 wt% 5CT) [25]. E7 presents a nematic-to-isotropic transition temperature at $T_{NI} = 334.15 \text{ K}$, has positive dielectric anisotropy thus the nematic director tends to align parallel to the imposed electric field and has ordinary and refractive indexes of $n_o = 1.5183$ and $n_e = 1.7378$ ($\lambda = 632.8 \text{ nm}$), respectively, measured at 293.15 K [26].

After assembly, the cell was incubated at 383.15 K for 30 min and allowed to slowly cool to 373.15 K. The NLC was then inserted by capillary rise.

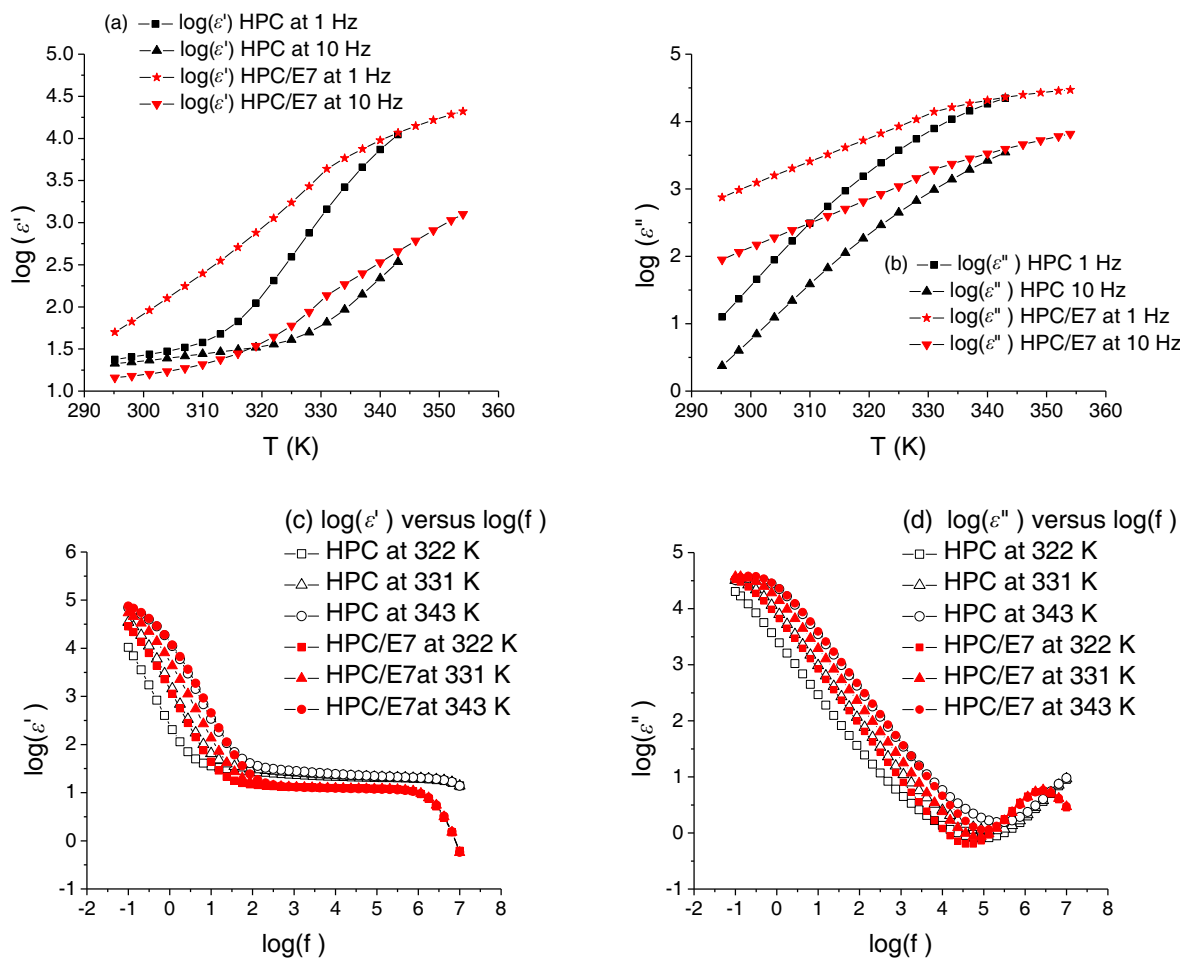


Fig. 2. Comparative presentation: (a) permittivity dependence on the temperature of the HPC cell without LC and of HPC/E7 at 1 Hz and at 10 Hz; (b) dielectric loss dependence on temperature of the HPC cell without LC and of HPC/E7 at 1 Hz and at 10 Hz; (c) permittivity dependence on frequency, at three constant temperatures, of the HPC cell and the HPC/E7; (d) dielectric loss dependence on frequency, at three constant temperatures of the HPC cell and the HPC/E7.

2.2 Dielectric measurements (DS)

The DS characterisation was performed using a broadband dielectric spectrometer, NOVOCONTROL, consisting of the alpha-A high performance frequency analyser in the LF domain $0.01\text{--}10^7$ Hz, equipped with the WinDETA software [27]. Temperatures were controlled within 0.2 K and the alternating voltage was 0.5 V.

2.3 Electro-optic set-up

For the electro-optic characterization, a classical set-up [22, 28–30] was used. The set-up consists of a monochromatic laser beam at 632.8 nm (coherent HeNe laser system) that pumps the sample, which is subjected to an external electric field with a frequency of 50 Hz. The electrical signal characteristics are read on a high-resolution voltmeter.

3 Results and discussions

3.1 DS results

The DS characterization of the HPC/E7 was performed in the low frequency (LF) and high frequency (HF) range, in the temperature domain 293–350 K.

Figure 2(a) presents the dependencies of the permittivity on temperature at two constant representative frequencies, 1 Hz and 10 Hz, of the cell with HPC fibres deposited, before filling in the LC. Figure 2(b) shows the dielectric loss of the same cell before and after the E7 LC was introduced. A change in the slope for the HPC/E7 was associated to the LC nematic-isotropic phase transition observed in figs. 2(a) and (b), at 330 K, practically a frequency-independent process.

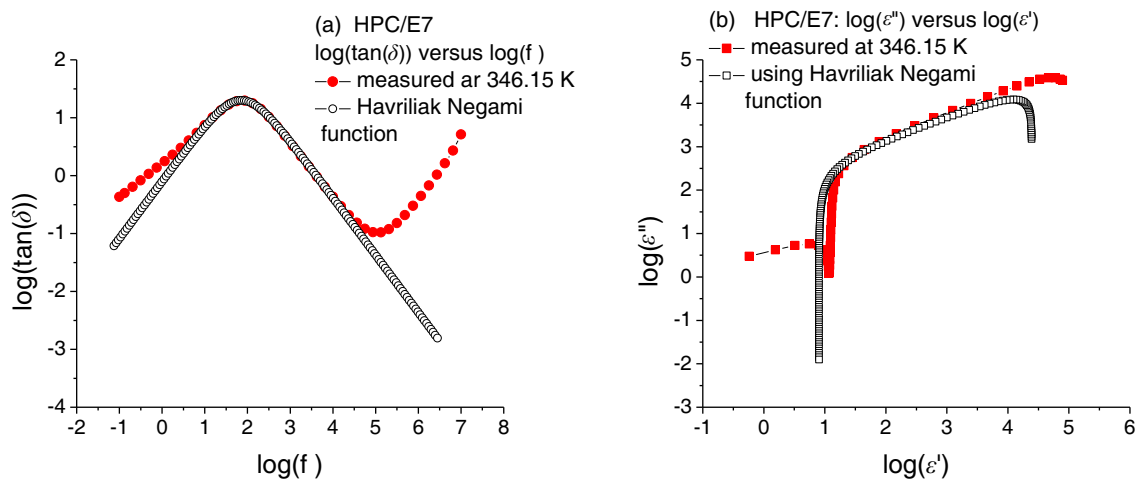


Fig. 3. Comparative presentations for HPC/E7: (a) measured quality factor ($\tan(\delta)$) versus frequency (solid red circles) and Havriliak-Negami fitting function (open black circles); (b) dielectric loss versus permittivity measured at 346.15 K (solid red squares) and Havriliak-Negami fitting function (open black squares).

Since, for all the samples, permittivity increases dramatically with temperature, our study constitutes a breakthrough in designing compensation electronic circuits for temperature variation.

Representations of the dielectric loss at the same frequencies (fig. 2(b)) showed an increase of two orders of magnitude due to the LC, in the temperature interval 293.15–323.15 K.

Figure 2(c) presents the permittivity dependence on frequency, at three constant representative temperatures, of the HPC and the HPC/E7. The selected spectra are registered under the phase transition temperature of the LC (322 K), at the phase transition temperature of the LC (331 K) and above the phase transition temperature of the LC (343 K).

The HPC spectra have, in the LF domain, two relaxation processes, almost overlapped (one at 1 Hz and the other at 500 Hz). Figure 2(d) shows the dielectric loss dependence on frequency, at three constant representative temperatures for the HPC and HPC/E7. In the HF domain, for the HPC/E7, one relaxation process is observed at 10^6 Hz, therefore attributed to the LC.

The characteristic relaxation times were obtained by fitting the spectra of the dielectric loss with the Havriliak-Negami (HN) functions [31]:

$$\varepsilon_{\text{HN}}^*(\omega) = \varepsilon'(\omega) - i\varepsilon''(\omega) = \varepsilon_{\infty} + \frac{\varepsilon_{\text{LF}} - \varepsilon_{\infty}}{(1 + (i\omega \cdot \tau_{\text{max}})^{\alpha})^{\beta}}, \quad (1)$$

$$0 < \alpha < 1, \quad 0 < \beta < 1,$$

where $\varepsilon'(\omega)$ is the permittivity and $\varepsilon''(\omega)$ is the dielectric loss, ε_{LF} is the low-frequency permittivity and ε_{∞} is the permittivity in the HF limit and τ_{max} is the characteristic relaxation time of the medium [32].

Figure 3(a) shows the variation of the quality factor ($\tan(\delta)$) versus frequency, logarithmic scale, and fig. 3(b) presents the Nyquist diagram (also known as Cole-Cole diagram), $\varepsilon'' = \varepsilon''(\varepsilon')$, also logarithmic scale. The represented values are obtained from the dielectric spectra measured at the temperature 346.15 K. These figures are illustrating the fitting procedure with one Havriliak-Negami (HN) function. They also emphasize in a clearer way the presence of the three relaxation processes mentioned in fig. 2. So, by examining fig. 3(a), a “main” relaxation process, at 100 Hz is observed (at the respective temperature), on which the HN fitting function is centered (open black circles). In the low frequency domain, the experimental curve gets away from the HN function, indicating the presence of a “secondary” process, observed as a “shoulder” of the increasing branch of the “main” relaxation process. In the high frequency (above 100 KHz) range, the increasing branch of a third process is relaxation process is noticed (solid red circles).

Figure 3(b) confirms the above-mentioned processes. In its left side there is an incomplete semicircle, deformed by the logarithmic scale, corresponding to the high frequency process. In the right side of fig. 3(b), the experimental data move away from the fitting curve (open black squares curve), due to the influence of the relaxation process from very low frequencies. The processes present at the two above mentioned limits are not entirely comprised in the studied frequency range. Therefore, they could not be analysed, because the fitting parameters are affected by too large errors. The above mentioned arguments explain our choice for one HN function centered on a single relaxation process.

A special attention should be paid to the interpretation of the results related to the two low frequency relaxation mechanisms, which are, to a good extend, superposed. The main mechanism may be attributed to the dynamics of the molecules present in the surface layer of composite systems. The structure of such a layer might be considered as

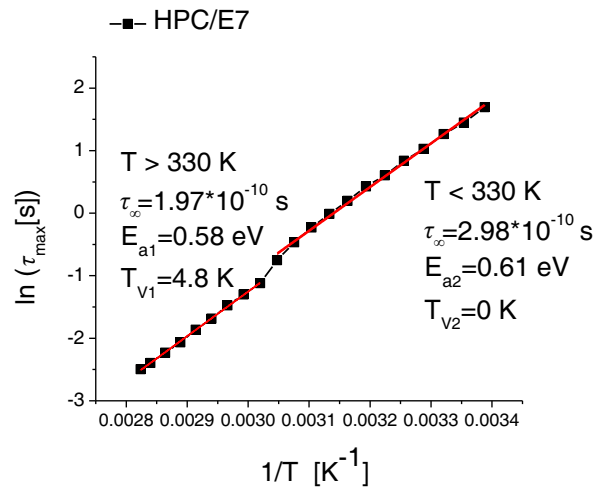


Fig. 4. Temperature dependence of the characteristic relaxation time for HPC/E7: measured values (black squares) and the fitting two red straight lines; the phase transition temperature of the LC is $T' \approx 330$ K. For $T < 330$ K, the activation energy was found 0.61 eV and for $T > 330$ K the activation energy is 0.58 eV.

Table 1. DS characteristic constants for HPC/E7.

No.	Sample type	Investigation method	Temperature domain	Activation energy	Vogel temperature	Relaxation time
			[K]	E_a [eV]	T_V [K]	τ [s]
1	HPC/E7	DS Vogel-Fulcher-Tammann	295–328	0.61	0	2.98×10^{-10}
			331–346	0.58	4.84	1.97×10^{-10}
2	HPC/E7	I-V curves Arrhenius [20]	308–330	0.66	–	–
			330–353	0.42	–	–

constituted by: a) LC molecules directly linked to the surface by a chemical bond; b) a certain number of molecules unbound to the interface but whose dynamics is different from the one specific to the bulk behaviour, being hindered by the short distance interaction with the adsorbed molecules. In the dielectric spectra, a relaxation process whose characteristic frequency is smaller than the one corresponding to the relaxation process in the bulk LC appears. This interpretation is in agreement with those given by Lippens *et al.* [33], Cramer *et al.* [34] and Brás *et al.* [35].

The second process (LF), due to the interfacial polarization, manifested at very low frequencies, of about 1 Hz, might be attributed to the Maxwell-Wagner-Sillars effect [2, 31, 36–38]. This effect is present at the interface between two media with different dielectric constants and electric conductivities. It results in a supplementary increase of the dielectric constant and of the dielectric losses at the decrease of the frequency, as one can see in fig. 3(a).

Figure 4 shows the temperature dependence of the characteristic relaxation time for HPC/E7, which presents two linear segments, slightly shifted between them. The transition temperature of the LC is included in the region at which this shift occurs. The magnitude of this shift is rather small, because parts of the LC molecules are attached to the HPC fibres and are part of the surface layer. This results in a reduced mobility of the LC molecules as they are in a movement limiting confined structure. The rest of LC molecules, part of the bulk volume, have higher mobility.

The dependency $\tau_{\max} = f(1/T)$ can be modelled using the Vogel-Fulcher-Tammann (VFT) law:

$$\tau_{\max} = \tau_{\infty} \exp \left[\frac{A}{K_B(T - T_V)} \right], \quad (2)$$

where A is a material constant, K_B is Boltzmann’s constant, T is the current temperature, T_V is the Vogel temperature and τ_{∞} is a pre-exponential factor. The activation energies were calculated for the HPC/E7 samples, by fitting the dependency $\ln(\tau_{\max}) = f(1/T)$ to two straight line segments, for two temperature domains, as presented in table 1. The slope of the lines is $m = A/K_B$ and from their intersection with the ordinate axis, the relaxation time was determined. It should be noted that, since the obtained Vogel temperature is very low, the VFT equation becomes the Arrhenius equation, as the material constant A is assimilated by the activation energy E_a . The previous data [20], obtained with slightly different electrospinning conditions and using the Arrhenius formula, are very similar.

The two sets of results are in good agreement; in both cases, the activation energy has lower values in the higher temperature domain, in the isotropic phase of the LC.

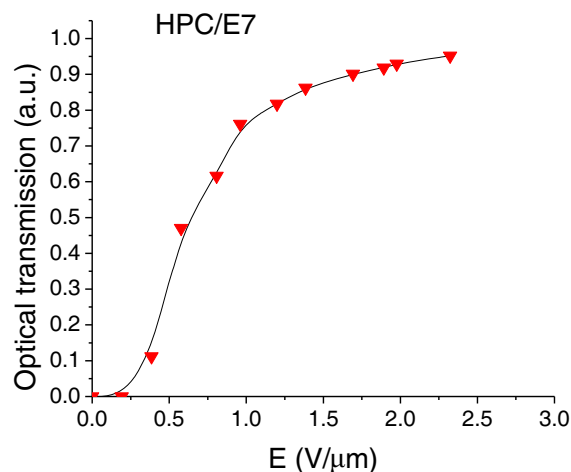


Fig. 5. Optical transmission *versus* RMS electric field for the HPC/E7 sample.

3.2 Electro-optical transmission

The optical transmission value, under the influence of an external electrical field, was determined. Thermal effects that accumulated in the samples made the DC electric fields unfitted for use, as the temperature rise changes the phase of the sample from nematic to isotropic. Therefore, a variable amplitude AC field was applied to the samples [1, 2, 13], and the optical transmission through the sample was measured.

The voltage U_{RMS} was gradually increased and the optical transmission was measured after enough time until no transient effects occur. At low electric fields, the optical transmission retains a low value and thus the sample acts as a light blocker. This is known as the “off” state. As the voltage increases, the overall behaviour of the composite leads to an increase in the optical transmission to an almost unitary value. This is known as the “on” state. The voltage level at which the optical transmission attains the value 0.9 is known as the *threshold voltage*. The static optical behaviour of the sample is presented in fig. 5. Based on the graph, we have estimated the threshold voltage at less than $1 \text{ V}/\mu\text{m}$.

4 Conclusions

The electrospinning method was chosen to obtain a non-woven fibre mat, deposited on ITO-covered glass. Using one glass with the HPC non-woven mat deposited on and the other one as received, an electro-optic cell was obtained.

By filling in the nematic liquid crystal E7, an organic optoelectronic device was obtained, functioning as a light scattering - light transmitting device (optical valve), similar to the PDLC type.

A dielectric spectroscopy study was performed on the electro-optic cells before and after filling in the LC. The dependence of the dielectric constant and electric energy loss on frequency and temperature was studied. By comparing the spectra of the dielectric permittivity of the samples with LC (HPC/E7) to the ones of the sample without LC (HPC), the following conclusions were drawn: a) the presence of the LC modifies the dielectric permittivity spectra, the variations depend on frequency and temperature; b) the phase transition of the liquid crystal is determined by the molecular dynamics in confined configurations; c) the existence of a main process (in the 100 Hz–1 MHz frequency range) due to the dynamics of the permanent dipoles of the molecules adsorbed at the fibre surface; d) the presence of a supplementary dielectric process, with the characteristic frequency about 1 Hz, due to the relaxation of the interfacial polarization (Maxwell-Wagner-Sillars relaxation).

The activation energy of the E7 liquid crystal in the HPC fibre mat was determined in good agreement with previous data.

The electro-optic study shows a very good optical transmission curve, with an on-off switching voltage of less than $1 \text{ V}/\mu\text{m}$.

This work was partially funded by FEDER funds through the COMPETE 2020 Program and National Funds through FCT - Portuguese Foundation of Science and Technology under the Projects Nos. POCI-01-0145-FEDER-007688 (Reference UID/CTM/50025) and PTDC/FIS-NAN/0117/2014. CPG thanks the Romanian Ministry of Education and Research for financial support under Core Program, Project CEFIZMATINT (PN18-11). DMM thanks L. Frunza and S. Frunza for useful discussions.

References

1. M. Mucha, Prog. Polym. Sci. **28**, 837 (2003).
2. Paul S. Drzaic, *Liquid Crystal Dispersions* (World Scientific, 1995).
3. M. Kleeman, O.D. Lavrentovich, *Soft Matter in Physics* (Springer, New York, 2002, Fizmatlit, Moscow, 2002).
4. L. Bedjaoui-Alachaher, F. Semdani, R. Meziane, U. Maschke, Mol. Cryst. Liq. Cryst. **546**, 87 (2011).
5. D. Manaila-Maximean, C. Rosu, S. Klosowicz, K.L. Czuprynski, J.M. Gilli, M. Aleksander, Mol. Cryst. Liq. Cryst. **417**, 199 (2004).
6. V.A. Loiko, A.V. Konkolovich, V.Ya. Zyryanov, A. Miskevich, Opt. Spectrosc. **122**, 984 (2017).
7. M. Micutz, M. Iliş, T. Staicu, F. Dumitraşcu, I. Pasuk, Y. Molard, T. Roisnel, V. Cîrcu, Dalton Trans. **43**, 1151 (2014).
8. V. Cîrcu, T.J.K. Gibbs, L. Omnès, P.N. Horton, M.B. Hursthouse, D.W. Bruce, J. Mater. Chem. **16**, 4316 (2006).
9. V. Cîrcu, P.N. Horton, M.B. Hursthouse, D.W. Bruce, Liq. Cryst. **34**, 1463 (2007).
10. C. Rosu, D. Manaila-Maximean, A.J. Paraskos, Mod. Phys. Lett. B **16**, 473 (2002).
11. J.M. Gilli, S. Thiberge, D. Manaila-Maximean, Mol. Cryst. Liq. Cryst. **417**, 691 (2004).
12. K.B. Zegadlo, H. El Ouazzani, I. Cieslik, R. Weglowski, J. Zmija, S. Klosowicz, A. Majchrowski, J. Mysliwiec, B. Sahraoui, M.A. Karpierz, Opt. Mater. **34**, 1704 (2012).
13. R. Miedzinski, J. Ebothe, I. Fuks-Janczarek, I.V. Kityk, A. Majchrowski, R. Weglowski, S.J. Klosowicz, J. Mater. Sci. Mater. Electron. **21**, 659 (2010).
14. V.A. Loiko, *Polymer Films with Nanosized Liquid-Crystal Droplets: Extinction, Polarization, Phase, and Light Focusing, in Nanodroplets* (Springer, New York, 2013) pp. 195–235.
15. P.L. Almeida, S. Kundu, J.P. Borges, M.H. Godinho, J.L. Figueirinhas, Appl. Phys. Lett. **95**, 043501 (2009).
16. C. Sena, M.H. Godinho, C.L.P. de Oliveira, A.M. Figueiredo Neto, Cellulose **18**, 1151 (2011).
17. Y. Geng, P. Brogueira, J.L. Figueirinhas, M.H. Godinho, P.L. Almeida, Liq. Cryst. **40**, 769 (2013).
18. M.H. Godinho, P.L. Almeida, J.L. Figueirinhas, Materials **7**, 4601 (2014).
19. A. Hinojosa, S.C. Sharma, Appl. Phys. Lett. **97**, 081114 (2010).
20. C. Rosu, D. Manaila-Maximean, S. Kundu, P.L. Almeida, O. Danila, J. Electrostat. **69**, 623 (2011).
21. C. Rosu, D. Manaila-Maximean, M.H. Godinho, P.L. Almeida, Mol. Cryst. Liq. Cryst. **391**, 1 (2003).
22. D. Manaila Maximean, O. Danila, P.L. Almeida, C.P. Ganea, Beilstein J. Nanotechnol. **9**, 155 (2018).
23. M. Aflori, D. Serbezeanu, I.D. Carja, G. Fortunato, Chem. Lett. **44**, 1440 (2015).
24. D. Serbezeanu, A.M. Popa, I. Sava, I.D. Carja, M. Amberg, R.M. Rossi, G. Fortunato, Eur. Polym. J. **64**, 10 (2015).
25. P. Raynes, S.J. Cowling, J.W. Goodby, Anal. Methods **1**, 88 (2009).
26. Y. Derouiche, F. Dubois, R. Douali, C. Legrand, U. Maschke, Mol. Cryst. Liq. Cryst. **541**, 201 (2011).
27. C.P. Ganea, D. Manaila-Maximean, U.P.B. Sci. Bull. Series A **73**, 4 (2011).
28. C. Roşu, C., D. Manaila-Maximean, V. Cîrcu, Y. Molard, T. Roisnel, Liq. Cryst. **38**, 757 (2011).
29. V. Cîrcu, A.S. Mocanu, C. Roşu, D. Manaila-Maximean, F. Dumitraşcu, J. Therm. Anal. Calorim. **107**, 877 (2012).
30. D. Manaila-Maximean, R. Bena, A.M. Albu, Mod. Phys. Lett. B **11**, 431 (1997).
31. F. Kremer, A. Schönhal (Editors), *Broadband Dielectric Spectroscopy* (Springer-Verlag, Berlin-Heidelberg, 2003).
32. S. Frunza, A. Schönhal, L. Frunza, P. Ganea, H. Kosslick, J. Harloff, A. Schulz, J. Phys. Chem. B **114**, 12840 (2010).
33. D. Lippens, J.P. Parneix, A. Chapoton, J. Phys. **38**, 1465 (1977).
34. C.H. Cramer, T.H. Cramer, F. Kremer, R. Stannarius, J. Chem. Phys. **106**, 3730 (1997).
35. A.R. Brás, S. Frunza, L. Guerreiro, I.M. Fonseca, A. Corma, L. Frunza, M. Dionísio, A. Schönhal, J. Chem. Phys. **132**, 224508 (2010).
36. M.T. Viciosa, A.M. Nunes, A. Fernandes, P.L. Almeida, M.H. Godinho, M.D. Dionísio, Liq. Cryst. **29**, 429 (2002).
37. D. Manaila-Maximean, M. Furlani, R. Bena, B.E. Mellander, C. Rosu, T. Pop, C. Motoc, Mod. Phys. Lett. B **13**, 759 (1999).
38. D. Manaila-Maximean, R. Bena, C. Rosu, M. Furlani, Mol. Cryst. Liq. Cryst. **365**, 645 (2001).



Dielectric properties of a bisimidazolium salt with dodecyl sulfate anion doped with carbon nanotubes

Doina Manaila Maximean^{*1}, Viorel Cîrcu² and Constantin Paul Ganea^{*3}

Full Research Paper

Open Access

Address:

¹University Politehnica of Bucharest, Department of Physics, 313 Spl. Independentei, 060042, Bucharest, Romania, ²Department of Inorganic Chemistry, University of Bucharest, 23 Dumbrova Rosie st, sector 2, Bucharest 020464, Romania and ³National Institute of Materials Physics, POBox MG 07, 077125 Magurele, Romania

Email:

Doina Manaila Maximean^{*} - doina.manaila@physics.pub.ro;
Constantin Paul Ganea^{*} - paul.ganea@infim.ro

^{*} Corresponding author

Keywords:

activation energy; carbon nanotubes; dielectric spectroscopy; ionic liquid crystal; relaxation time

Beilstein J. Nanotechnol. **2018**, *9*, 164–174.

doi:10.3762/bjnano.9.19

Received: 22 August 2017

Accepted: 20 December 2017

Published: 16 January 2018

This article is part of the Thematic Series "Nanostructured liquid crystal systems and applications".

Guest Editor: A. Emelyanenko

© 2018 Maximean et al.; licensee Beilstein-Institut.

License and terms: see end of document.

Abstract

A new bisimidazolium salt with dodecyl sulfate as counterion has been designed and prepared. This salt shows a SmA phase that is stable at room temperature. The new ionic liquid crystal (ILC) was characterized by ¹H NMR, ¹³C NMR and IR spectroscopy. Its liquid crystalline properties were analyzed by polarizing optical microscopy (POM), differential scanning calorimetry (DSC) and powder X-ray diffraction (XRD) studies. The dielectric spectra of the ILC doped with different concentrations of carbon nanotubes (CNT) were recorded over a wide frequency and temperature range of 10⁻¹ to 10⁷ Hz and 293–338 K, respectively. The values of the activation energy were found in the range of 0.46–0.61 eV; the characteristic time was obtained by fitting the spectra of the dielectric loss with the Havriliak–Negami functions. As a result of doping the ILC with CNT, the electric conductivity increases significantly. Ionic conductivity is dominant and it was indirectly observed through the electrode polarization (EP) effect. The very high dielectric permittivity values and the decrease of the electric conductivity at low frequencies confirm the presence of EP.

Introduction

Ionic liquid crystals (ILCs) represent a very appealing class of materials that has found various recent applications in dye-sensitized solar cells, battery materials, electrochemical sensors or energy storage devices. Their interesting properties result from the combination of liquid crystal (LC) and ionic liquid (IL) properties. The recent progress and development in the field of ILCs were reviewed in several publications [1-3]. There

is a growing interest in ILs based on imidazolium cations. Particular attention is paid to the flexibly or rigidly linked bisimidazolium salts, the so-called gemini ILs. Gemini ILs can show interesting surfactant and liquid crystalline properties [4-12] and such salts were used in many applications, ranging from catalysis [13] to biological [14-16] or biochemical applications [17-19]. Recently, we have shown that it is possible to exchange

the smaller anions (Br^-) with alkyl sulfate ions to yield new ILCs based on bisimidazolium salts with flexible methylene spacer and long alkyl tails [20]. The LC properties are influenced, in the order of impact, by spacer length, alkyl tail length and, finally, by the length of alkyl chains attached to the sulfate groups [21]. Furthermore, the liquid crystalline compounds with alkyl sulfate anions have lower melting and clearing points. Hence, there is the interest to design such materials for further electro-optical applications [22–32].

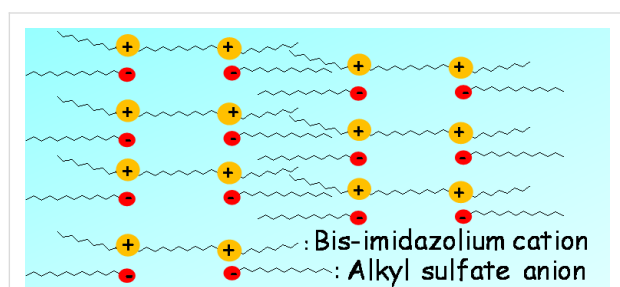


Figure 1: Schematic representation of the bilayer interdigitated SmA phase of the ILC based on bisimidazolium salts with alkyl sulfate ion.

Carbon nanotubes (CNTs) and nanoparticles were also dispersed in LCs [33–36]. It is well-known that the order of the LCs can be imposed on the CNTs in such a way that the alignment axis of the CNTs is driven by the LC reorientation controlled by an electric field [37]. The concentration and the spatial distribution of charges in the LC matrix will be affected by the presence of CNTs and, hence, the conductivity will be changed [38–44].

There are studies dedicated to the dielectric spectroscopy (DS) of ILCs doped with CNT [45]. In the present work we studied

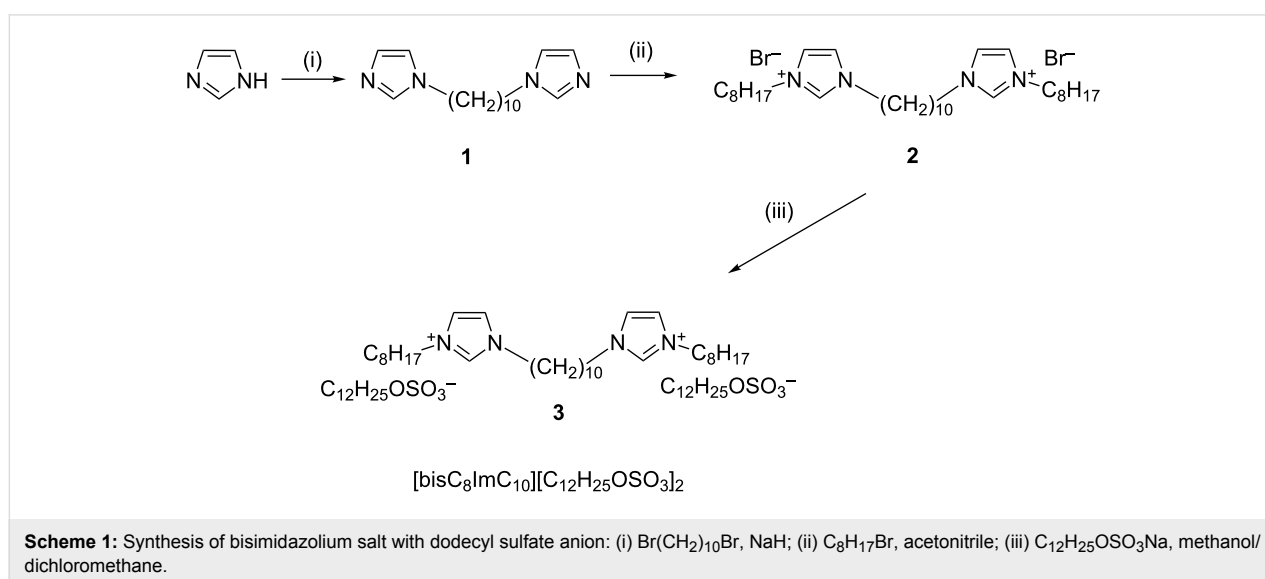
the effect of added CNTs on the dielectric properties of a new ILC based on a bisimidazolium salt with a dodecyl sulfate ion. The dielectric spectra of pure and CNT-doped ILC were recorded in the frequency range from 10^{-1} to 10^7 Hz and in the temperature range from 293 to 338 K corresponding to the different phases of the ILC (mesophase and isotropic state). The values of the permittivity, dielectric loss and conductivity were deduced from the dielectric studies. The activation energy was calculated by employing the Vogel–Fulcher–Tammann law while the characteristic time was obtained by fitting the spectra of the dielectric loss with the Havriliak–Negami functions.

Results and Discussion

Synthesis of the bisimidazolium salt

The preparation of new bisimidazolium salt with dodecyl sulfate anion employed in this study, along with the numbering scheme of intermediates, is presented in Scheme 1.

In the first step 1,1'-(1,10-hexanediy)bisimidazole (**1**) was prepared starting from imidazole and 1,10-dibromodecane, as described by Bara and co-workers [7]. The bromide salt **2** was prepared by alkylation of **1** with 1-bromooctane in acetonitrile under reflux. The product was precipitated with ethyl ether, and purified by several recrystallizations from dichloromethane/ethyl ether. The metathesis reaction of the bromide anion with sodium dodecyl sulfate, $\text{C}_{12}\text{H}_{25}\text{OSO}_3\text{Na}$, yielded the corresponding salt $[\text{bisC}_8\text{ImC}_{10}][\text{C}_{12}\text{H}_{25}\text{OSO}_3]_2$ (**3**). Compound **3** was characterized by several physico-chemical techniques, such as elemental analysis (C, H, N), IR, ^1H and ^{13}C NMR spectroscopy, supporting the proposed structure. The exchange of bromide anion with dodecyl sulfate ion was easily confirmed by IR spectroscopy. The IR spectrum of $[\text{bisC}_8\text{ImC}_{10}][\text{C}_{12}\text{H}_{25}\text{OSO}_3]_2$ shows a strong band at 1225 cm^{-1} assigned to the sulfate group.



Moreover, the ^1H and ^{13}C NMR spectra give additional support for the exchange of bromide ions with dodecyl sulfate ions. The signals assigned to the three protons belonging to the two imidazolium rings are shifted upfield in the ^1H NMR spectrum of $[\text{bisC}_8\text{ImC}_{10}][\text{C}_{12}\text{H}_{25}\text{OSO}_3]_2$ compared to their position in the ^1H NMR of the bromide salt **2**. The most significant change was observed for the signal assigned to the proton adjacent to the two nitrogen atoms (Scheme 1). For the bromide salt **2** this signal is located at 10.42 ppm, while for the dodecyl sulfate salt $[\text{bisC}_8\text{ImC}_{10}][\text{C}_{12}\text{H}_{25}\text{OSO}_3]_2$ this signal is shifted to 9.58 ppm. It is well documented that the anion–cation interactions have a strong effect on the NMR chemical shifts of protons belonging to the imidazolium ring. The NMR signals are shifted downfield due to the presence of hydrogen-bonding interactions in imidazolium-based ILC systems [32,46–51].

Polarized optical microscopy (POM)

The LC phase of $[\text{bisC}_8\text{ImC}_{10}][\text{C}_{12}\text{H}_{25}\text{OSO}_3]_2$ was determined based on the POM observations. Two different pictures of the textures developed on cooling from the isotropic state are shown in Figure 2. These observations were confirmed later by

XRD studies. On cooling the sample from the isotropic state, typical fan-shape or focal conic textures together with several homeotropic areas were found, leading to an unambiguously assignment of a SmA phase. ILCs are well known to exhibit predominantly lamellar phases, with the SmA phase being the most common phase for such materials, in particular due to electrostatic interactions and ion–ion stacking in ILCs.

Differential scanning calorimetry (DSC)

The transitions and their corresponding temperatures together with the enthalpy values associated to these processes are presented in Figure 3. The transitions of $[\text{bisC}_8\text{ImC}_{10}][\text{C}_{12}\text{H}_{25}\text{OSO}_3]_2$ between mesophase and isotropic state observed by DSC are broad, with $T_{\text{onset}} = 321.15$ K. The temperature range of the liquid crystalline phase is limited to approx. 10 K during the heating run. The first heating run of the bisimidazolium salt shows a broad peak including the transition from the crystalline state to the LC phase and the following transition to the isotropic state, giving only the combined enthalpy of the two processes. However, POM observations clearly indicated that the two transformations are well separated. The

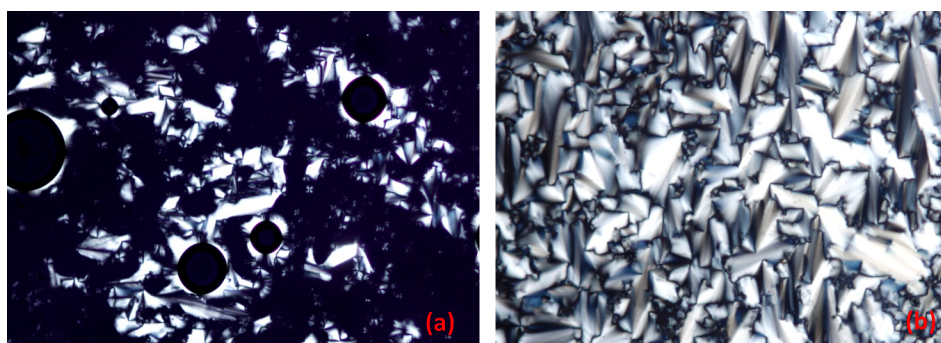


Figure 2: POM pictures of $[\text{bisC}_8\text{ImC}_{10}][\text{C}_{12}\text{H}_{25}\text{OSO}_3]_2$ on cooling from the isotropic state: at 318 K (a) and at 303 K (b).

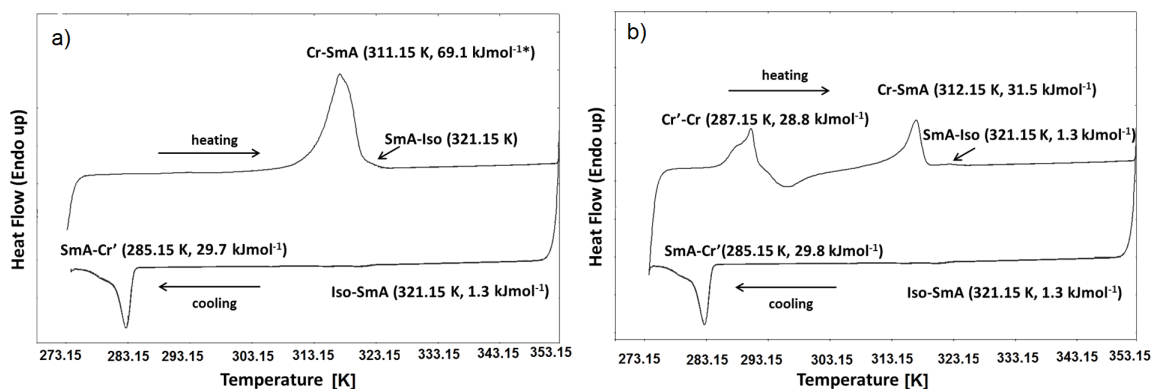


Figure 3: DSC traces for $[\text{bisC}_8\text{ImC}_{10}][\text{C}_{12}\text{H}_{25}\text{OSO}_3]_2$: (a) first and (b) second heating–cooling cycle recorded in the temperature range of 273–353 K with a scan rate of 10 K/min. Thermal parameters are given in brackets. The given enthalpy contains the combined values for the two transitions Cr–SmA and SmA–Iso.

following cooling run shows the Iso-SmA phase transition at 321.15 K followed by a second transition at 285.15 K, which was assigned to a transition from the LC phase to a different crystalline phase (Cr'). This second Cr' phase is not thermodynamically stable at room temperature and it transitions to the first crystalline phase at 287.15 K during the subsequent heating run (in fact, it is a melting transition followed by the cold crystallization to the Cr phase). The following heating–cooling cycles are perfectly reproducible with the two transitions Cr–SmA and SmA–Iso well separated during the heating runs (Figure 3b). Importantly, POM observations show that on cooling from the isotropic state, the SmA phase is stable down to room temperature over time with a slow crystallization occurring over the course of hours based on POM observations. Obviously, the stability domain of the SmA phase is higher (ca. 36 K) during the cooling step, allowing for precise dielectric measurements in the LC phase.

Powder X-ray diffraction measurements

The nature of the LC phase was unequivocally confirmed by powder X-ray diffraction measurements. The XRD measurements were performed at 298 K after the sample was previously heated at 333 K to reach the isotropic state and then cooled down to room temperature in the mesophase temperature domain. The results are presented in Figure 4. The XRD pattern of $[\text{bisC}_8\text{ImC}_{10}][\text{C}_{12}\text{H}_{25}\text{OSO}_3]_2$ salt shows one sharp and intense diffraction peak in the small-angle region (27.3 Å) and a second broad peak at wide angles (around 4.5 Å). The first peak was assigned to the (001) reflection corresponding to

a lamellar structure while the broad peak is due to the liquid-like order of the molten alkyl chains.

The results of a simple molecular calculation based on an all-trans extended model revealed a molecular length of about 39 Å. Indeed, by comparison of the experimental value of the layer thickness (27.3 Å) with the molecular length resulting from molecular calculations, it is justified to assume an interdigitated double layer structure for the SmA mesophase [4,20].

Dielectric spectroscopy

The DS measurements were performed both for the pure ILC and for various mixtures of CNT-doped ILC (concentration 0.05% w/w and 0.5% w/w) in the frequency range from 10^{-1} to 10^7 Hz. The temperature range was chosen in agreement with the DSC and the POM observations for the phase transitions, between 293 and 338 K.

The logarithmic permittivity for the pure ILC and the CNT-doped ILC as a function of the temperature is presented in Figure 5. It was found that the permittivity has higher values for the CNT-doped ILC and, in the range of 320–338 K, the plots of the permittivity for the 0.05% CNT and 0.5% CNT concentrations overlap.

The temperature variation of the dielectric loss for the pure ILC and the CNT-doped ILC is shown in Figure 6. It was found that the dielectric loss increases with the temperature and with the CNT concentration.

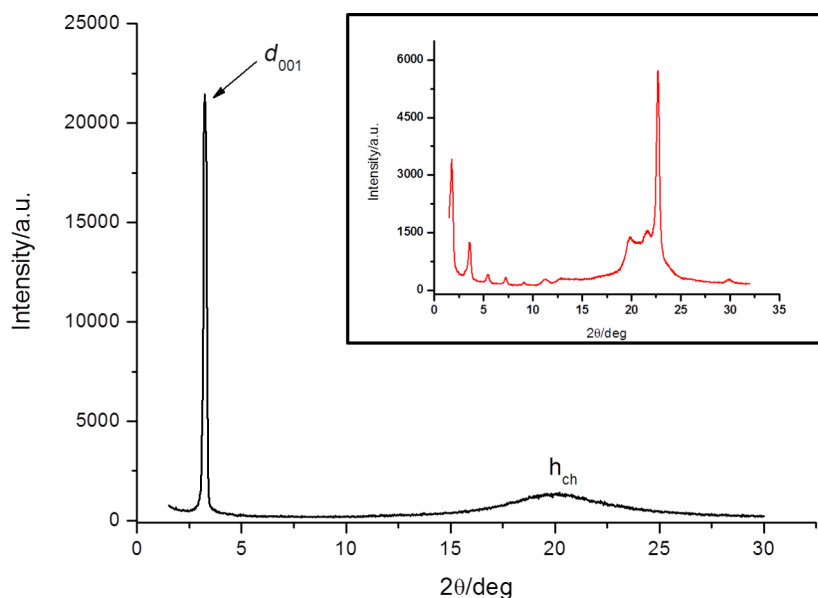


Figure 4: Powder XRD pattern of $[\text{bisC}_8\text{ImC}_{10}][\text{C}_{12}\text{H}_{25}\text{OSO}_3]_2$ recorded at 298 K, after cooling from the isotropic state. Inset: the XRD pattern recorded at 298 K in the crystalline state (prior to heating).

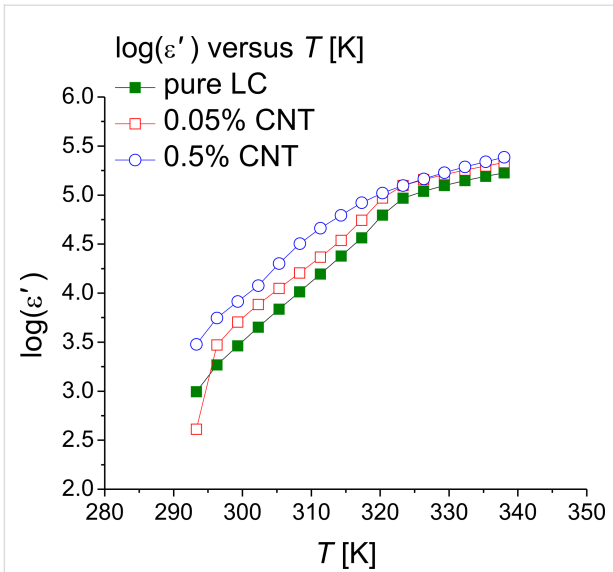


Figure 5: Permittivity as a function of the temperature (logarithmic scale) for pure ILC (green solid squares), ILC doped with 0.05% CNTs (red open squares) and ILC doped with 0.5% CNTs (blue open circles).

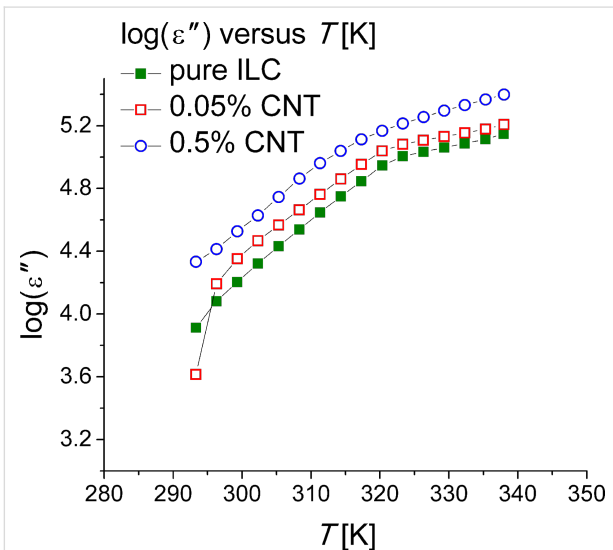


Figure 6: Dielectric loss as a function of the temperature (logarithmic scale) for pure ILC (green solid squares), ILC doped with 0.05% CNTs (red open squares) and ILC doped with 0.5% CNTs (blue open circles).

The characteristic relaxation times were obtained by fitting the spectra of the dielectric loss with the Havriliak–Negami (HN) function [52]:

$$\epsilon_{\text{HN}}^*(\omega) = \epsilon'(\omega) - i\epsilon''(\omega) = \epsilon_{\infty} + \frac{\epsilon_{\text{LF}} - \epsilon_{\infty}}{\left(1 + (i\omega \cdot \tau_{\text{max}})^{\alpha}\right)^{\beta}} \quad (1)$$

with $0 < \alpha < 1$ and $0 < \beta < 1$,

where $\epsilon'(\omega)$ is the permittivity and $\epsilon''(\omega)$ is the dielectric loss, ϵ_{LF} is the low-frequency (LF) permittivity and ϵ_{∞} is the permittivity in the high-frequency (HF) limit and τ_{max} is the characteristic relaxation time of the dielectric relaxation process.

The dependency $\tau_{\text{max}} = f(1/T)$ can be modeled using the Vogel–Fulcher–Tammann (VFT) law, as follows:

$$\tau_{\text{max}} = \tau_{\infty} \exp\left[\frac{A}{k_{\text{B}}(T - T_{\text{V}})}\right], \quad (2)$$

where A is a material constant, k_{B} is Boltzmann's constant, T is the temperature, T_{V} is the Vogel temperature and τ_{∞} is a pre-exponential factor.

Figure 7 presents the characteristic relaxation time as a function of the inverse temperature for the pure ILC and the CNT-doped ILC. For the pure ILC and for the lower CNT doping concentrations, there are two slopes, attributed to the isotropic and the SmA phases. At the higher CNT concentration (0.5%) the transition isotropic–SmA could not be detected clearly, probably due to the very low energies involved in the transition. In the isotropic phase, the curves of the relaxation time for the 0.05% CNT and 0.5% CNT concentrations overlap, and for lower temperatures, the relaxation time decreases with the CNT concentration. The pure ILC has a relaxation time higher than the doped ILC in the temperature range of the mesophase.

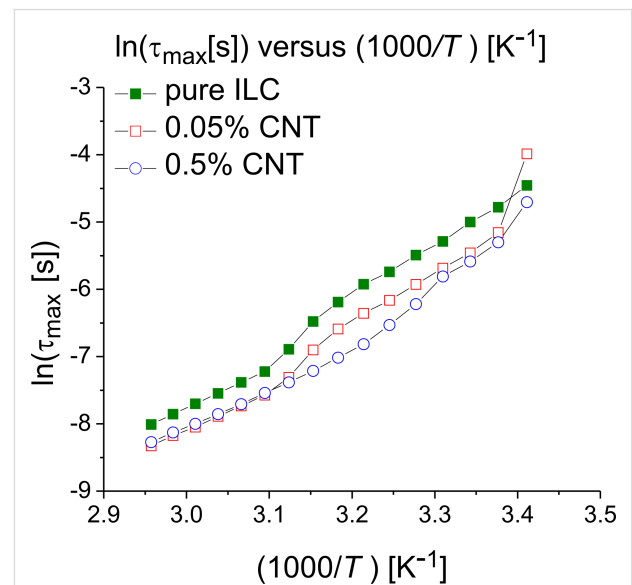


Figure 7: Relaxation time as function of the inverse temperature (logarithmic scale) for pure ILC (green solid squares), ILC doped with 0.05% CNTs (red open squares) and ILC doped with 0.5% CNTs (blue open circles).

Table 1 gives the values of the activation energy and the relaxation times in the corresponding temperature domains. The following observations can be made according to data presented in Table 1: a) the activation energy increases with CNT concentration; b) for the same CNT concentration, the activation energy is smaller in the isotropic phase (at higher temperatures).

There are “jumps” in the characteristic relaxation time around certain temperatures such as 293–296 K for the CNT-doped samples and 314.15–323.15 K for the pure ILC and the 0.05% CNT doped sample (Figure 7). These jumps can be attributed either to the fitting procedure or to one or more phase transitions. The isotropic–SmA transition is found in the range of 314–323 K. In order to study this phenomenon, the permittivity and dielectric loss were plotted as functions of the frequency in the abovementioned temperature ranges. These curves are shown in Figure 8 and Figure 9. The ILC permittivity as a function of the frequency has three distinct slopes, one between 10^{-1} and 10^2 Hz, one between 10^2 and 10^4 Hz and the third one between 10^4 and 10^7 Hz. This type of dependence also occurs for the CNT doping concentrations of 0.05% and 0.5%.

The dielectric loss of the ILC can be divided in two regions, between 10^{-1} and 10^2 Hz and between $2 \cdot 10^2$ and 10^7 Hz (Figure 8). At lower temperatures, for the CNT-doped samples (Figure 9a,b), the straight lines with the greater slope are seen over a wider frequency range (more evident in Figure 9c, at 293 K). In the dielectric loss spectra, presented in Figure 8 and Figure 9, a dipolar relaxation process was identified in the range of 10^2 – 10^3 Hz, with only the descendent slope being observed. The Havriliak–Negami fitting function (Equation 1) are centered on this process. In the fitting procedure the exponent β was set to 1, and the other parameters were left optimized by fitting the HN function to the experimental data. It was found that the permittivity and the dielectric loss values increase with the temperature for pure ILC and for all CNT-doped samples.

The permittivity and the dielectric loss have high values in the LF domain, both for the pure and the doped-ILC. The high values in the range of 10^6 – 10^8 Hz are due to the presence of

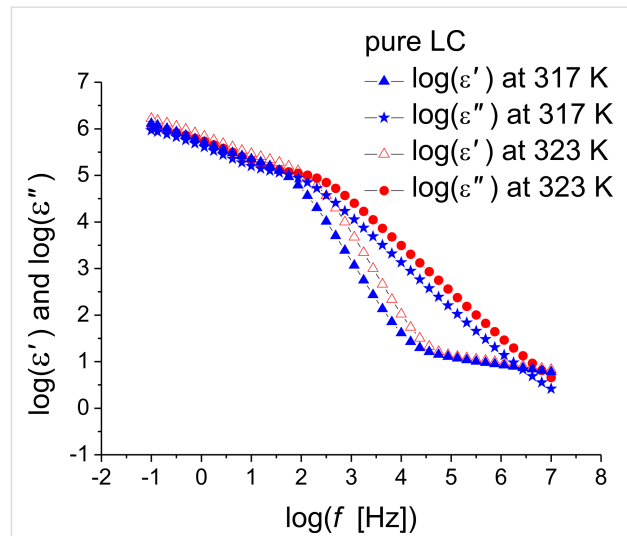


Figure 8: Permittivity and dielectric loss as functions of the frequency (logarithmic scale) for the pure ILC at two constant temperatures, 317 and 323 K.

free ions. Figure 10 shows the variation of the real part of the conductivity as a function of the temperature for the ILC and the CNT-doped ILC. A linear dependency is observed, the change of the slope being attributed to the different phases. This behavior is more clearly observed for the ILC (solid squares) and the ILC doped with 0.05% CNTs (open squares). The conductivity increases with the CNT concentration.

Figure 11 shows the real part of the conductivity of the pure ILC as a function of the frequency (logarithmic scale), at three different constant temperatures. An increase of the conductivity with CNT concentration and temperature is also observed as presented in Figure 12.

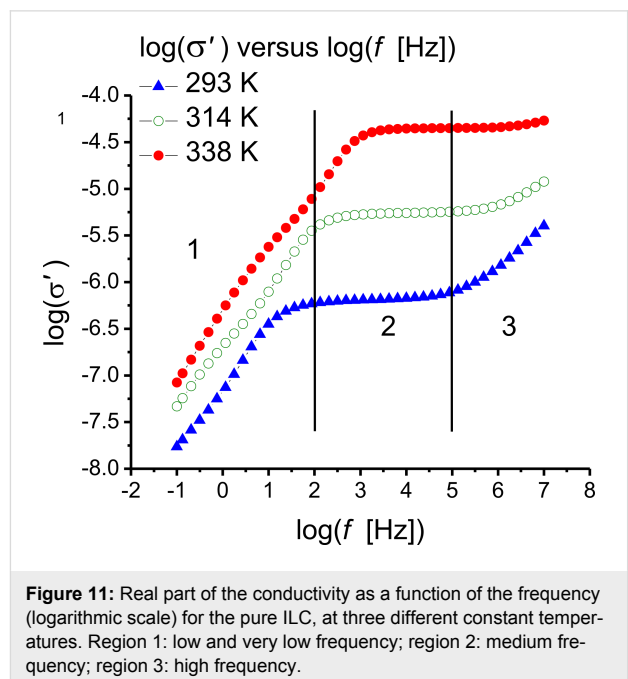
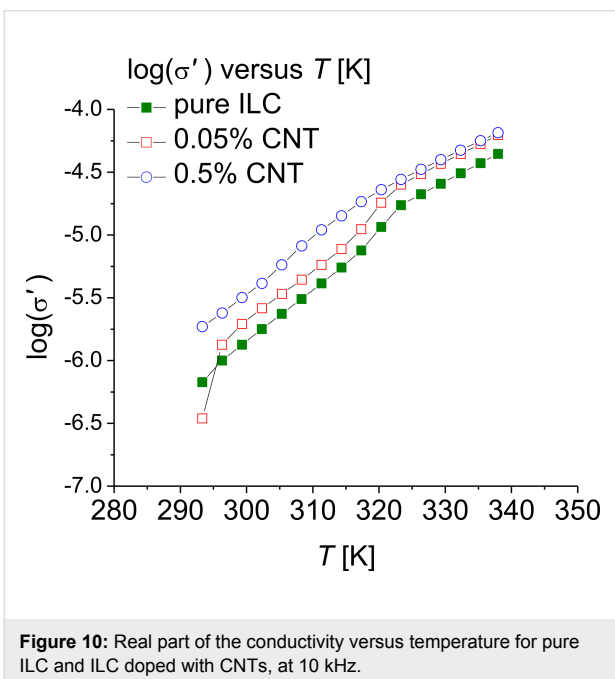
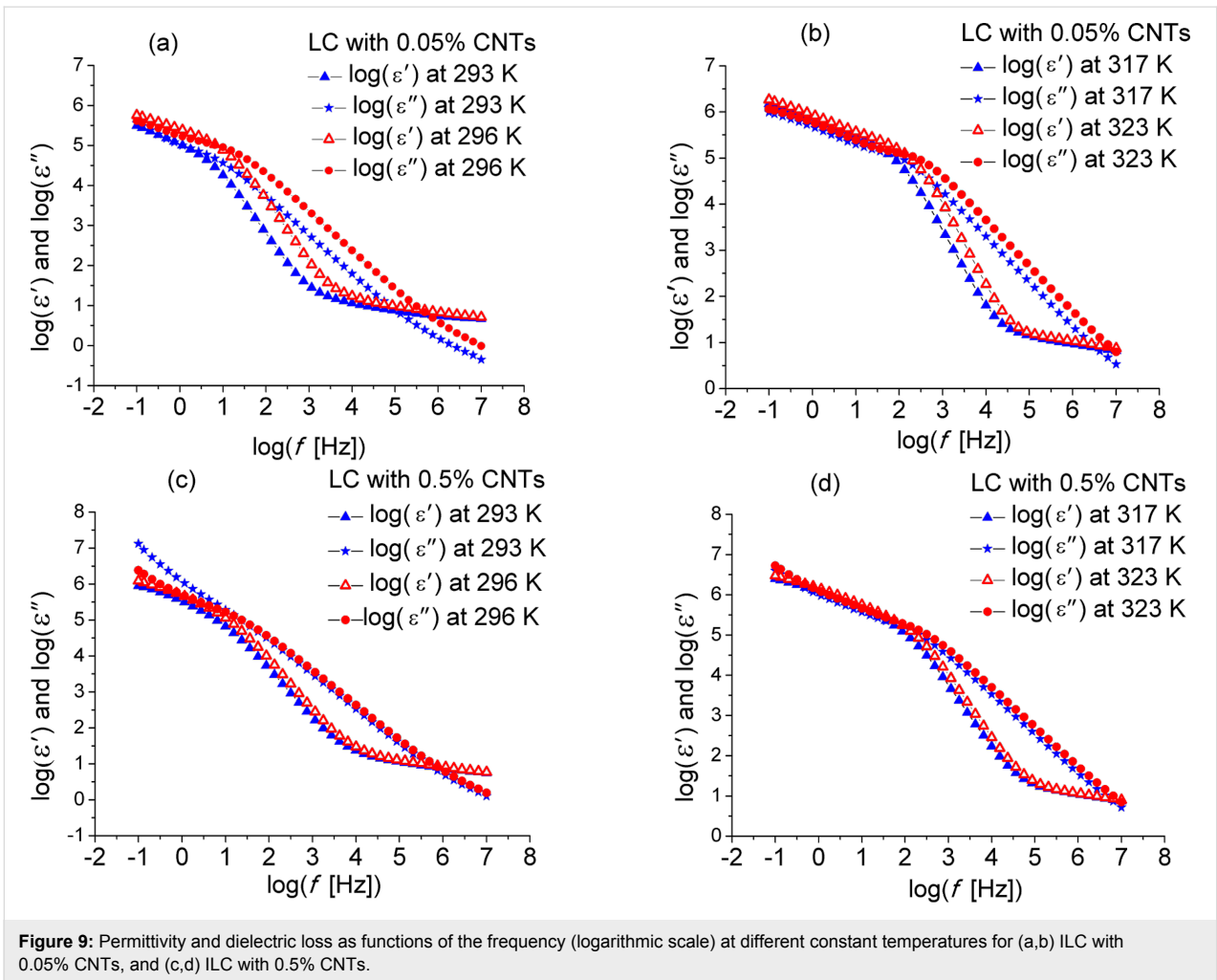
Ionic conductivity

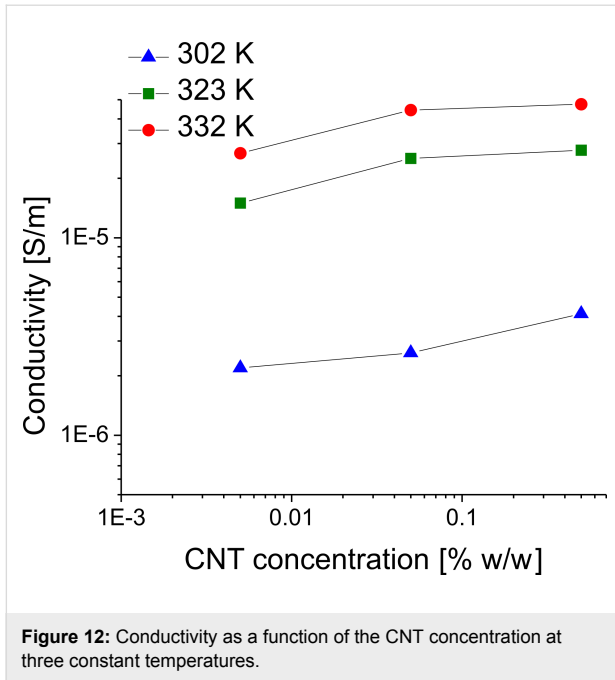
Two major polarizing mechanisms can be studied by means of DS: a) polarization due to orientation of permanent molecular electrical dipoles and b) polarization due to the movement of mobile charge carriers. Due to the presence of mobile charge carriers in LCs, a supplementary induced polarization needs to

Table 1: DS characteristic constants for pure and CNT-doped ILC.

no.	sample type	temperature domain [K]	activation energy, E_a^a [eV]	relaxation time, τ_{max} [s]
1	pure ILC	296–317	0.61	5.500×10^{-13}
		323–338	0.49	1.700×10^{-11}
2	ILC doped with 0.05% CNT	293–317	0.59	1.169×10^{-13}
		323–338	0.47	2.364×10^{-11}
3	ILC doped with 0.5% CNT	309–338	0.46	3.105×10^{-11}

^aIn these calculations, the Vogel temperature was considered zero in the initial fitting. Hence, the VFT equation approximates an Arrhenius-like expression, the material constant A being incorporated into the activation energy E_a .





be considered when interpreting experimental data, namely the electrode polarization, resulting from charge accumulation at the electrode/sample interface.

Experimental data can be presented either by means of the complex dielectric function or of electric conductivity. The AC conductivity $\sigma^*(\omega)$ is a complex function:

$$\sigma^*(\omega) = \sigma'(\omega) + i\sigma''(\omega). \quad (3)$$

In agreement with Maxwell's equations, a direct general relationship can be established between the electrical conductivity and the dielectric permittivity of a medium. For a sinusoidal electric field Equation 3 becomes:

$$\sigma^*(\omega) = \sigma_0 + i\omega\varepsilon_0\varepsilon^*(\omega). \quad (4)$$

The real and the imaginary parts are $\sigma'(\omega) = \sigma_0 + \omega\varepsilon_0\varepsilon''(\omega)$ and $\sigma''(\omega) = \omega\varepsilon_0\varepsilon'(\omega)$, respectively.

As shown in Figure 11, at medium frequencies (10^3 – 10^5 Hz), the ac conductivity and permittivity spectra are controlled by ion movements in the bulk of the electrolyte. At low frequencies (10^{-1} – 10^3 Hz), approximately region 1 in Figure 11, the behavior is controlled by “electrode polarization” effects. Thus, the electric conductivity decreases significantly when the frequency decreases. In the frequency range below 100 MHz, the ionic conductivity spectra obey the Jonscher power law [52,53]:

$$\sigma'(\omega) = \sigma_{dc} + K_c\omega^{1-N}, \quad (5)$$

where $0 < N \leq 1$ and σ_{dc} is the dc conductivity (usually $0.1 \leq N \leq 0.4$). The parameter σ_{dc} is obtained from the electrical conductivity spectra by extrapolation to the $\omega \rightarrow 0$ limit.

For samples with ionic carriers, obtaining the conductivity values, σ_{dc} , is not trivial [38,54,55]. In this case the effects of the electrode polarization and of the ionic conductivity overlap at medium and low frequencies in the conductivity spectra (Figure 11). The electric conductivity is $\sigma_{dc} = q\mu n$, where q is the electrical charge (in C), n is the concentration (in cm^{-3}), and μ is the mobility (in $\text{cm}^2\cdot\text{s}^{-1}\cdot\text{V}^{-1}$).

The bulk electrical ionic conductivity σ_{dc} obeys the Arrhenius law [5]:

$$\sigma_{dc} = \frac{B}{T} \exp\left(-\frac{W_A}{k_B T}\right), \quad (6)$$

where T is the absolute temperature, B is a pre-exponential constant of the material and W_A is a constant associated with the activation energy. Usually, the activation energy includes the energy terms for the formation and migration of ions.

The experimental results showed that the real part of the permittivity, ε' , representing the dielectric conductivity, increases with the increase of CNT concentration; the same behavior was seen for the imaginary part of the permittivity, ε'' , representing the dielectric loss. The permittivity being linked to dipole movements, an increase of the CNT concentration will lead to possible sample heating. Moreover, the ionic conductivity, σ , increases with CNT concentration (Figure 12). In this way, additional heating results from an increase of the CNT concentration, this process being frequency dependent.

Conclusion

A new ILC based on bisimidazolium salt with a spacer of ten carbon atoms and octyl tails and dodecyl sulfate as counterion was synthesized. The SmA phase was unambiguously assigned based on polarized optical microscopy observations and XRD studies while the corresponding phase transition enthalpies were obtained by DSC. The ILC was doped with CNT in concentration of 0.05% w/w and 0.5% w/w. The dielectric spectra were recorded in the frequency range from 10^{-1} to 10^7 Hz. The dependence of the dielectric constant and electric energy loss on frequency and temperature was studied. The activation energy was determined and the characteristic time was obtained by fitting the spectra of the dielectric loss with the

Havriliak–Negami function. The study of the dielectric spectra leads to the following observations: (1) The study of the dielectric permittivity and electric conductivity spectra is complex, due to the superposition of ionic conductivity effect and dipolar relaxation specific to LC. Ionic conductivity is dominant and its effects are indirectly seen through the electrode polarization (EP) effect. (2) The very high dielectric permittivity values and the decrease of the electric conductivity at low frequencies confirm the presence of EP. (3) The doping with CNTs results in an increase of the conductivity. (4) Relaxation times decrease with CNT concentration. (5) In the lower temperature range, the presence of CNTs leads to a decrease of the activation energy while for higher temperatures, the activation energies are very similar for the pure ILC and the doped samples. As expected, the activation energies are lower at higher temperatures.

These preliminary studies revealed an interesting influence of the CNT concentration on the dielectric behavior of the bisimidazolium salt. This investigation will be extended to new ionic liquid crystals with a large range of doping concentration in order to complete the existing image on these aspects. Special attention will be paid to low-frequency studies of the effects related to very low CNT concentration.

Experimental

Characterization methods

All chemicals were used as supplied. C, H, N analyses were carried out with an EuroEA 3300 instrument. IR spectra were recorded on a Bruker spectrophotometer using KBr discs or by using a Jasco FTIR 4200 spectrophotometer coupled to an ATR PIKE GladiATR device. ^1H and ^{13}C NMR spectra were recorded on a Bruker spectrometer operating at 500 MHz, using CDCl_3 as solvent. ^1H chemical shifts were referenced to the solvent peak position, $\delta = 7.26$ ppm. The phase assignment for the bisimidazolium salt was evaluated by polarizing optical light microscopy (POM) [56,57], placed on untreated glass slides, using a Nikon 50iPol microscope equipped with a Linkam THMS600 hot stage and TMS94 control processor. Temperatures and enthalpies of transitions were recorded by using differential scanning calorimetry (DSC) technique employing a Diamond DSC Perkin Elmer instrument. The bisimidazolium salt was studied at a scanning rate of 10 K/min after being encapsulated in an aluminum pan. Three heating–cooling cycles were performed for this sample.

Synthesis of $[\text{bisC}_8\text{ImC}_{10}][\text{C}_{12}\text{OSO}_3]_2$

A solution of sodium dodecyl sulfate (2.18 g, 7.5 mmol) in methanol (60 mL) was added dropwise to a solution of compound **2** (2 g, 3.0 mmol) in dichloromethane (50 mL). The mixture was stirred at room temperature for 1 h after which 100 mL

of deionised water was added. The organic layer was separated and washed repeatedly with water until no reaction with silver nitrate for Br^- was noticed. The organic phase was dried over sodium sulfate followed by solvent removal with a rotary evaporator. The product was recrystallized twice from a mixture of dichloromethane and ethyl ether to yield an off-white waxy solid. Yield 75%, off-white waxy solid. Anal. calcd for $\text{C}_{56}\text{H}_{110}\text{N}_4\text{O}_8\text{S}_2$: C, 65.20; H, 10.75; N, 5.43; found: C, 65.59; H, 11.03; N, 5.27; ^1H NMR (500 MHz, CDCl_3) δ 9.58 (s, 2H), 7.78 (s, 2H), 7.24 (s, 2H), 4.32–4.20 (m, 8H), 4.01 (t, 4H), 1.94–1.84 (t, 8H), 1.64 (t, 4H), 1.42–1.22 (m, 68H), 0.86 (t, 12H); ^{13}C NMR (125 MHz, CDCl_3) δ 136.9, 123.3, 121.6, 67.8, 49.9, 49.4, 31.9; 29.7, 29.6, 29.5, 29.4, 22.7, 14.1; IR (ATR, cm^{-1}): 3136, 3109, 2957, 2919, 2851, 1568, 1467, 1379, 1225, 1169, 1063, 1044, 1005, 932, 792, 723, 623, 580.

Preparation of the mixtures of LC doped with CNTs

Single-walled CNTs (Aldrich code 519308) with a diameter between 1.2 and 5 nm were employed in this study. Two $\text{CNT}/[\text{bisC}_8\text{ImC}_{10}][\text{C}_{12}\text{H}_{25}\text{OSO}_3]_2$ mixtures with different amounts of CNTs (0.5% w/w and 0.05% w/w) were prepared for dielectric measurements by consecutive dilution of an initial sample containing 2% CNTs. The starting sample was prepared by dissolving first the bisimidazolium salt (0.2 g) in a minimum volume of dichloromethane (1 mL) followed by addition of CNT (0.004 g) [58]. The resulting mixture was sonicated for at least 60 min followed by the removal of the solvent, drying in vacuum and cooling at 0 °C. All samples were kept at 0 °C before the physical measurements. Prior to dielectric measurements, the samples were heated to 50 °C and sonicated for at least 15 min to ensure an homogeneous dispersion of CNTs in the ionic liquid crystalline sample.

X-ray diffraction

The X-ray diffraction measurements were made on a D8 Advance diffractometer (Bruker AXS GmbH, Germany), in parallel beam setting, with monochromatized $\text{Cu K}\alpha_1$ radiation ($\lambda = 1.5406$ Å), scintillation detector, and horizontal sample stage. The measurements were performed in symmetric (θ – θ) geometry in the 2θ range from 1.5 to 30° in steps of 0.02°, with measuring times per step in the range of 5–40 s. The sample was deposited on a Si(100) plate, heated to the isotropic state and then cooled down to room temperature prior to data acquisition.

Dielectric spectroscopy

The dielectric spectroscopy measurements were performed using a broadband dielectric spectrometer, NOVOCONTROL, with an Alpha-A high-performance frequency analyzer in the LF domain (0.01 to 10^7 Hz), equipped with WinDETA soft-

ware. The temperature was controlled within 0.2 K, at a constant ac voltage of 0.5 V.

Acknowledgements

Constantin Paul Ganea thanks the Romanian Ministry of Education and Research for financial support under PN16-480101 of CORE Program. Viorel Cîrcu acknowledges the funding from UEFISCDI, project number PN-II-ID-PCE-2011-3-0384. Doina Manaila Maximean thanks Ligia Frunza and Stefan Frunza for useful discussions.

ORCID® iDs

Viorel Cîrcu - <https://orcid.org/0000-0001-9725-9577>

References

- Goossens, K.; Lava, K.; Bielawski, C. W.; Binnemans, K. *Chem. Rev.* **2016**, *116*, 4643–4807. doi:10.1021/cr400334b
- Axenov, K. V.; Laschat, S. *Materials* **2011**, *4*, 206–259. doi:10.3390/ma4010206
- Cîrcu, V. Ionic Liquid Crystals Based on Pyridinium Salts. In *Progress and Developments in Ionic Liquids*; Handy, S., Ed.; InTech: Rijeka, Croatia, 2017; pp 285–311. doi:10.5772/65757
- Yang, M.; Stappert, K.; Mudring, A.-V. *J. Mater. Chem. C* **2014**, *2*, 458–473. doi:10.1039/C3TC31368A
- Robertson, L. A.; Schenkel, M. R.; Wiesenauer, B. R.; Gin, D. L. *Chem. Commun.* **2013**, *49*, 9407–9409. doi:10.1039/C3CC44452J
- Noujeim, N.; Samsam, S.; Eberlin, L.; Sanon, S. H.; Rochefort, D.; Schmitzer, A. R. *Soft Matter* **2012**, *8*, 10914–10920. doi:10.1039/C2SM26213D
- Bara, J. E.; Hatakeyama, E. S.; Wiesenauer, B. R.; Zeng, X.; Noble, R. D.; Gin, D. L. *Liq. Cryst.* **2010**, *37*, 1587–1599. doi:10.1080/02678292.2010.521859
- Kumar, S.; Gupta, S. K. *Tetrahedron Lett.* **2010**, *51*, 5459–5462. doi:10.1016/j.tetlet.2010.08.022
- D'Anna, F.; Noto, R. *Eur. J. Org. Chem.* **2014**, *20*, 4201–4223. doi:10.1002/ejoc.201301871
- Pană, A.; Iliș, M.; Staicu, T.; Pasuk, I.; Cîrcu, V. *Liq. Cryst.* **2016**, *43*, 381–392. doi:10.1080/02678292.2015.1116630
- Anderson, J. L.; Ding, R. F.; Ellern, A.; Armstrong, D. W. *J. Am. Chem. Soc.* **2005**, *127*, 593–604. doi:10.1021/ja046521u
- Pană, A.; Iliș, M.; Micutz, M.; Dumitrașcu, F.; Pasuk, I.; Cîrcu, V. *RSC Adv.* **2014**, *4*, 59491–59497. doi:10.1039/C4RA11023D
- Bhadani, A.; Misono, T.; Singh, S.; Sakai, K.; Sakai, H.; Abe, M. *Adv. Colloid Interface Sci.* **2016**, *231*, 36–58. doi:10.1016/j.cis.2016.03.005
- Pietralik, Z.; Kolodziejska, Ż.; Weiss, M.; Kozak, M. *PLoS One* **2015**, *10*, e0144373. doi:10.1371/journal.pone.0144373
- Zhou, T.; Llizo, A.; Li, P.; Wang, C.; Guo, Y.; Ao, M.; Bai, L.; Wang, C.; Yang, Y.; Xu, G. *J. Phys. Chem. C* **2013**, *117*, 26573–26581. doi:10.1021/jp4061363
- Andrzejewska, W.; Wilkowska, M.; Chrabaszczewska, M.; Kozak, M. *RSC Adv.* **2017**, *7*, 26006–26018. doi:10.1039/C6RA24978G
- Kamboj, R.; Singh, S.; Bhadani, A.; Kataria, H.; Kaur, G. *Langmuir* **2012**, *28*, 11969–11978. doi:10.1021/la300920p
- Bhadani, A.; Singh, S. *Langmuir* **2011**, *27*, 14033–14044. doi:10.1021/la202201r
- Rodrigues, M.; Calpena, A. C.; Amabilino, D. B.; Garduño-Ramírez, M. L.; Pérez-García, L. *J. Mater. Chem. B* **2014**, *2*, 5419–5429. doi:10.1039/C4TB00450G
- Ilișcă, T. A.; Pasuk, I.; Cîrcu, V. *New J. Chem.* **2017**, *41*, 11113–11124. doi:10.1039/C7NJ02561K
- Saielli, G.; Bagno, A.; Wang, Y. *J. Phys. Chem. B* **2015**, *119*, 3829–3836. doi:10.1021/jp5104565
- Bruce, D. W.; Estdale, S.; Guillon, D.; Heinrich, B. *Liq. Cryst.* **1995**, *19*, 301–305. doi:10.1080/02678299508031983
- Cruz, C.; Heinrich, B.; Ribeiro, A. C.; Bruce, D. W.; Guillon, D. *Liq. Cryst.* **2000**, *27*, 1625–1631. doi:10.1080/026782900750037185
- Lava, K.; Evrard, Y.; Van Hecke, K.; Van Meervelt, L.; Binnemans, K. *RSC Adv.* **2012**, *2*, 8061–8070. doi:10.1039/C2RA21208K
- Cardinaels, T.; Lava, K.; Goossens, K.; Eliseeva, S. V.; Binnemans, K. *Langmuir* **2011**, *27*, 2036–2043. doi:10.1021/la1047276
- Haristoy, D.; Tsiourvas, D. *Liq. Cryst.* **2004**, *31*, 697–703. doi:10.1080/02678290410001675110
- Mihelj, T.; Popović, J.; Skoko, Ž.; Tomašić, V. *Thermochim. Acta* **2014**, *591*, 119–129. doi:10.1016/j.tca.2014.07.024
- Nikokavoura, A.; Tsiourvas, D.; Arkas, M.; Sideratou, Z.; Paleos, C. M. *Liq. Cryst.* **2002**, *29*, 1547–1553. doi:10.1080/0267829021000034808
- Rettenmeier, E.; Tokarev, A.; Blanc, C.; Dieudonné, P.; Guari, Y.; Hesemann, P. *J. Colloid Interface Sci.* **2011**, *356*, 639–646. doi:10.1016/j.jcis.2011.01.055
- Wang, Y.; Marques, E. F. *J. Phys. Chem. B* **2006**, *110*, 1151–1157. doi:10.1021/jp0552729
- Wang, Y.; Marques, E. F. *J. Therm. Anal. Calorim.* **2010**, *100*, 501–508. doi:10.1007/s10973-009-0653-8
- Westphal, E.; Henrique da Silva, D.; Molin, F.; Gallardo, H. *RSC Adv.* **2013**, *3*, 6442–6454. doi:10.1039/C3RA23456H
- Lagerwall, J. P. F.; Scalia, G. *J. Mater. Chem.* **2008**, *18*, 2890–2898. doi:10.1039/b802707b
- Rahman, M.; Lee, W. *J. Phys. D: Appl. Phys.* **2009**, *42*, 063001. doi:10.1088/0022-3727/42/6/063001
- Dolgov, L.; Kovalchuk, O.; Lebovka, N.; Tomylo, S.; Yaroshchuk, O. Liquid crystal dispersions of carbon nanotubes: dielectric, electro-optical and structural peculiarities. In *Carbon Nanotubes*; Marulanda, J. M., Ed.; InTech: Rijeka, Croatia, 2010; pp 451–484. doi:10.5772/39439
- Dierking, I.; Scalia, G.; Morales, P.; LeClere, D. *Adv. Mater.* **2004**, *16*, 865–869. doi:10.1002/adma.200306196
- Rosu, C.; Manaila-Maximean, D.; Donescu, D.; Frunza, S.; Sterian, A. R. *Mod. Phys. Lett. B* **2010**, *24*, 65–73. doi:10.1142/S0217984910022238
- Ganea, C. P.; Manaila-Maximean, D. *UPB Sci. Bull., Ser. A* **2011**, *73*, 209–216.
- Blinov, L. M.; Chigrinov, V. G. *Electrooptic Effects in Liquid Crystal Material*; Springer: New York, NY, U.S.A., 1996. doi:10.1007/978-1-4612-2692-5
- Koval'chuk, A. V.; Dolgov, L.; Yaroshchuk, O. *Semicond. Phys., Quantum Electron. Optoelectron.* **2008**, *11*, 337–341.
- Chen, H.-Y.; Lee, W. *Appl. Phys. Lett.* **2006**, *88*, 222105. doi:10.1063/1.2208373
- Lee, W.; Chen, H.-Y.; Shih, Y.-C. *J. Soc. Inf. Disp.* **2008**, *16*, 733–741.
- García-García, A.; Vergaz, R.; Algorri, J. F.; Quintana, X.; Otón, J. M. *Beilstein J. Nanotechnol.* **2015**, *6*, 396–403. doi:10.3762/bjnano.6.39
- Tomylo, S.; Yaroshchuk, O.; Koval'chuk, O.; Lebovka, N. *Phys. Chem. Chem. Phys.* **2017**, *19*, 16456–16463. doi:10.1039/C7CP01722G

45. Lee, J. J.; Yamaguchi, A.; Alam, Md. A.; Yamamoto, Y.; Fukushima, T.; Kato, K.; Takata, M.; Fujita, N.; Aida, T. *Angew. Chem., Int. Ed.* **2012**, *51*, 8490–8494. doi:10.1002/anie.201203284
46. Hunt, P. A.; Ashworth, C. R.; Matthews, R. P. *Chem. Soc. Rev.* **2015**, *44*, 1257–1288. doi:10.1039/C4CS00278D
47. Dong, K.; Zhang, S.; Wang, J. *Chem. Commun.* **2016**, *52*, 6744–6764. doi:10.1039/C5CC10120D
48. Men, S.; Mitchell, D. S.; Lovelock, K. R. J.; Licence, P. *ChemPhysChem* **2015**, *16*, 2211–2218. doi:10.1002/cphc.201500227
49. Wulf, A.; Fumino, K.; Michalik, D.; Ludwig, R. *ChemPhysChem* **2007**, *8*, 2265–2269. doi:10.1002/cphc.200700508
50. He, H.; Chen, H.; Zheng, Y.; Zhang, S.; Yu, Z. *Chem. Eng. Sci.* **2015**, *121*, 169–179. doi:10.1016/j.ces.2014.07.024
51. Headley, A. D.; Jackson, N. M. *J. Phys. Org. Chem.* **2002**, *15*, 52–55. doi:10.1002/poc.449
52. Kremer, F.; Schönhal, A., Eds. *Broadband Dielectric Spectroscopy*; Springer-Verlag: Berlin-Heidelberg, Germany, 2003. doi:10.1007/978-3-642-56120-7
53. Dyre, J. C.; Maass, P.; Roling, B.; Sidebottom, D. L. *Rep. Prog. Phys.* **2009**, *72*, 046501. doi:10.1088/0034-4885/72/4/046501
54. Jacobs, J. D.; Koerner, H.; Heinz, H.; Farmer, B. L.; Mirau, P.; Garrett, P. H.; Vaia, R. A. *J. Phys. Chem. B* **2006**, *110*, 20143–20157. doi:10.1021/jp061931l
55. Klein, R. J.; Zhang, S.; Dou, S.; Jones, B. H.; Colby, R. H.; Runta, J. *J. Chem. Phys.* **2006**, *124*, 144903. doi:10.1063/1.2186638
56. Kumar, J.; Manjuladevi, V.; Gupta, R. K.; Kumar, S. *Liq. Cryst.* **2016**, *43*, 488–496. doi:10.1080/02678292.2015.1119320
57. García-García, A.; Vergaz, R.; Algorri, J. F.; Zito, G.; Cacace, T.; Marino, A.; Otón, J. M.; Geday, M. A. *Beilstein J. Nanotechnol.* **2016**, *7*, 825–833. doi:10.3762/bjnano.7.74
58. Jagadish, K.; Srikantaswamy, S.; Byrappa, K.; Shruthi, L.; Abhilash, M. R. *J. Nanomater.* **2015**, *2015*, No. 381275. doi:10.1155/2015/381275

License and Terms

This is an Open Access article under the terms of the Creative Commons Attribution License (<http://creativecommons.org/licenses/by/4.0>), which permits unrestricted use, distribution, and reproduction in any medium, provided the original work is properly cited.

The license is subject to the *Beilstein Journal of Nanotechnology* terms and conditions: (<http://www.beilstein-journals.org/bjnano>)

The definitive version of this article is the electronic one which can be found at: [doi:10.3762/bjnano.9.19](https://doi.org/10.3762/bjnano.9.19)



Research articles

New grafted ferrite particles/liquid crystal composite under magnetic field



D. Manaila Maximean

Physics Department, University "Politehnica Bucuresti", Spl. Independentei 313, R-060042 Bucharest, Romania

ARTICLE INFO

Article history:

Received 23 July 2017

Received in revised form 20 November 2017

Accepted 28 December 2017

Available online 29 December 2017

Keywords:

Liquid crystals

Magnetic nanomaterials

Ferrofluids

Colloidal particles

Nanocomposites

Fredericksz transition

ABSTRACT

A new colloidal composite formed by specially synthesized dimethylphenyl ferrite particles and a nematic liquid crystal (LC) is presented. By applying a small magnetic field during polarizing optical microscopy observations, it was found that the magnetic moment of the synthesized ferrite is perpendicular to the director of the LC. The optical transmission of laser light across the ferrofluid was investigated under magnetic field. The critical magnetic field corresponding to the Fredericksz transition was obtained and discussed according to the Burylov and Raikher theory.

© 2017 Elsevier B.V. All rights reserved.

1. Introduction

Many organic substances do not present a unique transition between solid and liquid, but a serial of transitions, passing through states with intermediate properties between crystal and liquid [1,2]. Liquid crystals (LCs) are characterized by the presence of orientational order and the total or partial absence of positional order [1–3].

Application of LC as displays have boosted the scientific interest [3–5] and, in the last decade, new LCs [6–8] and nanoparticles dispersions in LCs [9–13] are designed for application in organic electronics, as e.g. organic light-emitting diode, thin film transistors, light valves, solar cells.

When used in conjunction with magnetite particles, new composite materials known as ferrofluids (FN) are obtained [14–16]. In this paper, a new highly ordered FN formed by using a specially synthesized ferrite particle with phenyl terminal groups, compatible with the LC, is presented. The mixtures exhibited long term stability (month-order). Sandwich type samples using glass plates with homeotropic and planar alignment to the substrate were manufactured.

The samples were placed in magnetic field, under crossed polarizers, and investigated by measuring the optical transmission of the laser light. When slowly increasing the magnetic field, at the

critical value B_c , the LC's molecular director exhibits a change in orientation, leading to a variation of the refractive index. This, in turn, leads to a change in the intensity of the emerging laser beam, indicating the start of the Fredericksz transition. Under static magnetic field conditions, the Fredericksz transition was obtained and the critical magnetic fields determined.

2. Experimental

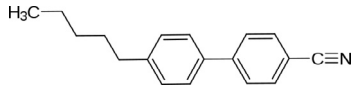
2.1. Particle synthesis

To obtain magnetic particles with a good compatibility with a liquid crystal having phenyl terminal groups, K15 (Merck) in this case, the phenyl group was chemically included in the magnetite particle, during its synthesis. The obtained particles are of the "hairy" type, with the phenyl ending groups towards the LC. Starting from Fe_3O_4 and CH_2Cl_2 a dispersion was formed by mechanic agitation at 350 rot/min, in controlled nitrogen atmosphere [17]. The dispersion was stirred for 30 min, ultrasonicated for 5 min and then the precursor dimethylphenyl ethoxysilane compatibilizer agent was added and the mixture was stirred for another 3 h. The final compound was washed with CH_2Cl_2 and dried. The mole fraction of the reactant (surfactant) at 100 g was determined by TGA and was 0.0408 for dimethylphenyl ethoxysilane (PhMe2ES). The final compound particles are dimethylphenyl ferrite, $Fe_3O_4(CH_3)_2C_6H_5$, particle code: DFF, and have a diameter of 168 nm determined by DLS.

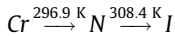
E-mail address: doina.manaila@physics.pub.ro

2.2. Sample preparation

The obtained particles were mixed with the K15 thermotropic LC, from Merck, as presented in Table 1. Liquid crystal K15 (or 5CB) is 4-cyano-4'-pentylbiphenyl, chemical formula $C_{18}H_{19}N$:



The transition temperatures are:



where *Cr* stands for crystalline state, *N* – nematic and *I* – isotropic and has a positive dielectric anisotropy $\Delta\epsilon > 0$. Being a thermotropic LC, its magnetic anisotropy, χ_a , is positive; thus, when subjected to a strong enough magnetic field, the LC molecules will reorient in the direction of the magnetic field [3].

Table 1
Characteristics of LC and FN samples.

No	Sample code	Composition	Alignment of glass plates	Concentration % by mass
1	H0(K15)	Liquid crystal K15	homeotropic	–
2	H1/(K15/DFF)	K15/dimethylphenyl ferrite particles	homeotropic	0.05
3	H2/(K15/DFF)	K15/dimethylphenyl ferrite particles	homeotropic	0.1
4	H3/(K15/DFF)	K15/dimethylphenyl ferrite particles	homeotropic	0.2
5	P0(K15)	Liquid crystal K15	planar	–
6	P1/(K15/DFF)	K15/dimethylphenyl ferrite particles	planar	0.05
7	P2/(K15/DFF)	K15/dimethylphenyl ferrite particles	planar	0.1
8	P3/(K15/DFF)	K15/dimethylphenyl ferrite particles	planar	0.2

Sandwich type glass cell, consisting of two glass plates separated by spacers have been prepared. For homeotropic-aligned cells DMOAP, Dimethyloctadecyl [3-(trimethoxysilyl) propyl] ammonium chloride was used, in the following ratios: 899 parts isopropanol, 100 parts distilled water, 1 part DMOAP. The solution was deposited onto glass plates by spin coating and polymerized for 15 min at 100 °C. For planar alignment, the glass plates were treated with a 0.1% concentration polyvinyl alcohol, deposited by spin coating and polymerized at 120 °C for one hour, slowly cooled down to room temperature, and rubbed with a smooth cloth in the direction of alignment. The cell thickness was of about 150 μm .

The nominal parameters of the samples are presented in Table 1. The LC and the LC-DFF composite have been filled in the cells and sealed.

2.3. Experimental apparatus

The experimental setup used to study the influence of magnetic field on the FN is schematically presented in Fig. 1 and discussed in detail in [18].

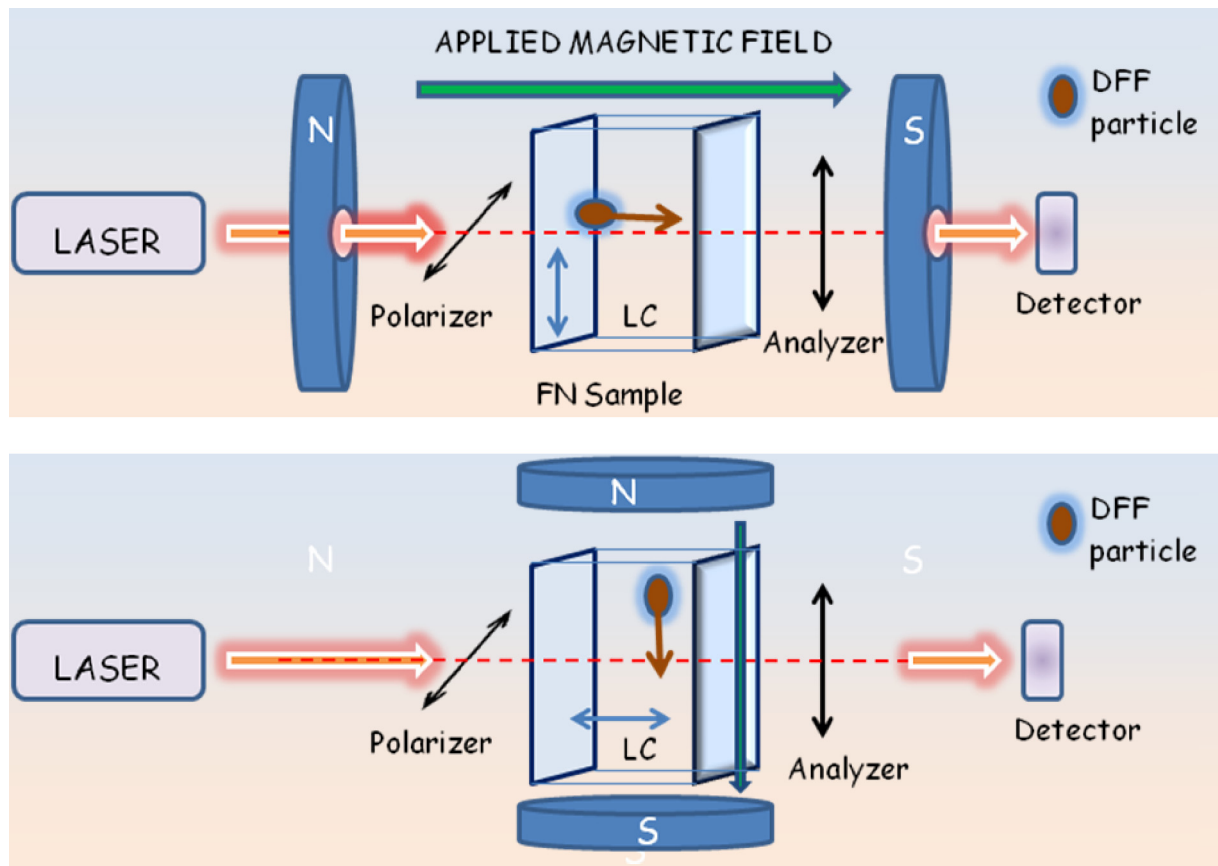


Fig. 1. Experimental set-up for: (up) planar aligned FN; (down) homeotropic alignment. The direction of initial alignment of LC is marked by double arrow.

A linearly polarized laser light, (632.8 nm; 2.5mW), with superior spatial and spectral resolution, passes through the sample placed under crossed polarizers, in magnetic field. The magnetic field is obtained using an electromagnet, with 35 cm diameter poles and iron core of 10 cm. To observe the samples in the same direction as the magnetic field, a 5 mm diameter hole was drilled in the center of the iron core. The light detection is ensured by a Silicon p-i-n photodiode connected to a high precision multimeter [19].

3. DFF particle – Liquid crystal interaction under magnetic field

3.1. Interaction between DF ferrite particles and LC

Due to the DFF particle properties, the LC homeotropic alignment to the particle surface is probable. Considering a very small chain of particles, as presented in Fig. 2, the direction of the magnetization of the particle \vec{m} is than perpendicular to the nematic director \vec{n} .

The first observation of a macroscopic collective behavior of a LC doped with magnetic particles was reported by Chen and Amer [20]. In their experiment, an observation cell was employed, having homeotropic alignment and filled with FN; the magnetic moment was oriented perpendicular to the LC director by using a very small magnetic field. This cell appears dark between crossed polarizers, due to the homeotropic alignment, if the magnetic field is zero. When applying a magnetic field parallel to direction of the glass plate alignment, the entire cell becomes birefringent, due to the reorientation of the magnetic moment of the particles that will drive the whole LC matrix. If the magnetic field is applied parallel to the magnetic moment of the particles, birefringence does not occur. This leads to the conclusion that initially the nematic director is perpendicular to the magnetic moment of the particle, $\vec{n} \perp \vec{m}$.

3.2. Theoretical considerations

Based on the observation of Chen and Amer, Burylov and Raiher [21–23] considering that the anchoring energy between the LC and the particle is finite, have proven that the equilibrium orientational state is achieved when the nematic director is perpendicular to the local magnetization and that an analogue of the classical Freedericksz transition in nematic LC is permitted in FN [22].

The free energy density for a magnetite-LC composite, f_{FN} is the sum of the density energies describing the interactions present in the system:

$$f_{FN} = f_{LC} + f_{LC-B} + f_{F-B} + f_T + f_{F-LC} \quad (1)$$

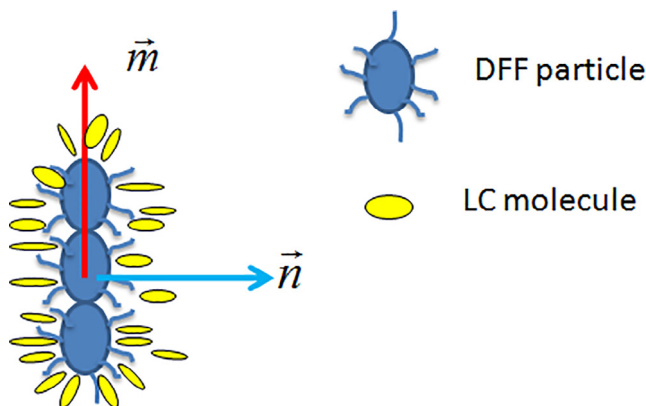


Fig. 2. Interaction of a small chain of DFF particles with LC.

where f_{LC} is the free energy density of the nematic LC, f_{LC-B} is the free energy density resulted from the interaction between the nematic LC and the magnetic field, f_{F-B} takes into consideration the interaction between the dimethylphenyl ferrite (DFF) particles and the magnetic field, and f_T accounts for the presence of particles in suspension and f_{F-LC} is the free energy density for the ferrite-LC interaction. Accordingly:

$$f_{LC} = \frac{1}{2} \left[k_1 (\vec{n} \nabla \vec{n})^2 + k_2 (\vec{n} \nabla \times \vec{n})^2 + k_3 (\vec{n} \times (\nabla \times \vec{n}))^2 \right] \quad (2)$$

where k_1, k_2, k_3 are the elastic constant for the splay, twist and bend deformations, respectively and \vec{n} is the nematic director;

$$f_{LC-B} = -\frac{1}{2} \mu_0^{-1} \chi_a (\vec{n} \vec{B})^2 \quad (3)$$

where μ_0 is the vacuum susceptibility, χ_a -magnetic anisotropy of the LC, $\chi_a > 0$, \vec{B} -magnetic field induction;

$$f_{F-B} = M_s f (\vec{m} \cdot \vec{B}) = -\frac{1}{2} \frac{f \chi_{am}}{\mu_0} (\vec{m} \cdot \vec{B})^2 \quad (4)$$

where M_s -saturation magnetisation of the particles, f is the particle concentration in LC, χ_{am} -magnetic anisotropy of the magnetite particles, $\chi_{am} > 0$, \vec{m} -unit vector of the magnetic moment of the ferroparticle;

$$f_T = \left(\frac{f k_B T}{v} \right) \ln f \quad (5)$$

where k_B -Boltzmann's constant, T -absolute temperature, v -volume of each particle, f is the particle concentration in LC.

$$f_{F-LC} = \left(\frac{fW}{a} \right) (\vec{n} \cdot \vec{m}) \quad (6)$$

where W is the surface density of the anchoring energy LC-particle and a is the particle diameter.

3.3. Homeotropic alignment and static magnetic field

In Fig. 3 is presented a FN cell with homeotropic alignment of the nematic. In the absence of the magnetic field, Fig. 3a), the unit vector of the magnetic moment of the ferrite is perpendicular on the nematic initial orientation. The increase of the magnetic field, distorts the nematic direction and the magnetic moment versor, as presented in Fig. 3b), thus destabilizing the LC matrix, and simultaneously stabilizing the magnetic particle alignment [24–28], since the \vec{m} is parallel to the magnetic field.

For very small angular deviations, the critical magnetic field for the FN in homeotropic aligned cells, $B_{c, FNhomeo}^2$ is obtained as [24]:

$$B_{c, FNhomeo}^2 = \frac{\mu_0 k_3}{\chi_a} \left(\frac{\pi}{d} \right)^2 + \frac{2\mu_0 fW}{a\chi_a} \quad (7)$$

where d is the thickness of the sample. By taking into account that $\frac{\mu_0 k_3}{\chi_a} \left(\frac{\pi}{d} \right)^2 = B_{c, LChomeo}^2$, where $B_{c, LChomeo}$ is the critical magnetic field for the pure nematic. Denoting $G^2 = \frac{2\mu_0 fM_s B W}{\chi_a (2W + M_s B a)} = \frac{2\mu_0 fW}{a\chi_a \left(\frac{2W}{M_s B a} + 1 \right)} \approx \frac{2\mu_0 fW}{a\chi_a}$,

valid for $\frac{2W}{M_s B a} \ll 1$, results [19]:

$$\tilde{B}_{c, FNhomeo}^2 = B_{c, LChomeo}^2 + G^2 \quad (8)$$

$$\tilde{B}_{c, FNhomeo}^2 = \frac{\mu_0 k_3}{\chi_a} \left(\frac{\pi}{d} \right)^2 + \frac{2\mu_0 fW}{a\chi_a} \quad (9)$$

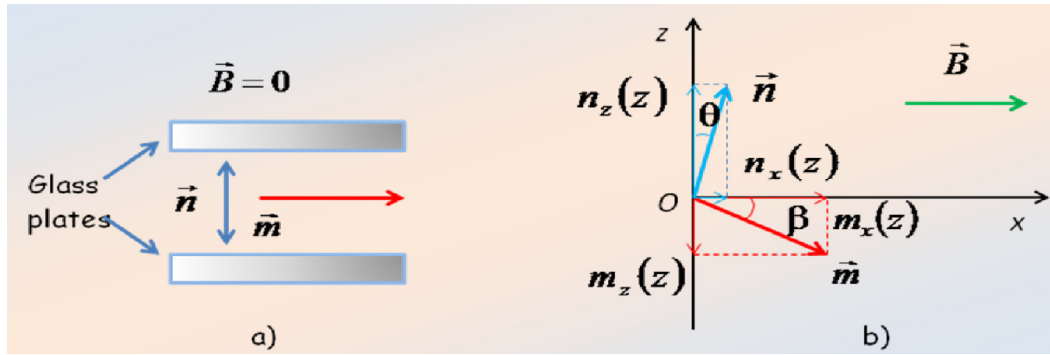


Fig. 3. Homeotropic alignment: $\vec{B} = 0$ a) and magnetic field applied along Ox axis b).

According to Eq. (9) the critical magnetic field at which the density energy minimizes is greater than in the case of pure LC, since the coupling between the magnetic particle and LC opposes to the reorientation of the LC matrix in the presence of magnetic field. This explains why the critical magnetic field increases with the magnetic particle concentration.

In lyotropic LC, because the magnetic anisotropy of the lyotropic LC is negative, the critical magnetic field of the LC-particle system decreases [13,15,16,18].

3.4. Planar alignment of LC under static magnetic field

In Fig. 4 is schematically presented a FN in homotropic alignment conditions. The magnetic moment of the particle is \vec{m} , and the magnetic field is perpendicular to the glass plates.

Considering the expression of free energy density for the ferromagnetic, f_{FN} , in the Euler-Lagrange eqs. [22], for very small deviation angles, it results the critical magnetic field of the FN, $B_{c,FNplanar}^2$:

$$B_{c,FNplanar}^2 = \frac{\mu_0 k_1}{\chi_a} \left(\frac{\pi}{d}\right)^2 + \frac{2\mu_0 fW}{a\chi_a} \tag{10}$$

Taking into account that $\frac{\mu_0 k_1}{\chi_a} \left(\frac{\pi}{d}\right)^2 = B_{c,LCplanar}^2$, where B_c is the critical magnetic field for the pure LC.

The critical magnetic field for the FN is:

$$B_{c,FNplanar}^2 = B_{c,LCplanar}^2 + G^2 \tag{11}$$

Thus, in the FN with planar alignment the critical magnetic field for the Fredericksz transition also increases, relation (11) being similar to relation (9), the difference consisting in the replacement of k_3 with k_1 .

4. Results and discussions

4.1. POM observations

In order to establish the initial mutual orientation between the magnetic moment of the DFF particle and the nematic director,

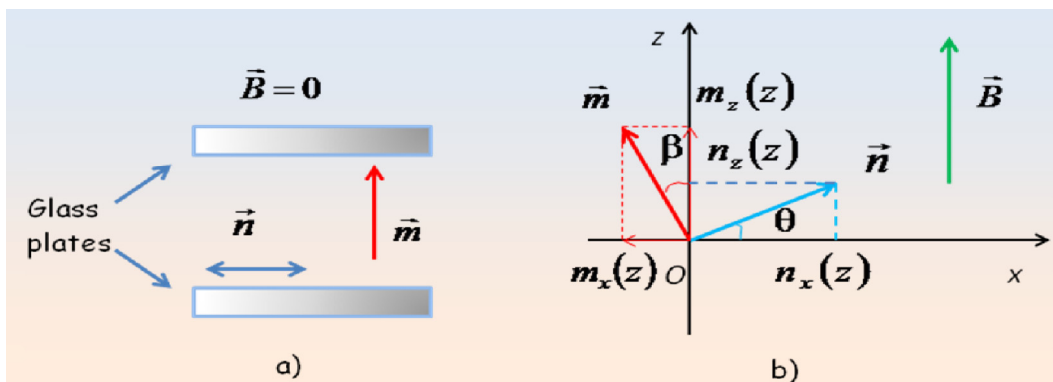


Fig. 4. Planar alignment: $\vec{B} = 0$ a) and magnetic field applied along Oz axis b).

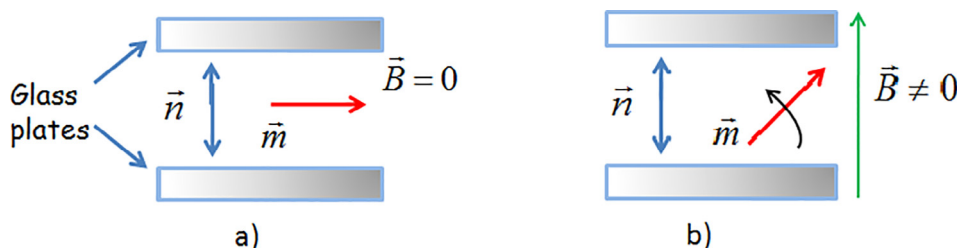


Fig. 5. Schematically presentation of the FN behavior, the double arrow marks the direction of the alignment, \vec{n} , and \vec{m} marks the magnetic moment of the particles. When the magnetic field is applied, \vec{m} turns to align to \vec{B} .

POM observations have been employed. A DFF/K15 sample of 150 μm thickness and 0.5% b.w. concentration with homeotropic treatment of the glasses was used, as schematically presented in Fig. 5a. Initially, a small magnetic field, of about 1G was applied, parallel to one side of the glass plate, as presented in Fig. 6a. It has the role to ensure the orientation of all DFF magnetic dipoles in the direction of the applied magnetic field. The sample was observed between

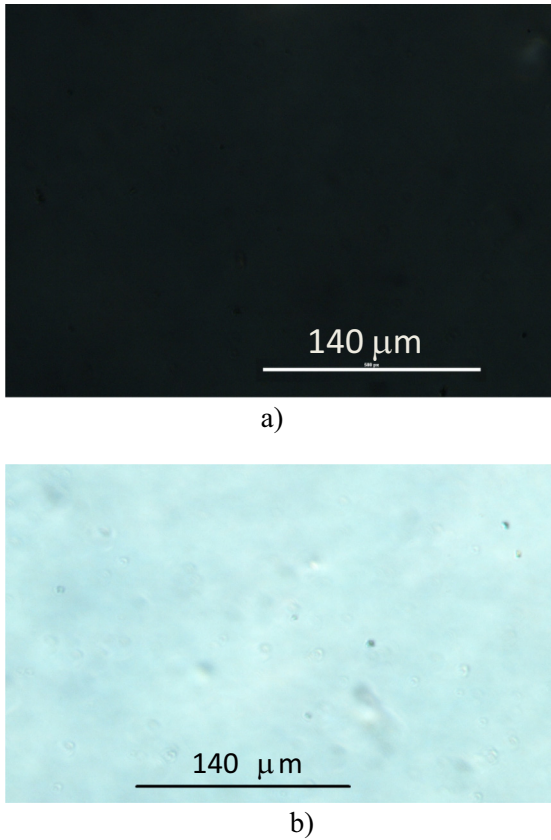


Fig. 6. POM images of a DFF/K15 sample: without applied magnetic field, between crossed polarizers, the sample is dark, (6a); when a 15G magnetic field is applied in the direction of the glass plate alignment (homeotropic), the sample is bright, (6b).

crossed polarizers, and a dark image was observed, as presented in Fig. 6a.

Then a 15 G magnetic field was applied parallel to the LC director, as presented in Fig. 5b. The observed image is bright, the sample becomes birefringent, as shown in the POM image presented in Fig. 6b. The explanation of the change is due to the reorientation of the DFF magnetic moment in the direction of the magnetic field and, due to the coupling between the particles and the LC, the LC molecules will be driven in the movement, as schematically shown in Fig. 6b. This leads to the conclusion that initially the nematic director is perpendicular to the magnetic moment of the particle, $\vec{n} \perp \vec{m}$.

4.2. Freedericksz transitions

4.2.1. Homeotropic alignment

When slowly increasing the magnetic field, the laser light transmission through the homeotropically aligned samples was measured. In Fig. 7a) is presented the light intensity versus magnetic field induction for the pure LC sample H0 and in Fig. 7b) the optical transmission for the FN sample H2. The critical magnetic field, B_c (homeo), corresponding to the Freedericksz transitions are presented in Table 2.

In Fig. 8 is presented the dependency of the square of the critical magnetic field on particle concentration. Considering Eq. (9), the slope p is:

$$\frac{B_c^2}{f} = \frac{2\mu_0 W}{\chi_a n a} = p \tag{12}$$

It was found from the graphical representation $p \approx 1.17^2$. Introducing numerical values for the magnetic anisotropy $\chi_a = 1.43 \cdot 10^{-6}$, $a = 170$ nm, results the value of the anchoring energy density $W = 1 \cdot 10^{-7} N/m$.

Table 2
Critical magnetic field for the homeotropic aligned samples.

	Sample	$B_{c(homeo)}$ [G]
1	H0	510
2	H1	583
3	H2	625
4	H3	701

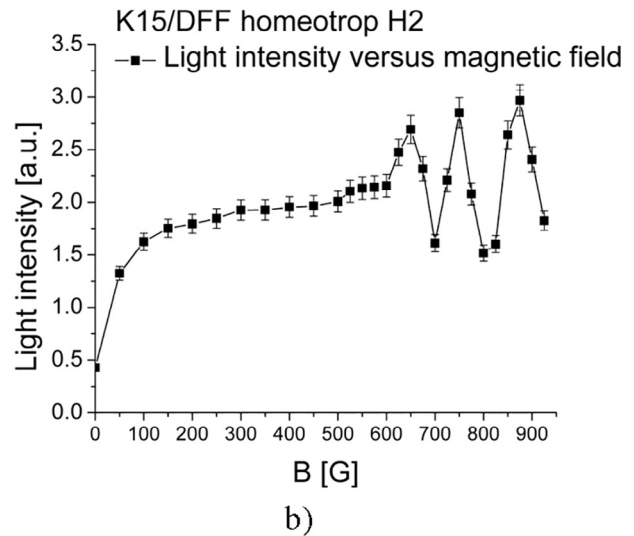
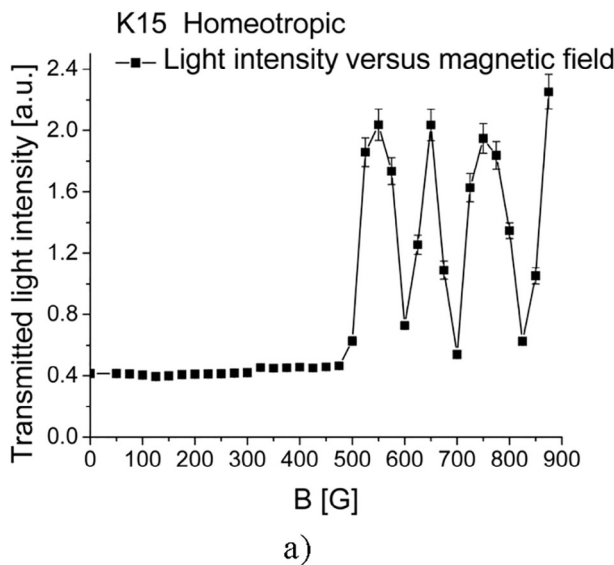


Fig. 7. Optical transmission response under static magnetic field for a) pure LC ($B_{c,K15}$ is about 510 G) and b) ferronematic H2 ($B_{c,H2}$ 625 G).

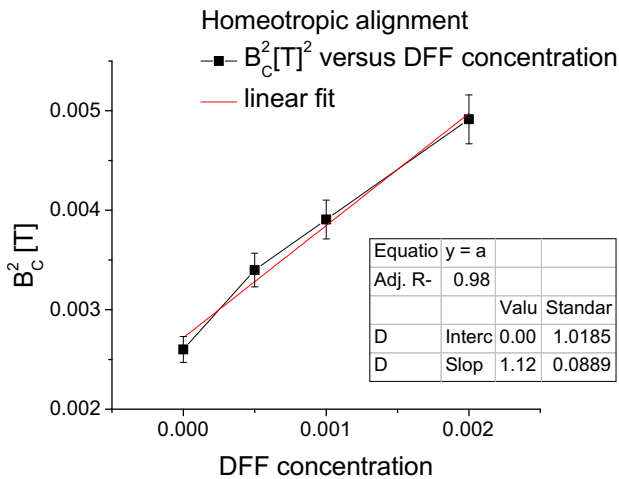


Fig. 8. Dependency of the square of the critical magnetic field on particle concentration in the case of homeotropic alignment.

Table 3
Critical magnetic field for the planar aligned samples.

	Sample	$B_{C(\text{planar})}$ [G]
1	P0	470
2	P1	540
3	P2	590
4	P3	735

4.2.2. Planar alignment

In Table 3 are presented the experimentally obtained values of the critical magnetic field at the Fredericksz for planar aligned samples. The critical magnetic field for the FN increases with the DFF particle concentration, in agreement with Eq. (11).

As in the previously discussed case of homeotropic alignment, the increase of the magnetic field will result in a competition of opposing factors: the stabilization of the orientation of the magnetic particles and the decrease of the LC matrix orientation, since $\vec{B} \perp \vec{n}$. Magnetic anisotropy of the LC is positive, the critical magnetic field for the Fredericksz transition increases.

In Fig. 9 is presented the dependency of the square of the critical magnetic field on particle concentration. For the same values of the constants as above, the anchoring energy was found $W' \cong 1.4 \cdot 10^{-7} \text{ N/m}$.

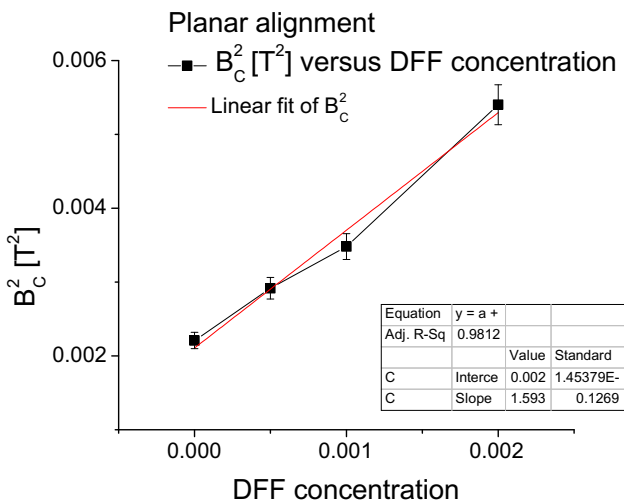


Fig. 9. Dependency of the square of the critical magnetic field on particle concentration in the case of planar alignment.

5. Conclusions

A new FN was obtained by using specially synthesized ferrite particles functionalized with phenyl terminal groups. These so-called “hairy” particles are compatible with K15 nematic LC, which presents phenyl groups. The alignment of the LC to the particle is homeotropic.

Mixtures of different concentrations have been prepared and studied under homeotropic and planar alignment substrate conditions. The mixtures exhibited long term stability (month-order).

It was found that, when applying a small magnetic field perpendicular to the glass plates alignment conditions, homeotropically aligned, the FN sample passes in a birefringent state, due to the molecular reorientation of the LC matrix, driven by the magnetic particle. Applications of this type of composite systems can be considered the magnetically controlled devices for information processing and storage [27].

The action of the magnetic field on the FN is also studied using the laser light transmitted through the sample under static magnetic field. The critical magnetic field corresponding to the Fredericksz transition experimentally determined showed an increase with particle concentration as predicted by Burylov and Raikher theory.

Acknowledgments

The author thanks dr. Dan Donescu, ICECHIM-Bucharest, Romania, for providing the dimethylphenyl ferrite particles and for useful discussions and professor Eleonora Rodica Bena, University Politehnica of Bucharest, for valuable discussions.

References

- [1] R. Reinitzer, Monatshefte Chemie, 9, (1898), 421 and Liquid Crystals, 5, 1, (1989), 7–18.
- [2] O. Lehman, Feitschrift fur Physikalische Chemie 4 (1989) 464–472.
- [3] F. Brochard, P.G. de Gennes, J. Phys. (Paris) 31 (1970) 691–708.
- [4] P. Toledano, A.M. Figueiredo Neto (Eds.), Phase Transition in Complex Fluids, World Scientific, Singapore, 1998.
- [5] F.C.M. Freire, C. Dascalu, R. Atasei, A.L. Alexe-Ionescu, G. Barbero, Appl. Phys. Lett. 99 (1) (2011) 014101-1–014101-3.
- [6] M. Micutz, M. Iliș, T. Staicu, F. Dumitrașcu, I. Pasuk, Y. Molard, T. Roisnel, V. Circu, Dalton Trans. 43 (3) (2014) 1151–1161.
- [7] V. Circu, T.J. Gibbs, L. Omnès, P.N. Horton, M.B. Hursthouse, D.W. Bruce, J. Mater. Chem. 16 (44) (2006) 4316–4325.
- [8] T.Y. Tsai, C.Y. Lee, C.J. Lee, W.C. Chang, W. Lee, P.C. Chen, J. Phys. Chem. Solids 71 (4) (2010) 595–599.
- [9] A. Hinojosa, S.C. Sharma, Appl. Phys. Lett. 97 (8) (2010) 081114.
- [10] C. Rosu, D. Manaila-Maximean, D. Donescu, S. Frunza, A.R. Sterian, Mod. Phys. Lett. B 24 (01) (2010) 65–73.
- [11] P. Oswald, G. Poy, F. Vittoz, V. Popa-Nita, Liq. Cryst. 40 (6) (2013) 734–744.
- [12] V. Popa-Nita, S. Kralj, J. Chem. Phys. 132 (2) (2010) 024902.
- [13] A.F. Neto, M.M.F. Saba, Phys. Rev. A 34 (4) (1986) 3483.
- [14] E. Petrescu, R.E. Bena, C.J. Cîrtoaje, Magn. Mater. 336 (2013) 44–48.
- [15] V. Berejnov, J.-C. Bacri, V. Cabuil, R. Perzynski, Y. Raikher, Europhys. Lett. 41 (5) (1998) 507–512.
- [16] V. Berejnov, Y. Raikher, V. Cabuil, J.C. Bacri, R. Perzynski, J. Colloid Interface Sci. 199 (2) (1998) 215–217.
- [17] R. Somoghi, R. Ianchis, M. Ghiurea, V. Purcar, D. Donescu, J. Optoelectron. Adv. Mater. 15 (5–6) (2013) 583–588.
- [18] D. Mănilă-Maximean, C. Cîrtoaje, O. Dănilă, D. Donescu, J. Magn. Mater. 438 (2017) 132–137.
- [19] C. Cîrtoaje, E. Petrescu, Physica E 84 (2016) 244–248.
- [20] S.H. Chen, N.M. Amer, Phys. Rev. Lett. 51 (25) (1983) 2298.
- [21] S.V. Burylov, Y.L. Raikher, Phys. Lett. A 149 (5–6) (1990) 279–283.
- [22] S.V. Burylov, Y.L. Raikher, J. Magn. Mater. 122 (1993) 62–65.
- [23] S.V. Burylov, Y.L. Raikher, Mol. Cryst. Liq. Cryst. 258 (1) (1995) 123–141.
- [24] C. Motoc, E. Petrescu, Mod. Phys. Lett. B 12 (13) (1998) 529–540.
- [25] R.E. Bena, E. Petrescu, J. Magn. Mater. 248 (2) (2002) 336–340.
- [26] C. Cîrtoaje, University “politehnica” of bucharest scientific bulletin-series a-applied, Math. Phys. 76 (1) (2014) 187–196.
- [27] V.I. Zadorozhnyi, V.Y. Reshetnyak, A.V. Kleshchonok, T.J. Sluckin, K.S. Thomas, Mol. Cryst. Liq. Cryst. 475 (1) (2007) 221–231.
- [28] P. Pieransky, F. Brochard, E. Guyon, J. Phys. 34 (1973) 35–48.

See discussions, stats, and author profiles for this publication at: <https://www.researchgate.net/publication/316567720>

Novel Colloidal System: magnetite–polymer Particles/Lyotropic Liquid Crystal under Magnetic Field

Article in *Journal of Magnetism and Magnetic Materials* · April 2017

DOI: 10.1016/j.jmmm.2017.02.034

CITATIONS

0

READS

52

4 authors, including:



Doina Manaila Maximean

University Politehnica of Bucharest, Buchare...

57 PUBLICATIONS 141 CITATIONS

SEE PROFILE



Cristina Cirtoaje

Polytechnic University of Bucharest

31 PUBLICATIONS 36 CITATIONS

SEE PROFILE



Octavian Danila

Polytechnic University of Bucharest

19 PUBLICATIONS 37 CITATIONS

SEE PROFILE

Some of the authors of this publication are also working on these related projects:



The study physical properties of micro-particles organized with nematic liquid crystals [View project](#)

All content following this page was uploaded by [Octavian Danila](#) on 26 February 2018.

The user has requested enhancement of the downloaded file.



Research articles

Novel colloidal system: Magnetite-polymer particles/lyotropic liquid crystal under magnetic field



D. Mănăilă-Maximean^{a,*}, C. Cîrtoaje^a, O. Dănilă^a, D. Donescu^b

^a Physics Department, Faculty of Applied Sciences, 'Politehnica' University of Bucharest, 313 Spl. Independenței, R-060082 Bucharest, Romania

^b ICECHIM, 202 Spl. Independenței, R-060021 Bucharest, Romania

ARTICLE INFO

Article history:

Received 18 November 2016

Received in revised form 17 February 2017

Accepted 19 February 2017

Available online 28 April 2017

Keywords:

Lyotropic liquid crystals

Magnetic nanomaterials

Ferronematics

Colloidal particles

Nanocomposites

Fréedericksz transition

ABSTRACT

We obtained a new highly ordered colloidal composite using specially manufactured magnetite-polymer nanoparticles and lyotropic liquid crystal. A good compatibility between the components was ensured by the functionalization of the particles during their synthesis. We studied the laser light transmission for the mixtures filled in sandwich-glass cells with homeotropic and planar treatment of the surfaces under external magnetic field. The Fréedericksz transition critical field was estimated, and its' behavior was compared to our new theoretical model based on the Brochard-de Gennes one.

© 2017 Elsevier B.V. All rights reserved.

1. Introduction

Liquid crystals (LC) have been in the center of attention for the last four decades, when their application in displays attracted the interest of companies, scientists and engineers. Liquid crystals are characterized by the presence of orientational order and total or partial absence of positional order [1]. Due to their properties, they have proven themselves extremely useful in a variety of application fields, from optics, electronics, to medicine and biology. For medicine and biology, lyotropic liquid crystals are favored to thermotropic ones. In lyotropic LCs, the known phase transitions (smectic, nematic, isotropic) [2] are induced by a variation in the concentration of chemical compounds in a dissolving liquid, such as water. When used in conjunction with magnetite particles, new composite materials known as ferronematics are obtained [3,4]. These composites exhibit distinct characteristics (biocompatibility, non-immunogenic, non-toxic) and can be successfully used in industrial and biomedical applications, including magnetic drug targeting, hyperthermia and magnetic separation of cells. By incorporating a certain metal in the liquid crystal molecule, unique properties are obtained regarding the colour, polarizability, electric and magnetic properties [5,6]. In order to maintain their characteristics, homogeneity throughout the composite must be preserved.

This is generally achieved by introducing a surfactant [7,8], chosen in such a way that it anchors itself to the surface of the particle, forming a 'hairy' particle [9,10]. A better compatibility is obtained when the particles are especially synthesized to be compatible with a specific liquid crystal [11]. We present a new colloidal composite formed by combining a specially designed nano-structured magnetite-polymer and a lyotropic nematic liquid crystal. The magnetite-polymer composite was dispersed in a lyotropic liquid crystal based on sodium dodecyl sulfate (SDS), decanol (DeOH) and water. The mixture exhibited long term stability (month-order). The structural units of these lyotropic liquid crystalline materials are anisotropic micelles. Mixtures with two different amphiphiles show three nematic phases (calamitic, discotic and biaxial), where micelles have orthorhombic symmetry or flattened prolated ellipsoid shape [12,13]. Our samples were created using glass slabs, with planar and homeotropic alignments on the anchoring surface. The critical field for magnetic Fréedericksz transition B_c was estimated using the optical method presented in [14,15]. A laser beam was sent through the LC sample placed under crossed polarizers, while the magnetic field was gradually increased. When the field reaches a critical value B_c , the LC's molecular director exhibits a change in orientation, leading to a variation of the refractive index [16]. This, in turn, leads to a change in the intensity of the emerging laser beam, indicating the start of the transition [17].

* Corresponding author.

E-mail address: manaila@physics.pub.ro (D. Mănăilă-Maximean).

2. Experimental methods

2.1. Composite particles

To obtain a good chemical compatibility between the colloidal particles and the liquid crystal we used a novel polystyrene latex containing magnetite (Fe_3O_4) with covalent bonds to the polymeric chains, functionalized with alkoxy-silanes containing double bonds, synthesized as in [18]. The high-resolution TEM (HRTEM) images for the hybrid-type latex magnetite-polymer show magnetite crystals of 5–15 nm anchored within polymeric chains of tens of nanometers. A full characterization has previously been performed on the resulting magnetite-polymer particles in [18].

2.2. Sample preparation

The magnetite-polymer particles were mixed with a lyotropic liquid crystal, in two concentration versions, 0.1% and 0.2% b.w. Homogenization of the mixture was performed by ultrasound techniques. The concentrations of the components of the lyotropic LC are: 28.2% sodium dodecyl sulfate, 5.7% decanol and 66.1% water. From a structural point of view, the liquid crystal forms discotic nematic domains [19,20]. The samples containing the mixtures were manufactured using glass plates, with a spacing of 100 μm . To produce surface alignments, the following steps were executed: for a homeotropic alignment, a solution of DMOAP-metaxibenzen-butyl-anilin (N-dimethyl-N-octyl-3-aminopropyl-t-rimexyl-xylil) was used. The ratio of the components is 899 parts isopropanol, 100 parts distilled water, and 1 part DMOAP. Deposition of the solution was performed by spin coating, and polymerized for 10 min at 100 $^\circ\text{C}$ in an oven. For the planar alignment, a solution of polyvinyl alcohol (1% volume fraction). The solution was deposited by spin coating, and heated at 120 $^\circ\text{C}$ for one hour, slowly cooled to room temperature, and rubbed with a smooth cloth in the desired direction of alignment. In Fig. 1, we illustrate the observation of the nematic phase of the SDS/DeOH/water system and its' planar alignment by Polarizing Optical Microscopy. For the homeotropic alignment, a dark image was obtained [20].

The nominal parameters of the samples are given in Table 1.

2.3. Experimental apparatus

The experimental setup used consists of the following: a linearly polarized, 632.8 nm, continuous wave He-Ne laser having an output power of 2.5 mW with superior spatial and spectral resolution, two crossed polarizers having a transmission ratio of 99.3% and an cross-polarization extinction ratio of 99.7%, a Silicon p-i-n photodiode for the visible range, equipped with a controllable

Table 1

Nominal construction parameters for the samples used in testing.

Sample Code	Composite	Concentration [%]	Alignment
H2	LLC/PM-171	0.1	Homeotropic
H3	LLC/PM-171	0.2	Homeotropic
P2	LLC/PM-171	0.1	Planar
P3	LLC/PM-171	0.2	Planar

amplification of up to 70 dB and 5% distortion level at maximum amplification, and a high precision multimeter for recording the voltage offered by the photodiode. The magnetic field generator is an electromagnet ranging from 0.1 to 1 Tesla, with poles having a diameter of 35 cm, an iron core of 10 cm, and a pole-to-pole distance of 10 cm. For the homeotropic alignment, in which the laser beam has to be parallel to the magnetic field, the iron core has been drilled in its' center, forming a 5-mm diameter hole, which does not affect the field homogeneity. The scheme of the setup is presented in Fig. 2. The sample was placed under crossed polarizers, at the center of the pole-to-pole distance of the electromagnet and the optical intensity of the laser field was observed for different values of the applied magnetic field [21].

3. Results and discussions

The magnetic Fréedericksz transition experiment was conducted for samples containing magnetite-polymer in liquid crystal, in the circumstances of planar and homeotropic alignments. The experimental data for the planar alignment of the LC samples is shown in Fig. 3, while the data for the homeotropic alignment of the samples is shown in Fig. 4.

It is known that in the discotic nematic phase, the natural orientation of the micelles leads to a homeotropic alignment, with the director normal to the anchoring surface [20]. In order to reorient the liquid crystal director using a magnetic field, when rotating from a homeotropic to planar orientation, the field must also compensate for this natural tendency, and therefore $B_{CH} > B_{CP}$. Studies conducted on pure discotic liquid crystals have established the critical magnetic field of the Fréedericksz transition $B_C \approx 1\text{T}$, and exhibits a decrease when the liquid crystal is mixed with magnetic responsive materials, regardless of the surface orientation of the liquid crystal [12]. Experimental plots of the emergent beam intensity vs. magnetic field were recorded for each sample, and the critical field was estimated. In our estimations, we have considered the critical field as the value of the magnetic field for which we begin to observe an increase in the intensity of the emerging beam. Within the transition zone, the estimated critical field values were determined as follows: For the planar

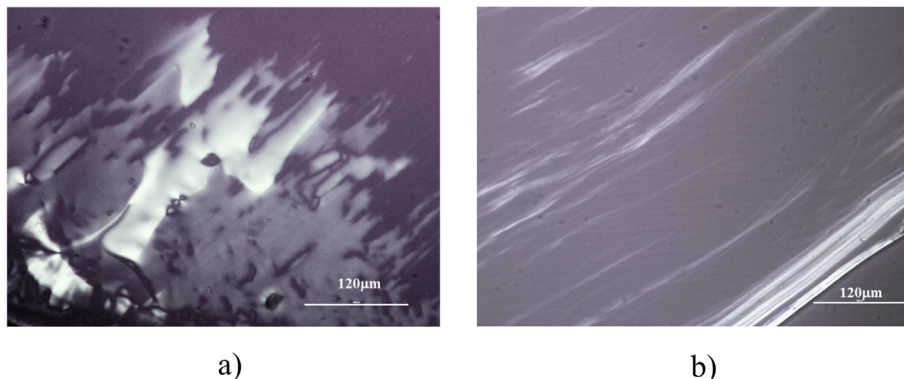


Fig. 1. Polarization Optical Microscopy images: observation of obtained nematic phase for SDS/DeOH/water system a) and planar alignment of LLC sample b).

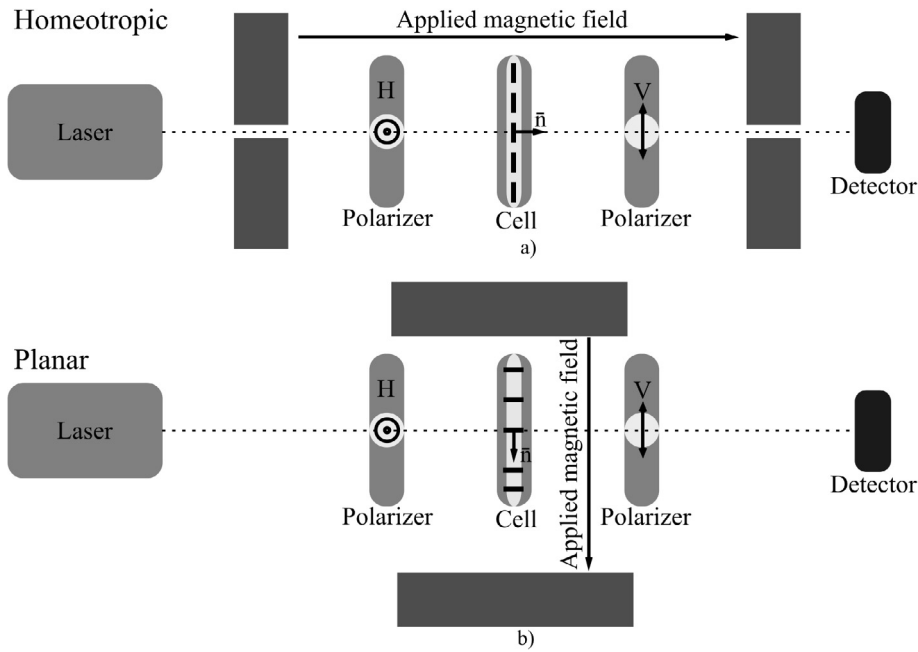


Fig. 2. The experimental setup for the two configurations: a) - homeotropic alignment, and b) - planar alignment. H and V denote a set of orthogonal polarization basis, rotated by 45° from the polarization axis of the laser beam.

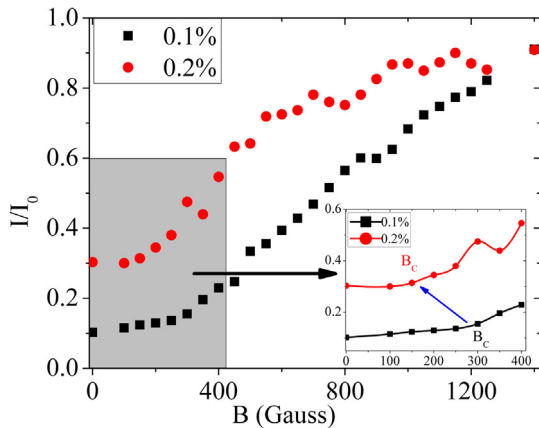


Fig. 3. Normalized transmitted light intensity through the sample having a planar alignment. Inset: The experimental data in the transition zone (gray area) was fitted by an interpolation (guide-eye) curve, and the critical field was roughly estimated as the value of the field at which the intensity of the transmitted light starts to increase.

alignment, the critical fields were $B_{CP_2} \approx 280 \pm 50$ Gauss, for the P2 (0.1%) sample and $B_{CP_3} \approx 150 \pm 20$ Gauss for the P3(0.2%) sample. For the homeotropic alignment, the critical fields were estimated at $B_{CH_2} \approx 700 \pm 30$ Gauss for the H2(0.1%) sample, and $B_{CH_3} \approx 600 \pm 20$ Gauss for the H3(0.2%) sample. These results are in good accordance with our theoretical reasoning presented at the beginning of this paragraph and with the theoretical model we develop in the next section.

4. Critical field determination model

According to the classic elastic continuum theory together with the Brochard-de Gennes model for the interaction between particles and liquid crystals [22], the free energy density for a magnetite-polymer/liquid crystal composite \mathcal{F} is given as:

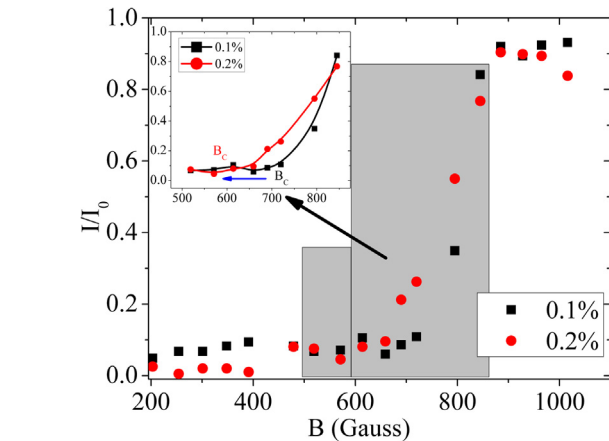


Fig. 4. Normalized transmitted light intensity through the sample having a homeotropic alignment. Inset: The experimental data in the transition zone (gray area) was fitted by an interpolation (guide-eye) curve, and the critical field was roughly estimated as the value of the field at which the intensity of the transmitted light starts to increase.

$$\mathcal{F} = \mathcal{F}_N + \mathcal{F}_{NB} + \mathcal{F}_{MB} + \mathcal{F}_T \quad (1)$$

where \mathcal{F}_N is the free energy density of the nematic liquid crystal, \mathcal{F}_{NB} is the free energy density component of the magnetic field, \mathcal{F}_{MB} accounts for the interaction between the magnetite-polymer particles and the magnetic field, and \mathcal{F}_T accounts for the interaction between the magnetite-polymer particle and the liquid crystal. The free energy density of the pure nematic liquid crystal is:

$$\mathcal{F}_N = \frac{1}{2} \left[k_1 \bar{n}(\nabla \bar{n})^2 + k_2 (\bar{n}(\nabla \times \bar{n}))^2 + k_3 (\bar{n} \times (\nabla \times \bar{n}))^2 \right] \quad (2)$$

where k_1 , k_2 and k_3 represent the elastic constants of the liquid crystals of the splay twist and bend deformations respectively, and \bar{n} represents the nematic director. The free energy density for the nematic-magnetic field interaction is:

$$\mathcal{F}_{NB} = -\frac{1}{2} \frac{\chi_a}{\mu_0} (\vec{n} \cdot \vec{B})^2 \quad (3)$$

where χ_a is the magnetic anisotropy of the liquid crystal, and \vec{B} is the magnetic field induction. The free energy density for the magnetite-polymer particles and magnetic field interaction is:

$$\mathcal{F}_{MB} = -\frac{1}{2} \frac{f\chi_{am}}{\mu_0} (\vec{m} \cdot \vec{B})^2 \quad (4)$$

where f represents the concentration of colloid in the liquid crystal, χ_{am} is the magnetic anisotropy of the particles, and \vec{m} is the orientation directory of the particles in the liquid crystal. The magnetite-polymer/LC interaction free energy density is:

$$\mathcal{F}_T = f \frac{kT}{V} \ln f \quad (5)$$

where k is Boltzmann's constant, T is the sample temperature, and V is the volume of each particle.

Due to their strong attraction forces, magnetite-polymer particles assemble together forming long chains [23]. Because the alignment of discotic liquid crystal micelles at the magnetite-polymer particles is homeotropic, the director of the magnetite \vec{m} and the director of the liquid crystal micelles \vec{n} are rigidly fixed, and perpendicular to each other. From a magnetic point of view, magnetite exhibits a positive magnetic anisotropy, and will rotate until $\vec{m} \parallel \vec{B}$, where \vec{B} denotes the magnetic field induction. Conversely, a nematic discotic LC exhibits a negative magnetic anisotropy [12], and therefore, it will rotate until $\vec{n} \perp \vec{B}$. When acting on the whole composite, the magnetic field will rotate both magnetite-polymer and liquid crystal micelles in the same direction. Due to the rigid bond between magnetite-polymer and LC micelles, the angle between \vec{m} and \vec{n} remains $\pi/2$, and therefore, any rotation of \vec{m} by an angle θ will induce the same angle rotation on \vec{n} . We will detail the theoretical model for both types of surface alignment of the glass cell in the following sections.

4.1. Planar alignment

When considering a planar alignment treatment of the glass cell, in the absence of the magnetic field, the director of the discotic LC is located in the surface plane of the glass cell, parallel to the grooves formed by rubbing. The structure of the composite in the

absence and presence of an external magnetic field are presented in Fig. 5. In our model, we will assume that $\vec{n}_0 \parallel Ox$, and $\vec{m}_0 \parallel Oz$. The magnetic field will act on Ox , and will rotate the whole composite structure with the same angle θ , as a result of the rigid bond between the discotic micelles to the magnetite chain.

Upon rotation, the nematic and magnetite directors are:

$$\vec{n} = \vec{e}_x \sin \theta + \vec{e}_z \cos \theta \quad (6)$$

$$\vec{m} = -\vec{e}_x \cos \theta + \vec{e}_z \sin \theta \quad (7)$$

where \vec{e}_x and \vec{e}_z represent the unit vectors of Ox and Oz , respectively. The free energy density for the liquid crystal becomes:

$$\mathcal{F}_N = \frac{1}{2} k_1 \sin^2 \theta \left(\frac{\partial \theta}{\partial z} \right)^2 + \frac{1}{2} k_3 \cos^2 \theta \left(\frac{\partial \theta}{\partial z} \right)^2 \quad (8)$$

In the same manner, we have:

$$\mathcal{F}_{NB} = -\frac{1}{2} \frac{\chi_a}{\mu_0} B^2 \cos^2 \theta \quad (9)$$

for the free energy density of the nematic-magnetic field interaction,

$$\mathcal{F}_{MB} = \frac{1}{2} \frac{f\chi_{am}}{\mu_0} B^2 \sin^2 \theta \quad (10)$$

for the free energy density of the interaction between the magnetite-polymer and the magnetic field, while \mathcal{F}_T remains unchanged. By applying the Euler-Lagrange equations on the total free energy density:

$$\frac{\partial}{\partial z} \left(\frac{\partial \mathcal{F}}{\partial \xi} \right) - \frac{\partial \mathcal{F}}{\partial \theta} = 0 \quad (11)$$

where the substitution $\xi = \frac{\partial \theta}{\partial z}$ has been made, Eq. 11 becomes:

$$k_1 \frac{\partial^2 \theta}{\partial z^2} + B^2 \left(\frac{f\chi_{am} - \chi_a}{\mu_0} \right) \sin \theta \cos \theta = 0 \quad (12)$$

When working in the small angle regime ($\sin \theta \simeq \theta$, $\cos \theta \simeq 1$), the above equation becomes:

$$\frac{\partial^2 \theta}{\partial z^2} + \frac{B^2}{k_1 \mu_0} (f\chi_{am} - \chi_a) \theta = 0 \quad (13)$$

By substituting:

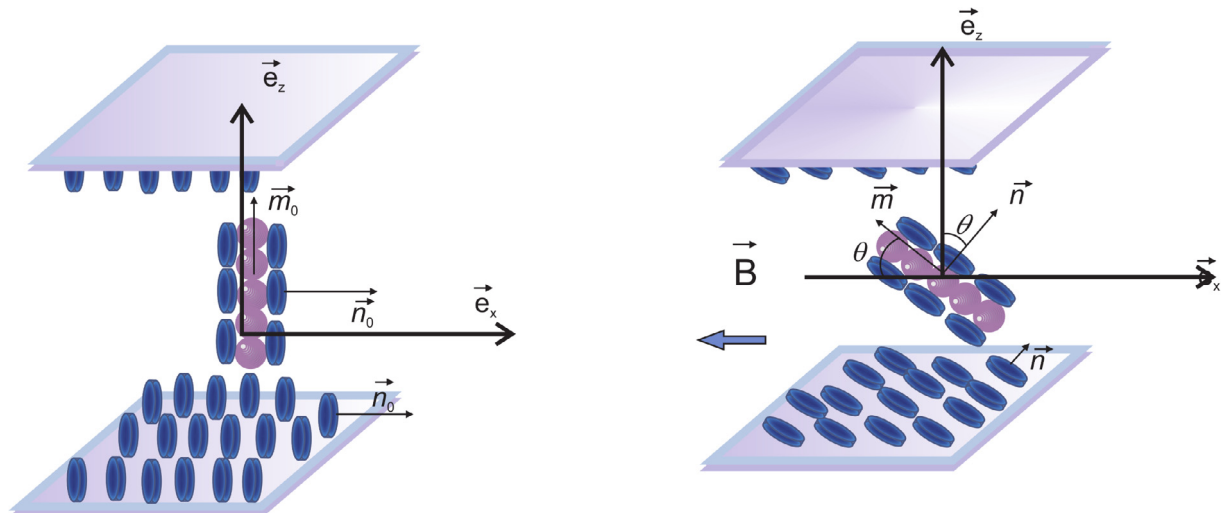


Fig. 5. Illustration of the structure of the magnetite-polymer/LC composite in the planar alignment context in the absence of the magnetic field (left side), and in the presence of the magnetic field (right side). To rotate the whole composite structure, the magnetic field is applied parallel to Ox .

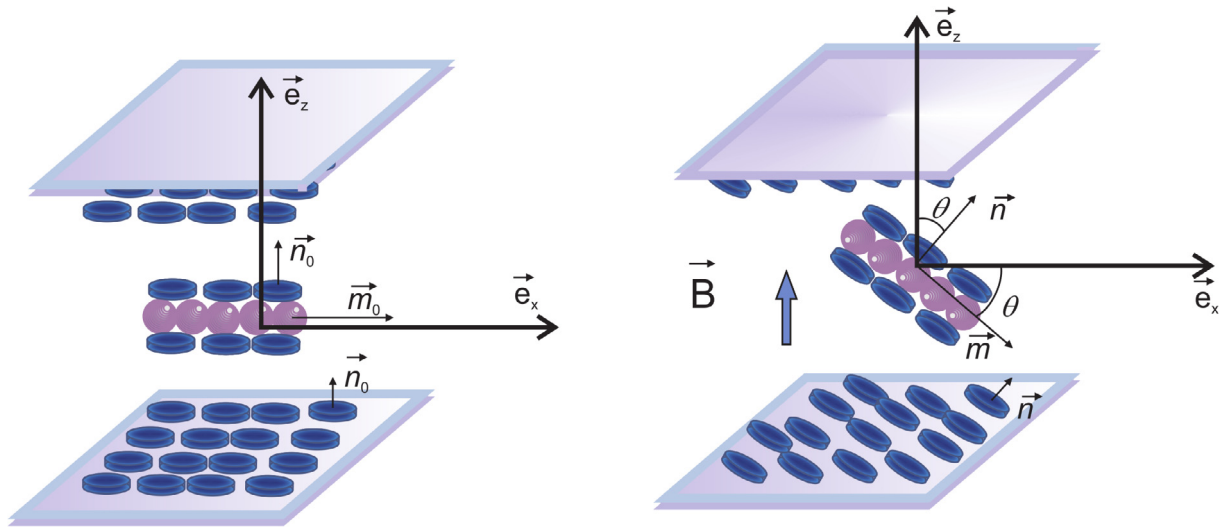


Fig. 6. Illustration of the structure of the magnetite-polymer/LC composite in the homeotropic alignment context in the absence of the magnetic field (left side), and in the presence of the magnetic field (right side). To rotate the whole composite structure, the magnetic field is applied parallel to Oz.

$$\eta^2 = \frac{B^2}{k_1 \mu_0} (f \chi_{am} - \chi_a) \quad (14)$$

Eq. (13) becomes a harmonic oscillator equation, having the general solution:

$$\theta(z) = C_1 \sin \eta z + C_2 \cos \eta z \quad (15)$$

Applying boundary conditions at $z = 0$ and $z = d$, where d is the thickness of the cell, we obtain:

$$C_2 = 0 \text{ and } \eta = \frac{\pi}{d} \quad (16)$$

and the corresponding critical field:

$$B_{CP}^2 = \left(\frac{\pi}{d}\right)^2 \frac{\mu_0 k_1}{f \chi_{am} - \chi_a} \quad (17)$$

This implies that in the case of discotic liquid crystals having $\chi_a < 0$, the critical field decreases with the increase of the concentration of the magnetite-polymer particles.

4.2. Homeotropic alignment

When considering the homeotropic alignment case, in the absence of the magnetic field, according to the planar alignment of the discotic LC, the director of the LC micelles \vec{n}_0 is perpendicular to the glass cell surface. The structure of the composite in the absence and in the presence of the magnetic field are presented in Fig. 6. In our model, we will consider that $\vec{n}_0 \parallel Oz$, $\vec{m}_0 \parallel Ox$, and the magnetic field acts on Oz.

By applying exactly the same model and approximations as in the planar alignment case, and by considering the rotated directors as:

$$\vec{n} = \vec{e}_z \cos \theta + \vec{e}_x \sin \theta \quad (18)$$

$$\vec{m} = -\vec{e}_z \sin \theta + \vec{e}_x \cos \theta \quad (19)$$

we obtain the critical field:

$$B_{CH}^2 = \left(\frac{\pi}{d}\right)^2 \frac{\mu_0 k_3}{f \chi_{am} - \chi_a} \quad (20)$$

The critical field exhibits the same monotonic behavior with the concentration f as in the case of the planar alignment. By corroborating the experimental values of the critical field with the theoret-

ical relations (20) and (17), the method can be used to determine the elastic constants k_1 and k_3 of the liquid crystal, in low magnetic fields (less than 0.1 T).

5. Conclusions

In this paper, we present a novel highly ordered structure in lyotropic liquid crystals, obtained by inserting specially synthesized magnetite-polymer nanoparticles in low concentrations. We investigate the optical transmission properties under an external magnetic field. The high positive anisotropy of magnetite combined with the negative anisotropy of the discotic lyotropic liquid crystal strongly decreases the Fréedericksz transition threshold to less than 1000 Gauss. This is in good agreement with results in literature [12,22]. Thus, the system acts like a nematic liquid crystal with a low transition critical field, making it suitable for magneto-optical applications.

References

- [1] S. Chandrasekar, *Liquid Crystals*, 2nd Edition., Oxford University Press, 1992.
- [2] P.G. De Gennes, J. Prost, *The Physics of Liquid Crystals*, second ed., Clarendon Press, 1993.
- [3] S. Odenbach, *Colloidal Magnetic Fluids: Basics, Development and Applications of Ferrofluids*. Lecture Notes in Physics, Springer, Berlin, 2009.
- [4] C.Y. Matuo, F.A. Tourinho, M.H. Souza, J. Deperyot, A.M. Figueiredo Neto, Lyotropic ferromagnetic liquid crystals based on new Ni, Cu and Zn ionic magnetic fluids, *Braz. J. Phys.* 32 (2002) 458–463.
- [5] V. Circu, T.J.K. Gibbs, L. Omnès, P.N. Horton, M.B. Hursthouse, D.W. Bruce, Orthometallated palladium(II) imine complexes as candidate materials for the biaxial nematic phase. crystal and molecular structure of three palladium imine complexes, *J. Mater. Chem.* 18 (2006) 4316–4325.
- [6] M. Micutz, M. Iliș, T. Stăicu, F. Dumitrașcu, I. Pasuk, Y. Molard, T. Roisnel, V. Circu, Luminescent liquid crystalline materials based on palladium(II) imine derivatives containing the 2-phenylpyridine core, *Dalton Trans.* 43 (2014) 1151–1161.
- [7] H. Stark, Physics of colloidal dispersions in nematic liquid crystals, *Phys. Rep.* 351 (2001) 387–474.
- [8] D. Mănăilă-Maximean, G. Bossis, F. Giulieri, C. Metayer, Study of composite system: silica colloidal particles in nematic liquid crystal, *Mol. Cryst. Liq. Cryst.* 417 (2004) 227–233.
- [9] M. Ghiurea, R. Munteanu, D. Donescu, D. Mănăilă-Maximean, The interaction of lyotropic liquid crystals with divinyl-benzene-maleic anhydride copolymer particles, *J. Optoelectron. Adv. Mater. Rapid Commun.* 4 (2010) 588–591.
- [10] C. Roșu, D. Mănăilă-Maximean, D. Donescu, S. Frunză, A.R. Sterian, Influence of polarizing electric fields on the electrical and optical properties of polymer-clay composite system, *Mod. Phys. Lett. B* 65–73 (2010).
- [11] D. Mănăilă-Maximean, C. Roșu, L. Frunză, P. Ganea, D. Donescu, M. Ghiurea, Investigations of electrical and electro-optical properties of liquid crystal/copolymer-clay nanostructured systems, *Mol. Cryst. Liq. Cryst.* 546 (2011) 143–163.

- [12] A.M. Figueiredo Neto, S.R.A. Salinas, *The Physics of Lyotropic Liquid Crystals: Phase Transitions and Structural Properties*, Oxford University Press, New York, 2005.
- [13] P. Tolédano, A.M. Figueiredo Neto (Eds.), *Phase Transition in Complex Fluids*, World Scientific, Singapore, 1998.
- [14] E. Petrescu, E.R. Bena, Influence of the magnetic field and laser fields on the director structures of a ferrocholesteric liquid crystal in homeotropic cells, *J. Magn. Magn. Mater.* 320 (2008) 299–303.
- [15] E. Petrescu, E.R. Bena, Surface anchoring energy and the Fréedericksz transitions in ferromagnetics, *J. Magn. Magn. Mater.* 321 (2009) 2757–2762.
- [16] P.A. Kosyrev, J. Qi, N.A. Priezjev, R.A. Pelcovits, G.P. Crawford, Virtual surfaces, director domains, and the Fréedericksz transition in polymer-stabilized nematic liquid crystals, *Appl. Phys. Lett.* 81 (2002) 2986–2988.
- [17] C. Cîrtoaje, C. Moțoc, E. Petrescu, New magnetic method for determining of elastic constants and rotational viscosity coefficient in nematic liquid crystals, *U.P.B. Sci. Bull. A - Appl. Math. Phys.* 72 (2010) 243–246.
- [18] D. Donescu, R. Somoghi, C.I. Spătaru, D. Mănăilă-Maximean, M. Panaitescu, E. Vasile, C.L. Nistor, Hybrid polymeric latexes containing magnetite, *Colloid Polym. Sci.* 291 (2013) 2345–2358.
- [19] P.O. Quist, B. Halle, I. Furo, Micelle size and order in lyotropic nematic phases from nuclear spin relaxation, *F. Chem. Phys.* 96 (1992) 3875.
- [20] P. Poulin, N. Francès, O. Mondain-Monval, Suspension of spherical particles in nematic solutions of disks and rods, *Phys. Rev. E* 59 (1999) 4384.
- [21] G. Iacobescu, A.L. Păun, C. Cîrtoaje, Magnetically induced Fréedericksz transition and relaxation phenomena in nematic liquid crystals doped with azo-dyes, *J. Magn. Magn. Mater.* 320 (2008) 2180–2184.
- [22] F. Brochard, P.G. De Gennes, Theory of magnetic suspension in liquid crystals, *J. Phys. (Paris)* 31 (1970) 691–708.
- [23] C. Cîrtoaje, E. Petrescu, C. Stan, D. Creangă, Ferromagnetic nanoparticles suspensions in twisted nematic, *Physica E* 79 (2016) 38–43.